

A Thesis Submitted for the Degree of PhD at the University of Warwick

Permanent WRAP URL:

<http://wrap.warwick.ac.uk/173116>

Copyright and reuse:

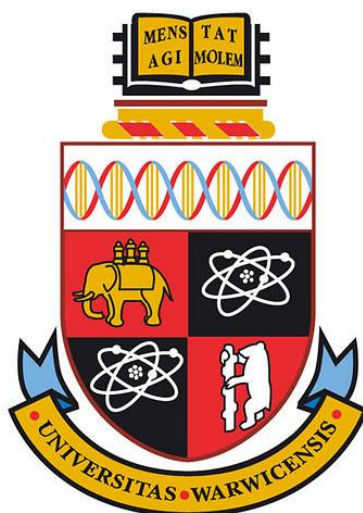
This thesis is made available online and is protected by original copyright.

Please scroll down to view the document itself.

Please refer to the repository record for this item for information to help you to cite it.

Our policy information is available from the repository home page.

For more information, please contact the WRAP Team at: wrap@warwick.ac.uk



Engineered Diamond Devices for Next Generation Applications

by

Joshua James Tully

A Thesis Submitted to the University of Warwick for the
Degree of Doctor of Philosophy in Chemistry

Department of Chemistry

April 2022



“There was a button, I pushed it.”

"Jesus Christ. That really is how you go through life, isn't it?"

- **James S.A. Corey, Nemesis Games**

Table of Contents

Table of Contents	I
List of Figures	VII
List of Tables	XV
List of Abbreviations	XVII
Acknowledgments	XX
Declarations	XXI
Abstract	XXIII
1 Introduction.....	1
1.1 Diamond.....	1
1.2 Diamond Synthesis.....	2
1.2.1 High-Pressure High Temperature.....	2
1.2.2 Chemical Vapour Deposition.....	3
1.3 Diamond Materials.....	4
1.3.1 Boron Doping in Diamond.....	4
1.4 Diamond Processing.....	8
1.4.1 Abrasive Polishing.....	8
1.4.2 Nanosecond Laser Processing.....	9
1.4.3 Ion Implantation.....	11
1.5 Electrochemistry.....	12
1.5.1 Three-Electrode Electrochemistry.....	12
1.5.2 Cyclic Voltammetry.....	13
1.5.3 Electrodes Under Steady State Control.....	14
1.5.4 Rotating Ring Disk.....	16
1.5.5 Two-Electrode Electrochemistry.....	17

1.5.6 Bipolar Electrochemistry.....	18
1.6 Applications of Intrinsic Diamond.....	19
1.6.1 Quantum Applications.....	19
1.7 Applications of Boron Doped Diamonds.....	20
1.7.1 Electrochemical Advanced Oxidation Processes.....	20
1.7.2 Electrochemical Ozone Production.....	22
1.8 3D Printing as a Tool for Research.....	24
1.8.1 Fusion Deposition Modelling.....	25
1.8.2 Stereolithography.....	26
1.9 Aims and Objectives.....	28
1.10 References.....	30
2 Materials and Methods.....	39
2.1 Materials.....	39
2.1.1 Single Crystal Diamond Materials.....	39
2.1.2 Boron Doped Diamond Materials.....	39
2.1.3 Carbon Materials.....	42
2.2 Chemicals.....	42
2.2.1 FcTMA.....	43
2.3 Fabrication Techniques.....	43
2.3.1 Laser Processing.....	43
2.3.2 Acid Cleaning.....	44
2.3.3 Thermal Annealing.....	44
2.3.4 Metal Film Deposition.....	44
2.4 Characterisation.....	45
2.4.1 White Light Interferometry.....	45

2.4.2 Gwyddion Analysis Software.....	47
2.4.3 Electron Microscopy.....	47
2.4.4 Electron Backscatter Diffraction.....	48
2.5 Electrochemical Techniques.....	48
2.5.1 Quinone Surface Coverage Measurements.....	48
2.5.2 Redox Mediator Tests.....	49
2.5.3 Uncompensated Resistance Measurements.....	50
2.6 Additive Manufacture.....	50
2.7 Electron Paramagnetic Resonance Spectroscopy.....	51
2.8 References.....	53
3 Optimisation of the Electrochemical Etch Step of Diamond Nanoscale Membrane Production.....	55
3.1 Introduction.....	55
3.2 Experimental Methods.....	56
3.2.1 Materials.....	56
3.2.2 Diamond Sample Preparation.....	56
3.2.3 Implant Simulations.....	57
3.2.4 Electrochemical Etching.....	58
3.2.5 Image Analysis.....	59
3.2.6 Tabulation of Experiments Conducted.....	59
3.2.7 Electron Paramagnetic Resonance Spectroscopy.....	60
3.2.8 UV-Vis Measurement of H ₂ O ₂	61
3.3 Results and Discussions.....	61
3.3.1 Measuring the Material Etch Rate.....	61
3.3.2 Electrochemical Etching in Low Conductivity Solutions.....	64
3.3.3 Electrochemical Etching in High Conductivity Solutions.....	65

3.3.4 Electron Paramagnetic Resonance Studies.....	66
3.3.5 The Effect of Concentration and pH in Sulphate Media.....	71
3.3.6 The Effect of Temperature in Sulphate Media.....	74
3.4 Conclusions.....	75
3.5 References.....	77
4 Understanding Anode Corrosion in BDD Advanced Oxidation Systems.....	81
4.1 Introduction.....	81
4.2 Experimental Methods.....	84
4.2.1 BDD Materials.....	84
4.2.2 Cell Design.....	84
4.3 Results and Discussions.....	85
4.3.1 Experimental Methodology.....	85
4.3.2 Solution Composition.....	88
4.3.3 BDD Material.....	89
4.3.4 Organic Content Nature.....	91
4.3.5 Current Density.....	94
4.3.6 Polarity Switching.....	95
4.3.7 Perfluorooctane Sulfonic Acid.....	97
4.4 Conclusions.....	98
4.5 References.....	99
5 The Importance of Stable Non-Diamond Carbon in Electrochemical Generation of Ozone using Boron Doped Diamond Electrodes	101
5.1 Introduction.....	101
5.2 Experimental Methods.....	102
5.2.1 Cell Design and Construction.....	102
5.2.2 Planar Electrode Creation.....	103

5.2.3 Planar Electrode Cell Assembly.....	105
5.2.4 Perforated Electrode Creation.....	106
5.2.5 Glassy Carbon Electrode Creation.....	107
5.2.6 Perforated Cell Assembly.....	108
5.2.7 Ozone Measurements.....	109
5.2.8 Long-Term Testing.....	110
5.2.9 Hydrogen Plasma Treatment.....	110
5.3 Results and Discussions.....	111
5.3.1 Measurement Metrics.....	111
5.3.2 The Effect of NDC Incorporation into Planar Electrodes.....	112
5.3.3 The Effect of NDC Incorporation into Perforated Electrodes.....	114
5.3.4 Performance of a Glassy Carbon Electrode.....	116
5.3.5 Effect of Electrode Thickness on Perforated Electrode Performance.....	117
5.3.6 Long-Term Testing.....	118
5.3.7 Hydrogen Plasma Treatment on Perforated Electrodes.....	119
5.4 Conclusions.....	121
5.5 References.....	122
5a Appendix to Chapter 5.....	124
A5.1 Planar Electrode Cells.....	124
A5.2 Perforated Electrode Cells.....	125
A5.3 Perforated Electrode Cells with Different BDD Thicknesses.....	127
A5.4 Long Term Testing.....	128
A5.5 Hydrogen Plasma Treatment.....	129
6 A Do-It-Yourself Method for Making Custom Rotating Ring Disk Electrodes.....	130
6.1 Introduction.....	130

6.2 Experimental Methods.....	131
6.2.1 Electrode Preparation.....	131
6.2.2 3D Printing.....	132
6.2.3 Bill of Materials.....	132
6.2.4 Electrochemical Characterisation.....	132
6.2.5 Pt Deposition.....	133
6.2.6 Hydrogen Peroxide Experiments.....	133
6.3 Results and Discussions.....	134
6.3.1 RRDE Fabrication.....	134
6.3.2 Thread Sizing.....	135
6.3.3 Step-by-Step Assembly.....	136
6.3.4 Rough Electrodes.....	138
6.3.5 Foil and Rod Materials.....	138
6.3.6 RRDE Characterisation.....	139
6.3.7 Collection Efficiency Characterisation.....	141
6.3.8 Pt Deposition and Hydrogen Peroxide Calibration.....	143
6.3.9 Case Study: Hydrogen Peroxide Generation.....	146
6.4 Conclusions.....	148
6.5 References.....	150
7 Conclusions and Further Work.....	153

List of Figures

Figure 1.1: Representations of diamond structure and the three main crystal directions. a) 3D ball and stick representation of the diamond unit cell where $a_0 = 0.357$ nm. b) Top, representations of the three main crystal directions in diamond. Bottom, ball and stick representations along those crystal directions where red atoms are carbon atoms on the surface and black atoms are carbons on plane below.....	1
Figure 1.2: Phase diagram for carbon showing the regions of interest for diamond growth and synthesis. Adapted from Balmer et. al.....	3
Figure 1.3: Electronic band structure of diamond with various levels of boron doping. Coloured areas represent filled states. a) Intrinsic diamond, a wide band gap insulator with the Fermi level (E_f) equidistant between the conduction and valence bands. b) Heavily boron doped diamond ($\sim 10^{20}$ atoms cm^{-3}), leading to overlap of the dopant wavefunctions and metallic behaviour with E_f inside the dopant state. c) Extremely heavily boron doped diamond where the screening of impurities reduces the acceptor activation energy. Adapted from Blase et al.....	4
Figure 1.4: Ball and stick representation of the structure of boron doped diamond, showing the position the boron atom (blue) occupies in the lattice.....	5
Figure 1.5: (a) Schematic and (b) scanning electron microscopy (SEM) image of the side on growth of microcrystalline BDD. Both clearly show how the grains increase with size as the film thickness increases. (c) Optical image of freestanding microcrystalline BDD, which has been removed from the growth wafer, lapped on both sides, and laser cut into discs. Reproduced from Macpherson.....	6
Figure 1.6: Schematic of the mechanism of nanosecond-pulse laser ablation. a) Impurities in the diamond (black) absorb the laser radiation (green) heating it up (orange). b) Once the heated diamond reaches 2000°C it undergoes a transition to become graphite (grey). c) The graphite layer is heated until it reaches 4000°C and is vapourised (blue). d) The plume of carbon vapour absorbs some of the incident laser radiation and forms a plasma (purple). e) The pulse ends, the plume detaches.....	10
Figure 1.7: Plasma Formation during Single Pulse Laser Ablation for Different Values of Fluence. Reproduced from Hermani et al.....	10
Figure 1.8: a) HAADF STEM image with white rectangle indicating EELS survey area, pixel size $\frac{1}{4}$ 33 nm. b) EELS spectra of BDD (green), graphite (blue) and amorphous carbon (red),	

obtained from the BDD substrate, layers I and II respectively. Spectra have been scaled to fit the axis. c) Multilinear Least Squares fitting of the 3 spectra in b), showing the distribution of BDD, graphite and amorphous carbon. d) High magnification BF TEM image confirming that layer I is composed of graphite. Reproduced from Cobb et al.....11

Figure 1.9: Schematic of the implantation and lift-off process employed to produce sub- μm diamond membranes.....12

Figure 1.10: Schematic of a typical 3-electrode electrochemical set-up. Current flows between the counter and working electrodes whilst potential is controlled between the working and reference electrodes. Adapted from Colburn et.al.....13

Figure 1.11: Schematics to show a) a CV potential waveform, b) a typical current-voltage shape observed for a reversible process on a macroelectrode.....14

Figure 1.12: Schematics to show a) the diffusion profile of a UME at most scan b) the diffusion profile for a UME at scan rates $\geq 10 \text{ V s}^{-1}$. c) a typical current-voltage response observed for a UME and RDE.....15

Figure 1.13: a) Schematic of a RRDE electrode showing a generalised redox process. b) Schematic of the current responses for the disk (red) and ring (blue) with approximately 30% collection efficiency.....16

Figure 1.14: Schematic of a typical 2-electrode electrochemical set-up. Current flows between the anode and cathode whilst the potential is controlled between them.....17

Figure 1.15: Schematic of a bipolar electrode set-up showing how the potential is dropped between the driving electrodes.....18

Figure 1.16: Schematic of the nitrogen (yellow) vacancy defect in diamond in a) the neutral charge state and b) the negative charge state.....19

Figure 1.17: Schematic of an FDM 3D Printer.....25

Figure 1.18: Schematic of an SLA 3D Printer.....27

Figure 2.1: In-Lens FE-SEM images of highly polished a) electroanalytical (EA) grade and b) electroprocessing (EP) grade BDD. SEM imaging is discussed in section 2.4.3.....40

Figure 2.2: Electron backscatter diffraction data for a) electroanalytical (EA) grade and b) electroprocessing (EP) grade BDD. The dotted squares represent the approximate areas of the FE-SEM from 2.1a and b respectively. EBSD is discussed in section 2.4.4.....41

Figure 2.3: SE2 detector FE-SEM images of the “as-grown” DIACHEM Condias surface used in this work at various magnifications.....	42
Figure 2.4: Schematic of the operation of a white light interferometer. Modified from O'Mahony et. al. and Schmit.....	46
Figure 3.1: Vacancy density plot for a 2 MeV implantation of carbon into single crystal diamond. The line (blue) indicates the minimum vacancy threshold for graphitisation. The shaded area (grey) indicates the region that is damaged above this threshold.....	57
Figure 3.2: Schematic of the etch cell showing the arrangement of diamond sample (yellow), electrodes (grey), and polycarbonate support (light blue). Front: a front view as seen by the USB microscope showing the diamond sample attached to the polycarbonate support and placed between the two platinum electrodes. Top: a top view showing how the diamond sample is aligned in plane with the electrodes. Side: a side view with the electrodes omitted for clarity which shows how the USB microscope images through the solution and polycarbonate support in transmission using a backlight to maximise the contrast between etched and un-etched areas of the sp^2 carbon.....	58
Figure 3.3: Top, optical image capture of the etch progress on a 4.2 mm × 4.2 mm HPHT diamond in aerated 250 mM K_2SO_4 solution with 30 V applied between two Pt electrodes, from $t = 0$ to $t = 2$ hr. Each image is separated by approximately 8 min of etching in 250 mM K_2SO_4 . Anode and cathode positioned to the left and right of the frame (out of view), respectively. The origin of the white spots, seen most prominently in the middle images, is currently unknown, but these were only observed in about 10% of samples investigated. Bottom, photograph of the membrane after separation.....	62
Figure 3.4: Exemplar etch profile from in-situ transmission microscope imaging. The raw data points ($n = 6500$, red) are fitted with a sigmoidal function (black) and three distinct regions are defined. Etching is considered complete at 3 hr as no visible remnants of the sp^2 carbon layer remains. Conditions: 4.1 mm × 4.1 mm CVD sample in aerated 250 mM solution of K_2SO_4 with 30 V applied between the electrodes at 25°C. Raw image capture for this plot can be seen in Figure 3.3.....	63
Figure 3.5: EPR spectra after 15 mins of applied 30 V in 400 mM boric acid. Experimental conditions: a non-saturating microwave power of 20 mW; central magnetic field, 352 mT; scan width, 10 mT and a modulation amplitude, 0.05 mT. All spectra reported are an average of 9 scans.....	65

Figure 3.6: a) Etch profiles for etching of 4.2 mm × 4.2 mm HPHT single crystal diamonds in aerated 250 mM solutions of KNO₃ (blue), KCl (black) and K₂SO₄ (pink). Inset, etch profile for KCl and K₂SO₄ from 0–2 hr, the inset has the same units as the larger plot. 30 V was applied between the two Pt electrodes until etching was complete. Data was collected as n = 1. b) Comparison of the bulk etch rates for each different electrolyte, plus aerated 400 mM H₃BO₃.....66

Figure 3.7: EPR spectra after 15 minutes of applied 30 V in 250 mM solutions of aerated KNO₃, KCl and K₂SO₄ (blue), as well as simulated spectra for the DMPO-OH spin adduct and D' quartz signal (black). Experimental Conditions: A non-saturating microwave power of 20 mW; central magnetic field, 352 mT; scan width, 10 mT and a modulation amplitude, 0.05 mT. All spectra reported are an average of 9 scans.....67

Figure 3.8: Concentration of H₂O₂ produced for each electrolysis time determined by UV/Vis measurement. In solutions of 250 mM KNO₃ (blue triangle) KCl (black circle), and K₂SO₄ (pink square) using two platinum electrodes at 30 V.....69

Figure 3.9: (a) Bulk etch rates for a 3.5 mm × 3.5 mm CVD single crystal diamond in aerated KNO₃ solution at 0 mM sulphate and 30, 60, 125, and 250 mM solutions of K₂SO₄. Lines added as guides to the eye and do not represent fits.....71

Figure 3.10: Etch rates for a 4.1 mm × 4.1 mm square CVD single crystal diamond in aerated solutions with constant sulphate (250 mM) comprised of K₂SO₄ and H₂SO₄, but with pH varying between 0.8 – 7.1. The solution was held at 25 °C.....73

Figure 3.11: a) Rate vs temperature plot for a 3.5 mm × 3.5 mm square HPHT single crystal diamond from 283, 303, 323, and 343 K in 50 mM H₂SO₄, 30 V was applied between two platinum electrodes until etching was complete. b) Arrhenius plot of etch rate versus 1000/T for a in 50 mM H₂SO₄. Data in this figure was completed as n=3.....74

Figure 3.12: Comparison of all etch solution and conditions trialled, and comparisons to the literature.....75

Figure 4.1: Rendering of the flow cell designed for BDD corrosion experiments. a) Exploded view showing all the cells components. b) Cross-section through the assembled cell showing the flow path for solution.....86

Figure 4.2: EP-BDD anode characterisation after a 72-hour electrolysis at 10,000 A m⁻² in 0.5 M K₂SO₄. a) WLI image of the surface, showing the smooth masked edge and rough eroded

region. b) photograph of the 10 mm diameter EP-BDD electrode showing the eroded region. c) Line profile in X across the centre of the WLI image showing the change in height.....87

Figure 4.3: WLI of the EP-BDD anodes after electrolysis in a) 0.5 M KNO₃, b) 0.5M KCl, c) 0.5 M K₂SO₄. Photographs of the 10 mm diameter EP-BDD anodes after electrolysis in d) 0.5 M KNO₃, e) 0.5M KCl, f) 0.5 M K₂SO₄.....89

Figure 4.4: Corrosion rates seen during a 72-hour electrolysis at 10,000 A m⁻² in a 0.5 M solution of K₂SO₄ with varied concentrations of Acetic Acid or Glucose. The corrosion rate for an EP-BDD electrode in just 0.5 M K₂SO₄ is 1.65 ± 0.08 nm hr⁻¹.....92

Figure 4.5: Corrosion rates seen during a 72-hour electrolysis at in a solution of 1 M acetic acid and 0.5 M K₂SO₄ at current densities from 2,500 to 15,000 A m⁻².....94

Figure 4.6: Average of the corrosion rates of both electrodes measured after a 72-hour electrolysis at in a solution of 1 M acetic acid and 0.5 M K₂SO₄. Switching intervals of 6, 60, 300, 450, and 600s were tested.....96

Figure 5.1: Left, white light interferometry images of the planar electrode surfaces. Right, Surface profiles showing the surface structure.....104

Figure 5.2: a) Render showing an internal view of one planar electrode half-cell with key components labelled. b) Photograph of the half-cell, showing the electrode, seal, and contact. c) Render of the full cell cross section, with blue arrows denoting the flow path through the cell.....105

Figure 5.3: a) Render showing an internal view of one perforated electrode half-cell with key components labelled. b) Photograph of the half-cell, showing the electrode, seal, and contact. c) Render of the full cell cross section, with blue arrows denoting the flow path through the cell. d) Example flow profiles of the perforated electrode cell showing the BDD electrodes (Black), Nafion membrane (Light Grey), cell body (Dark Grey), copper contacts (Orange) and flow path (Blue).....109

Figure 5.4: Schematic of the experimental set-up for ozone calibrations.....110

Figure 5.5: Schematic of the experimental set-up for long-term experiments.....111

Figure 5.6: a) a) EOP gradient in ppm A⁻¹ versus the deliberately incorporated solution accessible NDC fraction of the planar BDD electrodes. b) Peak current efficiency versus the solution accessible NDC fraction of the planar BDD electrodes. The potentials, ozone output, current efficiency, EOP gradient, and adj-R² for these data points can be found in the appendix, section A5.1.....113

Figure 5.7: a) Normalised EOP gradient in ppm cm² A⁻¹ versus the solution accessible sp² fraction of the perforated BDD electrodes. b) Peak current efficiency versus the solution accessible sp² fraction of the perforated BDD electrodes. Insets, schematics of some electrode geometries, schematics of all geometries can be found in Table 5.2. The potentials, ozone output, current efficiency, EOP gradient, and adj-R² for these data points can be found in the appendix, section A5.2.....115

Figure 5.8: a) Photograph of the damage to a 300 µm thick glassy carbon electrode cut with identical geometry to the 70% NDC electrode after a single calibration from 0.1 to 0.3A operating as the anode (half a run, electrode operating for less than 10 minutes). b) Optical microscopy of the electrode from a showing the severe etching on the remaining bars.....117

Figure 5.9: a) Ozone gradient versus electrode thickness for a single perforated electrode design. b) Peak current efficiency versus electrode thickness for a single perforated electrode design. Inset, NDC content percentages for each electrode. The potentials, ozone output, current efficiency, EOP gradient, and adj-R² for these data points can be found in the appendix, section A5.3.....117

Figure 5.10: a) Ozone output in ppm vs current for the 70% NDC electrode before and after 20-hour testing. b) Peak current efficiency versus current before and after long-term testing. EOP gradient, and adj-R² for these calibrations can be found in the appendix, section A5.4.....119

Figure 5.11: QSC Measurements of a) the 70% NDC electrode and b) the Hydrogen plasma treated 70 % electrode. Three CVs were collected in pH 2 Carmody buffer at 100 mV s⁻¹ with the oxidative sweep of the third scan presented.....119

Figure 5.12: a) Ozone output in ppm vs current for the 70% NDC and hydrogen plasma treated electrodes. b) Peak current efficiency versus current for both electrodes. Inset, schematics of both electrode geometries. EOP gradient, and adj-R² for these calibrations can be found in the appendix, section A5.5.....120

Figure A5.1: UV absorbance at 258 nm over 20 hr with the A side as anode for the 70% NDC electrode cell. Data was smoothed using a second order polynomial Savitzky-Golay filter with a smoothing window length of 500 points.....128

Figure 6.1: (a) Render of a cross-section through the centre of the RRDE electrode, showing the arrangement of the ring and disk contacts. The five components are labelled as: (i) insulating outer case; (ii) brass outer core; (iii) brass inner core; (iv) insulating tube, and; (v)

insulating spacer. b) Photograph of an assembled RRDE containing BDD ring and disk electrodes.....135

Figure 6.2: Steps 1-3 of RRDE assembly. a) collecting all the parts: i) insulating outer case, ii) brass outer core, iii) brass inner core, iv) RRDE assembly stand, v) insulating spacer, vi) insulating tube, vii) BDD Ring Electrode, iix) BDD Disk Electrode. b) Removing 3D-printed sparts from support. c) Checking alignment between inner and outer brass parts with a ruler.....136

Figure 6.3: Steps 4-6 of RRDE fabrication including, a) attaching the parts together with a rapid epoxy. b) Test fitting the ring and disk electrodes. c) adding conductive epoxy to the brass contacts.....137

Figure 6.4: Steps 7-9 of RRDE fabrication including, a) curing the conductive epoxy on a stand to ensure the electrodes are co-planar. b) Flooding the electrodes surfaces with insulating resin. c) UV curing the insulating resin.....137

Figure 6.5: Steps 10 and 11 of RRDE fabrication including, a) sanding the insulating resin to expose the electrodes. b) The electrodes are exposed. c) Alumina polish to clean the electrodes.....138

Figure 6.6: Cyclic Voltammetry for ring and disk electrodes in 1 mM FcTMA⁺ made up in 0.1 M KNO₃. a) Disk electrode of the blank RRDE. b) Disk electrode of the sp² RRDE electrode. c) Ring electrode of the blank RRDE. d) Ring electrode of the sp² RRDE. Presented data is the third scan of three.....139

Figure 6.7: White Light Interferometry images using a 5× objective of a) The blank BDD disk electrode, giving an RMS of 10 nm. b) The sp² BDD disk electrode, giving an RMS of 460 nm. The circular tracks in this image are the raster of the laser micromachining system. c) Line profile diagonally across a showing the surface height variation. d) Line profile diagonally across b showing the surface height variation.....140

Figure 6.8: QSC Measurements of a) Blank b) sp² disk electrodes. Measurements conducted in pH 2 Carmody Buffer at 0.1 V s⁻¹ scan rate. Note that a different integration window had to be chosen for each electrode due to the difference in peak shape and position.....141

Figure 6.9: LSVs for a) blank disk RRDE, and b) NDC disk RRDE. Recorded at 100 mV s⁻¹ in an aerated solution of 1 mM FcTMA⁺ in 0.1 M KNO₃. Ring held at 0.05 V vs SCE.....142

Figure 6.10: Levich analysis for the disk of a) blank disk RRDE, and b) NDC disk RRDE in 1 mM FcTMA ⁺ in 0.1 KNO ₃ at rotation rates from 1,000 to 2,500 rpm.....	143
Figure 6.11: FE-SEM image of the Pt-Np modified ring electrode.....	144
Figure 6.12: Forward sweep of CVs on the Pt-NP BDD ring in 0.1 M HClO ₄ with increasing concentrations of H ₂ O ₂ from 0 to 3.37 mM. Dotted line, the potential chosen (1.00 V <i>vs</i> SCE) for the ring in H ₂ O ₂ generation collection experiments.....	144
Figure 6.13: Before and after calibrations for the Pt nanoparticle deposited ring on the RRDE with blank BDD disk electrode. Ring held at 1.0 V <i>vs</i> SCE and H ₂ O ₂ added via standard addition. a) Current-time responses for the ring before generation-collection experiments. b) Calibration plot of the average current over the last 5s <i>vs</i> H ₂ O ₂ concentration before generation-collection experiments. c) Current-time responses for the ring after generation-collection experiments. d) Calibration plot of the average current over the last 5s <i>vs</i> H ₂ O ₂ concentration after generation-collection experiments. The ring was calibrated before and after generation-collection experiments to ensure that the before calibration was still valid.....	145
Figure 6.14: Before and after calibrations for the Pt nanoparticle deposited ring on the RRDE with NDC modified BDD disk electrode. Ring held at 1.0 V <i>vs</i> SCE and H ₂ O ₂ added via standard addition. a) Current-time responses for the ring before generation-collection experiments. b) Calibration plot of the average current over the last 5s <i>vs</i> H ₂ O ₂ concentration before generation-collection experiments. c) Current-time responses for the ring after generation-collection experiments. d) Calibration plot of the average current over the last 5s <i>vs</i> H ₂ O ₂ concentration after generation-collection experiments. The ring was calibrated before and after generation-collection experiments to ensure that the before calibration was still valid.....	146
Figure 6.15: Generation collection experiments conducted at 2000 rpm in 0.1 M HClO ₄ on both RRDE in oxygen saturated and degassed conditions: a) LSVs on the disk electrodes scanned at 5 mV s ⁻¹ . b) Generated H ₂ O ₂ concentration <i>vs</i> disk potential for the oxygen saturated condition.....	147

List of Tables

Table 2.1: Tabulation of all the single crystal diamond plates used in this thesis.....	39
Table 2.2: Tabulation of all freestanding BDD used in this thesis.....	39
Table 2.3: Tabulation of all thin-film BDD used in this thesis.....	41
Table 2.4: Tabulation of all the chemicals utilised in this thesis.....	42
Table 2.5: Details of the 3D printer and material used for 3D printed parts in this thesis....	50
Table 3.1: Tabulation of all etch experiments conducted. Starting Edges: L = Left, R = Right, T = Top, B = Bottom.....	59
Table 4.1: Tabulation of the corrosion depth and corrosion rate of three EP-BDD electrodes in 0.5 M K ₂ SO ₄	88
Table 4.2: Corrosion rates for each electrode and the mean average of both for switching intervals of 6 to 600s in a solution of 1 M acetic acid and 0.5 M K ₂ SO ₄	96
Table 5.1: RMS roughness and area of each planar electrode design.....	105
Table 5.2: Comparison of electrode areas, NDC proportion and geometries. Electrodes of the same geometry as the 70% are also used in Figures 5.9, 5.10, and 5.13.....	106
Table A5.1: Mean parameters for a triplicate run of the 0% NDC Planar Electrode Cell...	124
Table A5.2: Mean parameters for a triplicate run of the 65% NDC Planar Electrode Cell..	124
Table A5.3: Mean parameters for a triplicate run of the 90% NDC Planar Electrode Cell...	124
Table A5.4: Mean parameters for a triplicate run of the 100% NDC Planar Electrode Cell...	125
Table A5.5: Mean parameters for a triplicate run of the 5% NDC Perforated Electrode Cell.....	125
Table A5.6: Mean parameters for a triplicate run of the 30% NDC Perforated Electrode Cell.....	125
Table A5.7: Mean parameters for a triplicate run of the 40% NDC Perforated Electrode Cell.....	126
Table A5.8: Mean parameters for a triplicate run of the 50% NDC Perforated Electrode Cell.....	126
Table A5.9: Mean parameters for a triplicate run of the 60% NDC Perforated Electrode Cell.....	126

Table A5.10: Mean parameters for a triplicate run of the 69% NDC Perforated Electrode Cell.....	126
Table A5.11: Mean parameters for a triplicate run of the 70% NDC Perforated Electrode Cell.....	127
Table A5.12: Mean parameters for a triplicate run of the 80% NDC Perforated Electrode Cell.....	127
Table A5.13: Mean parameters for a triplicate run of the 200 μm thick cell.....	127
Table A5.14: Mean parameters for a triplicate run of the 300 μm thick cell.....	127
Table A5.15: Mean parameters for a triplicate run of the 700 μm thick cell.....	128
Table A5.16: Mean parameters for the triplicate run of the 70% NDC cell before long-term testing.....	128
Table A5.17: Mean parameters for the triplicate run of the 70% NDC cell after long-term testing.....	129
Table A5.18: Mean parameters for the triplicate run of the hydrogen plasma treated cell....	129
Table 6.1: Bill of materials for a single RRDE electrode.....	132
Table 6.2: Uncompensated Resistance Values for all electrodes.....	140
Table 6.3: Faradaic efficiencies for the generation of hydrogen peroxide on both disk electrodes.....	148

List of Abbreviations

3D	Three Dimensional
ABS	Acrylonitrile Butadiene Styrene
AO	Advanced Oxidation
BDD	Boron Doped Diamond
BiPot	Bi-potentiostat
BPE	Bipolar Electrode
BSE	Back Scattered Electrons
CCD	Charge Coupled Detector
CE	Counter Electrode
CNC	Computer Numerical Control
CTE	Coefficient of Thermal Expansion
CV	Cyclic Voltammetry
CVD	Chemical Vapour Deposition
DC	Direct Current
DE	Driving Electrode
DIY	Do It Yourself
EA	Electroanalytical
EA-BDD	Electroanalytical Grade BDD
EAO	Electrochemical Advanced Oxidation
EAOP	Electrochemical Advanced Oxidation Processes
EBS	Electron Back Scatter Diffraction
EC	Electrochemical
EC-AO	Electrochemical Advanced Oxidation
EOP	Electrochemical Ozone Production
EOP	Electrochemical Ozone Production
EP	Electroprocessing

EP-BDD	Electroprocessing Grade BDD
EPR	Electron Paramagnetic Resonance
FDM	Fusion Deposition Modelling
FE	Faradaic Efficiency
FE-SEM	Field Effect Scanning Electron Microscopy
GC	Glassy Carbon
HPHT	High Pressure High Temperature
LSV	Linear Sweep Voltammetry
MPCVD	Microwave Power Chemical Vapour Deposition
MW	Microwave
NDC	Non-Diamond Carbon
NMR	Nuclear Magnetic Resonance
NP	Nanoparticles
NRR	Nitrogen Reduction Reaction
ns	Nanosecond
NV	Nitrogen Vacancy Defect
OER	Oxygen Evolution Reaction
ORR	Oxygen Reduction Reaction
PEEK	Polyether Ether Ketone
PET	Polyethylene Terephthalate
PET/PETG	Polyethylene Terephthalate
PLA	Polylactic Acid
PSI	Phase Shift Interferometry
PTFE	Polytetrafluoroethylene
QCM	Quartz Crystal Microbalance
QSC	Quinone Surface Coverage
RDE	Rotating Disk Electrode

RE	Reference Electrode
RGB	Red, Green and Blue
RMS	Root Mean Squared
RPM	Revolutions Per Minute
RRDE	Rotating Ring Disk Electrode
SCD	Single Crystal Diamond
SCE	Saturated Calomel Electrode
SE	Secondary Electrons
SE2	Secondary Electron 2 Detector
SEM	Scanning Electron Microscopy
SLA	Stereolithography
SRIM	Stopping Range of Ions in Matter
SRIM	Stopping Range of Ions in Matter
TEM	Transmission Electron Microscopy
TF	Thin Film
TF-BDD	Thin Film BDD
TRIM	Transport of Ions in Matter
UME	Ultra-micro Electrode
USB	Universal Serial Bus
UV	Ultra-Violet
UV-Vis	Ultraviolet-Visible
VP	Vat Photopolymerisation
VSI	Vertical Scanning Interferometry
WE	Working Electrode
WLI	White Light Interferometry
XPS	X-Ray Photoelectron Spectroscopy
ZGC	Zero Gap Cell

Acknowledgements

First and foremost, I would like to take the opportunity to thank my supervisor Prof. Julie Macpherson, for years of her support, patience, expertise, and enthusiasm for all things electrochemistry and boron doped diamond. I'd also like to thank Prof. Mark Newton for answering any questions I had when things got too close to physics. Throughout my PhD I have had the opportunity to work with a number of people from Element 6, all of whom have been kind enough to share their extensive knowledge on diamond materials, without which I wouldn't know half as much about diamond as I do today. Special thanks go to Dr. Tim Mollart for answering emails at any time of day, and rapidly navigating samples through the internal workings of Element 6.

I would also like to express my gratitude the Royal Society for funding me under the industry fellows PhD studentship scheme for paying me to do science for the last three and a half years.

I'd like to thank all members of the Warwick Electrochemistry and Interfaces Group past, present and future for making it such a friendly, supportive, and fun environment to work in, long may it continue. I'd also like to take this opportunity to offer my thanks to Dr. Sam Cobb, for helping me get started during my MChem and PhD. I'd also like to acknowledge Dr. Gabriel Melon, Dana Druka and Dr. Nicole Riley-Horne for the hundreds of tea (and later coffee) breaks and infinite support you've given me over the years, it really wouldn't (and hasn't) been the same without you all!

I'd also like to thank Jimmy, Harry, Mai, Manisa, and Anjali for providing me with interesting problems, questions, and doubts while I've supervised you. It's been a pleasure to see you all develop as scientists, and I wish you the best of luck for all your future endeavours.

To my friends to whom PhD life has been a mystery, thanks for nodding along when I explain my science problems and not mentioning how good your "normal" jobs are too often! Thanks for the weekends away, evenings playing games, camping trips, and escaping from locked rooms.

Last but certainly not least I'd like to thank my family. To Mum and Dad for supporting emotionally, (and sometimes financially) through the last three and a half years (and much longer before that). To my sister Maddy I wish you all the best as you start your own university adventure! I'm glad it's not in Chemistry as I wouldn't be much help, especially with organic synthesis! To Grandma, who was always my biggest fan and supporter, I'm sorry you didn't get to see this through with me, but you never would have had any doubt. Finally, to Fiona, my best friend and partner, throughout my PhD (and everything else), thanks for putting up with my insanity, working late, and replying to emails when I should have been listening!

Declarations

I declare that all the work presented in this thesis is entirely my own, except when carried out in collaboration, as outlined below. I also confirm that this thesis has not been submitted for a degree at another university.

In Chapter 2, FE-SEM images were collected by Dr. Georgia Wood and Daniel Houghton. EBSD measurements were collected by Dr. Geoff West.

In Chapter 3, EPR and UV/Vis measurements and analysis were carried out by Dr. Emily Braxton. The MATLAB script used for analysis of the etch timelapse was written by Dr. David Perry.

The work in Chapter 5 was a real team effort. I lead the cell and electrode design and fabrication, as well as performing the electrochemical characterisation of the electrodes. EOP calibrations were performed by Dr. Georgia Wood and Irina Terrero Rodríguez. We all had input on experimental design throughout the project. Hydrogen Plasma treatments were performed at Cardiff University by Dr. Soumen Mandel.

In Chapter 6, initial experiments were conducted by Zhaoyan Zhang under my supervision. Fitting of the i-t curves for uncompensated resistance was performed by Irina Terrero Rodríguez.

Parts of this thesis have been published, submitted, or are in preparation to be submitted, as detailed below:

The 3D-printing sections of Chapter 1 are published as:

J.J.Tully, G. N. Meloni, A Scientist's Guide to Buying a 3D Printer: How to Choose the Right Printer for Your Laboratory. *Anal. Chem.* 2020, 92 (22), 14853–14860.

Work from Chapter 3 is published as:

J. J. Tully, E. Braxton, S. J. Cobb, B. G. Breeze, M. Markham, M. E. Newton, P. Rodriguez and J. V. Macpherson, Diamond membrane production: The critical role of radicals in the non-contact electrochemical etching of sp^2 carbon, *Carbon N. Y.*, 2021, **185**, 717–726.

Work from Chapter 4 is in preparation as:

J. J. Tully, T. P. Mollart, J. V. Macpherson, Examining the factors affecting anodic corrosion in boron doped diamond advanced oxidation systems, *In Preparation*.

Work from Chapter 5 is published as:

G. F. Wood*, I. M. Terrero Rodríguez*, J. J. Tully, S. Chaudhuri and J. V. Macpherson, Electrochemical Ozone Generation Using Compacted High Pressure High Temperature Synthesized Boron Doped Diamond Microparticle Electrodes, *J. Electrochem. Soc.*

Work from Chapter 5 is also in preparation as:

J. J. Tully*, G. F. Wood*, I. M. Terrero Rodríguez, M. Kaewsen, S. Mandal, O. A. Williams, H. Zarrin, T. P. Mollart, J. V. Macpherson, The Importance of Stable Non-Diamond Carbon in Electrochemical Generation of Ozone using Boron Doped Diamond Electrodes, *In Preparation*.

Work from Chapter 6 is submitted as:

J. J. Tully*, Z. Zhang, I. M. Terrero Rodríguez, L. Butcher, and J. V. Macpherson*, A Low-Cost DIY Route to Custom Rotating Ring Disk Electrodes, *Anal. Chem.* 2022.

Abstract

Doped and undoped lab grown diamond is rapidly finding applications in a wide variety of fields from quantum computing to electrochemical sensing. In this thesis four different applications of lab grown diamond are investigated with a view to improving or understanding their fabrication or use.

In Chapter 3, the electrochemical etch step for producing thin-diamond membranes is investigated. Sub-micrometre single crystal diamond membranes are of huge importance for next generation optical, quantum and electronic device applications. In this work, a new method of non-contact electrochemical etching is presented which uses high conductivity, high concentration, fully dissociated aqueous electrolytes.

In Chapter 4, the factors affecting the corrosion of BDD anodes in electrochemical advanced oxidation systems are investigated. These advanced oxidation systems show great promise in the treatment of harmful or persistent organic pollutants. In this chapter a novel and rapid method of directly measuring electrode corrosion is demonstrated and used to test the effect of several solution and operational parameters on the rate of BDD corrosion.

Chapter 5 concerns the design and optimisation of a BDD electrode for electrochemical dissolved ozone generation. Electrochemical ozone production from water is an attractive, green technology for disinfection. Boron doped diamond electrodes, grown by chemical vapor deposition, have been widely adopted for ozone production due to their wide anodic window in water and excellent chemical and electrochemical stability. The affect of geometry and non-diamond carbon content is investigated to optimise the efficiency of ozone production.

The aim of Chapter 6 is the development of a low-cost DIY rotating ring disk electrode which can be assembled easily. Two custom electrodes are fabricated by this method with boron doped diamond rings and disks. The effectiveness of these electrodes in studying the importance of surface incorporated non-diamond carbon on H_2O_2 generation via oxygen reduction is demonstrated.

Chapter 1: Introduction

1.1 Diamond

Throughout history diamonds have been valued as a decorative item due to their clarity and sparkle, in more recent years diamonds have found industrial uses in drilling and cutting tools. Diamond is well known for being the hardest natural material, with its strength arising from a lattice of tetrahedrally bonded carbon atoms in sp^3 hybridisation. The resulting crystal structure of this arrangement is shown in Figure 1.1 and can be described as two face centred cubic lattices, one offset by a quarter of the diagonal. The octahedral structure of diamond has three primary planes to consider, (111), (100), and (110).¹ The average carbon-carbon bond length in diamond is 1.54 Å, and it is this close packing that gives rise to diamonds high density of $3.5 \times 10^3 \text{ kg m}^{-3}$.²

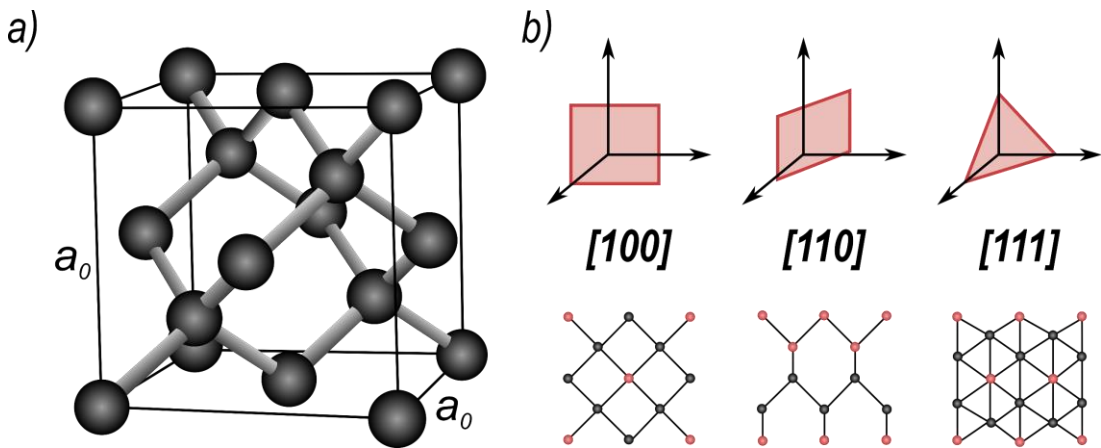


Figure 1.1: Representations of diamond structure and the three main crystal directions. a) 3D ball and stick representation of the diamond unit cell where $a_0 = 0.357 \text{ nm}$. b) Top, representations of the three main crystal directions in diamond. Bottom, ball and stick representations along those crystal directions where red atoms are carbon atoms on the surface and black atoms are carbons on plane below.

The structure of diamond gives rise to its unique properties that make it a desirable for a wide variety of applications. While lab grown diamond has been used in cutting tools for decades, diamond has several other “best in field” properties, such as its wide optical transmission spectrum, thermal conductivity, chemical inertness, and electrical insulation³. These intrinsic properties make diamond a desirable material for a large number of applications,³ such as integrated photonics, opto-mechanics and quantum information processing.^{4,5} With a thermal conductivity of $22.3 \text{ W cm}^{-1} \text{ K}^{-1}$ (five times higher than copper), and a combustion point (in air) of 900°C diamond has found applications in thermal management in areas such as high-

power radio devices.⁶ Diamond's wide optical transmission window has also drawn interest as optics for high powered lasers.⁶ Doping of diamond with high concentrations of boron also opens it to electrochemical applications. Although diamond's mechanical hardness is desirable in several applications, it also leads to one of the biggest challenges when working with the material, how to machine and fabricate usable devices out of such an extreme material.

1.2 Diamond Synthesis

The scarcity of technologically useful natural diamonds stems from the extreme and rare conditions needed for their formation. The formation of natural diamonds requires very high temperatures ($>1,400\text{ }^{\circ}\text{C}$) and pressures (70-80 kbar), and consequently there are few places on earth where diamonds can form.⁷ As a result the cost and variation in the material properties of natural diamonds, has prevented their use for technological and commercial applications.³ It was not until 1955 that the first laboratory scale production of man-made diamonds was achieved.⁸

1.2.1 High-pressure High Temperature

The basis of high pressure, high temperature (HPHT) synthesis is to emulate the conditions under which natural diamonds are formed. HPHT synthesis can be thought of as thermodynamically stable synthesis, as it takes place in a region of the diamond phase diagram where diamond is more thermodynamically favourable than graphite (Figure 1.2).³ In this growth process, a natural diamond seed, high purity carbon source, usually a graphite rod, and a metal (or inorganic salt),⁹ are placed into the centre of a press. When the press is heated above $1,400^{\circ}\text{C}$ the metal (or salt) melts, and acts as a solvent, dissolving the carbon source, which then precipitates onto the diamond seed. The press itself is used to provide the high pressures required for diamond synthesis.

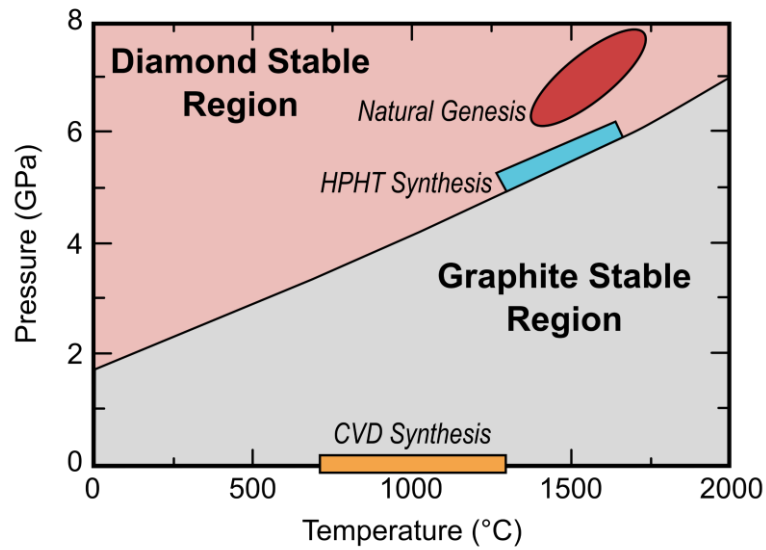


Figure 1.2: Phase diagram for carbon showing the regions of interest for diamond growth and synthesis. Adapted from Balmer et. al.¹⁰

HPHT diamond often contains a high concentration of incorporated nitrogen, typically 200 ppm for type Ib diamonds.¹¹ The nitrogen content of HPHT grown diamond can be reduced by the addition of nitrogen getters, an element with a strong affinity for nitrogen such as titanium, zirconium or most often aluminium, into the press.^{12,13} These getters react with the nitrogen, trapping it as a nitride and preventing its incorporation into the diamond.¹² However, it is impossible to completely prevent nitrogen incorporation via this method.

1.2.2 Chemical Vapour Deposition

Developed in the 1980s chemical vapour deposition (CVD) is diamond growth in a region where diamond is metastable compared to the thermodynamically stable graphite,³ with a large energy barrier preventing spontaneous conversion. Unlike HPHT, CVD synthesis is performed at lower pressures, typically under $1/3^{\text{rd}}$ – $1/4^{\text{th}}$ of an atmosphere containing a small fraction of carbon containing gases ($< 5\%$) in an excess of hydrogen.^{3,14} The substrate onto which the diamond is deposited controls its crystallinity. When a single crystal diamond (SCD) substrate is used the homoepitaxial growth of single crystal diamond is observed, although large areas of SCD can be expensive.³ However, non-diamond substrates such as silicon, copper, tungsten, steel, and molybdenum can be used with additional preparation steps. For example, the nucleation densities on these substrates can be increased by scratching the substrate or seeding it with diamond nanoparticles. In either case heteroepitaxial polycrystalline diamond growth occurs as nucleation events occur simultaneously from each seed.¹⁵

CVD synthesis involves breaking up gas molecules into reactive species which then deposit onto the substrate, forming diamond. The feature unifying almost all types of CVD is gas temperatures in excess of 2,000 K and substrate temperatures around 1,000 K.³ As diamond is only metastable in this regime the formation of graphite by deposition is much more likely than the formation of diamond. Having a vast excess of hydrogen in the gas mixture suppresses the formation of sp^2 carbon, as well as preferentially etching these species over diamond.¹⁶ The build-up of diamond over the surface is statistical (i.e. kinetically driven) as any diamond formed remains, whereas the deposited sp^2 carbon is constantly etched and redeposited. The most common CVD method uses microwaves¹⁷ to heat the gas molecules and achieve a plasma. However, other versions of the technique use a hot filament,¹⁸ flame,¹⁹ or arc jet.²⁰

1.3 Diamond Materials

1.3.1 Boron Doping in Diamond

While intrinsic diamond is a useful insulator due to its wide bandgap of 5.47 eV,²¹ (Figure 1.3a), for some applications conductive diamond is desired. Mature doping methodologies developed in silicon can also be employed in diamond. Introducing donors (group V elements) such as nitrogen or phosphorus can create n-type semi-conductivity and adding acceptors (group III) such as boron results in p-type semi-conductivity being achieved.²²

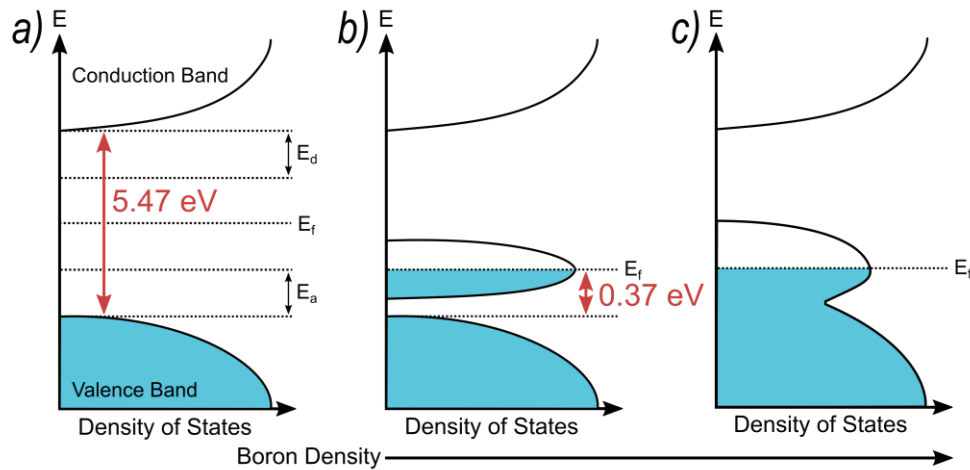


Figure 1.3: Electronic band structure of diamond with various levels of boron doping. Coloured areas represent filled states. a) Intrinsic diamond, a wide band gap insulator with the Fermi level (E_f) equidistant between the conduction and valence bands. b) Heavily boron doped diamond ($\sim 10^{20}$ atoms cm^{-3}), leading to overlap of the dopant wavefunctions and metallic behaviour with E_f inside the dopant state. c) Extremely heavily boron doped diamond where the screening of impurities reduces the acceptor activation energy. Adapted from Blase et al.²¹

N-type doping in diamond has not seen a great degree of success due to both phosphorus and nitrogen having large activation energies. Nitrogen has an activation energy of 1.7 eV, resulting in very few charge carriers being thermally activated at room temperature.²³ Phosphorus has a smaller activation energy of 0.55 eV, but suffers from issues related to its larger size making doping at high levels difficult.²⁴ While still substitutional (taking the position of a carbon in the lattice) in nature boron atoms incorporate much more readily in the diamond lattice, and have a lower activation energy of 0.37 eV allowing for some ($< 1\%$) charge carriers to be activated at room temperature. If sufficient boron is added ($> 10^{20}$ B atoms cm^{-3}) semi-metallic behaviour can be achieved as the dopants are close enough for their wave-functions to overlap, (Figure 1.3b).²³ On further doping the two bands begin to overlap and the metal – insulator transition takes place, simultaneously the screening of impurities lowers the ionization energy, extending the states until they overlap. (Figure 1.3c).²¹ Boron doped diamond (BDD) boasts many best-in-class properties such as, wide solvent window in aqueous solution, low background (non-faradaic) currents, reduced fouling, and a high resistance to chemical corrosion under harsh operating conditions.^{23,25}

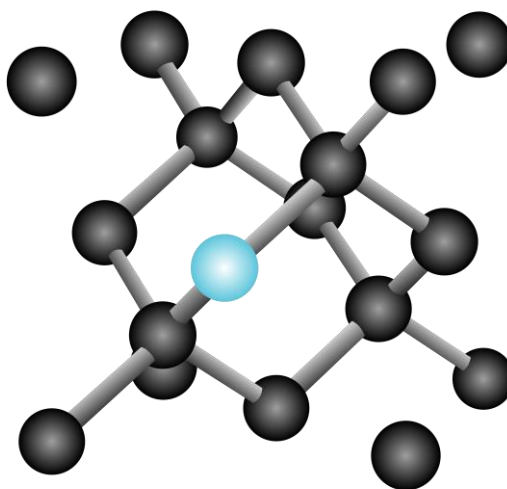


Figure 1.4: Ball and stick representation of the structure of boron doped diamond, showing the position the boron atom (blue) occupies in the lattice.

BDD electrodes have been studied for a wide range of electrochemical applications due to their electrochemical exceptional properties stated above.^{23,25–27} Focusing on why BDD has a wide solvent window in aqueous solutions, this is due to the low adsorption properties of the BDD surface hindering both water oxidation and reduction. This is observed by the onset for water oxidation/reduction moving to larger potentials vs other electrode materials. In particular these high potentials result from weak interactions of water and radical intermediates with the electrode surface.²⁸ Concentrating specifically on water oxidation, the

chemical inertness of the BDD surface results in a weak interaction with generated hydroxyl radicals ($\cdot\text{OH}$). As a result, these radicals are released into solution before oxygen (O_2), the majority product on most other electrode materials, can be produced.²⁸ This weak association serves to increase their effective oxidising power and as such BDD is used widely in processes where the generation of free hydroxyl radicals is required.^{28,29}

Generally, BDD is grown via CVD with a boron containing gas such as diborane (B_2H_6) fed into the reactor during growth.³⁰ All commercially available metallurgically doped BDD is polycrystalline and falls into one of two categories; (1) freestanding BDD which is grown thick enough ($>50\text{ }\mu\text{m}$) that it can be removed from the growth substrate leaving a solid piece of BDD; (2) thin-film BDD, which is grown much thinner ($\sim\mu\text{m}$) and left attached to the growth substrate. In either case the growth parameters used are critical to controlling the crystal size, film texture and the amount of non-diamond carbon (NDC) incorporated into the film. The majority of NDC is incorporated in the grain boundaries of the polycrystalline material, rather than the crystals themselves.²³ For a given set growth conditions increasing growth time will also increase the size of the crystals on the growth face, resulting in a lower density of grain boundaries and therefore reduced NDC incorporation (Figure 1.5).²³

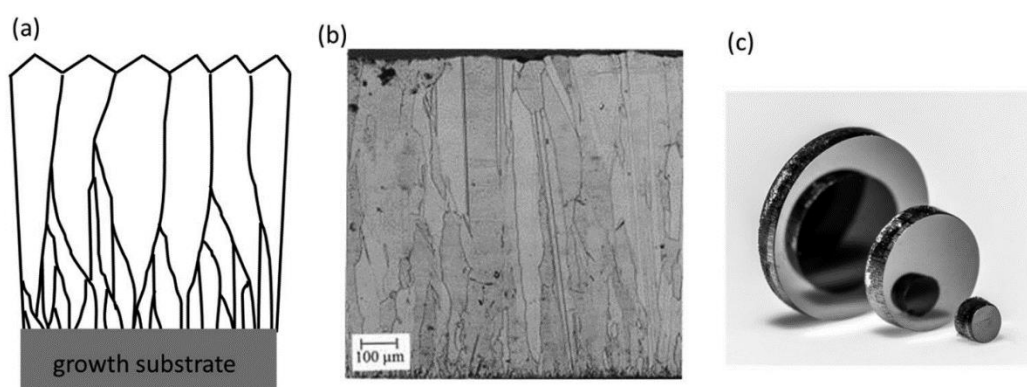


Figure 1.5: (a) Schematic and (b) scanning electron microscopy (SEM) image of the side on growth of microcrystalline BDD. Both clearly show how the grains increase with size as the film thickness increases. (c) Optical image of freestanding microcrystalline BDD, which has been removed from the growth wafer, lapped on both sides, and laser cut into discs. Reproduced from Macpherson.²³

NDC is problematic for electrochemical applications as the NDC (sp^2 bonded) carbon incorporated at the grain boundaries will be much more electrocatalytically active than the sp^3 carbon of the BDD, allowing even small amounts of NDC to dramatically change the background electrode response. The increased catalytic ability of this incorporated NDC decreases the potential required for both oxidation and reduction of water. This decrease in

potential reduces the potential window in which redox analyte processes can be studied and is often referred to as the aqueous solvent window.

Capacitance represents the ability of an electrode to store charge in response to a change in potential. Capacitance, expressed in units of $\mu\text{F cm}^{-2}$ is an intrinsic property of an electrode material with BDD having a very low capacitance $\ll 10 \mu\text{F cm}^{-2}$ compared to metal electrodes such as Au and Pt ($\sim 30 \mu\text{F cm}^{-2}$).²³ As sp^2 bonded carbons typically have higher capacitances than sp^3 bonded carbons such as BDD, incorporation of NDC will serve to increase the overall capacitance of the electrode. For applications in analytical electrochemistry low capacitances are desired as they result in electrodes with low background currents, and therefore offer an improved limit of detection when sensing. As a result of this BDD which is grown thicker will usually have a wider electrochemical solvent window and smaller capacitance than a thinner material grown under the same conditions.²³

Recently a method of producing freestanding BDD via a two-step HPHT process has been developed.³¹ In the first step individual particles of highly doped BDD are produced in a standard HPHT step using aluminium diboride as a boron source. As is typical for low nitrogen HPHT synthesis a nitrogen getter was added to prevent nitrogen incorporation into the diamond. This is especially critical in BDD as charge neutralisation from nitrogen doping will serve to reduce the number of available charge carriers. Once these particles are recovered and cleaned a second HPHT step is used to compact the particles into freestanding BDD disks. This is a metal-binder-free compaction process under 6.6 GPa and 1700 °C in a cubic anvil HPHT press. Interestingly, this compaction step produces material with surface and sub-surface macroscopic porosity which, makes it an interesting electrode for applications which require large surface area electrodes such as electrochemical capacitors, electrosynthesis and electrochemical advanced oxidation (EC-AO). This material also shows promise as a cheaper and more scalable route of BDD production, since HPHT processes can be more easily scaled than CVD processes.³¹

1.3.2 Surface Termination

The surface termination of diamond materials can impact properties such as the rate of electron transfer kinetics (for BDD) and the coherence time of defects within the diamond for applications in quantum information processing.³² Diamond grown by CVD is often hydrogen terminated out of the reactor, this results in a hydrophobic surface with a contact angle of $\sim 90^\circ$.³³ H-terminated surfaces can be stable in air for several months, however they will slowly oxidise over time. For practical applications, the diamond is often processed, which can include polishing, lapping, and cleaning of the surface. The latter is typically performed with

strong oxidising agents resulting in an oxygen terminated surface. In the case of O-terminated surfaces the method of oxidation and crystal direction can result in different chemical functionalities on the surface, each with their own chemical properties.^{23,34,35}

For [100] textured surfaces the surface termination has been demonstrated to consist of carbonyl, ester, and hydroxy groups at low surface coverage of O₂. However, as the surface coverage is increased the hydroxy termination is no longer observed, with the ester groups dominating with a small carbonyl presence.^{36–38} On [110] textured diamond the surface termination has been shown to be dominated by a stable phase of coexisting and adjacent carbonyl and ether groups from 0 – 1000 K. At lower temperatures and pressures increasing peroxide groups are also observed.³⁵ Studies on [111] textured surfaces reveal the opposite effect to the [100] case, at low oxygen coverages epoxy groups dominate the surface chemistry with carboxyl groups dominating at higher oxygen coverages.³⁹

1.4 Diamond Processing

1.4.1 Abrasive Polishing

The extreme hardness of diamond makes processing extremely challenging with most methods still relying on diamond grits and slurries to process diamond. For optical applications it is important that the diamond surfaces are optically smooth (smooth on the length scale of the wavelength of interest), so as not to scatter light passing through them. For electrochemical applications the surfaces can be left “as grown” or polished to give a well-defined planar surface. As-grown surfaces have applications in areas where a high surface area electrode is required however, for more fundamental work the planar nature of a highly polished electrode is easier to fit to electrochemical theory. In the case of polycrystalline BDD polishing also serves to reveal a predominantly [110] textured surface, reducing the surface complexity. Three main techniques are commonly used to polish and planarize diamond surfaces.

Lapping: Lapping is suitable for both single crystal and polycrystalline diamond processing. Lapping is a high removal rate process often used as the first step in diamond processing to planarize the surface or remove a significant amount material to achieve a target thickness. During lapping a slurry containing diamond particles (~ 10s µm in size) is drip fed onto a rotating cast iron plate, the diamond to be polished is then held in a rotating workpiece holder, which removes anisotropy due to polishing direction and allows for the polishing of polycrystalline diamond. Typically lapping results in a surface roughness of 100’s of nm RMS and significant sub-surface damage in the diamond, the depth of which is related to size of the grit used.⁴⁰

Scaife Polishing: Scaife polishing is typically used to give a final finish to single crystal diamond surfaces, however due to polishing anisotropy related to crystal facets and polishing direction this technique cannot be used for polycrystalline materials. Scaife polishing shows significant polishing rate anisotropy with respect to the orientation of the crystal facets, [110] directions polish fastest with [100] directions polishing slightly slower however the [111] direction polishes extremely slowly. The approximate ratio of removal rates is 1:0.5:0.1 respectively. Additionally, each crystal face has both hard and soft polishing directions, with polishing rates up to $800 \times$ faster than the hard direction observed for the soft direction of the [100] face.⁴¹ While the basic principles of scaife polishing date back as far as the mid-15th century, the first academic study reported in 1920.⁴¹ A cast iron wheel is charged with fine diamond grit (typically $0.2 - 2 \mu\text{m}$ in size, not in slurry form) and rotated at high speed. As the sample is pushed onto the plate the mechanical abrasion of the grit on the workpiece removes protruding parts of the diamond, eventually flattening and smoothing it. While the rate of removal is slower than is seen for lapping (typically $\mu\text{m s}^{-1}$) sub-nm surface roughness can be achieved.^{40,42} With scaife polishing it is important to polish along the “soft” direction for the surface crystallographic orientation to achieve a good surface finish. As with lapping, sub-surface damage is caused due to the high-energy nature of the polishing process, but as smaller diamond grit is typically used the depth of this damage is less than seen with lapping.⁴⁰

Resin Bonded Wheel Polishing: In resin bond polishing, diamond grit is immobilised in an epoxy resin matrix. As with lapping, both the wheel and workpiece rotate allowing this technique to be used for both polycrystalline and single crystal diamond. As the workpiece and resin wheel are pushed together the embedded diamond grit can mechanically remove material from the surface of the workpiece. Resin bond polishing can achieve finish as good as a nm RMS and is therefore often the final polishing step for polycrystalline diamond, however, the final surface finish is not as good as that achieved using scaife polishing.⁴⁰

1.4.2 Nanosecond Pulse Laser Processing

Laser processing is commonly employed as a low waste method of shaping diamonds for industrial applications. Laser cutting is far more precise than using mechanical approaches and allows for high-rate removal with the additional advantage that there is no cutting edge to wear. Typically, short pulse lasers with nanosecond (ns) pulse duration are used resulting in a five-step ablation process (Figure 1.6).^{43,44}

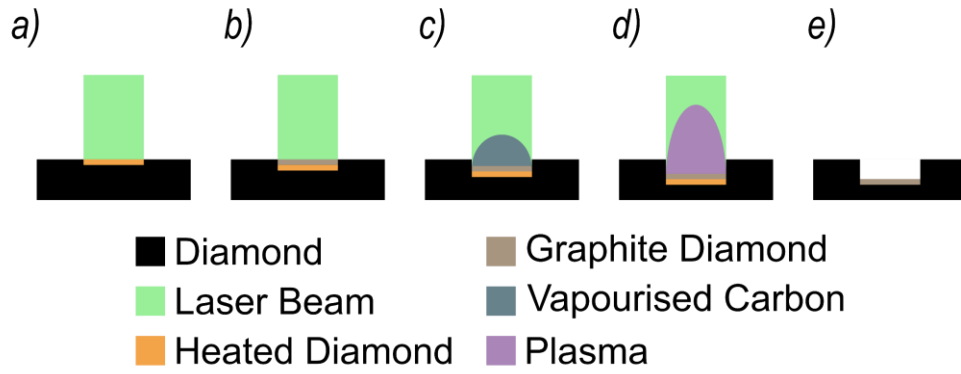


Figure 1.6: Schematic of the mechanism of nanosecond-pulse laser ablation. a) Impurities in the diamond (black) absorb the laser radiation (green) heating it up (orange). b) Once the heated diamond reaches 2,000 °C it undergoes a transition to become graphite (grey). c) The graphite layer is heated until it reaches 4,000 °C and is vapourised (blue). d) The plume of carbon vapour absorbs some of the incident laser radiation and forms a plasma (purple). e) The pulse ends, the plume detaches.

As the beam is initially incident on the diamonds surface it is absorbed by impurities, defects, and grain boundaries in the diamond (Figure 1.6a). This absorption causes the material to heat up and when the graphitisation temperature (2,000 °C) is reached the material undergoes a phase transition to sp^2 bonded carbon (graphite), (1.6b). This sp^2 bonded carbon layer is much better at absorbing the laser than the diamond and is rapidly heated to its vaporisation point (4,000 °C), (1.6c). The vapourised carbon then creates a plume, which absorbs some of the incident laser radiation and forms a plasma (1.6d) the size of which has been shown to be related to the fluence employed Figure 1.7.⁴⁴ After the pulse ends the plume detaches, leading to redeposition of the vapourised carbon (1.6e), this leaves the diamond with two distinct layers on the surface, a layer of graphite formed from the diamond and a layer of redeposited amorphous carbon from the plume. The thickness of these sp^2 bonded carbon layers has been shown to be dependent on the fluence employed.^{43,45–54}

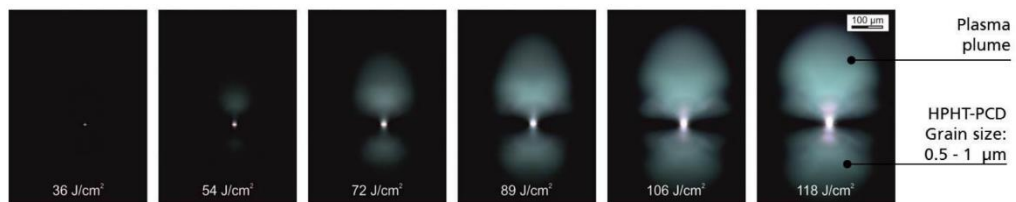


Figure 1.7: Plasma Formation during Single Pulse Laser Ablation for Different Values of Fluence. Reproduced from Hermani et al.⁴⁴

While the amorphous and graphitic layers can be partially removed by aggressive acid cleaning treatments Cobb et. al.⁵⁵ showed that a thin layer of 100 nm thick graphite capped with an even thinner amorphous carbon layer remained, Figure 1.8. This layer is highly robust surviving oxidative acid cleaning providing a route to permanent surface modification of diamond by laser micromachining as well as and air annealing up to 500°C While for some applications this robust sp^2 bonded carbon may be advantageous in other applications it presents one of many unique challenges when working with diamond.

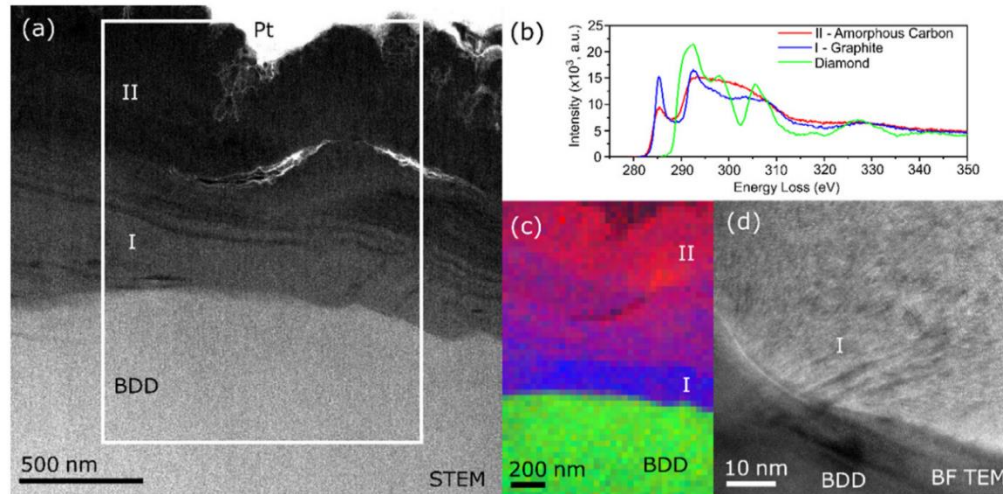


Figure 1.8: a) HAADF STEM image with white rectangle indicating EELS survey area, pixel size $\frac{1}{4}$ 33 nm. b) EELS spectra of BDD (green), graphite (blue) and amorphous carbon (red), obtained from the BDD substrate, layers I and II respectively. Spectra have been scaled to fit the axis. c) Multilinear Least Squares fitting of the 3 spectra in b), showing the distribution of BDD, graphite and amorphous carbon. d) High magnification BF TEM image confirming that layer I is composed of graphite. Reproduced from Cobb et al.⁵⁵

1.4.3 Ion Implantation

Ion implantation is a surface and sub-surface modification technique in which ions are accelerated into the target material to change the electronic, physical or chemical properties of the target.^{56–59} To date, other than incorporation during growth, ion implantation is the only method that has been successfully used to dope diamond. This technique gives much more choice of dopant as well as control of the concentration and position than incorporation during growth.⁵⁷ By careful choice of the dose and acceleration energy both the amount and depth of the doped ions can be closely controlled, and modelled by SRIM and TRIM simulations.⁶⁰ Doping by ion implantation has been used to fabricate a host of semiconductor devices in diamond using both n and p-type doping.⁵⁹ The major pitfall of this technique is the radiation damage that accompanies ion implantation.^{56–59} If this damage is kept below a certain

threshold, often called the threshold of graphitisation, the radiation damage can be partially or fully recovered by high-temperature annealing.^{56,57} However, if the damage exceeds this threshold an sp^3 carbon to sp^2 carbon transition occurs upon annealing as the damaged region is amorphised.^{58,61}

While this radiation damage is problematic for doping by ion implantation it does present opportunities in the field of thin diamond membrane production (Figure 1.9). In this application of ion implantation high energy (\sim MeV) ions (usually of C or He) are used to damage a shallow sub-surface region beyond the threshold of graphitisation, leaving a thin cap layer. Following this implantation, the layer can be annealed to form an sp^2 bonded carbon layer, and this layer can be subsequently removed with a dry,⁶² or electrochemical,⁶³ etch step to free the cap layer. This technique was first proposed in 1992 by Parikh et. al and forms the basis for the work discussed in Chapter 3 of this thesis.⁶²

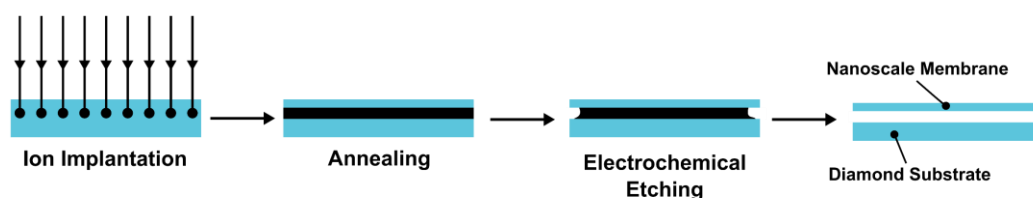


Figure 1.9: Schematic of the implantation and lift-off process employed to produce sub- μ m diamond membranes.

1.5 Electrochemistry

1.5.1 Three-Electrode Electrochemistry

The majority of electrochemical systems used in research employ a three-electrode set-up (Figure 1.10). The three electrodes used are the working electrode (WE), where the process of interest happens, the counter electrode (CE) which passes an equal and opposite current to the working electrode to complete the circuit, and the reference electrode (RE). The reference electrode is a critical part of the electrochemical system, its purpose is to hold a stable potential against which other potentials can be measured and applied. There are numerous types of reference electrodes, but a saturated calomel electrode (SCE) was employed for the work in this thesis.

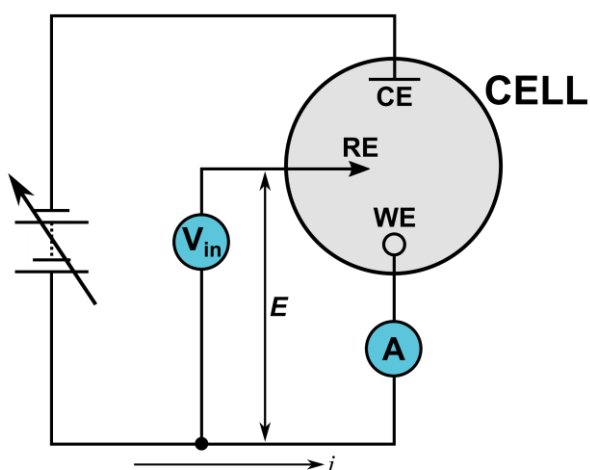


Figure 1.10: Schematic of a typical 3-electrode electrochemical set-up. Current flows between the counter and working electrodes whilst potential is controlled between the working and reference electrodes. Adapted from Colburn et.al.⁶⁴

In operation the potentiostat applies a potential between the WE and RE, with the current flowing between the WE and CE so as not to perturb the potential of the reference electrode. As a result of this it is important that the CE has a surface area significantly larger than the WE, so as not to impact reactions happening at the surface of the WE. To achieve these large areas in a small form-factor, a mesh or coil CE is often utilised. All three electrodes are connected to the potentiostat, which applies potentials and records the resultant currents. Typically, a background electrolyte is added to the solution to increase the solution conductivity and ionic strength, reducing the ohmic drop resulting from ion migration. Care must be taken when selecting the supporting electrolyte, as it cannot be electrochemically active within the potential window to be employed. KClO_4 and KNO_3 are commonly employed as background electrolytes in aqueous solutions.⁶⁵

1.5.2 Cyclic Voltammetry

Cyclic voltammetry (CV) is a powerful and popular electrochemical technique used to study the oxidation and reduction of species in solution.⁶⁶ Practical applications for CV include electrode characterisation, electrochemical sensing, and initiating reactions at catalysts. In detail, an initial potential is applied to the WE with respect to the RE by the potentiostat. This potential is then swept at a controlled rate (the scan rate) in one direction to a vertex potential. Once the vertex potential is reached the potential is swept in the opposite direction to the other vertex, this process can be repeated for as many cycles as desired, Figure 1.11 a. The output of

a CV is a current versus potential plot as seen in Figure 1.11b for a macroelectrode undergoing reversible (diffusion-controlled electron transfer).

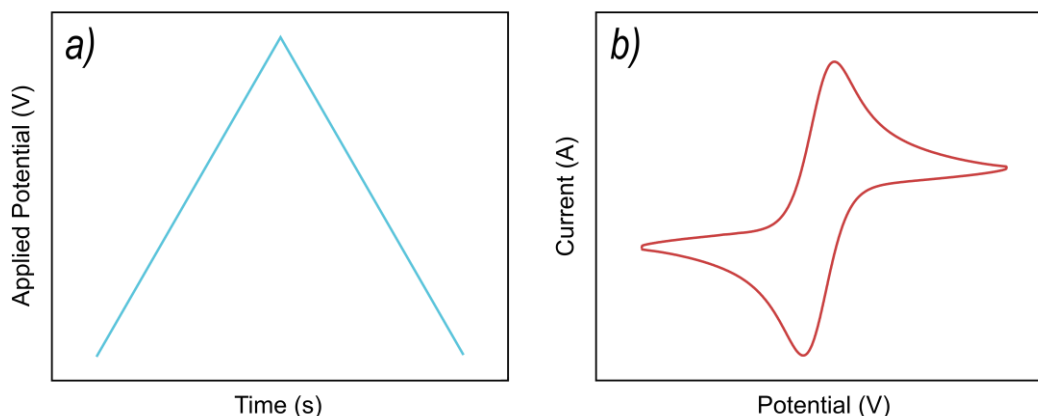


Figure 1.11: Schematics to show a) a CV potential waveform, b) a typical current-voltage shape observed for a reversible process on a macroelectrode.

As Figure 1.9 shows, for a macroelectrode (≥ 1 mm) in an ideal, electrochemically reversible process limited by mass transport a characteristic peak shaped CV is observed, which is defined by a peak-to-peak separation on the voltage axis of $57 / n$ mV, where n equals the number of electrons transferred.⁶⁶ From the relationship between scan rate and peak current it is also possible to obtain quantitative information on the diffusion coefficient or electrode area (assuming the electrode is planar).⁶⁷ Away from reversible conditions, it is possible to extract information such as the electron transfer kinetics of the redox couple, the electrocatalytic reactivity of the electrode etc. CVs can also be run in the absence of a redox mediator to extract basic characterisation of an electrode, such as capacitance and solvent window. Linear Sweep voltammetry (LSV) is essentially like running half a CV, as a sweep is run only in one direction (positive or negative).

1.5.3 Electrodes under Steady-State Control

The characteristic current response observed for macro electrodes under reversible conditions i.e. where electron transfer at the electrodes surface is faster than mass transport of species to the electrode, is peak shaped. However, it is possible to achieve mass transport limited, steady-state currents by increasing mass transport to the electrode.

One method of doing this is to shrink the electrode until it becomes an ultra-micro electrode (UME) with a diameter of less than 25 μm . For UMEs there are two characteristic current-voltage behaviours observed.⁶⁸ At most scan rates the diffusion field around the electrode is large, and radial diffusion from the edge of the electrode becomes significant compared to linear diffusion from the bulk solution (Figure 1.12a). As radial diffusion is much faster than

linear diffusion we arrive at a case where mass transport (diffusion) is much faster than for a macroelectrode. At this point the concentration gradient within the diffusion layer has been established, with a concentration of 0 at the electrodes surface leading to a constant diffusional flux, and a steady-state current response is seen (Figure 1.12c). For an ideal UME the return sweep should also track back exactly along the forward sweep, as diffusion of the products is so fast that they are undetectable. The second case occurs at very fast scan rates ($\sim 10 \text{ V s}^{-1}$) when scanning this fast the diffusion layer remains thin and as a result the UME is large in comparison to its diffusion field, because of this diffusion is dominated by linear diffusion perpendicular to the electrodes surface (Figure 1.12b). As linear diffusion is slower than the electron transfers a characteristic peak shape as per a macroelectrode is observed (Figure 1.11b). UMEs have several benefits over macro electrodes, especially for sensing, such as reduced capacitance, low background currents, and steady state response.

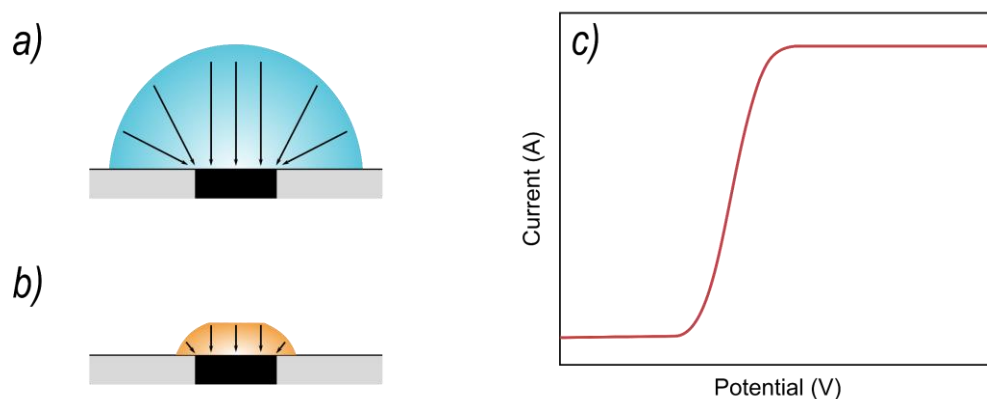


Figure 1.12: Schematics to show a) the diffusion profile of a UME at most scan rates b) the diffusion profile for a UME at scan rates $\geq 10 \text{ V s}^{-1}$. c) a typical current-voltage response observed for a UME and RDE.

Another method of achieving limiting currents is to increase mass transport by adding artificial convection to a macroelectrode system. This is most commonly achieved using a rotating disk electrode (RDE), although other methods such as flow cells are also employed. In an RDE system the rotation of the electrode ($> 1000 \text{ RPM}$) pumps solution up from the bulk and across the electrodes surface. This induced convection increases mass-transport over diffusion alone, leading to a constant diffusional flux, and steady state currents as seen for the UME case. The most common application of RDEs is Levich and Koutecký–Levich analysis to extract diffusion coefficients and reaction kinetics respectively.⁶⁷

1.5.4 Rotating Ring-Disk

The rotating ring disk electrode (RRDE) is a powerful electrochemical tool for the mechanistic analysis of electrochemical reactions at electrode surfaces (Figure 1.13).^{69,70} This is due primarily to the ability of the RRDE to detect the products of the disk electron transfer reaction at the surrounding ring electrode under transport controlled conditions (generation-collection).⁷⁰ For example RRDEs are commonly used to benchmark catalysts for processes such as ORR⁷¹ and NRR.⁷² For some applications the ring electrode can also be used as a pH sensor to detect pH changes resulting from reactions on the disk.⁷³ The RRDE has two electrodes, a central disk of solid electrode material surrounded by a concentric ring electrode. The ring and disk electrodes can be made from the same, or different electrode materials, dependant on the process to be studied. The entire electrode system is typically encased in an insulating housing containing the contacts and threads required to attach and electrically connect the two electrodes to the rotating apparatus. As the RRDE is rotated, solution is moved from the bulk toward the face of the disk electrode, which then exits parallel to the electrode surface, flowing over the ring electrode as it moves outward towards the edge of the RRDE.

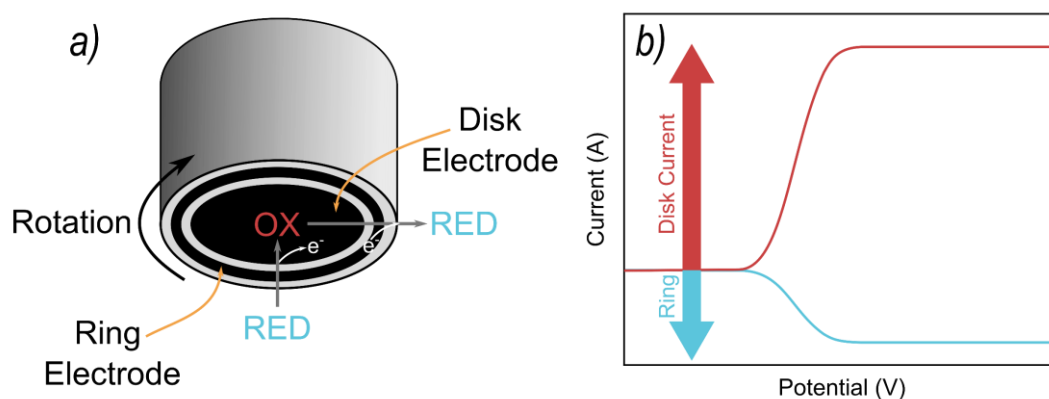


Figure 1.13: a) Schematic of a RRDE electrode showing a generalised redox process. b) Schematic of the current responses for the disk (red) and ring (blue) with approximately 30% collection efficiency.

Due to the well-defined hydrodynamic flow,⁷⁴ not only is transport of species from the disk to the ring greatly enhanced, compared to stationary conditions, but it is possible to quantify what proportion of electroactive species produced at the disk will be detected on the ring. Figure 1.13b shows the typical disk (red) and ring (blue) current responses for a generation-collection experiment with a simple redox mediator. As the disk is swept from a potential where no electron transfer occurs to a potential where the oxidation of the redox mediator is possible the current increases, eventually reaching a steady-state current even as the potential continues to rise. While the disk potential is swept the ring potential is held at a potential

sufficient to reduce the oxidised redox couple produced at the disk. As oxidised species begin to be produced at the disk, the ring current also increases, showing the same shape as the disk response. The ratio between these two currents is defined as the collection efficiency, which is the maximum proportion of species generated on the disk that can be detected on the ring and is an intrinsic property of an RRDE, based on the relative radii of the ring and disk electrodes.⁷⁰ In the case of Figure 1.10b the collection efficiency is approximately 30%.

1.5.5 Two-Electrode Electrochemistry

It is common for deployed electrochemical systems to operate in a two-electrode configuration (Figure 1.14) rather than the three-electrode system used in research. It is important to note that this system is different from the two-electrode set-up often employed in research when using UMEs. In that configuration the two electrodes are the working and a reference; a counter is not required due to the small currents passed.

In this anode and cathode configuration the system has only two electrodes, which can be made of the same, or different materials. In some configurations these systems may have a permanent anode and cathode, which is usually the case if the electrodes are made of different materials, or they may switch polarity to give both electrodes time as the “active” electrode, to alleviate concerns about biofouling, or electrode wear.

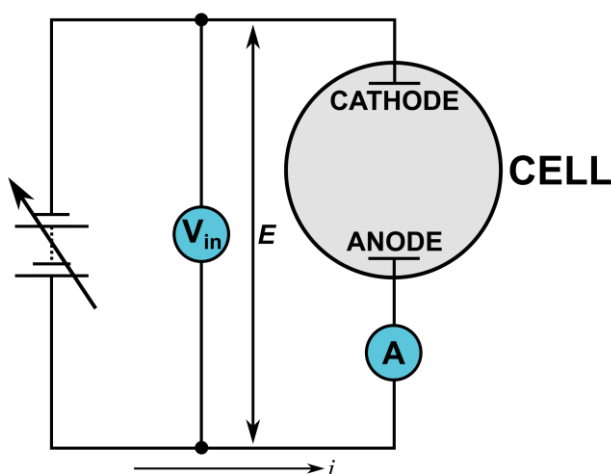


Figure 1.14: Schematic of a typical 2-electrode electrochemical set-up. Current flows between the anode and cathode whilst the potential is controlled between them.

In these systems it is impossible to measure the potential applied to each electrode directly due to the lack of a reference electrode. However, the potential difference between the two electrodes can be measured. Two-electrode systems can be operated in either current limiting (galvanostatic) or potential limited (potentiostatic) modes depending on the application. This

electrochemical set-up is commonly employed in applications where precise potential control isn't required, or where the current passing through a system is more critical for the process of interest.

1.5.6 Bipolar Electrochemistry

Bipolar electrochemistry is another powerful alternative to the standard 3-electrode set-up which have been widely adopted in batteries, electrosynthesis,^{75,76} and solar cells,^{77,78} but have seen limited use in analytical electrochemistry.⁷⁹ In most applications bipolar electrochemistry represents a simple set-up which provides a route to large area electrodes with reduced complexity. A bipolar electrochemical set-up has two driving electrodes (DE), to which the potential is applied, between these DEs sits the bipolar electrode (BPE), so named because each electrode has both an anodic and cathodic end (Figure 1.15). Unlike in standard electrochemical set-ups the interfacial potential at the BPE is not controlled, and there is no direct electrical contact to the BPE. Instead, the driving electrodes control the potential of the solution, which in turn creates an interfacial potential at either end of the BPE. In order for a material placed between the DE to act as a BPE it must have a higher conductivity than the surrounding solution, so that the current passing between the DEs passes through it preferentially.

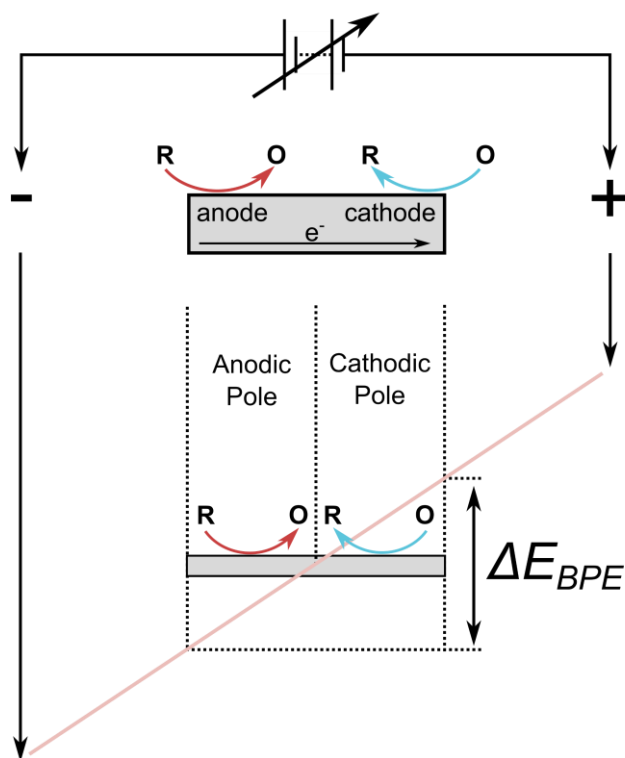


Figure 1.15: Schematic of a bipolar electrode set-up showing how the potential is dropped between the driving electrodes.

The potential experienced by the ends of the BPE can be increased in three main ways, by (1) increasing the potential on the DEs, (2) decreasing the solution conductivity, or by (3) increasing the length of the BPE. It is also common for the BPE to be placed inside a microchannel which has the effect of further decreasing the conductance of the solution, as well as making determination of the current passing through the BPE easier.^{79–81}

1.6 Applications of Intrinsic Diamond

1.6.1 Quantum Applications

A colour centre in diamond is an optically active lattice point defect.⁸² Single crystal diamond is known to host as many as 500 different colour centres, with each defect having a characteristic absorption varying from ultraviolet to infrared.⁸² The vast majority of these centres are due to nitrogen incorporation.⁸² Many of these colour centres are bright enough to be used as single photon sources, sources which emit light as single photons. Some also display desirable quantum properties, such as spin coherence.⁸³ The most studied of these centres is the nitrogen vacancy defect (NV).⁸³ This point defect in diamond consists of two adjacent carbon atoms substituted by a Nitrogen-Vacancy pair oriented along the [111] crystallographic direction (Figure 1.16).⁸⁴ Since Nitrogen is trivalent it can only form three bonds with the diamond lattice, using three of its five valence electrons. The remaining two electrons then form a lone pair pointing towards the vacancy. The NV defect exists in two charge states, neutral NV^0 and negative NV^- .⁸⁵ In the neutral state the vacancy has three valence electrons, one from each incomplete bond. In the negative state the vacancy has an additional electron forming an $S=1$ pair with the unpaired vacancy electron.

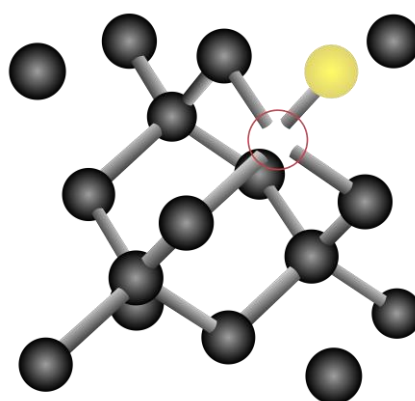


Figure 1.16: Schematic of the nitrogen (yellow) vacancy defect in diamond.

NV defects are found “as grown” in CVD diamond.¹² They can also be intentionally incorporated into diamond either as a product of radiation damage from a wide variety of ions such as H^+ and He^+ , with energies varying from keV for heavier ions to MeV for lighter ions.⁸⁶

⁸³ Alternatively, ion implantation of nitrogen can be used to introduce these centres into the substrate directly, rather than relying on the nitrogen already present in the diamond. Nitrogen ions can be implanted at energies varying from tens to hundreds of keV, depending on the depth of implantation required.^{19,23} The NV⁻ defect in diamond has applications across many emerging and current fields. These include, photonics,^{4,89} quantum computing,⁴ magnetometry and sensors.⁹⁰ However, these application requires an NV defect that resides very close to the diamonds surface.

1.7 Applications of Boron Doped Diamond

1.7.1 Electrochemical Advanced Oxidation Processes

Electrochemical advanced oxidation processes (EAOPs) are a promising technology for the removal of persistent or harmful contaminants from wastewater. A common factor that unites all forms of EAOPs is the generation of hydroxyl radicals at the electrode's surface, which react indiscriminately with a wide range of organic contaminants (Equation 1.1).^{91,92} Even compounds which have limited reactivity towards the hydroxyl radical can be oxidised by direct electron transfer from the electrode.^{93,94} Various electrode materials have been investigated for EAOPs and the most common materials include doped-SnO₂,^{94,95} PbO₂ and doped-PbO₂,^{96,97} and boron-doped diamond (BDD).^{93,98–102} The generation of useful hydroxyl radicals ([•]OH) on these electrodes is due to the high over potential needed for electrochemical O₂ production, which allows the generation of hydroxyl radicals to take place at a potential lower than that of oxygen pairing and evolution.¹⁰³



BDDs reputation for hardness and chemical inertness, and initial studies demonstrating a low corrosion rate have prompted deployment of BDD based advanced oxidation (AO) systems in the field. However, more recent studies have shown that BDD fails to live up to this reputation at high current densities, with considerable anodic corrosion being demonstrated typically in the presence of organic electrolytes.¹⁰⁴

The majority of AO systems which are commercially available use thin-film polycrystalline BDD grown on top of a non-diamond substrate, and as such the majority of research done on BDD anodic corrosion has employed this material. While thin-film BDD is significantly cheaper than it is freestanding counterparts, it does have a variety of disadvantages not present for free standing BDD. The inclusion of a non-diamond substrate can negatively impact the overall strength of the electrode, silicon is regularly used as a substrate, however its fragility is problematic for industrial electrode applications.¹⁰³ Other substrates such as tantalum,

niobium, tungsten, and titanium have been investigated,^{105–108} but due to the often-weak bond between the BDD film and these substrates can lead to film delamination, often as a result of pin-holes etching through the diamond to the substrate, is the most common failure mode for these BDD electrodes.^{105,109–111}

It is generally suggested that maintaining a low current density serves to slow down or prevent anodic corrosion, although this is not always practically possible.^{104,112} Reducing the current density reduces the effectiveness of contaminant removal, in turn reducing the usefulness of the system. Due to the high start-up costs of using diamond electrodes the performance of these systems must be significantly better than competing technologies to be commercially viable, which is not true at low current densities.

The role of boron concentration in the corrosion mechanism is not fully understood. In one study thin BDD films of varying boron concentrations (100 – 5,000 ppm) were grown, and anodic corrosion in 10% v/v H₂SO₄ was found to occur more slowly for the films with higher boron concentrations.¹⁰⁰ The authors attributed this difference in corrosion rates to the higher doped (and therefore more conductive) films having a lower potential for the same current density, and therefore providing less energy to overcome energetic barriers to surface reconstruction. Conversely, in a more recent piece of work the authors observed that the [111] oriented grains of the BDD material were removed preferentially during anodic polarisation in 3 M acetic acid.¹⁰⁴ The authors attributed the increased etch rate of these grains to the fact that the [111] oriented grains in polycrystalline BDD incorporate five times more boron than the [100] oriented grains.¹¹³ This increase in boron concentration is suggested to make the [111] grains more electrocatalytically active, and that this increase in activity causes the etching of these grains to be fastest.

It is widely agreed that polarisation outside the solvent window changes the diamond surface. Anodic polarisation oxidises the diamond surface sites, creating hydroxyl and ether groups, as demonstrated by x-ray photoelectron spectroscopy (XPS).^{112,114} A decrease in background currents has also been observed after anodic polarisation, which was attributed in this study, to the removal of the softer, yet more electrochemically active sp² carbon regions found along the grain boundaries in polycrystalline BDD.¹¹⁵ Anodic polarisation in NaClO₄ lead to a broadening of the water oxidation peak, which is attributed to the breaking of C-C bonds leading to distortion of the diamond lattice, creating sites which are not electrochemically equal.¹¹² Polarisation in 3 M acetic acid has also been shown to reduce the surface boron concentration.¹⁰⁴

Although the precise mechanism of anodic corrosion in BDD electrodes is likely solution dependant, previous work has begun to elucidate possible mechanistic routes. In one study it was suggested that anodic corrosion could take place via two distinct mechanisms.¹¹² The first mechanism involves the creation of sp^2 carbon from the C-H functional groups on the diamond surface. The removal of hydrogen from two adjacent carbons causes the two carbon atoms to reconstruct forming a C=C bond. The rate limiting step in this process is the removal of the hydrogen from C-H bonds, which can occur at very low potentials (> 0.5 V). Once the sp^2 carbon is created the harsh environment from generation of the hydroxyl radical (amongst other oxidising species) at the electrodes surface will etch this material, resulting in a loss of mass from the BDD. The second, and higher energy route, involves the reaction of a hydroxyl radical with a surface C=O functionality to form a COOH radical surface termination, which can then reconstruct to form a carboxylic acid. This carboxylic acid is then suggested to be attacked by another hydroxyl radical forming an aqueous carbonic acid (H_2O_3). The multiple steps and higher activation energies of this process indicate that this is likely the less favoured of the two routes.

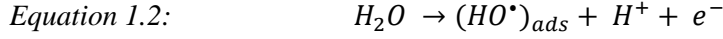
It was also observed previously that solutions of acetic acid and propanoic acid gave rise to a very high anodic corrosion rate.^{104,114} Significantly lower corrosion rates were seen for solutions of formic acid, glucose, perchloric acid and methanol. It has also been suggested that it is only at current densities where the hydroxyl radicals are being predominantly used for oxygen evolution (> 0.2 A cm^{-2}), and therefore cannot react with the carbon radicals to recover the C-OH surface termination, that is etching seen.¹⁰⁴

1.7.2 Electrochemical Ozone Production

As an extension of EAOPs, electrochemical ozone production (EOP) has also gained in popularity as a method of sterilising water systems. This popularity is largely due to its simplicity, as ozone can be produced directly from water by electrochemical oxidation. The benefits of EOP compared to corona discharge are numerous: no gas feedstock is required, generators are easily scalable and robust, and high-power efficiencies can be achieved. However, the most significant advantage of EOP for the treatment of waterborne contaminants is the direct generation of dissolved ozone with no need for further steps to dissolve the ozone in the aqueous phase.¹¹⁶

The mechanism proposed by Da Silva in 2003¹¹⁷ is generally accepted as the mechanism for EOP:

Electrochemical Steps:



Chemical Step:



Oxygen Evolution:



Ozone Formation:



In short, this mechanism involves the electrochemical generation of surface bound $\cdot OH$ (Equation 1.2) which can then decay to form adsorbed oxygen radicals (Equation 1.3). These radicals can then react chemically to form adsorbed oxygen molecules (Equation 1.4). These adsorbed oxygen molecules can then detach from the surface to evolve oxygen gas (Equation 1.5). Alternatively, once adsorbed oxygen molecules are available on the electrode surface ozone can be generated by the reaction of an adsorbed oxygen molecule with an adsorbed oxygen radical (Equation 1.6). Once ozone is generated on the surface it can then desorb to form ozone, which can dissolve if conditions are right (Equation 1.7).

Due to the high potentials required for EOP, this process is in direct competition with the oxygen evolution reaction (OER), and it is thought that the ratio of adsorbed oxygen molecules to adsorbed oxygen radicals controls the efficiency of EOP vs OER. As such, electrodes with high overpotentials for OER such as SnO_2 , PbO_2 ,^{118,119} Pt, and glassy carbon,¹²⁰ have previously been successfully used to generate ozone. However they have major drawbacks related to their lack of durability and concerns with heavy metal contamination.¹²¹ Boron doped diamond (BDD) electrodes have also been used and are the most popular choice for commercial EOP devices as BDD electrodes exhibit no safety concerns and excellent electrochemical stability.^{121,122}

The use of BDD however is slightly counterintuitive as despite its high overpotential for OER, hydroxyl radicals are known to be “loosely-adsorbed”, facilitating the use of BDD in advanced oxidation and wastewater treatment as these radicals can easily desorb and react with species in solution, not just at the electrode surface.^{28,123} This loose adsorption could reduce the surface coverage and residence time of adsorbed hydroxyl radicals and thus result in lower ozone production than comparable surfaces with “strongly-adsorbed” hydroxyl radicals.

In general, commercial EOP cells which use electrolyte-free media such as tap or deionised water, contain a piece of Nafion sandwiched between two perforated BDD electrodes, a configuration often referred to as a zero-gap cell (ZGC) as there is no space between the electrodes. The Nafion acts as a solid electrolyte. It has been suggested that the importance of the slots in the electrode is to allow solution access to the Nafion or to create a Nafion-solution-BDD “triple-point” where the ozone is believed to be generated.^{121,122} These slots or holes in the electrode can be formed by laser cutting pieces from a piece of freestanding BDD,¹²¹ or by growing thin-film BDD over a substrate with holes.^{122,124} It is important to note that while these methods may give the same geometric result the diamond electrode created will be significantly different. An electrode laser cut from freestanding BDD will have two pristine diamond surfaces, usually with large grains, compared to thin-film material, due to its long growth time. The inside edges of the slots will be graphitised during laser processing (as discussed in section 1.5.2),⁵⁵ giving rise to an external sp^2 bonded carbon layer, a nuance often not considered in previous literature.¹²¹ The advantage of freestanding electrodes for EOP is that the entire electrode can be BDD, leading to a robust and chemically inert surface. Thin-film electrodes will generally have much smaller diamond grains due to the shorter growth times, however the edges of the slots will have the same material properties as the rest of the electrode. The chief advantage of these thin-film electrodes is the reduced cost of diamond growth, however, complete BDD coverage is difficult to achieve on geometrically complicated substrates and pinholes in the BDD film can cause delamination leading to premature electrode failure, especially when working at high current densities.¹⁰⁵

1.8 3D Printing as a Tool for Research

Throughout the work presented in this thesis 3D printing, or additive manufacturing, has been used extensively to make cells, holders, and electrodes. Once a niche for engineering or hobby, applications of 3D printings now span from structural to functional with 3D printed parts now actively participating in chemical reaction for catalysis,^{125–127} energy storage.^{128,129} On the structural side, 3D printing has gone beyond instrumentation applications,^{130,131} and printing useful one-of-a-kind holders and laboratory appliances,¹³² or helpful teaching resources¹³³ and now modular and custom designed reactionware, tailored for particular chemical reactions can be produced.^{134–136} The two most common types of desktop 3D printers have been employed in this work: fusion deposition modelling (FDM) and stereolithography (SLA).

1.8.1 Fusion Deposition Modelling

The most common type of desktop and consumer 3D printers are based on Fusion Deposition Modelling (FDM) also known as fused filament fabrication. The basis of this technique involves a hot-end in which the thermoplastic filament (the printable material) is melted and then extruded through a nozzle, all located at the printing head, which then follows a preprogrammed path to build up the model layer-by-layer (Figure 1.17).

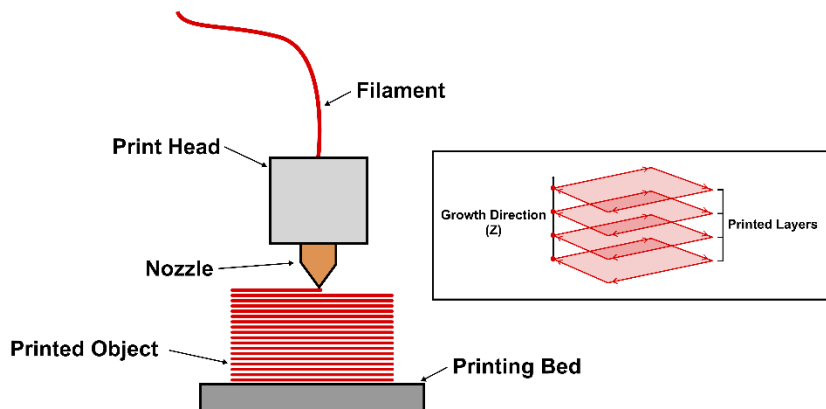


Figure 1.17: Schematic of an FDM 3D Printer.

FDM 3D printers are particularly suited to centimetre and larger sized objects where surface finish is not a critical feature. Parts with a mechanical function i.e. holders and stands are particularly suited to FDM printing. Minimum printable feature size falls between a couple to tens of millimetres and anything smaller than this can become poorly resolved in the printed object. Although it is possible to achieve good quality prints at these reduced sizes (features smaller < 10s of millimetres) by proper calibration of the printer and printing parameters, if parts this small are routinely needed other technologies are more suitable, such as vat

polymerization (see below). A whole range of different material properties can be accessed by using different filaments including flexible, water soluble,¹³⁷ and electric conductive,^{131,138} among others. FDM prints are inherently anisotropic, as the bond formed between the printed layers is weaker than the material itself. As a result, the part is always weaker along the Z-Axis than along the X-Y plane. As such, if a part is going to come under tensile stress, attention should be paid to its orientation on the print bed. This anisotropy also extends to other material properties when using functionalized materials and can be observed, for instance, on material electrical conductance of carbon filled filaments.¹³¹ Lastly, due to the thermoplastic nature of the printable materials used for FDM, printed parts are generally unsuited to high-temperature environments, although the exact maximum temperature in which they can be used is material specific.

A huge variety of thermoplastic filaments are available for FDM printing, and the open-source nature of most FDM printers allows the use of filaments from different manufacturers. Polylactic Acid (PLA) is the most common, due to the ease with which it prints. PLA is suitable for light-duty structural prints but has a poor chemical resistance. In the early days of 3D printing acrylonitrile butadiene styrene (ABS) was used widely, however this material has several drawbacks, in particular the styrene¹³⁹ fumes produced when it prints in addition to its difficulty to print without a heated enclosure make it non-ideal for use in a research environment.¹⁴⁰ Polyethylene terephthalate (PET/PETG) provides similar properties and improved chemical resistance compared to ABS, without the difficulties in printing and associated risks. Polypropylene is commonly used in chemistry settings due to its excellent chemical resistance, and as a thermoplastic is also available in filament form. While not as easy to print as PLA, due to its poor bed adhesion and tendency to warp the chemical and impact resistance makes it an attractive choice for low strength applications that require a high durability.

Polytetrafluoroethylene (PTFE) and polyether ether ketone (PEEK) are both also commonly used in scientific research environments and are available as 3D printer filaments. However, due to the extremely high melting points of these materials (> 350 °C) most desktop 3D printers are unable to print them. Specialized machines do exist for these materials; however, they are often unsuitable for traditional filaments. For applications where mechanical durability and toughness are important Nylon filaments are often the best choice, however these filaments are challenging to print with, requiring high extrusion and bed temperatures, as well as requiring airtight storage and drying to remove absorbed moisture before printing.

Functional and functionalized filaments are also commercially available with flexible thermoplastic elastomers been the most common, and used for hinges, gaskets, seals, and

corks/lids. Functionalized materials like carbon impregnated filaments are used for manufacturing conductive parts such as electrodes and circuits.¹⁴¹ It is worth noting that functionalized filaments can be custom made by blending the base thermoplastic with functional groups/molecules and extrude as a filament creating new materials with unique proprieties.¹⁴²

1.8.2 Stereolithography

The second most common desktop 3D printing technology is vat photopolymerization (VP), the basis of which is the use of ultra-violet (UV) light to polymerize specific areas of a vat of photo-activated polymer resin, to build up an object layer by layer. SLA 3D printer are the oldest 3D printing technology, having been invented in 1980s.¹⁴³ In SLA a UV laser diode is used as the UV light source and mirror galvanometers are used to move the laser beam, allowing it to trace the shape of the part into a thin layer of the photopolymer to solidify it. They are much simpler in operation than their FDM counterparts with only a few moving parts (Figure 1.18).

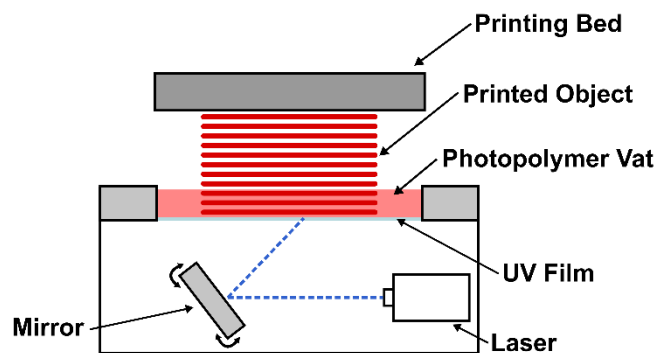


Figure 1.18: Schematic of an SLA 3D Printer.

VP printers are suitable for printing objects down to mm in size with an excellent surface finish and can be used to make parts too small or highly detailed for FDM. The minimum feature size (resolution) of these printers is dictated by the smallest area of resin that can be exposed to the UV light. In SLA this is the spot size of the laser (typically ~ 0.1 mm). A good initial rule is to keep features bigger than 0.2 mm initially, but certain printers maybe able to reliably produce smaller features.

The most significant difference in using a VP printer compared to an FDM is the amount of post processing required. With an FDM print the object can immediately be removed from the printer and once separated from any support, if there is any, is ready to use. This process is much more complicated for VP printers, after the print completes the objects must be washed in alcohol to remove excesses unpolymerized resin from its surface and internal features. After

drying the part needs to be further cured under additional UV light before they can be used, a process that can take upwards of an hour. Careful washing and curing of printed parts are essential to achieving a good surface finish and advertised material properties. While it is possible to build or buy accessories to automate the processes of washing and curing, even with these tools some operator intervention is still required.

The variety of materials accessible with VP printer is even larger than those available for FDM. Transparent parts for custom optics can be made by polishing a clear resin, something very difficult to achieve in FDM. The addition of pigments to the resin can allow for the blending of custom colors. Elastomeric polymers can be printed to provide custom gaskets and seals, while temperature resistant resins can be autoclaved without issue. For applications where polymers are not suitable, objects can be printed in a wax-like material, which can then be used to cast metal parts, or printed in a ceramic filled resin, which can be fired, leaving an entirely ceramic part.¹³⁶

1.9 Aims and Objectives

This thesis aims to explore emerging applications for lab-grown diamond in both its un-doped and boron-doped form. Electrochemical methods are used for preparation, characterisation, or application throughout

Specifically, in Chapter 3, the implantation and lift-off route for thin diamond membrane production is explored, with particular attention paid to improving the rate of the electrochemical etch step. This step is used to remove the embedded graphitic layer from the single crystal diamond, freeing a sub- μm thick membrane. An in-situ optical monitoring method is developed and used to study the electrochemical etch as it progresses, providing unique insights into the etch process. Electron paramagnetic resonance (EPR) was also employed to study the radical reactions which may be occurring during the etch. Improving the rate of this step is critical to the commercialisation of this route to membrane production as it currently represents the least developed and most time-consuming step. Easy fabrication routes, or commercial availability of these membranes will undoubtedly help researchers trying to develop NV defect-based quantum devices.

In Chapter 4 the factors effecting the anodic corrosion of BDD electrodes used in electrochemical advanced oxidation systems will be investigated. We aim to use a novel white light interferometry (WLI) method to directly measure corrosion on short laboratory-relevant timescales. Using this WLI method and a custom designed flow cell initial investigations into the effect of solution and operational parameters on corrosion rate are investigated. BDD-EAO systems show a lot of promise for treating environmentally harmful or difficult to

remove waste however uncertainty over the rate of corrosion on the electrodes has hampered wide utilisation. By elucidating the reasons for high corrosion rates shown in some solutions and providing a quick test for the suitability of BDD electrodes in a particular effluent it is hoped that BDD-EAO systems will see wider deployment in the field.

The work discussed in Chapter 5 concerns the optimisation of a cell for EOP, focussing particularly on electrode design. We move away from incorporating NDC carbon during the growth process to deliberate and controlled NDC incorporation in freestanding BDD by laser micromachining. Several cell design parameters are investigated and what we believe to be an optimal cell design presented.

Chapter 6 details efforts to construct a low-cost and flexible RRDE electrode which can be easily assembled by researchers. Excluding the electrodes themselves the electrode costs < £20, much reduced from the > £1,500 cost of a commercial electrode. The RRDE consists of five parts, designed to be produced in advance and assembled, as required by the researcher, without need for specialised tools, as required. The fabrication method is also designed to work with foil, bar and sheet electrode materials, allowing for custom electrodes to be constructed in much more exotic materials than the Au, Pt and Glassy Carbon normally available.

Finally, Chapter 7 summarises the work discussed throughout this thesis and discusses potential future work in from each chapter.

1.10 References

- 1 W. H. Bragg, 1913, **88**, 428–438.
- 2 J. E. Field, *Reports Prog. Phys.*, , DOI:10.1088/0034-4885/75/12/126505.
- 3 R. S. Balmer, J. R. Brandon, S. L. Clewes, H. K. Dhillon, J. M. Dodson and I. Friel, *J. Phys. Condens. Matter*, 2009, **21**, 364221.
- 4 I. Aharonovich, A. D. Greentree and S. Prawer, *Nat. Photonics*, 2011, **5**, 397–405.
- 5 A. Faraon, P. E. Barclay, C. Santori, K. M. C. Fu and R. G. Beausoleil, *Nat. Photonics*, 2011, **5**, 301–305.
- 6 R. S. Balmer, J. R. Brandon, S. L. Clewes, H. K. Dhillon, J. M. Dodson, I. Friel, P. N. Inglis, T. D. Madgwick, M. L. Markham, T. P. Mollart, N. Perkins, G. a Scarsbrook, D. J. Twitchen, a J. Whitehead, J. J. Wilman and S. M. Woollard, *J. Phys. Condens. Matter*, 2009, **21**, 364221.
- 7 H. Blatt, R. J Tracy and B. E Owens, in *Petrology: igneous, sedimentary, and metamorphic*, 2006, p. 212.
- 8 F. P. Bundy, H. T. Hall, H. . Strong and R. H. Wentorf, *Nature*, 1955, 51–55.
- 9 M. Akaishi, H. Kanda and S. Yamaoka, *Jpn. J. Appl. Phys.*, 1990, **29**, L1172–L1174.
- 10 R. S. Balmer, J. R. Brandon, S. L. Clewes, H. K. Dhillon, J. M. Dodson, I. Friel, P. N. Inglis, T. D. Madgwick, M. L. Markham, T. P. Mollart, N. Perkins, G. A. Scarsbrook, D. J. Twitchen, A. J. Whitehead, J. J. Wilman and S. M. Woollard, *J. Phys. Condens. Matter*, , DOI:10.1088/0953-8984/21/36/364221.
- 11 Y. Tian, X. Jia, C. Zang, S. Li, H. Xiao, Y. Zhang, G. Huang, R. Li, Q. Han, L. Ma, Y. Li, X. Chen, C. Zhang and H. Ma, *Chinese Sci. Bull.*, 2009, **54**, 1459–1462.
- 12 I. I. Vlasov, V. G. Ralchenko, A. V. Khomich, S. V. Nistor, D. Shoemaker and R. A. Khmelnitskii, *Phys. Status Solidi Appl. Res.*, 2000, **181**, 83–90.
- 13 Y. N. Palyanov, Y. M. Borzdov, I. N. Kupriyanov, Y. V. Bataleva and A. F. Khohkhryakov, *Diam. Relat. Mater.*, 2015, **58**, 40–45.
- 14 and M. J. C. Philip M. Martineau Simon C. Lawson, Andy J. Taylor, Samantha J. Quinn, David J. F. Evans, *Gems Gemol.*, 2013, **XLIX**, 2–25.
- 15 H. Bensalah, I. Stenger, G. Sakr, J. Barjon, R. Bachelet, A. Tallaire, J. Achard, N. Vaissiere, K. H. Lee, S. Saada and J. C. Arnault, *Diam. Relat. Mater.*, 2016, **66**, 188–

- 195.
- 16 J. C. Angus, Y. Wang and M. Sunkara, *Annu. Rev. Mater. Sci.*, 1991, 221–248.
- 17 E. Sevillano, in *Low-Pressure Synthetic Diamond*, Springer, Berlin, Heidelberg, 1998, pp. 11–39.
- 18 J. Herlinger, *Thin Solid Films*, 2006, **501**, 65–69.
- 19 P. K. Bachmann, D. Leers and H. Lydtin, *Diam. Relat. Mat.*, 1991, **1**, 1–12.
- 20 J. Luque, W. Juchmann, E. A. Brinkman and J. B. Jeffries, *J. Vac. Sci. Technol. A Vacuum, Surfaces, Film.*, 1998, **16**, 397–408.
- 21 X. Blase, E. Bustarret, C. Chapelier, T. Klein and C. Marcenat, *Nat. Mater.*, 2009, **8**, 375–382.
- 22 L. Diederich, O. M. Küttel, P. Ruffieux, T. Pillo, P. Aebi and L. Schlapbach, *Surf. Sci.*, 1998, **417**, 41–52.
- 23 J. V. Macpherson, *Phys. Chem. Chem. Phys.*, 2015, **17**, 2935–2949.
- 24 S. Koizumi, M. Kamo, Y. Sato, S. Mita, A. Sawabe, A. Reznik, C. Uzan-Saguy and R. Kalish, *Diam. Relat. Mater.*, 1998, **7**, 540–544.
- 25 L. J. Simcox, R. P. A. Pereira, E. M. H. Wellington and J. V. Macpherson, *ACS Appl. Mater. Interfaces*, 2019, **11**, 25024–25033.
- 26 E. Fujishima, A., Einaga, Ya., Rao, T.N., and Tryk, D.A., *Elektrokhimiya*, 2005, **41**, 1401–1403.
- 27 S. T. Sultana, J. T. Babauta and H. Beyenal, *Biofouling*, 2015, **31**, 745–758.
- 28 N. Vatisstas, *Int. J. Electrochem.*, 2012, **2012**, 1–7.
- 29 B. Marselli, J. Garcia-Gomez, P.-A. Michaud, M. A. Rodrigo and C. Comninellis, *J. Electrochem. Soc.*, 2003, **150**, D79.
- 30 S. Morooka, T. Fukui, K. Semoto, T. Tsubota, T. Saito, K. Kusakabe, H. Maeda, Y. Hayashi and T. Asano, *Diam. Relat. Mater.*, 1999, **8**, 42–47.
- 31 G. F. Wood, C. E. Zvoriste-Walters, M. G. Munday, M. E. Newton, V. Shkirskiy, P. R. Unwin and J. V. Macpherson, *Carbon N. Y.*, 2021, **171**, 845–856.
- 32 S. Kawai, H. Yamano, T. Sonoda, K. Kato, J. J. Buendia, T. Kageura, R. Fukuda, T. Okada, T. Tanii, T. Higuchi, M. Haruyama, K. Yamada, S. Onoda, T. Ohshima, W.

- Kada, O. Hanaizumi, A. Stacey, T. Teraji, S. Kono, J. Isoya and H. Kawarada, *J. Phys. Chem. C*, 2019, **123**, 3594–3604.
- 33 R. Boukherroub, X. Wallart, S. Szunerits, B. Marcus, P. Bouvier and M. Mermoux, *Electrochem. commun.*, 2005, **7**, 937–940.
 - 34 R. E. Thomas, R. A. Rudder and R. J. Markunas, *J. Vac. Sci. Technol. A Vacuum, Surfaces, Film.*, 1992, **10**, 2451–2457.
 - 35 S. Chaudhuri, S. J. Hall, B. P. Klein, M. Walker, A. J. Logsdail, J. V. Macpherson and R. J. Maurer, *Commun. Mater.*, 2022, **3**, 0–8.
 - 36 L. M. Struck and M. P. D'Evelyn, *J. Vac. Sci. Technol. A Vacuum, Surfaces, Film.*, 1993, **11**, 1992–1997.
 - 37 P. E. Pehrsson, T. W. Mercer and J. A. Chaney, *Surf. Sci.*, 2002, **497**, 13–28.
 - 38 P. E. Pehrsson and T. W. Mercer, *Surf. Sci.*, 2000, **460**, 74–90.
 - 39 K. P. Loh, X. N. Xie, S. W. Yang and J. C. Zheng, *J. Phys. Chem. B*, 2002, **106**, 5230–5240.
 - 40 H. Luo, K. M. Ajmal, W. Liu, K. Yamamura and H. Deng, *Int. J. Extrem. Manuf.*, , DOI:10.1088/2631-7990/abe915.
 - 41 T. Schuelke and T. A. Grotjohn, *Diam. Relat. Mater.*, 2013, **32**, 17–26.
 - 42 J. R. Hird and J. E. Field, *Wear*, 2005, **258**, 18–25.
 - 43 A. V Bulgakov and N. M. Bulgakova, *Quantum Electron.*, 1999, **29**, 433–437.
 - 44 J. P. Hermani, M. Emonts and C. Brecher, *INTERTECH 2015 - An Int. Tech. Conf. Diamond, Cubic Boron Nitride their Appl.*
 - 45 M. Piccardo, F. Bosia, P. Olivero and N. Pugno, *Diam. Relat. Mater.*, 2014, **48**, 73–81.
 - 46 Z. Zhang, Q. Zhang and J. Xu, *J. Appl. Phys.*, , DOI:10.1063/5.0057163.
 - 47 T. V. Kononenko, V. G. Ralchenko, I. I. Vlasov, S. V. Garnov and V. I. Konov, *Diam. Relat. Mater.*, 1998, **7**, 1623–1627.
 - 48 E. Cappelli, G. Mattei, S. Orlando, F. Pinzari and P. Ascarelli, *Diam. Relat. Mater.*, 1999, **8**, 257–261.
 - 49 J. Li, C. L. Bentley, S. Y. Tan, V. S. S. Mosali, M. A. Rahman, S. J. Cobb, S. X. Guo,

- J. V. Macpherson, P. R. Unwin, A. M. Bond and J. Zhang, *J. Phys. Chem. C*, 2019, **123**, 17397–17406.
- 50 T. Okuchi, H. Ohfuji, S. Odake, H. Kagi, S. Nagatomo, M. Sugata and H. Sumiya, *Appl. Phys. A Mater. Sci. Process.*, 2009, **96**, 833–842.
- 51 S. Gloor, W. Lüthy, H. P. Weber, S. M. Pimenov, V. G. Ralchenko, V. I. Konov and A. V. Khomich, *Appl. Surf. Sci.*, 1999, **138–139**, 135–139.
- 52 P. W. Butler-Smith, D. A. Axinte, M. Pacella and M. W. Fay, *J. Mater. Process. Technol.*, 2013, **213**, 194–200.
- 53 S. Odake, H. Ohfuji, T. Okuchi, H. Kagi, H. Sumiya and T. Irifune, *Diam. Relat. Mater.*, 2009, **18**, 877–880.
- 54 L. Zhao, C. Song, J. Zhang, Y. Huang, C. Zhang, Y. Liu, B. Dong, Z. Xu, G. Li and T. Sun, *Appl. Surf. Sci.*, 2022, **578**, 151995.
- 55 S. J. Cobb, F. H. J. Laidlaw, G. West, G. Wood, M. E. Newton, R. Beanland and J. V. Macpherson, *Carbon N. Y.*, 2020, **167**, 1–10.
- 56 V. S. Vavilov, *Radiat. Eff.*, 1978, **37**, 229–236.
- 57 R. Kalish, *Appl. Surf. Sci.*, 1997, **117–118**, 558–569.
- 58 J. F. Prins, *Semicond. Sci. Technol.*, , DOI:10.1088/0268-1242/18/3/304.
- 59 J. F. Prins, *Mater. Sci. Reports*, 1992, **7**, 275–364.
- 60 J. F. Ziegler, M. D. Ziegler and J. P. Biersack, *Nucl. Instruments Methods Phys. Res. Sect. B Beam Interact. with Mater. Atoms*, 2010, **268**, 1818–1823.
- 61 B. A. Fairchild, S. Rubanov, D. W. M. Lau, M. Robinson, I. Suarez-Martinez, N. Marks, A. D. Greentree, D. McCulloch and S. Prawer, *Adv. Mater.*, 2012, **24**, 2024–2029.
- 62 N. R. Parikh, J. D. Hunn, E. McGucken, M. L. Swanson, C. W. White, R. A. Rudder, D. P. Malta, J. B. Posthill and R. J. Markunas, *Appl. Phys. Lett.*, 1992, **61**, 3124–3126.
- 63 M. Marchywka, P. E. Pehrsson, S. C. Binari and D. Moses, *J. Electrochem. Soc.*, 1993, **140**, L19–L22.
- 64 A. W. Colburn, K. J. Levey, D. O’Hare and J. V. Macpherson, *Phys. Chem. Chem. Phys.*, 2021, **23**, 8100–8117.

- 65 J. Wang, *Analytical electrochemistry*, 2006.
- 66 N. Elgrishi, K. J. Rountree, B. D. McCarthy, E. S. Rountree, T. T. Eisenhart and J. L. Dempsey, *J. Chem. Educ.*, 2018, **95**, 197–206.
- 67 A. J. Bard and L. R. Faulkner, *Electrochemical Methods - Fundamentals and Applications*, Wiley, 2nd edn., 2001, vol. 2.
- 68 R. M. Wightman, *Anal. Chem.*, 1981, **53**, 1125A-1134A.
- 69 A. N. Frumkin, L. N. Nekrasov, B. Levich and J. Ivanov, *J. Electroanal. Chem.*, 1959, **1**, 84–90.
- 70 W. J. Albery and S. Bruckenstein, *Trans. Faraday Soc.*, 1966, **62**, 1920–1931.
- 71 U. A. Paulus, T. J. Schmidt, H. A. Gasteiger and R. J. Behm, *J. Electroanal. Chem.*, 2001, **495**, 134–145.
- 72 M. Ferrara, M. Bevilacqua, C. Tavagnacco, F. Vizza and P. Fornasiero, *ChemCatChem*, 2020, **12**, 6205–6213.
- 73 S. Hessami and C. W. Tobias, *AIChE J.*, 1993, **39**, 149–162.
- 74 Z. Jia, G. Yin and J. Zhang, *Rotating Ring-Disk Electrode Method*, Elsevier B.V., 2014.
- 75 M. Fleischmann, J. Ghoroghchian and S. Pons, *J. Phys. Chem.*, 1985, **89**, 5530–5536.
- 76 J. Ghoroghchian, S. Pons and M. Fleischmann, *J. Electroanal. Chem.*, 1991, **317**, 101–108.
- 77 S. Cervera-March, E. S. Smotkin, A. J. Bard, A. Campion, M. A. Fox, T. Mallouk, S. E. Webber and J. M. White, *J. Electrochem. Soc.*, 1988, **135**, 567–573.
- 78 E. Smotkin, A. J. Bard, A. Campion, M. A. Fox, T. Mallouk, E. Stephen and J. M. White, 1986, 4604–4607.
- 79 F. Mavr , R. K. Anand, D. R. Laws, K. F. Chow, B. Y. Chang, J. A. Crooks and R. M. Crooks, *Anal. Chem.*, 2010, **82**, 8766–8774.
- 80 R. M. Crooks, *ChemElectroChem*, 2016, **3**, 357–359.
- 81 G. Loget, D. Zigah, L. Bouffier, N. Sojic and A. Kuhn, *Acc. Chem. Res.*, 2013, **46**, 2513–2523.
- 82 A. M. Zaitsev, *Phys. Rev. B*, 2000, **61**, 12909–12922.

- 83 A. H. Piracha, K. Ganesan, D. W. M. Lau, A. Stacey, L. P. McGuinness, S. Tomljenovic-Hanic and S. Prawer, *Nanoscale*, 2016, **8**, 6860–6865.
- 84 G. Davies and M. F. Hamer, *Proc. R. Soc. A Math. Phys. Eng. Sci.*, 1976, **348**, 285–298.
- 85 M. W. Doherty, N. B. Manson, P. Delaney, F. Jelezko, J. Wrachtrup and L. C. L. Hollenberg, *Phys. Rep.*, 2013, **528**, 1–45.
- 86 G. Davies, *J. Phys. Part C Solid State Phys.*, 1972, **5**, 2534–.
- 87 R. Kalish, C. Uzan-Saguy, B. Phiosoph, V. Richter, J. P. Lagrange, E. Gheeraert, A. Deneuville and A. T. Collins, *Diam. Relat. Mater.*, 1997, **6**, 516–520.
- 88 J. Meijer, B. Burchard, M. Domhan, C. Wittmann, T. Gaebel, I. Popa, F. Jelezko, J. Wrachtrup, J. Meijer and B. Burchard, 2016, **261909**, 1–13.
- 89 B. J. M. Hausmann, I. Bulu, V. Venkataraman, P. Deotare and M. Loncar, *Nat. Photonics*, 2014, **8**, 369–374.
- 90 M. Pomorski, B. Caylar and P. Bergonzo, *Appl. Phys. Lett.*, 2013, **103**, 2106.
- 91 G. V. Buxton, C. L. Greenstock, W. P. Helman and A. B. Ross, *J. Phys. Chem. Ref. Data*, 1988, **17**, 513–886.
- 92 N. M. dos Santos, M. R. de V. Lanza, N. G. Ferreira and M. R. Baldan, *Rev. Bras. Apl. Vácuo*, 2016, **35**, 17.
- 93 K. E. Carter and J. Farrell, *Environ. Sci. Technol.*, 2008, **42**, 6111–6115.
- 94 Q. Zhuo, S. Deng, B. Yang, J. Huang and G. Yu, *Environ. Sci. Technol.*, 2011, **45**, 2973–2979.
- 95 B. Adams, M. Tian and A. Chen, *Electrochim. Acta*, 2009, **54**, 1491–1498.
- 96 C. Borrás, P. Rodríguez, T. Laredo, J. Mostany and B. R. Scharifker, *J. Appl. Electrochem.*, 2004, **34**, 583–589.
- 97 Y. Liu, H. Liu and Y. Li, *Appl. Catal. B Environ.*, 2008, **84**, 297–302.
- 98 P. Cañizares, J. Lobato, R. Paz, M. A. Rodrigo and C. Sáez, *Water Res.*, 2005, **39**, 2687–2703.
- 99 A. Farhat, J. Keller, S. Tait and J. Radjenovic, *Environ. Sci. Technol.*, 2015, **49**, 14326–14333.

- 100 N. Katsuki, *J. Electrochem. Soc.*, 1998, **145**, 2358.
- 101 S. Hammami, N. Bellakhal, N. Oturan, M. A. Oturan and M. Dachraoui, *Chemosphere*, 2008, **73**, 678–684.
- 102 J. F. Zhi, H. Bin Wang, T. Nakashima, T. N. Rao and A. Fujishima, *J. Phys. Chem. B*, 2003, **107**, 13389–13395.
- 103 B. P. Chaplin, *Environ. Sci. Process. Impacts*, 2014, **16**, 1182–1203.
- 104 T. Kashiwada, T. Watanabe, Y. Ootani, Y. Tateyama and Y. Einaga, *ACS Appl. Mater. Interfaces*, 2016, **8**, 28299–28305.
- 105 B. P. Chaplin, I. Wyle, H. Zeng, J. A. Carlisle and J. Farrell, *J. Appl. Electrochem.*, 2011, **41**, 1329–1340.
- 106 V. Fisher, D. Gandini, S. Laufer, E. Blank and C. Comninellis, 1998, **44**, 521–524.
- 107 I. Gerger, R. Haubner, H. Kronberger and G. Faflek, *Diam. Relat. Mater.*, 2004, **13**, 1062–1069.
- 108 M. Fryda, D. Herrmann, L. Schäfer, C. P. Klages, A. Perret, W. Haenni, C. Comninellis and D. Gandini, *New Diam. Front. Carbon Technol.*, 1999, **9**, 229–240.
- 109 X. R. Lu, M. H. Ding, C. Zhang and W. Z. Tang, *Thin Solid Films*, 2018, **660**, 306–313.
- 110 N. Katsuki, E. Takahashi, M. Toyoda, T. Kurosu, M. Iida, S. Wakita, Y. Nishiki and T. Shimamune, *J. Electrochem. Soc.*, 1998, **145**, 2358–2362.
- 111 X. R. Lu, M. H. Ding, C. Zhang and W. Z. Tang, *Diam. Relat. Mater.*, 2019, **93**, 26–33.
- 112 B. P. Chaplin, D. K. Hubler and J. Farrell, *Electrochim. Acta*, 2013, **89**, 122–131.
- 113 T. Kolber, K. Piplits, R. Haubner and H. Hutter, *Fresenius. J. Anal. Chem.*, 1999, **365**, 636–641.
- 114 M. Panizza, G. Siné, I. Duo, L. Ouattara and C. Comninellis, *Electrochem. Solid-State Lett.*, 2003, **6**, 17–19.
- 115 M. C. Granger and G. M. Swain, *J. Electrochem. Soc.*, 1999, **146**, 4551.
- 116 P. A. Christensen, T. Yonar and K. Zakaria, *Ozone Sci. Eng.*, 2013, **35**, 149–167.
- 117 L. M. Da Silva, L. A. De Faria and J. F. C. Boodts, *Electrochim. Acta*, 2003, **48**, 699–

709.

- 118 M. I. Awad and M. M. Saleh, *J. Solid State Electrochem.*, 2010, **14**, 1877–1883.
- 119 L. M. Da Silva, D. V. Franco, L. G. Sousa and I. C. Gonçalves, *J. Appl. Electrochem.*, 2010, **40**, 855–864.
- 120 P. C. Foller and M. L. Goodwin, *Ozone Sci. Eng.*, 1984, **6**, 29–36.
- 121 K. Arihara, C. Terashima and A. Fujishima, *J. Electrochem. Soc.*, 2007, **154**, E71.
- 122 A. Kraft, M. Stadelmann, M. Wünsche and M. Blaschke, *Electrochem. commun.*, 2006, **8**, 883–886.
- 123 Y.-H. Wang and Q.-Y. Chen, *Int. J. Electrochem.*, 2013, **2013**, 1–7.
- 124 Y. Nishiki, N. Kitaori and K. Nakamuro, *Ozone Sci. Eng.*, 2011, **33**, 114–120.
- 125 C. Hurt, M. Brandt, S. S. Priya, T. Bhatelia, J. Patel, P. R. Selvakannan and S. Bhargava, *Catal. Sci. Technol.*, 2017, **7**, 3421–3439.
- 126 C. R. Tubío, J. Azuaje, L. Escalante, A. Coelho, F. Guitián, E. Sotelo and A. Gil, *J. Catal.*, 2016, **334**, 110–115.
- 127 J. C. Bui, J. T. Davis and D. V. Esposito, *Sustain. Energy Fuels*, 2020, **4**, 213–225.
- 128 C. Zhu, T. Liu, F. Qian, W. Chen, S. Chandrasekaran, B. Yao, Y. Song, E. B. Duoss, J. D. Kuntz, C. M. Spadaccini, M. A. Worsley and Y. Li, *Nano Today*, 2017, **15**, 107–120.
- 129 A. Ambrosi and R. D. Webster, *Curr. Opin. Electrochem.*, 2020, **20**, 28–35.
- 130 G. N. Meloni, *Anal. Chem.*, 2017, **89**, 8643–8649.
- 131 G. N. Meloni and M. Bertotti, *PLoS One*, 2017, **12**, e0182000.
- 132 R. J. White, White’s group 3D print repository.
- 133 C. W. Pinger, M. K. Geiger and D. M. Spence, *J. Chem. Educ.*, 2020, **97**, 112–117.
- 134 S. S. Zalesskiy, P. J. Kitson, P. Frei, A. Bubliauskas and L. Cronin, *Nat. Commun.*, 2019, **10**, 6–13.
- 135 P. J. Kitson, S. Glatzel, W. Chen, C.-G. Lin, Y.-F. Song and L. Cronin, *Nat. Protoc.*, 2016, **11**, 920–936.
- 136 C. Parra-Cabrera, C. Achille, S. Kuhn and R. Ameloot, *Chem. Soc. Rev.*, 2018, **47**,

209–230.

- 137 S. Khan, S. Ali and A. Bermak, *Sensors (Switzerland)*, , DOI:10.3390/s19051230.
- 138 E. M. Richter, D. P. Rocha, R. M. Cardoso, E. M. Keefe, C. W. Foster, R. A. A. Munoz and C. E. Banks, *Anal. Chem.*, 2019, **91**, 12844–12851.
- 139 J. Bours, B. Adzima, S. Gladwin, J. Cabral and S. Mau, *J. Ind. Ecol.*, 2017, **21**, S25–S36.
- 140 I. Gümperlein, E. Fischer, G. Dietrich-Gümperlein, S. Karrasch, D. Nowak, R. A. Jörres and R. Schierl, *Indoor Air*, 2018, **28**, 611–623.
- 141 S. J. Leigh, R. J. Bradley, C. P. Purssell, D. R. Billson and D. A. Hutchins, *PLoS One*, 2012, **7**, e49365.
- 142 L. Kool, A. Bunschoten, A. H. Velders and V. Saggiomo, *Beilstein J. Nanotechnol.*, 2019, **10**, 442–447.
- 143 I. Gibson and P. Jorge Bartolo, “History of Stereolithography.” *Stereolithography: Materials, Processes, and Applications*.

Chapter 2: Materials and Methods

2.1 Materials

2.1.1 Single Crystal Diamond Materials:

Chapter 3 of this thesis concerns the use of single crystal diamond plates. These plates are synthesised by either HPHT or CVD growth. All single crystal diamond samples were supplied by Element Six (UK) Limited. The plates used are summarised in Table 2.1.

Table 2.1: Tabulation of all the single crystal diamond plates used in this thesis.

Type	Synthesis Method	Nitrogen Concentration (ppm)	Orientation	Size (mm)
Standard Grade	CVD	< 1	[100]	4.2
Standard Grade	CVD	< 1	[100]	3.5
Type 1b	HPHT	< 200	[100]	3.5

2.1.2 Boron Doped Diamond Materials:

In Chapters 4 through 6 of this thesis extensive use is made of polycrystalline boron doped diamond (BDD) material. Freestanding BDD materials, supplied by Element Six (UK) Limited are summarised in Table 2.2.

Table 2.2: Tabulation of all freestanding BDD used in this thesis.

Type	Boron Dopant Density (cm^{-3}) ^{1,2}	Surface Finishes (RMS)
Electroanalytical (EA) Grade	3×10^{20}	Growth: ~ 2 nm Nucleation: 500 nm
As Grown Electrochemical Processing (EP) Grade	$\sim 3 \times 10^{20}$	Growth: ~ 15 μm (Unprocessed) Nucleation: 100 nm (Unprocessed)
Electrochemical Processing (EP) Grade	$\sim 3 \times 10^{20}$	Growth: ~ 50 nm Nucleation: 500

Electroanalytical (EA) grade and Electroprocessing (EP) are grown under different conditions. The emphasis during the growth of EA-BDD is to ensure a material with high phase purity, at the cost of growth speed. EP-BDD conversely is designed for applications where large area electrodes are required. Because of this it is grown faster to reduce the material cost. This difference in growth conditions, results in very different crystal morphology, as can be seen in Figure 2.1.

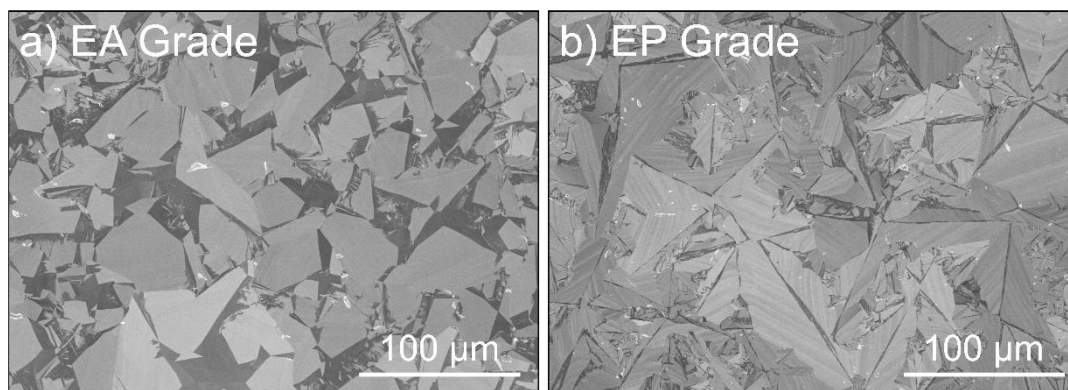


Figure 2.1: In-Lens FE-SEM images of highly polished a) electroanalytical (EA) grade and b) electroprocessing (EP) grade BDD. SEM imaging is discussed in section 2.4.3.

In these SEM images the difference in crystal morphology is immediately apparent, the EA grade surfaces have large trapezoid grains whereas the EP grade shows a distinctive “palm tree” crystal structure typical of this material. Note the striations in the grains in the EP grade image, which are much less prevalent for EA grade. These striations are as a result of extended stacking faults which incorporate more boron than the surrounding grain, leading to the contrast seen in SEM. To understand the crystal orientation and typical grain size distribution these areas of the sample were characterised by electron backscatter diffraction (EBSD) which is described more fully in section 2.4.4. Crystal direction maps of the areas in Figure 2.1 a and b can be seen in figure 2.2 a and b respectively.

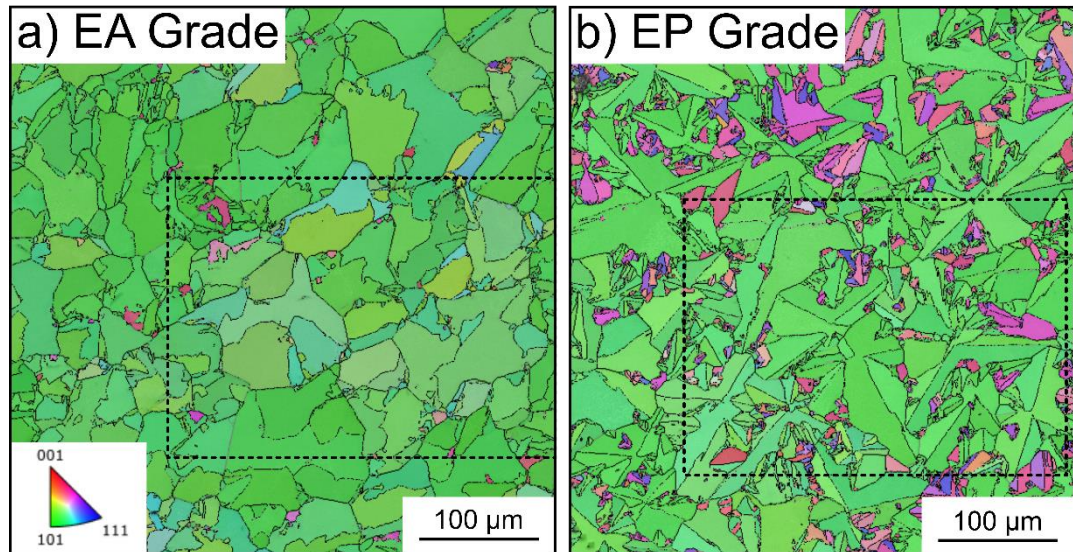


Figure 2.2: Electron backscatter diffraction data for a) electroanalytical (EA) grade and b) electroprocessing (EP) grade BDD. The dotted squares represent the approximate areas of the FE-SEM from 2.1a and b respectively. EBSD is discussed in section 2.4.4.

EBSD shows that polishing the as grown face of the BDD surface for both materials reveals a predominantly [110] textured surfaces, although other textures such as [111] and [113] are also present. Crystal directions other than [110] are much more prevalent in the EP-BDD material than in the EA-BDD. Additionally, groups of very small crystallites are visible between larger grains for EP-BDD. On average the grains in EA-BDD are 25% larger than for EP-BDD with an area weighted equivalent circle diameter of 43 μm for EA-BDD vs 32 μm for EP-BDD.

More limited use is also made of thin-film BDD supported on a non-diamond (Niobium) substrate, this material is summarised in Table 2.3. Thin-film BDD material was purchased from CONDIAS GmbH (Germany). The surface of this material has been characterised by SEM and can be seen in Figure 2.3.

Table 2.3: Tabulation of all thin-film BDD used in this thesis.

Type	Boron Dopant Density ¹ (cm^{-3}) ¹	Surface Finish (RMS)	Size
DIACHEM	1.9×10^{20}	Growth: $\sim 6 \mu\text{m}$	8 mm Diameter Circles

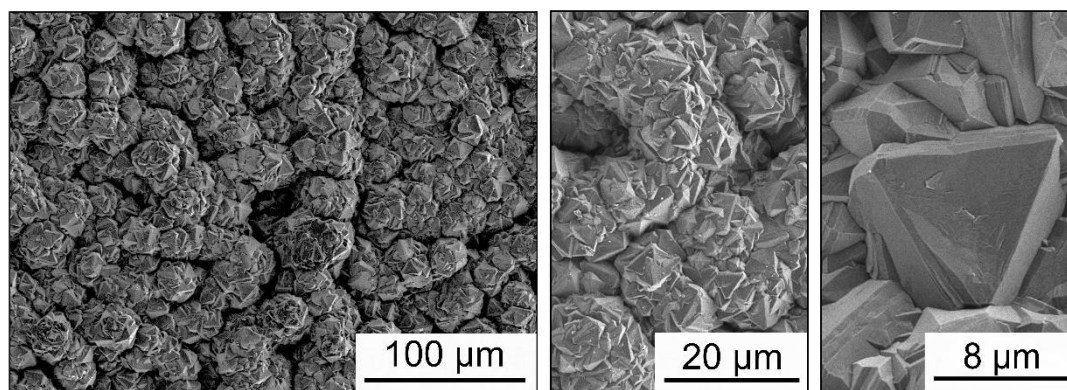


Figure 2.3: SE2 detector FE-SEM images of the “as-grown” DIACHEM Condias surface used in this work at various magnifications.

2.1.3 Carbon Materials:

In chapter 5, a glassy carbon (GC) material is also used to compare to BDD, the material used was 300 µm thick SIGRADUR G, purchased from HTW Hochtemperatur-Werkstoffe GmbH (Germany).

2.2 Chemicals

All solutions were prepared using 18 MΩ ultra-pure water (Milli-Q, Millipore, UK).

Chemicals were used as supplied without additional purification.

Table 2.4: Tabulation of all the chemicals utilised in this thesis.

Chemical	Formula	Purity	Supplier
Sulphuric Acid	H ₂ SO ₄	> 96%	Merck
Potassium Nitrate	KNO ₃	99.97%	Sigma Aldrich
Boric Acid	H ₃ BO ₃	99.97%	Sigma Aldrich
Potassium Chloride	KCl	≥ 99%	Sigma Aldrich
Potassium Sulphate	K ₂ SO ₄	Analysis Grade	Sigma Aldrich
Potassium Sulphate	K ₂ SO ₄	Pure	Acros Organics
5,5-dimethyl-1-pyrroline-N-oxide	DMPO	Pure	Enzo Life Sciences
Titanium (IV) Oxide Anatase	TiO ₂	99.7%	Alfa Aesar
Hydrogen Peroxide	H ₂ O ₂	30% w/w	Sigma Aldrich

Acetic Acid	CH ₃ COOH	99%	Sigma Aldrich
D-(+)-Glucose	C ₆ H ₁₂ O ₆	≥99.5%	Sigma Aldrich
Perfluorooctane Sulfonic Acid	PFOS-K	95%	Sigma Aldrich
Hexaamineruthenium(III) Chloride	Ru(NH ₃) ₆ Cl ₃	99%	Strem Chemicals
Citric Acid	C ₆ H ₈ O ₇	≥ 99.5%	Fisher Chemicals
Tertiary Sodium Phosphate	Na ₃ PO ₄	≥ 99.0%	Acros Organics
Hydrochloric Acid	HCl	99%	Sigma Aldrich
Potassium Hexachloroplatinate	K ₂ PtCl ₆	99%	Sigma Aldrich
Perchloric Acid	HClO ₄	70%	Sigma Aldrich

2.2.1 FcTMA

The ferrocenylmethyl trimethylammonium, (FcTMA⁺ PF₆⁻) used in this thesis was synthesised in house according to the procedure described by Lemay et.al.³

2.3 Fabrication Techniques

2.3.1 Laser Processing:

Laser processing of diamond was performed using two commercial laser micromachining systems:

Oxford Lasers (Oxford, UK) E-Series: A 10 W frequency tripled (355 nm) Nd:YAG UV laser with 34 ns pulse duration was used for all diamond cutting and some surface modification. The system was also fitted with a trepan, which enlarges the size of the laser spot to allow for wider and deeper cuts. The E-Series has an optical autofocus system which allows for precise focusing of the laser on the material surface. This system is used for cutting the BDD electrodes in Chapter 4, Chapter 5, and Chapter 6, it is also used to create the surface NDC on the BDD disk for Chapter 6.

Oxford Lasers (Oxford, UK) A-Series: This compact laser system has a 3W frequency doubled (532 nm) Nd:YAG green laser with a 15 ns pulse duration. This system is primarily used for low-power applications such as surface roughening and modification and has no additional equipment fitted. This system was used to roughen the contact tabs of the slotted ozone electrodes, and to pattern the surfaces of the non-slotted cells in Chapter 5.

2.3.2 Acid Cleaning:

After laser processing samples were cleaned in a highly oxidising acid mixture. Initially diamond is added to concentrated H_2SO_4 with 0.75 g per ml of KNO_3 added and heated to boiling for 30 minutes. After being allowed to cool the acid is removed and the samples rinsed a minimum of three times with ultrapure water. This is then followed by another 30 minutes in boiling H_2SO_4 , to remove any KNO_3 residue before once again rinsing in ultrapure water. After rinsing, the samples are air dried on a lint-free cloth. This acid clean is standard for diamond processing and is used to remove loose redeposited carbon from laser micromachining as well as any other surface contaminants.^{4,5}

2.3.3 Thermal Annealing

Thermal annealing in air was performed to reduce the electrochemical impact of the layer of non-diamond carbon left on the surface after laser micromachining.⁴ Annealing was performed in a tube furnace (Carbolite, MTF 12/25/400) in air. The furnace was heated at a rate of 15 °C per minute and then held at 600°C for five hours before cooling to room temperature at a rate of 15 °C per minute.

2.3.4 Metal Film Deposition

To ensure an Ohmic electrical contact to the BDD samples a titanium / gold film was deposited onto the contact area using a magnetron sputtering system (MiniLab 060, Moorfield, UK). The MiniLab is a quartz crystal microbalance (QCM) monitored physical vapour deposition tool. First the chamber is evacuated to pressures $< 10^{-5}$ mbar to remove atmospheric gases or potential contaminants, then argon process gas is fed into the chamber to achieve a pressure suitable for plasma formation ($\sim 9 \times 10^{-3}$ mbar). After that the targets are struck with the plasma forming on top of them, and the films deposited sequentially. First 10 nm of titanium is deposited at a rate of 3 \AA s^{-1} with the rate and thickness monitored by QCM. After the titanium has been deposited a gold layer is deposited on top, without breaking vacuum, at a rate of 8 \AA s^{-1} until a thickness of 400 nm is achieved. The QCMs are regularly (~ 3 monthly) calibrated by depositing 100 nm of each material individually and measuring the thickness using white light interferometry, as discussed in section 2.4.1.

The titanium layer is thought to form a carbide layer with the BDD when annealed, which helps to lower the potential barrier from the diamond into the metal contact, resulting in a reduced contact resistance.^{6,7} The gold layer is then used to protect the titanium from the air, preventing oxidation. Issues with this two-metal scheme are often raised as on annealing the titanium layer can diffuse into the gold, reducing the amount of carbide formed and decreasing the conductivity of the gold layer.⁸ Typically this issue is overcome by depositing a platinum barrier layer between the titanium and gold layers, which block diffusion of the titanium.⁸ This is however not an option for the MiniLab 060 system utilised in this work,

which only has two sources, instead the titanium layer is kept thin (10 nm) to minimise the effect of diffusion into the gold.

Photolithography is not used to define the areas for coating as the features required are relatively large (> 0.5 mm), instead a mask can be laser cut from Kapton tape or a thin (0.1 mm) steel sheet on the laser micromachining systems. For geometries that are sputtered routinely, like the 10 mm disks used in Chapter 4, jigs are fabricated with a recess into which the electrode can be placed, and a steel mask bolted on top, this allows multiple samples to be coated at once and saves time aligning the mask and sample. For less routinely used samples the mask is laser cut into self-adhesive Kapton tape, which is then positioned on the sample by hand, this method was used to produce the contacts on the ring electrode in Chapter 6.

After deposition the masking material is removed, and the samples annealed at 400°C in air (Carbolite, MTF 12/25/400) for five hours. This anneal helps to form the titanium-carbide layer and improves the adhesion of the contacts onto the diamond surfaces.^{6,9}

2.4 Characterisation

2.4.1 White Light Interferometry

Throughout this thesis extensive use is made of white light interferometry (WLI) to characterise diamond surfaces. WLI is a non-contact optical profilometry technique in which interference fringes caused by differences in pathlength between a reference beam and a beam reflected from the sample are used to construct a 3D surface for the sample.^{10–13} A schematic of a white light interferometer can be seen in Figure 2.4.

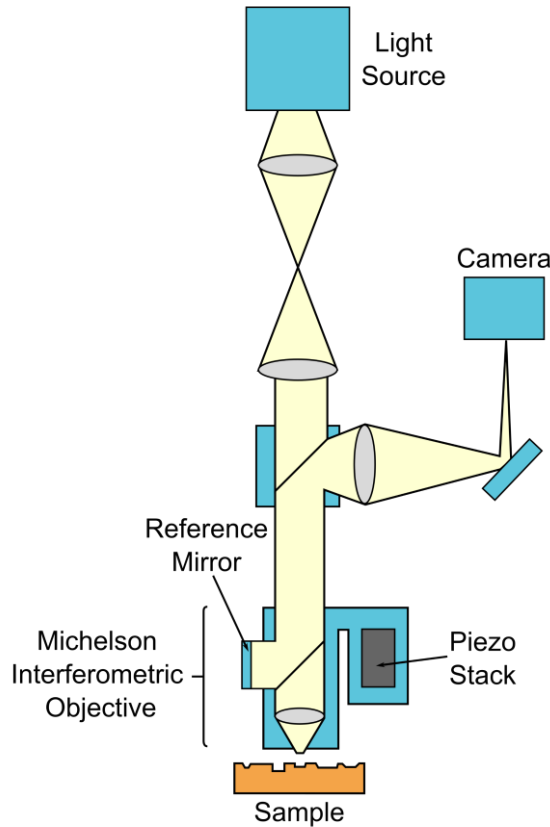


Figure 2.4: Schematic of the operation of a white light interferometer. Modified from O'Mahony et. al.¹¹ and Schmit.¹³

The incoming light is split into two beams inside the instrument. One beam is directed at an internal reference surface and the other to the surface to be studied. Reflected light from both surfaces interact, causing light and dark fringes, as a result of constructive and destructive interference respectively. These fringes are an interferogram, and represent the 3D-structure of the surface and are recorded using a high-resolution CCD camera and reconstructed by the instrument's software.¹⁰⁻¹³ While the Z-resolution is dependent on the imaging mode the X-Y resolution is determined by resolution of the camera and the objective employed. WLI has two main imaging modes:

Phase Shift Interferometry (PSI): PSI offers the greatest Z-resolution of the two techniques, at the expense of total Z range.^{10,12,13} In this measurement mode a mono-chromatic light source is used, and the maximum Z-depth is defined as a quarter of the wavelength of the light used. In this mode the relative distance between the sample and the light source is kept constant and only one interferogram is collected for the measurement.

Vertical Scanning Interferometry (VSI): VSI measurements use a white or monochromatic light source and offer an improved Z-range (up to several mm) at the cost of Z resolution.¹⁰⁻

¹³ To achieve this the distance between the sample and the light source is scanned across a

user selected range, and an interferogram collected at each Z position. Each interferogram is then individually processed and combined into the final 3D surface.

All interferometry reported in this thesis is collected using a Bruker Contour GT (Bruker, Germany). This system has both a 5× and 50× objective, as well as 0.55×, 1×, and 2× zoom lenses, allowing a wide range of magnifications from 2.75× to 100× in combination. The PSI imaging mode has a Z resolution of > 0.02 nm and the VSI claims an accuracy of < 0.75% although in practice these are based on instrument set-up and sample choice. The camera is a standard monochrome with a resolution of 640 × 480 pixels.

Roughness measurements on as-received BDD material are conducted in a single location using a 5× objective, giving a field of view of 1 × 0.8 mm. RMS values are then extracted as discussed below.

2.4.2 Gwyddion Analysis Software

Interferometry data was processed in Gwydion version 2.55.¹⁴ To obtain roughness values data was levelled by mean plane subtraction, then three-point levelled (using three points known to be at equivalent z-height) and finally polynomial background subtraction. The statistical quantities feature was then used to extract the root mean squared (RMS) roughness or S_q from the image according to Equation 2.1. Where A is the area, Z is the Z height, and x and y are the coordinates in the X-Y plane.

$$\text{Equation 2.1: } S_q = \sqrt{\frac{1}{A} \iint_A Z^2(x, y) dx dy}$$

Other analysis methods were also used, and these are discussed in more detail in the relevant chapters.

2.4.3 Electron Microscopy

In this thesis scanning electron microscopy (SEM) was also employed to characterise diamond surfaces. SEM is an imaging technique that involves scanning a high energy electron beam across the surface of a sample.¹⁵ Interaction of the electrons with the surface can produce three characteristic signals: secondary electrons (SE), back scattered electrons (BSE) and X-rays. Each of these signals is collected by a specialised detector and its intensity used to build up an image. The in-lens detector is used for all the images in this thesis, as this collects SE which result from very shallow interactions and therefore carry information about surface structure. All the samples studied in this thesis are conductive BDD so are suitable for SEM without further preparation.

Where FE-SEM was used images were collected on a Zeiss Gemini FE-SEM 500 (Zeiss, Germany) or a Zeiss Supra 55-VP FE-SEM. The instrument, detector, and acceleration voltage used are noted in the captions of SEM images.

2.4.4 Electron Backscatter Diffraction

Electron backscatter diffraction (EBSD) is a SEM based microstructural crystallographic characterisation technique used to identify the crystal direction in single crystal or polycrystalline materials.¹⁶ A stationary beam of electrons impacts the sample surface at a 70° and the backscatter pattern of the material down to about 20 nm depth is projected onto a transparent phosphor screen. The backscatter Kikuchi pattern consists of a regular arrangement of bright, parallel bands on a dark background and can be thought of as a projection of the crystal lattice on the flat screen. When used in a mapping arrangement EBSDs can be collected at multiple points across the surface to collect a map of the crystal orientation at each X-Y coordinate.

The EBSD data presented in this thesis was collected on a JEOL 7800F SEM (Tokyo, Japan) with and Oxford Instruments Symmetry S2 EBSD camera (Oxfordshire, UK) and analysed with AztecCrystal (Oxford Instruments, UK).

2.5 Electrochemical Techniques

All electrochemical measurements were conducted using commercial potentiostats. A CHI 760e BiPot (CH Instruments, USA) was used for the electrochemical measurements in Chapter 5 and 6. A PGSTAT128N with ADC10M.S module (Metrohm Autolab, Switzerland) was used for the uncompensated resistance measurements in Chapter 6. With the exception of measurements using the rotator (Pine Research, USA) all measurements were conducted in a faraday cage to minimise electrical interference.¹⁷ A saturated calomel electrode (SCE, CH Instruments Inc, USA) was used as a reference electrode and a platinum coil with an area larger than the working electrode (WE) being used was used as the counter electrode (CE). As described more fully in section 1.5.1 the potentiostat is used to apply a potential to the WE, versus the RE. In response to this potential current then flows between the WE and the CE.

2.5.1 Quinone Surface Coverage Measurements

Quinone surface coverage can act as an approximate measure of the amount of solution accessible non-diamond carbon (NDC) present on the electrode surface.^{5,18} To pre-treat the electrode surface a cyclic voltammetry (CV) experiment is run from -2 to + 2 V *vs* SCE at 0.1 V s⁻¹ for 20 cycles in a solution of 0.1 M H₂SO₄. The electrodes are then rinsed and transferred to a pH 2 Carmody buffer solution.¹⁹ Quinone surface coverage (QSC) analysis is

conducted via a CV from 0 to 0.7 V vs SCE at 0.1 V s⁻¹. This gives rise to a peak which is typically between 0.25 and 0.6 V and has an intensity related to the number of quinone groups on the electrode surface. A baseline is drawn across the data in this window, and the region encompassed is integrated to give the area under the peak (A_p). In cases where the area of the electrode is unknown A_p can then be multiplied by scan rate (v) to give the charge passed by the quinone groups, this can be used to give an approximate comparison of the QSC on electrodes of similar geometries where the precise area is unknown. This approach is used when determining the QSC of the slotted electrode geometries in Chapter 5.

If the precise area of the electrode is known, or can be measured by WLI, the quinone surface coverage can be expressed as a surface concentration (Γ) using Equation 2.2.

$$\text{Equation 2.2: } \Gamma = \frac{A_p}{n A F v}$$

Where n is the number of electrons transferred, A is the electrode surface area, F is Faraday's constant, and v is scan rate.

2.5.2 Redox Mediator Tests

A well-defined redox mediator such as FcTMA⁺ can be used to probe the quality of both the BDD material and the electrical contact made to it.²⁰ This particular redox mediator is chosen as it shows fast, outer-sphere electron transfer, without the concerns about fouling on non-diamond carbon as seen for ruthenium hexamine. For these measurements a CV was recorded between 0 and 0.8 V vs SCE at 0.1 V s⁻¹, initially sweeping in an oxidative (+ ve) direction. The potential separation between the oxidative and reductive peaks (ΔE_p) can be compared to theory to give an indication of the charge transfer, material, and contact resistance. While a ΔE_p of 57/ n mV is expected theoretically,²¹ a ΔE_p of ~70 mV is more commonly seen for BDD, due to its slow electron transfer kinetics. Additionally, the peak current can be predicted for a given concentration and scan rate according to the Randles-Sevcik equation, Equation 2.3.

$$\text{Equation 2.3: } i_p = 0.4463 n F A C \left(\frac{n F v D}{R T} \right)^{\frac{1}{2}}$$

Where, n is the number of electrons transferred, F is Faraday's constant, A is the area of the electrode, C is the concentration of the redox species, v is scan rate, D is the diffusion coefficient of the redox couple, R is the ideal gas constant, and T is the temperature. For a rotating disk electrode as discussed in Chapter 6, the Levich equation should be used instead of Randles-Sevcik, Equation 2.4.

$$\text{Equation 2.4: } i_L = 0.620 n F A D^{\frac{2}{3}} \omega^{\frac{1}{2}} \nu^{-\frac{1}{6}} C$$

Where I_L is the limiting current, n is the number of electrons transferred, F is Faraday's constant, A is the electrode area, D is the diffusion coefficient, ω is the rotation rate (in Rad s^{-1}), ν is the kinematic viscosity of the solution, and C is the concentration of the analyte.

2.5.3 Uncompensated Resistance Measurements

The uncompensated resistance (R_u) of electrodes can also be measured using a pulse voltammetry technique. Measuring uncompensated resistance in the absence of a redox couple removes charge transfer resistance as a factor and as a result gives a more accurate measurement of the solution and contact resistance than redox mediator tests. By using a highly conductive electrolyte such as 0.1 M KNO_3 solution resistance effects can be reduced and the R_u value measured will be dominated by the electrode contact resistance. In a potential region where no faradaic reactions occur the electrode can be treated as ideally polarisable, and the shape of an i - t decay curve seen after a potential pulse fitted to Equation 2.5.

$$\text{Equation 2.5: } i(t) = \frac{\Delta E}{R} e^{-t / R C}$$

Where ΔE represents the height of the potential pulse, R represents the uncompensated resistance of the system and C the capacitance.

2.6 Additive Manufacture

Throughout this thesis numerous parts made using additive manufacturing (3D printing) have been utilised. Two types of 3D printer were used, a fusion deposition modelling (FDM, Taz 6, Lulzbot, USA) printer was used for large functional parts where surface finish was of secondary importance. A stereolithography (SLA, Form 3, FormLabs, USA) was used for smaller parts with finer details. Details of materials and printer used for parts in this thesis can be found in Table 2.5.

Table 2.5: Details of the 3D printer and material used for 3D printed parts in this thesis.

Chapter	Part	Printer	Material
3	Lift-Off Etch Cell	Taz 6	PET, Inofil
4	BDD Corrosion Cell	Form 3	High Temp, FormLabs
5	Ozone Cells	Form 3	Standard Clear, Form Labs
6	RRDE Parts	Form 3	Standard Clear, Form Labs

FDM parts were used immediately off the printer. SLA parts were washed (FormWash, FormLabs) in IPA to remove uncured resin then post-cured with 405 nm light at elevated

temperatures (FormCure, FormLabs) according to manufacturer's instructions for the resin used.

2.7 Electron Paramagnetic Resonance Spectroscopy

Electron paramagnetic resonance spectroscopy (EPR) is an analytical technique analogous to nuclear magnetic resonance (NMR) but for electron spins. EPR can be used to study paramagnetic species with one or more unpaired electrons. Very few systems meet this criterion for being EPR active, however this can be advantageous as background signals are reduced. In EPR low power microwave (MW) electromagnetic radiation irradiates the sample while the applied magnetic field is swept.²²⁻²⁴

Without an applied field two electrons in the same orbital but with different spins will be degenerate in energy however, this degeneracy is lost upon the application of a magnetic field. Interaction of the electron spins with the magnetic field gives rise to two energy states, known as Zeeman splitting. As a higher magnetic field is applied the energy levels continue to split according to Equation 2.6.

$$\text{Equation 2.6: } \Delta E = g_e \mu_B B \Delta m_s$$

Where g_e is the free electron g-factor, μ_B is the Bohr magneton, B is the applied magnetic field, and m_s is the electron spin angular momentum quantum number. As g_e and μ_B are constants the energy difference between the levels is controlled by the applied magnetic field. As the magnetic field is swept it eventually reaches a resonance with the applied MW radiation when ΔE is equal to the MW excitation energy. These transitions can occur until the population of both energy states (which were initially populated according to Boltzmann statistics) becomes equal, at which point the system is said to be saturated.

The presence of additional local magnetic fields at the electron resulting from interaction of the nuclei magnetic moments will cause the electron to experience a different magnetic field than the one applied. This is expressed as the effective g-factor. This parameter is a property of the chemical environment of a radical and can therefore be useful in identifying the radical giving rise to the measured signal.

Interactions between the nuclear magnetic spin and the applied magnetic field can also give rise to Zeeman splitting. Additionally, it is possible for these nuclear spins to interact with electronic spins in the system leading to hyperfine interactions. These hyperfine interactions lead to line splitting as they change the amount of energy needed to promote an electron by adding to or subtracting from the applied magnetic field. This hyperfine splitting is characteristic of the number and type of nuclei present and is therefore also useful in identifying the species present.

Radicals are typically short-lived in solution, which presents an issue for EPR as it is very challenging to produce a detectable steady state concentration. For some radicals, such as the hydroxyl radical, the relaxation time is very quick, leading to a linewidth that cannot be measured without spin trapping.²⁵ Generally these spin traps react with the radical to form a persistent paramagnetic species referred to as a spin adduct. Spin trapping is discussed in more detail in Chapter 3.

2.8 References

- 1 L. A. Hutton, J. G. Iacobini, E. Bitziou, R. B. Channon, M. E. Newton and J. V. Macpherson, *Anal. Chem.*, 2013, **85**, 7230–7240.
- 2 Element Six Ltd., *DiafilmTM EP A solid solution for sanitising and electrochemical processing*, 2020.
- 3 S. G. Lemay, D. M. Van Den Brook, A. J. Storm, D. Krapf, R. M. M. Smeets, H. A. Heering and C. Dekker, *Anal. Chem.*, 2005, **77**, 1911–1915.
- 4 S. J. Cobb, F. H. J. Laidlaw, G. West, G. Wood, M. E. Newton, R. Beanland and J. V. Macpherson, *Carbon N. Y.*, 2020, **167**, 1–10.
- 5 Z. J. Ayres, A. J. Borrill, J. C. Newland, M. E. Newton and J. V. Macpherson, *Anal. Chem.*, 2016, **88**, 974–980.
- 6 S. A. Manifold, G. Klemencic, E. L. H. Thomas, S. Mandal, H. Bland, S. R. Giblin and O. A. Williams, *Carbon N. Y.*, 2021, **179**, 13–19.
- 7 C. A. Hewett and J. R. Zeidler, *Diam. Relat. Mater.*, 1993, **2**, 1319–1321.
- 8 S. A. Manifold, G. Klemencic, E. L. H. Thomas, S. Mandal, H. Bland, S. R. Giblin and O. A. Williams, *Carbon N. Y.*, 2021, **179**, 13–19.
- 9 C. Zhen, X. Liu, Z. Yan, H. Gong and Y. Wang, *Surf. Interface Anal.*, 2001, **32**, 106–109.
- 10 L. Deck and P. de Groot, *Appl. Opt.*, 1994, **33**, 7334.
- 11 C. O’Mahony, M. Hill, M. Brunet, R. Duane and A. Mathewson, *Meas. Sci. Technol.*, 2003, **14**, 1807–1814.
- 12 J. C. Wyant, in *Proceedings of SPIE*, ed. H. J. Caulfield, Elsevier, 2002, vol. 4737, pp. 98–107.
- 13 J. Schmit, in *Encyclopedia of Modern Optics*, ed. R. D. Guenther, Elsevier, 2005, pp. 375–387.
- 14 P. Klapetek, D. Nečas and C. Anderson, *Gwyddion user guide*, 2009.
- 15 J. I. Goldstein, D. E. Newbury, P. Echlin, D. C. Joy, C. E. Lyman, E. Lifshin, L. Sawyer and J. R. Michael, *Scanning Electron Microscopy and X-ray Microanalysis*, Springer US, Boston, MA, Third Edit., 2003.
- 16 A. J. Schwartz, M. Kumar, B. L. Adams and D. P. Field, *EBSD in Materials Science*,

2011, vol. 86.

- 17 A. W. Colburn, K. J. Levey, D. O'Hare and J. V. Macpherson, *Phys. Chem. Chem. Phys.*, 2021, **23**, 8100–8117.
- 18 Z. J. Ayres, S. J. Cobb, M. E. Newton and J. V. Macpherson, *Electrochem. commun.*, 2016, **72**, 59–63.
- 19 W. R. Carmody, *J. Chem. Educ.*, 1961, **38**, 559–560.
- 20 J. V. Macpherson, *Phys. Chem. Chem. Phys.*, 2015, **17**, 2935–2949.
- 21 R. S. Nicholson and I. Shain, *Anal. Chem.*, 1964, **36**, 1212.
- 22 J. C. McGowan, *Magnetic Resonance Spectroscopy: Fundamentals*, 2001.
- 23 N. D. Yordanov, *Appl. Magn. Reson.*, 1994, **6**, 241–257.
- 24 S. S. Eaton, G. R. Eaton and L. J. Berliner, *Biomedical EPR*, KLUWER ACADEMIC PUBLISHERS, 24th edn., 2005.
- 25 G. R. Buettner, *Free Radic. Biol. Med.*, 1987, **3**, 259–303.

Chapter 3: Optimisation of the Electrochemical Etch Step of Diamond Nanoscale Membrane Production

3.1 Introduction

To develop the next generation of optical, quantum and electronic devices,¹⁻³ nano-structuring of the diamond is often required. In particular for quantum technology applications, high-quality single crystal diamond membranes of sub-micron thickness, containing colour centres are essential.^{1,4,5} While diamond membranes can be prepared using mechanical polishing, such membranes are typically wedge-shaped due to the complexities of achieving co-planarity over a large area (mm^2). Moreover, mechanical polishing can result in sub-surface damage, penetrating microns deep, which requires further processing steps to achieve the high surface quality desired for quantum applications.⁶⁻⁸ Mechanical polishing also limits the minimum thickness of the membranes that can be produced to 10s of μm in thickness.³

Another route to producing thin membranes is to use ion implantation to damage a well-defined sub-surface region of diamond, followed by high temperature annealing to convert this damaged region of diamond to sp^2 carbon. After the sub-surface sp^2 carbon layer has been prepared the membrane can be removed via etching of this layer, also known as “lift-off”. This method has been proposed as an alternative to mechanical polishing for producing thin, uniform diamond membranes.^{3,9-12} Diamond membrane thickness is determined by the implantation energy and, as the amorphised layer implants parallel to the top surface, the resulting membrane has a consistent thickness at all points. The lift off process is key to success of the diamond membrane nanofabrication process. Oxygen dry etching¹² has been used, but was found to be slow (5 hr for separation of a 2 mm square membrane) with some damage to the membrane also observed due to etching of the diamond as well as the sp^2 carbon layer.¹²

Electrochemical (EC) etching has also been proposed as an etch method, due to the advantages electrochemistry brings in terms of reduced cost of the set-up and negligible damage to the diamond.⁹ However, unlike traditional EC etching/electropolishing where direct contact is made to the conductive material and a potential applied to promote oxidative dissolution of the material itself,^{13,14} a non-contact EC set-up is required due to the nano-sized features of the embedded sp^2 carbon. In order for the implanted sp^2 carbon to experience a potential difference across the sp^2 carbon, the use of low conductivity solutions was advocated;⁹ to drop a meaningful potential across the sp^2 carbon/electrolyte interface, the resistance of the solution must be higher than that of the sp^2 carbon layer. This concept is often referred to as bipolar electrochemistry.^{15,16} Unfortunately, using this approach, etch rates were found to be slower

than reported for dry etching,¹² taking 10 hr to separate a 3×3 mm membrane in a dilute chromic acid solution, even with an applied voltage of 100 V.⁹ Thus, despite the importance of this process to the quantum optical communities, the EC etch process is still far from optimised for efficient sp^2 carbon removal rates.^{3,12,17–20} Previous work in this area has been conducted by researchers interested in the use of these membranes for quantum optical applications, who are understandably not highly proficient in electrochemistry. As a result, we felt that by applying more standard electrochemical approaches to this etch the etch rate could be improved, without any loss of membrane quality.

The work in this chapter demonstrates a new non-contact EC nanofabrication method which can be used where direct electrical contact to the conductive material is challenging. Rather than relying on a bipolar etch mechanism and low conductivity solutions, this method uses high conductivity, fully dissociated electrolytes in conjunction with electrochemical initiation of radical generating chemical pathways in solution. Etch rates of the sp^2 carbon layer are measured using in-situ optical microscopy. We explore how the choice of electrolyte and electrolyte concentration can significantly enhance sp^2 carbon etch rates.

3.2 Experimental Methods

3.2.1 Materials

All solutions were prepared from ultrapure water (>18.2 M Ω cm, Milli-Q, Millipore Corp.). Etch solutions comprised either 400 mM boric acid (H_3BO_3 , 99.97%, Sigma Aldrich, UK) or 250 mM salts in ultrapure water. Salts investigated included potassium nitrate (KNO_3 , 99.97%, Sigma Aldrich, UK), potassium chloride (KCl , $\geq 99\%$, Sigma Aldrich, UK), and potassium sulphate (K_2SO_4 , Pure, Acros Organics, US). Sulfuric acid (H_2SO_4 , $>96\%$, Merck, UK) was used at 0.3% v/v (50 mM) in ultrapure water. Mixed K_2SO_4/H_2SO_4 solutions were made to 250 mM total sulphate concentrations in ultrapure water. Solutions for electron paramagnetic resonance (EPR) spectroscopy comprised of either KNO_3 , KCl , potassium sulphate (K_2SO_4 , Analysis Grade, Sigma Aldrich, UK) at a concentration of 250 mM or 400 mM boric acid salt in ultrapure water.

3.2.2 Diamond Sample Preparation

Standard grade chemical vapour deposition (CVD) and high-pressure high temperature (HPHT, type 1b) single crystal diamond plates (Element Six Ltd., Harwell, UK) of ~ 500 μm thickness, and either 3.5 mm (3.5×3.5 mm), 4.1 mm (4.1×4.1 mm) or 4.2 mm (4.2×4.2 mm) in size were used as the substrates for all studies, unless otherwise stated. The front face of each sample was scaife polished to $\sim nm$ roughness, and the rear face lapped to $\sim \mu m$ roughness. Before ion implantation, samples were acid cleaned as described in Chapter 2, Section 2.3.2, and then the implantation surface cleaned in an oxygen/argon plasma (Emitech, K1050X

Plasma Asher, 80 W, 60 s). The polished face was then implanted (Ion Beam Centre, University of Surrey, UK) with 2×10^{16} carbon atoms (at 2 MeV) per square centimetre. The implanted samples were annealed at 1300 °C for 2 hr, to convert the amorphous region into sp^2 carbon.²¹ After annealing the samples were acid cleaned again. Due to the limited availability of the samples used, it was necessary to complete some work without repeats.

3.2.3 Implant Simulations

A stopping and range of ions in matter (SRIM) simulation²² was used to calculate the approximate depth and width of the end-of-range damage layer from ion implantation. A plot of the vacancies produced during implantation with 2 MeV carbon ions is shown in Figure 3.1.

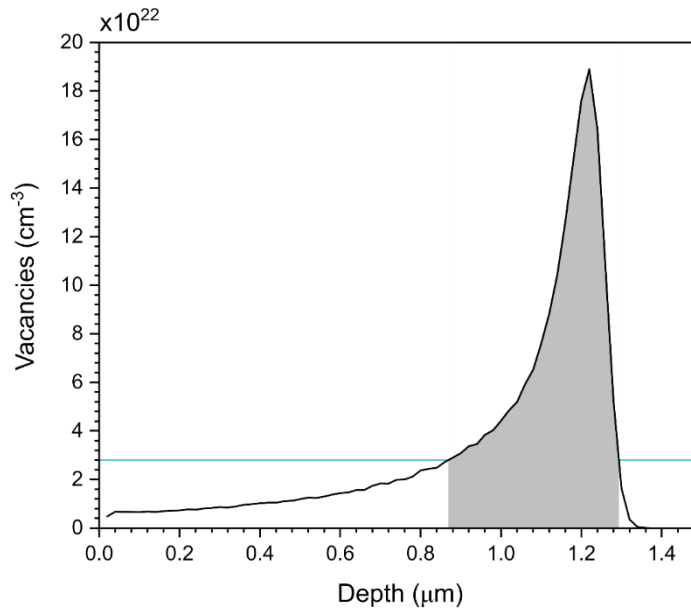


Figure 3.1: Vacancy density plot for a 2 MeV implantation of carbon into single crystal diamond. The line (blue) indicates the minimum vacancy threshold for graphitisation. The shaded area (grey) indicates the region that is damaged above this threshold.

In diamond, there is a critical threshold of damage (D_c), expressed as vacancies per cm^3 , where, upon high temperature annealing, the diamond will convert to sp^2 bonded carbon. However, literature values for D_c vary from 1×10^{22} to 9×10^{22} vacancies per cm^3 , demonstrating the uncertainty in this value.^{21,23–26} Furthermore, SRIM simulations themselves are an overestimate of the true vacancy density in the material due to there being no consideration of dynamic annealing²⁷ or damage saturation effects.²⁸ The issue with damage saturation is present in Figure 3.1, where the peak number of vacancies is more than the number of carbon atoms in the diamond lattice ($\sim 10^{23}$). Hence, any parameters obtained using SRIM are likely to be an estimate at best. For our calculations of implant depth and damage region width, we now use a value for D_c of 2.8×10^{22} vacancies per cm^3 , obtained by Fairchild

*et al*²⁹ using transmission electron microscope (TEM). Using this D_c value gives an implant depth of ~ 900 nm and a damage region width of ~ 400 nm, with the associated caveats. Using the width of the damage layer the total volume of sp^2 bonded carbon can be calculated as 0.0049 mm^3 for $3.5 \text{ mm} \times 3.5 \text{ mm}$ samples, 0.0067 mm^3 for $4.1 \text{ mm} \times 4.1 \text{ mm}$ samples and 0.0071 mm^3 for $4.2 \text{ mm} \times 4.2 \text{ mm}$ samples.

3.2.4 Electrochemical Etching

Etching of single crystal diamond substrates took place in a custom designed 3D printed (Taz 6, Lulzbot, USA) polyethylene terephthalate cell. The electrodes used were two Pt wires (0.75 mm in diameter and 2 cm in length) spaced 6 mm apart, as shown in Figure 3.2. A variable DC power supply (EA-PS 9750-04, Elektro-Automatik GmbH, Germany) was employed to apply a potential between the two electrodes, operating in a potential limiting mode at 30 V (approximately +15 V and -15 V versus ground), with a current value dependent on the solution composition. The diamond substrate, with embedded sp^2 carbon layer, was bonded (lapped face on) to a polycarbonate (RS Components, UK) support using a low-bloom cyanoacrylate adhesive (Loktite 460, Henkel, Germany), making sure no adhesive was visible to solution. This piece of polycarbonate was then placed into a slot, for centring purposes, with the polycarbonate face on which the diamond is adhered, held against the Pt electrodes. This ensures that the diamond plate was orientated such that the square face was perpendicular to the base of the etch cell, aligning the sp^2 carbon layer in plane with the Pt wire electrodes. The cell was designed with a light path for transmission imaging of samples undergoing etching.

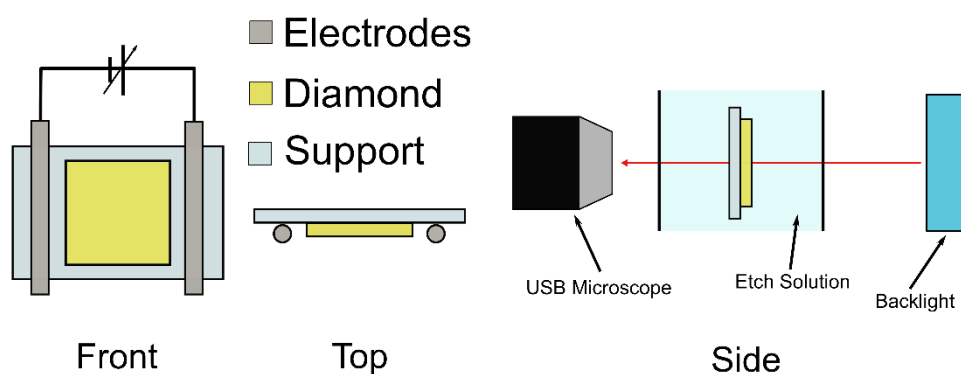


Figure 3.2: Schematic of the etch cell showing the arrangement of diamond sample (yellow), electrodes (grey), and polycarbonate support (light blue). Front: a front view as seen by the USB microscope showing the diamond sample attached to the polycarbonate support and placed between the two platinum electrodes. Top: a top view showing how the diamond sample is aligned in plane with the electrodes. Side: a side view with the electrodes omitted for clarity which shows how the USB microscope images through the solution and

polycarbonate support in transmission using a backlight to maximise the contrast between etched and un-etched areas of the sp^2 carbon.

A digital USB microscope (VMS-001, $\times 20$ –90 magnification, Veho, UK) was used to capture time lapse images of etch progress. To maintain constant solution composition and temperature, a flow system was also employed with a temperature-controlled reservoir operating in the range of 10–70 °C. Unless otherwise stated etches were performed at 25 °C. Etch solution was circulated from this reservoir into the cell and returned via an outflow at a flow rate of 200 ml min⁻¹. The inlet and outlet were intentionally placed away from the platinum electrodes to minimise solution flow across the diamond sample and electrodes. Although flow will increase mass-transport to and from the electrodes it is likely the production of gas bubbles from water electrolysis at the Pt electrodes will be a much more significant contributor to increased mass-transport.

3.2.5 Image Analysis

A MATLAB (Version 2017b, MathWorks) script was used to analyse all time-lapse data of the etch processes. Each frame from the video capture was extracted. The region of interest (*i.e.* the diamond substrate) is defined on the first image and the script used to calculate what proportion of that area corresponds to the etched region; these match RGB values provided in the script. This proportion is then converted to an area and the area etched is then plotted versus etch time to create an etch profile.

3.2.6 Tabulation of Experiments Conducted

A complete tabulation of all experiments conducted, samples used, and starting edges can be found in Table 3.1.

Table 3.1: Tabulation of all etch experiments conducted. Starting Edges: L = Left, R = Right, T = Top, B = Bottom.

Condition	pH	Temperature (°C)	Diamond Type	Diamond Size (mm)	Starting Edges
250 mM K ₂ SO ₄	7.1	25	HPHT	4.2	L, B
250 mM K ₂ SO ₄	7.1	25	CVD	4.2	T, R, B
400 mM H ₃ BO ₃	4.4	25	HPHT	4.2	-
250 mM KNO ₃	8.4	25	HPHT	4.2	T, B
250 mM KCl	7.0	25	HPHT	4.2	T, B
250 mM K ₂ SO ₄	7.1	25	HPHT	4.2	T, B
0 mM K ₂ SO ₄ (250 mM KNO ₃)	8.4	25	CVD	3.5	T, R, B

30 mM K ₂ SO ₄	6.8	25	CVD	3.5	R, B
60 mM K ₂ SO ₄	7.3	25	CVD	3.5	T, B
125 mM K ₂ SO ₄	6.9	25	CVD	3.5	T, B
250 mM K ₂ SO ₄	7.1	25	CVD	3.5	T, B
250 mM SO ₄ ²⁻	0.8	25	CVD	4.1	L, T
250 mM SO ₄ ²⁻	1.0	25	CVD	4.1	T, B
250 mM SO ₄ ²⁻	1.2	25	CVD	4.1	B, T, R
250 mM SO ₄ ²⁻	7.1	25	CVD	4.1	T, B
50 mM H ₂ SO ₄	1.25	10	HPHT	3.5	L, B
50 mM H ₂ SO ₄	1.25	10	HPHT	3.5	T, B
50 mM H ₂ SO ₄	1.25	10	HPHT	3.5	T, B
50 mM H ₂ SO ₄	1.25	30	HPHT	3.5	T, B
50 mM H ₂ SO ₄	1.25	30	HPHT	3.5	T, B
50 mM H ₂ SO ₄	1.25	30	HPHT	3.5	T, B
50 mM H ₂ SO ₄	1.25	50	HPHT	3.5	T, B
50 mM H ₂ SO ₄	1.25	50	HPHT	3.5	T, B
50 mM H ₂ SO ₄	1.25	50	HPHT	3.5	T, B
50 mM H ₂ SO ₄	1.25	70	HPHT	3.5	T, B
50 mM H ₂ SO ₄	1.25	70	HPHT	3.5	T, B
50 mM H ₂ SO ₄	1.25	70	HPHT	3.5	T, B

3.2.7 Electron Paramagnetic Resonance Spectroscopy

For EPR measurements, electrolysis of solutions containing either 250 mM K₂SO₄, 250 mM KCl, 250 mM KNO₃ or ~ 400 mM H₃BO₃ was performed with no recirculating flow, in a single compartment cell. 30 V was applied between the two platinum electrodes of the same geometry as those used in the etch cell in the solution of interest. After an electrolysis time of 15 minutes the potential was switched off and approximately 10 mM of the spin trap 5,5-dimethyl-1-pyrroline-N-oxide (DMPO; Enzo Life Sciences, USA) was added to the solution and mixed thoroughly. The time from switching off the potential to adding the spin trap was ca. 30 s. From the resultant solution, an aliquot of the electrolysis mixture was sampled and the EPR spectrum recorded. The EPR signals for the DMPO spin adduct were recorded on an X-band spectrometer (EMX, Bruker, Germany) fitted with a HS cylindrical resonator (4119HS/0207, Bruker, Germany). Measurements were performed in a quartz EPR tube with a 1 mm inner diameter (Wilmad® quartz (CFQ) EPR tubes, Sigma-Aldrich, UK). For all measurements the following spectrometer parameters were used: a non-saturating microwave power of 20 mW; central magnetic field, 352 mT; scan width, 10 mT and a modulation amplitude, 0.05 mT. All spectra reported are an average of 9 scans. Fitting and simulation of the EPR spectra was performed using the MATLAB package EasySpin (Version 5.2.25).³⁰

3.2.8 UV-Vis Measurement of H_2O_2

For detection of hydrogen peroxide by UV-Vis, a solution of $TiSO_4$ was prepared by heating under reflux titanium (IV) oxide anatase (99.7%, Alfa Aesar) in concentrated H_2SO_4 for 12 hours at 150 °C.³¹ The solution was left for 16 hours so the remaining titanium (IV) oxide anatase can sediment out of solution. The supernatant was collected, diluted to make 1 L with deionised water and finally filtered through a 0.2 μm filter before use.

A calibration curve ($y = 755.72x + 0.067$, $R^2 = 0.995$) was produced for a range of hydrogen peroxide concentrations between 0.75 μM and 7.5 mM, by serially diluting a stock hydrogen peroxide (30 % v/v) solution (9.8 M). UV-Vis spectra were collected between 200 to 600 nm (Lambda 850, PerkinElmer). The limit of detection of this method is taken as the lowest concentration tested (0.75 μM) as remaining titanium anatase particles in solution absorbed at low levels in the baseline. Electrolysis of three individual solutions containing either 250 mM KNO_3 , 250 mM KCl , or 250 mM K_2SO_4 was performed in a one-compartment cell by applying 30 V between two platinum electrodes (electrode area, 0.50 cm^2) using a power supply (Elektro-Automatik GmbH, EA 9750-04) under static conditions for 1, 2, 3, 4, 5 and 6 minutes, per electrolyte. The electrolysis solution was then mixed with the prepared $TiSO_4$ solution in a 4:5 ratio and measured for H_2O_2 quantification using UV-Vis. This ratio was used to provide a sufficiently high H_2O_2 concentration while ensuring excess $TiSO_4$ is present to react with the H_2O_2 . Each time point was a separate experiment with fresh solutions used each time.

3.3 Results and Discussions

3.3.1 Measuring the Material Etch Rate

The etch rate, as a function of solution composition, of the ~ 400 nm thin sp^2 carbon layer embedded in the freestanding single crystal diamond substrates, was monitored optically, in transmission mode, using a USB microscope. An exemplar optical image of the time-dependent removal of the sp^2 carbon layer is shown in Figure 3.3, here recorded over a period of 2 hours in 250 mM K_2SO_4 . Images were recorded every 10 s from application of the potential. At time, $t = 0$ min, the image appears black, due the presence of a complete sp^2 carbon layer. EC etching of this layer is monitored via the colour change of the sample from black to colourless, the latter representing the translucent diamond as the sp^2 carbon layer is removed. This colour change was used to quantify the area of sp^2 carbon removed as a function of etch time. The heterogeneous nature of the etch process, as shown by Figure 3.3, is typical of all etches in the different solutions observed under these flow conditions, the only difference being the timescale of the removal process. In most cases, etching begins at two edges of the sp^2 carbon layer and then proceeds inwards. The locations at which etching commenced for each different experiment are tabulated in Table 3.1.

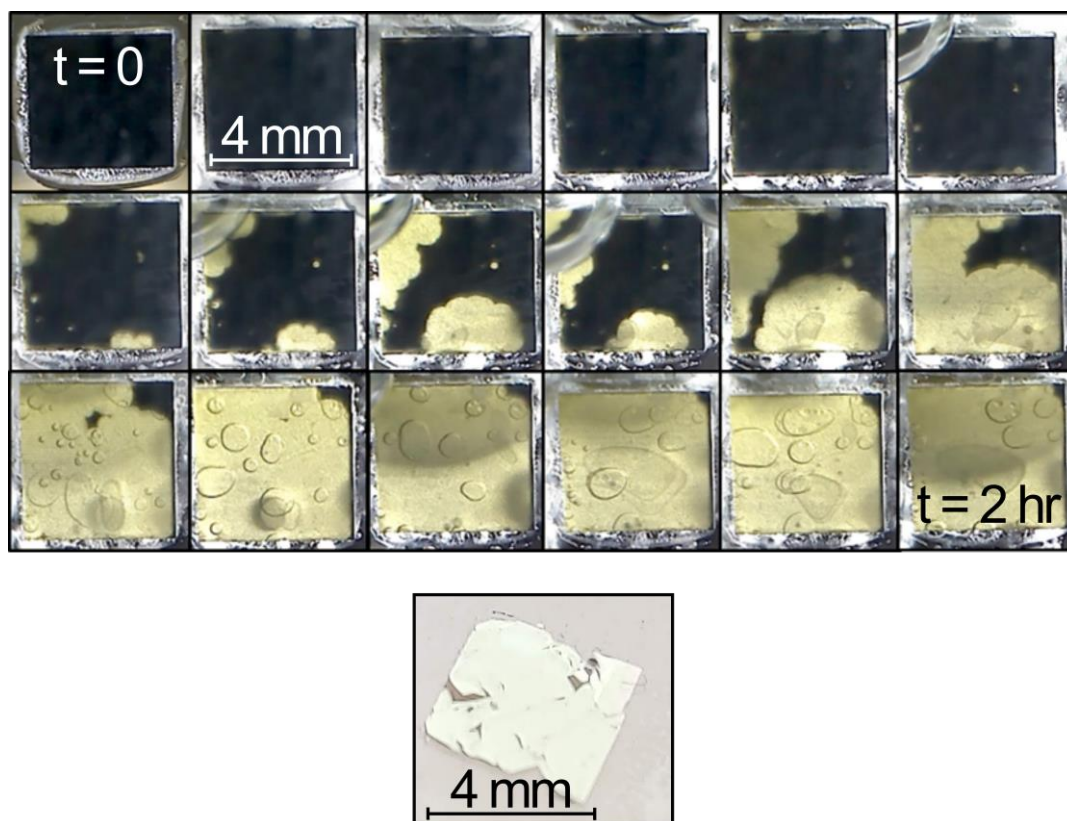


Figure 3.3: Top, optical image capture of the etch progress on a 4.2 mm \times 4.2 mm HPHT diamond in aerated 250 mM K_2SO_4 solution with 30 V applied between two Pt electrodes, from $t = 0$ to $t = 2$ hr. Each image is separated by approximately 8 min of etching in 250 mM K_2SO_4 . Anode and cathode positioned to the left and right of the frame (out of view), respectively. The origin of the white spots, seen most prominently in the middle images, is currently unknown, but these were only observed in about 10% of samples investigated. Bottom, photograph of the membrane after separation.

All etches in all solutions examined ($n = 27$ in total) had a sigmoidal shape, as shown in the exemplar etch rate data (etch volume vs. time) in Figure 3.4, for a 250 mM K_2SO_4 solution. All data was fitted with a sigmoid (black line, Figure 3.4) and this fit used to provide insight into the etch characteristics. Each curve could be divided into four distinct sections. First, the induction period, (yellow shaded area) second, the bulk etch region where the rate of etching is highest and pseudo-linear and where the majority of material removal occurs (pink shaded area). Third, the bulk etching limit, where the limited amount of material remaining leads to a decrease in rate (blue shaded area), before finally reaching the final region, the etching complete region (grey shaded area) and no sp^2 carbon remains. The majority of membranes ($\sim 90\%$) recovered after the etch process were completely intact. Membranes were removed by floating the membrane off the SCD in DI water, then catching it on the desired substrate and allowing the water to dry, creating a temporary bond.

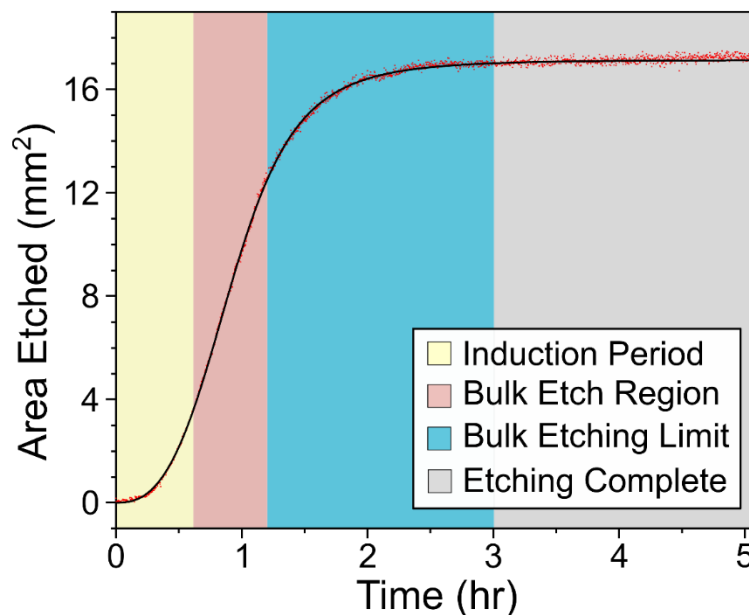


Figure 3.4: Exemplar etch profile from in-situ transmission microscope imaging. The raw data points ($n = 6500$, red) are fitted with a sigmoidal function (black) and three distinct regions are defined. Etching is considered complete at 3 hr as no visible remnants of the sp^2 carbon layer remains. Conditions: $4.1 \text{ mm} \times 4.1 \text{ mm}$ CVD sample in aerated 250 mM solution of K_2SO_4 with 30 V applied between the electrodes at 25°C . Raw image capture for this plot can be seen in Figure 3.3.

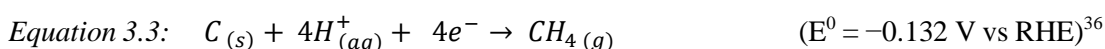
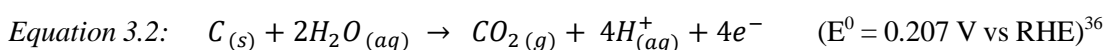
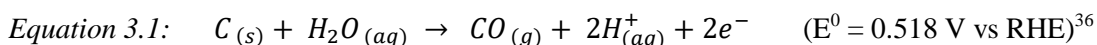
The induction period, during which very little etching takes place, varied in length for the range of conditions tested, however faster bulk etch rates typically resulted in shorter induction periods. We speculate that the existence of an induction period is as a result of either the sp^2 carbon region not extending completely to the edge of the diamond, or a structurally different form of sp^2 carbon at the edge versus the interior. In the majority of etches, etching began from two to three randomly distributed individual sites around the plate.

To assess the impact of solution conditions and composition on the etch rate, we focused on the bulk etch region (pink), which is where the majority of material is removed. In the bulk etching limit (blue area), as with the induction period (yellow area), we believe the material properties of the sp^2 carbon implanted diamond play a more significant role in controlling the etch characteristics. Bulk etch rates were thus used as the quantitative metric for comparing the efficacy of different electrolyte solutions. Area etch rates ($\text{in mm}^2 \text{ hr}^{-1}$) were determined by analysing the gradient over the region where 20% – 70% of the total area of sp^2 carbon had been removed (i.e. 3.5 mm^2 to 12.25 mm^2 in Figure 3.4). This threshold was chosen as in all etches conducted it was within the pseudo-linear region of the sigmoidal fit. Area, rather than volume, was also employed as a metric to acknowledge the uncertainty in the SRIM estimate of the sp^2 carbon layer thickness.

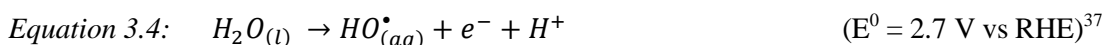
3.3.2 Electrochemical Etching in Low Conductivity Solutions

For these EC etch studies, half-saturated H_3BO_3 (~ 400 mM) was employed as the etch electrolyte, following literature precedent,³ in order to define a baseline etch rate under “bipolar” etch conditions. It is important to appreciate that whilst the concentration of H_3BO_3 is high, solution conductivity is very low (only $40 \mu\text{S cm}^{-1}$ which equates to a conductance of ~ 3 μS based on cell geometry) due to H_3BO_3 being a weak acid ($\text{pK}_a = 9.2$) and only partially deprotonated (dissociated).³² The conductivity of bulk amorphous sp^2 carbon is ~ 12.5 S cm^{-1} , which based on layer dimensions represents a conductance of ~0.6 mS.³³ As such, the sp^2 carbon layer is over two orders of magnitude more conductive than the solution, and the majority of the potential between the two Pt wire electrodes will be dropped across the solution. Consequently, a large potential will be present at the sp^2 carbon-electrolyte interface, which is capable of driving electron transfer reactions directly at this electrode surface. EC etching in this media gave an etch rate of $0.7 \text{ mm}^2 \text{ hr}^{-1}$ (for a $4.2 \text{ mm} \times 4.2 \text{ mm}$ substrate), taking 20 hr for complete separation once the induction period had passed. Bipolar electrochemistry is discussed in more detail in Chapter 1, Section 1.5.6.

Under bipolar conditions, etching most likely occurs via direct electrochemical oxidative (Equations 3.1 and 3.2) and/or reductive (Equation 3.3) dissolution of the sp^2 carbon. Note that the potentials given are thermodynamic potentials, with the experimentally observed potentials often being higher due to kinetic limitations.^{34,35}



It is also possible electrochemically generated species which are highly oxidising in nature e.g. radicals, can cause etching of the sp^2 carbon. For example, at high enough potentials, water can be oxidised to form hydroxyl radicals, $\text{HO}_{(aq)}^\bullet$, in solution (Equation 4).³⁷



However, other pathways for water oxidation are more energetically favourable meaning it is only on surfaces where traditional water oxidation routes are strongly hindered, such as boron doped diamond that direct $\text{HO}_{(aq)}^\bullet$ production is significant.³⁸ EC radical generation via oxidation of the electrolyte is also unlikely as oxidation of borate anions / boric acid is not

thought to result in radicals. This is also confirmed by the data in Figure 3.5, which shows no EPR evidence of radical formation in the 400 mM aerated H_3BO_3 solution.

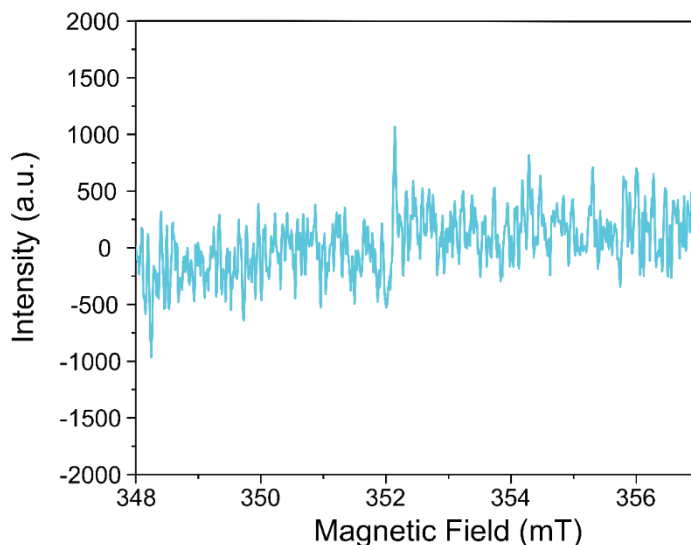
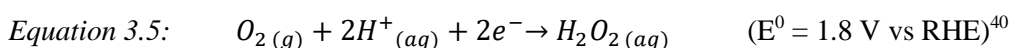


Figure 3.5: EPR spectra after 15 mins of applied 30 V in 400 mM boric acid. Experimental conditions: a non-saturating microwave power of 20 mW; central magnetic field, 352 mT; scan width, 10 mT and a modulation amplitude, 0.05 mT. All spectra reported are an average of 9 scans.

Cathodically, on sp^2 carbon, the oxygen reduction reaction (ORR) favours a 2-electron pathway which results in production of the oxidising agent hydrogen peroxide, H_2O_2 (Equation 3.5).³⁹ Dissolved oxygen will always be present due to the use of aerated solutions and the high potential difference applied across the two Pt electrodes; at the Pt anode, oxygen will be evolved from two-electron water oxidation.



Note, we find that immersing a sp^2 carbon implanted diamond sample into very high concentrations of H_2O_2 (30 wt%), much higher than those generated during ORR, at 25 °C for 24 hr, with no applied potential, results in no visible etching of the sp^2 carbon layer. This result suggested etching is either extremely slow or not possible using H_2O_2 alone.

3.3.3 Electrochemical Etching in High Conductivity Solutions

For the strong electrolyte (high solution conductivity) experiments three different electrolytes were employed, KNO_3 , KCl , and K_2SO_4 . The anion concentration was fixed at 250 mM, with solution conductivities almost three orders of magnitude higher than that for H_3BO_3 ; at 24 mS cm^{-1} (conductance $\sim 1.8 \text{ mS}$), 28 mS cm^{-1} ($\sim 2.1 \text{ mS}$) and 42 mS cm^{-1} ($\sim 3.2 \text{ mS}$) respectively. Note, with this increase in solution conductivity, bipolar contributions towards etching are expected to be significantly reduced due to considerably decreasing the potential

drop between the sp^2 carbon layer and electrolyte. Figure 3.6 shows the (a) etch profiles and (b) etch rates for the sp^2 carbon implanted diamond substrate, in the bulk etch regions for the three different electrolytes. H_3BO_3 is included for comparison in (b).

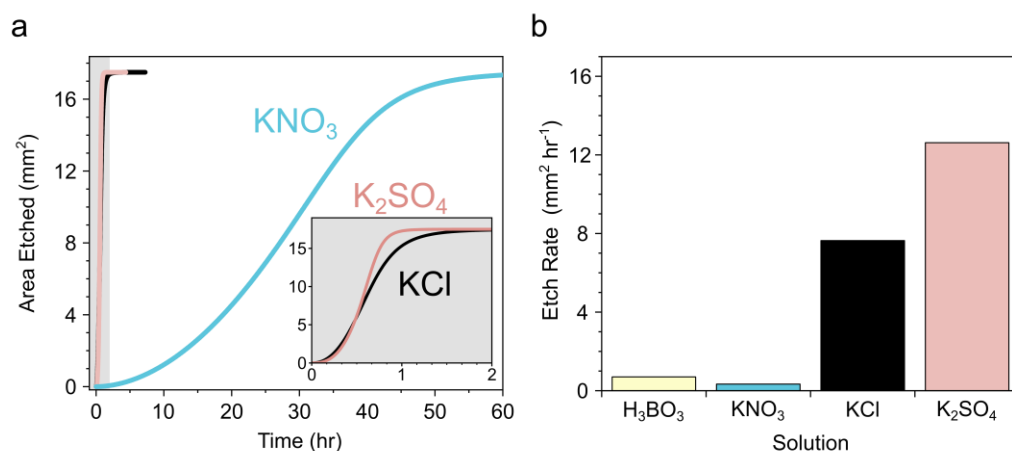


Figure 3.6: a) Etch profiles for etching of 4.2 mm × 4.2 mm HPHT single crystal diamonds in aerated 250 mM solutions of KNO₃ (blue), KCl (black) and K₂SO₄ (pink). Inset, etch profile for KCl and K₂SO₄ from 0–2 hr, the inset has the same units as the larger plot. 30 V was applied between the two Pt electrodes until etching was complete. Data was collected as n = 1. b) Comparison of the bulk etch rates for each different electrolyte, plus aerated 400 mM H₃BO₃.

Whilst the etch rate in KNO₃ was slower (0.3 mm² hr⁻¹) than that obtained using the H₃BO₃ both KCl (8.0 mm² hr⁻¹) and K₂SO₄ (13.0 mm² hr⁻¹) resulted in dramatic improvements in etch rate. The presence of sulphate anions increased the bulk etch rate compared to both nitrate and boric acid by over an order of magnitude.

3.3.4 Electron Paramagnetic Resonance Studies

To explore the origin of these observations in more detail, EPR spectroscopy was employed to identify radicals produced during electrolysis. A cell with Pt electrodes identical to those used for etching, but with no diamond substrate present, was employed for the EPR measurements with 250 mM KNO₃, KCl and K₂SO₄, undergoing electrolysis at 30 V for 15 minutes. In our non contact high conductivity experiments, the etchant species is expected to be generated primarily at the non contact electrodes, via EC means, and must move through solution to the sp^2 carbon. Hence, to be effective any radicals produced must either have a sufficiently long lifetime or, as most radicals in aqueous solution are notoriously short-lived e.g. $\leq \mu s$ timescales, are continually generated or regenerated through chemical reactions in solution. To show whether radicals were present at timescales significantly longer than their characteristic lifetimes, the DMPO spin trap was added after electrolysis had completed and the potential had been switched off; a process taking typically 30 s. This contrasts with the vast

majority of EC-EPR experiments where the spin trap is added before starting electrolysis.⁴¹ The spin trap is added before electrolysis so that the spin trap is present to trap radicals as they are generated. However, in this case we only wanted to trap radicals that were present after the potential had been switched off as these would be the radicals capable of diffusing to the edge of the sp^2 layer in order to etch it. DMPO was mixed into the solution and an aliquot taken for analysis in the EPR spectrometer, data shown in Figure 3.7. Note, the experiment was performed under stationary conditions which resulted in notable solution heating ($\sim 90^\circ\text{C}$) compared to the flow experiments.

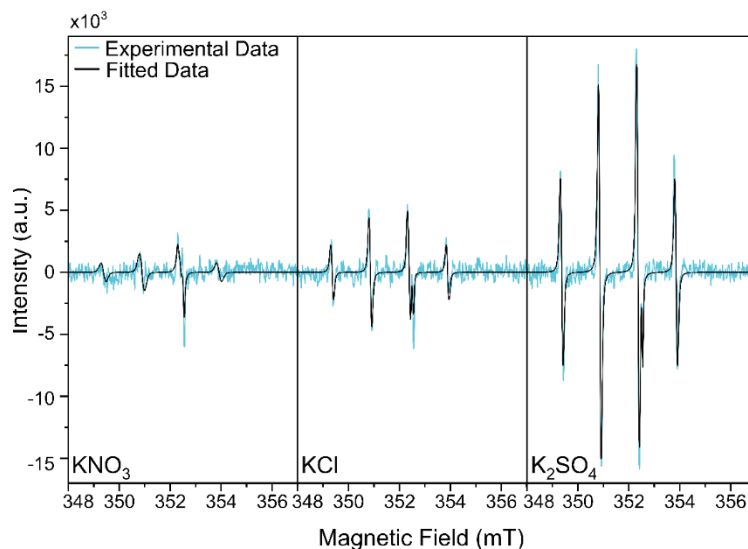
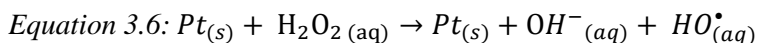


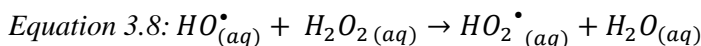
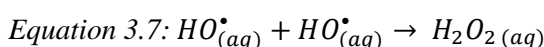
Figure 3.7: EPR spectra after 15 minutes of applied 30 V in 250 mM solutions of aerated KNO_3 , KCl and K_2SO_4 (blue), as well as simulated spectra for the DMPO-OH spin adduct and D' quartz signal (black). Experimental Conditions: A non-saturating microwave power of 20 mW; central magnetic field, 352 mT; scan width, 10 mT and a modulation amplitude, 0.05 mT. All spectra reported are an average of 9 scans.

In all solutions, a clear signature for the DMPO-OH spin adduct is seen in the EPR spectrum, as well as a D' signature at 352 mT from the quartz tube (included in the fit), Figure 3.7.⁴² The hyperfine coupling (A) extracted from the fitted data gave values of $A_N = 1.50 \pm 0.01$ mT $A_H = 1.50 \pm 0.01$ mT which is in agreement with those expected for DMPO-OH.⁴¹ The DMPO-OH signature, whose intensity is indicative of radical concentration, varies in intensity in the order $\text{NO}_3^- < \text{Cl}^- < \text{SO}_4^{2-}$. Formation of $\text{HO}^*_{(\text{aq})}$ via the water oxidation route (Equation 4) is unlikely to be significant on Pt due to the strong adsorption of HO^* on Pt electrodes leading to the formation of Pt oxide.⁴³ Given the extremely high reactivity of HO^* , its short lifetime ($\leq \mu\text{s}$)⁴⁴ and the fact that the spin trap is added after the potential has been switched off, observation of a DMPO-OH signal means that chemical routes in solution (initiated electrochemically) must be acting to generate or regenerate the HO^* radical (discussed below).

On Pt surfaces, any H₂O₂ present can decompose to produce HO• via the Weiss mechanism (Equation 3.6).⁴⁵



Whilst ORR on Pt is typically thought to predominantly occur via a 4-electron transfer pathway to form H₂O,⁴⁶ the amount of H₂O₂ produced on Pt via the 2-electron transfer pathway (Equation 3.5) has been shown to be dependent on solution composition.^{47–49} Once formed, HO• radicals can also combine to form H₂O₂ (Equation 3.7) or react with H₂O₂ (Equation 3.8) to form the hydroperoxyl radical (HO₂•). Although HO₂• is lower in oxidising ability than HO•, thermodynamically it is capable of direct oxidation of the sp² carbon layer.³⁷



As HO₂• is a much longer lived radical in solution (10 s – 100 s)⁵⁰ compared to HO•, if there is any HO₂• present when the electrode potential is switched off and DMPO is added to solution, HO₂• will react with DMPO to form DMPO-OOH. However, DMPO-OOH is not stable (lifetime ~ 1 min) and will decay to give the much more stable spin adduct DMPO-OH;^{51–53} a process which will be even quicker in the elevated solution temperature of this EPR experiment.⁵⁴ Since it takes a few minutes to transfer the sample into the EPR and tune the spectrometer, any DMPO-OOH present will have likely decayed to DMPO-OH.

Considering individual electrolytes, in KNO₃, very small amounts of DMPO-OH are observed in the EPR spectra, suggesting a low concentration of radicals are produced, via either Equation 3.6 and/or Equation 3.8. In KCl, EPR measurements reveal over twice the amount of DMPO-OH compared with KNO₃. Chloride ions have been shown to adsorb onto Pt surfaces and promote the generation of H₂O₂ via the 2-electron ORR route.^{47–49} To verify an increased concentration of H₂O₂ in the chloride electrolyte, UV-Vis spectroscopy experiments were recorded on the electrolysis solution every minute over a six minute period Figure 3.8.

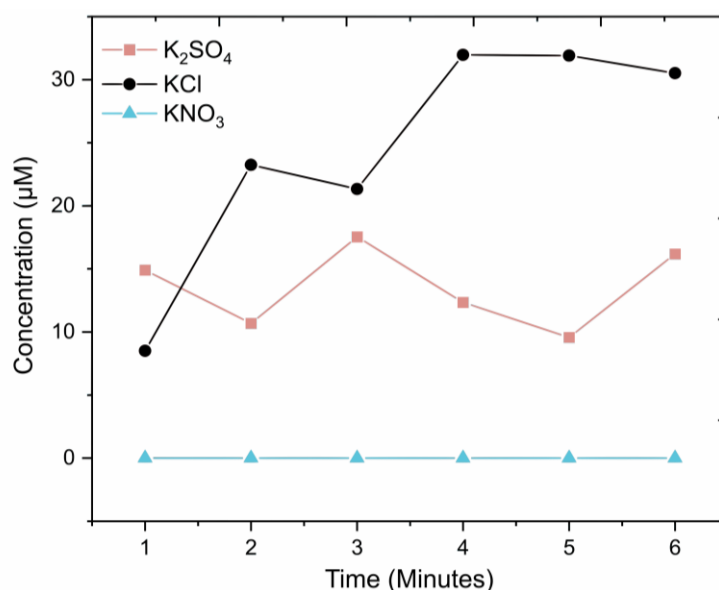


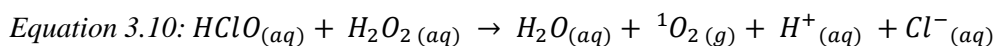
Figure 3.8: Concentration of H₂O₂ produced for each electrolysis time determined by UV/Vis measurement. In solutions of 250 mM KNO₃ (blue triangle) KCl (black circle), and K₂SO₄ (pink square) using two platinum electrodes at 30 V.

After electrolysis of 0.25 M KNO₃ the solution showed no detectable H₂O₂. Electrolysis in 0.25 M KCl revealed a much larger concentration than seen in the KNO₃ solution. The concentration of H₂O₂ increased with electrolysis time until four minutes, when it stabilised. Electrolysis in the 0.25 M K₂SO₄ solution showed an increase in H₂O₂ versus KNO₃, but less than in the KCl solution.

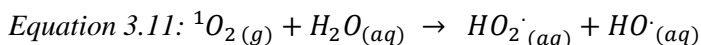
Interestingly, whilst the EPR data shows a two times increase in the amount of DMPO-OH in KCl compared to KNO₃, the sp² carbon bulk etch rate data (Figure 3.4) shows a greater than one order of magnitude increase in the etch rate in KCl compared to KNO₃. As well as radical species the production of non-radical oxidising species is also possible. For example, EC oxidation of the chloride ions not only results in chlorine radical production, (Equation 3.9)



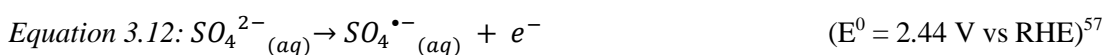
As well as formation of chlorine gas, hypochlorous acid or hypochlorite ions (dependent on solution pH). Because these species have lower thermodynamic oxidising potentials than H₂O₂, production of such species alone is unlikely to be sufficient to explain the observed etch rates. However, their subsequent chemical reactions are also possible chemical routes for generation of HO[•]_(aq) and singlet oxygen. Hypochlorous acid will react with H₂O₂ to produce the singlet oxygen, ¹O₂ (Equation 3.10).⁵⁵



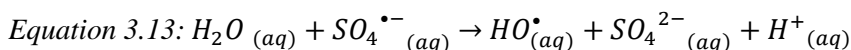
$^1\text{O}_2$ is extremely reactive and can react with water to produce hydroperoxyl radicals and HO^\bullet (Equation 3.11).



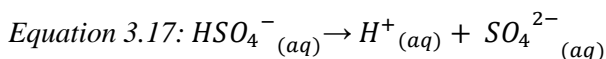
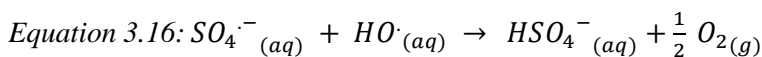
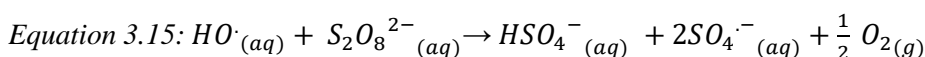
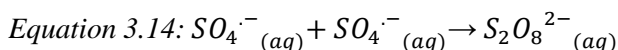
The EPR spectra after electrolysis of K_2SO_4 has the highest concentration of DMPO-OH for all three electrolytes, with the double integrated intensity being nine times larger than that in the KNO_3 solution. Sulphate radicals ($\text{SO}_4^{\bullet-}$), with a lifetime of μs , are highly oxidising ($E^0 = 2.44 \text{ V vs RHE}$)³⁷ and can be generated oxidatively on Pt electrodes in sulphate containing media,^{56,57} Equation 3.12. In the EPR spectrum, the splitting pattern of DMPO- SO_4 could be obscured by that of DMPO-OH when DMPO-OH is present in the majority.⁵⁸



The highly reactive $\text{SO}_4^{\bullet-}$ radicals are also able to abstract a hydrogen atom from water and produce HO^\bullet (Equation 3.13).⁵⁶ Given the high concentrations of sulphate ions and water molecules in the high conductivity solution, Equation 3.13 is thought to be a preferred route for HO^\bullet generation, resulting in high initial concentrations of HO^\bullet .



Once $\text{SO}_4^{\bullet-}$ and HO^\bullet radicals have been produced there are a host of reaction pathways that can occur.^{44,59} Both sulphate radicals and HO^\bullet can recombine with each other to form H_2O_2 (Equation 3.7) or $\text{S}_2\text{O}_8^{2-}$ (Equation 3.14) or react with other solution components to produce more radicals giving rise to a chaining mechanism (Equations 3.15 – 3.17).^{44,59}



These reaction pathways are referred to as chaining mechanisms and will result in the regeneration of the radicals and generation of more stable oxidising species. This, we believe, is the reason for the appearance of the HO^\bullet radicals at timescales much longer than their lifetime and their detection in the system once the electrode potential has been switched off.⁶⁰ This behaviour is thought to be the dominant factor behind the significant DMPO-OH signal in sulphate media. Increased HO^\bullet levels should also result in an increased prominence of Equation 3.7 and Equation 3.8, compared to KNO_3 solutions. H_2O_2 presence in sulphate

solutions is also verified by UV-Vis (Figure 3.8). As with KCl, the generation of non-radical species such as persulphate ions ($\text{S}_2\text{O}_8^{2-}$; $E^0 = 2.01 \text{ V vs RHE}$), and their subsequent reactions with radicals could also be contributing to etching.⁶¹

3.5 The Effect of Concentration and pH in Sulphate Media

As sulphate containing electrolytes gave rise to the highest bulk etch rates, this electrolyte was chosen for further study. The chaining reactions which are most critical for etching of the sp^2 carbon layer are those which increase the number of radicals at the surface of the sp^2 carbon layer. Once a sulphate radical, $\text{SO}_4^{\cdot-}$, is generated on the Pt electrodes it can react with any solution component. Reaction with water results in the generation of HO^{\cdot} as per Equation 3.13. However, if this happens too far away from the sp^2 carbon edge the radical cannot contribute to etching as it will not react with the sp^2 carbon during its very short lifetime. In contrast, if HO^{\cdot} encounters a SO_4^{2-} within its lifetime the reverse of Equation 3.13 is also possible, regenerating the $\text{SO}_4^{\cdot-}$. This chaining can continue until either the $\text{SO}_4^{\cdot-}$ or HO^{\cdot} radical reaches the edge of the sp^2 carbon layer and etching can take place.

To test this theory, the effect of sulphate concentration was investigated for concentrations over the range 30 – 250 mM K_2SO_4 . Data for 250 mM KNO_3 was also included for comparison and is the data point at 0 mM sulphate, shown in Figure 3.9.

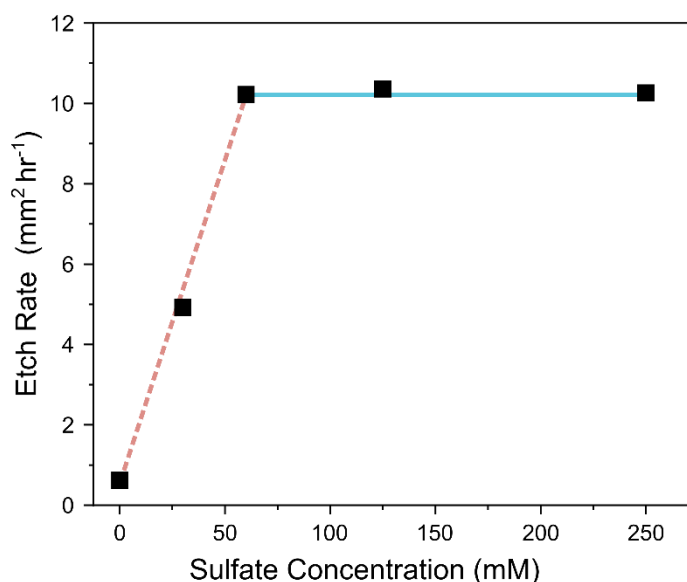
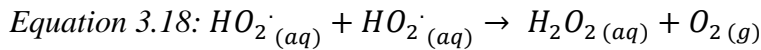


Figure 3.9: (a) Bulk etch rates for a 3.5 mm × 3.5 mm CVD single crystal diamond in aerated KNO_3 solution at 0 mM sulphate and 30, 60, 125, and 250 mM solutions of K_2SO_4 . Lines added as guides to the eye and do not represent fits.

At sulphate concentrations in the range 0 – 60 mM, the etch rate increases linearly (dashed, pink line) with increasing sulphate concentration. This is likely a result of the increased sulphate ion concentration which increases the chances of a HO^{\cdot} encountering SO_4^{2-} within

the distance it can travel during its lifetime. This results in an increased number of chaining events and ultimately results in a higher number of radicals available at the sp^2 carbon solution interface to etch the sp^2 carbon material. As the concentration of SO_4^{2-} increases, the $SO_4^{2-} - SO_4^{2-}$ inter-ion spacing decreases. While the spacing has not decreased to a point where a HO^\bullet is guaranteed to encounter a SO_4^{2-} in its short lifetime, at 60 mM a plateau is still observed (blue line, Figure 3.9). A likely explanation for this is that as the radical concentration increases, the chances of radical recombination also increase, as shown in Equations 3.7, 3.14 and 3.18.



Hence further increases in SO_4^{2-} concentration won't necessarily increase the number of radicals available at the edge of the sp^2 carbon layer. Note, as the concentration of K_2SO_4 increases, the conductivity also increases from 7 – 42 $mS\ cm^{-1}$ across the range, however the plateau region from 60 mM – 250 mM K_2SO_4 shows no noticeable change in etch rate. This suggests that conductivity has little effect on bulk etch rate in this region.

As the generation of HO^\bullet via $SO_4^{\bullet-}$ shows a pH dependence (Equation 10),⁵⁹ the effect of pH on etch rate was investigated. Mixtures of K_2SO_4 and H_2SO_4 were used to vary solution pH over the pH range 0.8 – 7.1 whilst maintaining the total sulphate concentration at 250 mM (Figure 3.10).

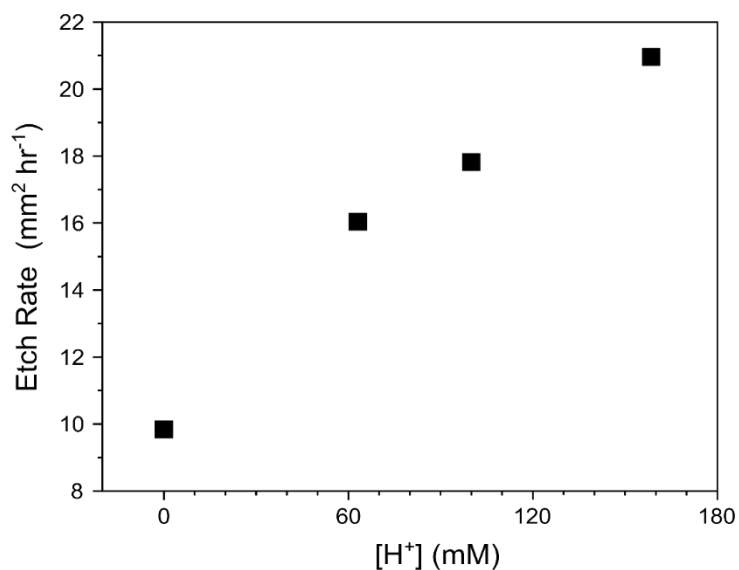


Figure 3.10: Etch rates for a 4.1 mm × 4.1 mm square CVD single crystal diamond in aerated solutions with constant sulphate (250 mM) comprised of K₂SO₄ and H₂SO₄, but with pH varying between 0.8 – 7.1. The solution was held at 25 °C.

A decrease in pH has the effect of increasing the bulk etch rate and a maximum bulk etch rate of 21.0 mm² hr⁻¹ is achieved at pH 0.8. As shown *vide supra* (Figure 3.9), increasing conductivity again has little effect on the etch rate. The increase in etch rate can therefore be attributed to the increase in proton concentration.

3.3.6 The Effect of Temperature in Sulphate Media

To investigate if further improvements to etch rate could be made by varying the temperature, etches were performed in a solution of 50 mM H_2SO_4 at temperatures from 283 K – 343 °C (Figure 3.11).

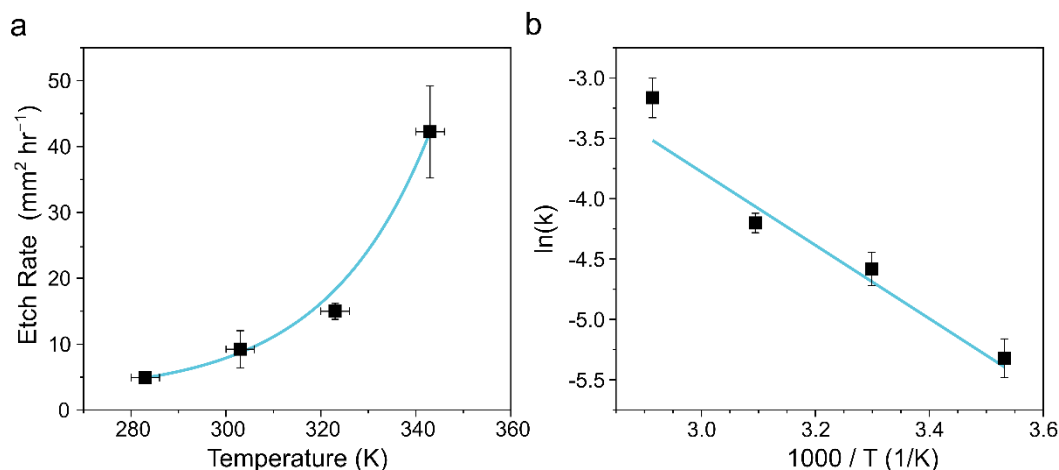


Figure 3.11: a) Rate vs temperature plot for a 3.5 mm \times 3.5 mm square HPHT single crystal diamond from 283, 303, 323, and 343 K in 50 mM H_2SO_4 , 30 V was applied between two platinum electrodes until etching was complete. b) Arrhenius plot of etch rate versus $1000/T$ for a in 50 mM H_2SO_4 . Data in this figure was completed as $n=3$.

The etch rate shows an exponential increase with temperature. An Arrhenius plot of the data gives an activation energy of $377 \pm 80 \text{ kJ mol}^{-1}$. This is a realistic value considering the removal of sp^2 bonded carbon will involve the breaking of C-C bond with a typical enthalpies in the range of 67 – 960 kJ mol^{-1} .⁶² The highest etch rate was observed at 70 °C, the highest temperature trialled, which gave a bulk etch rate of $42.0 \text{ mm}^2 \text{hr}^{-1}$, over $\times 40$ faster than the rate observed when boric acid was used.³ Whilst direct comparison with previously reported etch rates are slightly challenging due to differences in implant and annealing conditions, substrate size, and method of measurement, our measured values in boric acid are similar to reported literature values.^{3,9,11}

These data indicate the advantages of etching in solutions at elevated temperatures. Although the flow set-up utilised herein allowed for temperature control, for practical applications, an elevated temperature could be obtained simply by using smaller volume (100 mL) static cells which are heated as a result of joule heating, due to the large, applied potentials. Note, for the data in Figure 3.11, sufficient samples were available to obtain $n = 3$, and the errors obtained are a good indication of error in the measurement of etch rate using the technique outlined herein, for all experiments.

Overall, the data indicates that the most efficient etch solution is one which contains sulphate at a concentration of at least 60 mM in acidic media ($\text{pH} < 1$) at 70°C . A graphical comparison of all the etch conditions trialled in this Chapter is presented as Figure 3.12.

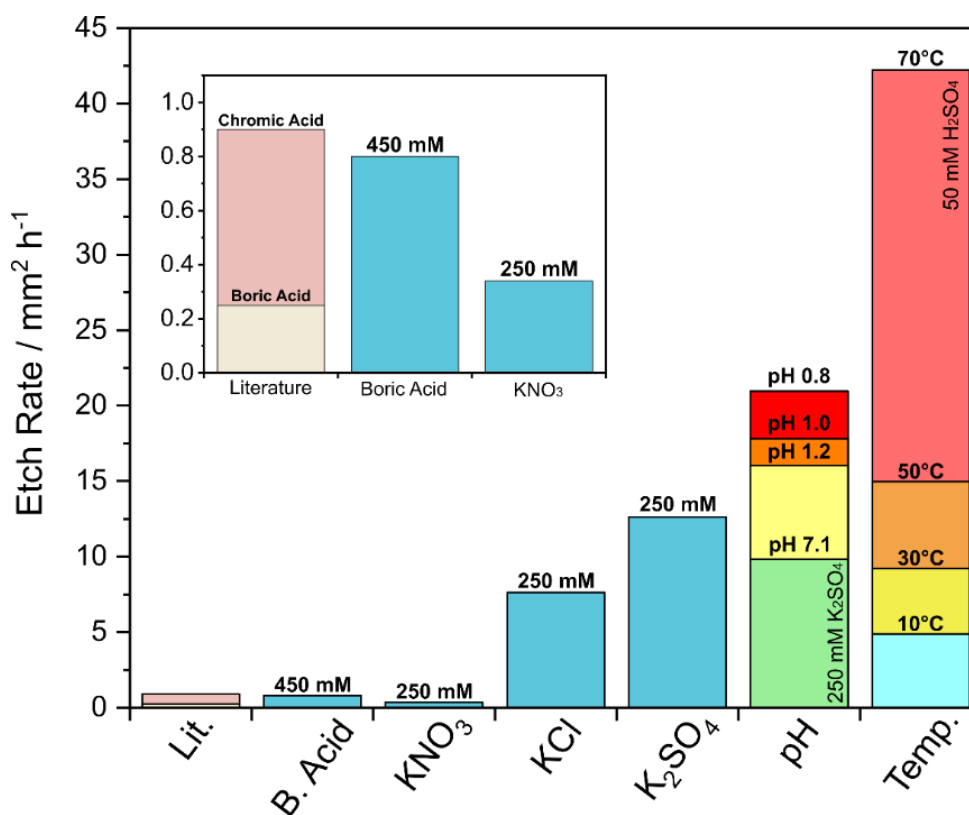


Figure 3.12: Comparison of all etch solution and conditions trialled, and comparisons to the literature.^{3,9}

This electrolyte also has the added practical advantage that in its pure form it is a liquid and therefore should solution evaporation occur the electrolyte will not leave salt residues. This also avoids further cleaning steps to remove salt deposits from the membranes.

3.4 Conclusions

The impact of electrochemical initiation of radical generating chemical pathways in solution, on increasing the bulk etch rate of implanted thin sp^2 carbon layers in single crystal diamond, has been demonstrated. A novel optical etch tracking method was used to monitor etching, via quantification of the colour change associated with removal of the black sp^2 carbon layer in the translucent diamond. Electrolyte chemical identity and concentration was found to play a crucial role, with conductive sulphate and chloride solutions showing significantly increased bulk etch rates (an order of magnitude) compared to conductive nitrate solutions and low conductivity boric acid solutions. The highest rate, $42 \text{ mm}^2 \text{hr}^{-1}$, was achieved using sulphate electrolyte in acidic media at elevated temperature. This represents a $\times 40$ increase compared to measurements in low conductivity, boric acid solutions (bipolar arrangement).

Complementary EPR experiments showed the chloride and sulphate electrolytes also produced sizeable quantities of HO[•] (DMPO-OH). Boric acid showed no radicals whilst nitrate showed a minimal amount. As the DMPO spin trap was added ca. 30 s after the potential had been switched off, any HO[•] (lifetime $\leq \mu\text{s}$) produced via electrochemical means should no longer be present. The detection of HO[•] demonstrated the existence of electrochemically initiated, solution chemistry radical generation pathways which enabled HO[•] to be observed on timescales much longer ($> 10^7$) than their lifetime. The chloride and sulphate anions (and their electrochemically oxidised forms) also contributed to the production of other species e.g. H₂O₂, which also aided radical production. The significant reduction in time during the bulk etch region of the process improves the viability of the implantation and non-contact electrochemical etch as a process to produce thin diamond membranes. However, there is still scope for advancement.

3.5 References

- 1 M. W. Doherty, N. B. Manson, P. Delaney, F. Jelezko, J. Wrachtrup and L. C. L. Hollenberg, *Phys. Rep.*, 2013, **528**, 1–45.
- 2 F. Jelezko and J. Wrachtrup, *Phys. Status Solidi Appl. Mater. Sci.*, 2006, **203**, 3207–3225.
- 3 A. H. Piracha, K. Ganesan, D. W. M. Lau, A. Stacey, L. P. McGuinness, S. Tomljenovic-Hanic and S. Prawer, *Nanoscale*, 2016, **8**, 6860–6865.
- 4 A. Zaitsev, *Optical properties of diamond*, 2001, vol. 134.
- 5 F. Jelezko and J. Wrachtrup, *Phys. Status Solidi Appl. Mater. Sci.*, 2006, **203**, 3207–3225.
- 6 N. Tatsumi, K. Harano, T. Ito and H. Sumiya, *Diam. Relat. Mater.*, 2016, **63**, 80–85.
- 7 C. Hsieh, H. Tsai, H. Lai, C. Hsieh, H. Tsai, H. Lai and H. Lin, *Proc. SPIE*, 2003, **4936**, 337.
- 8 T. Schuelke and T. A. Grotjohn, *Diam. Relat. Mater.*, 2013, **32**, 17–26.
- 9 M. Marchywka, P. E. Pehrsson, D. J. Vestyck and D. Moses, *Appl. Phys. Lett.*, 1993, **63**, 3521–3523.
- 10 P. E. Pehrsson, T. McCormick, W. B. Alexander, M. Marchywka, D. Black, J. E. Butler and S. Prawer, *MRS Proc.*, 1995, **416**, 51.
- 11 M. Marchywka, P. E. Pehrsson, S. C. Binari and D. Moses, *J. Electrochem. Soc.*, 1993, **140**, L19–L22.
- 12 N. R. Parikh, J. D. Hunn, E. McGucken, M. L. Swanson, C. W. White, R. A. Rudder, D. P. Malta, J. B. Posthill and R. J. Markunas, *Appl. Phys. Lett.*, 1992, **61**, 3124–3126.
- 13 A. P. Abbott, G. Capper, K. J. McKenzie, A. Glidle and K. S. Ryder, *Phys. Chem. Chem. Phys.*, 2006, **8**, 4214–4221.
- 14 W. O. Karim, A. P. Abbott, S. Cihangir and K. S. Ryder, *Trans. Inst. Met. Finish.*, 2018, **96**, 200–205.
- 15 R. M. Crooks, *ChemElectroChem*, 2016, **3**, 357–359.
- 16 F. Mavré, R. K. Anand, D. R. Laws, K. F. Chow, B. Y. Chang, J. A. Crooks and R. M. Crooks, *Anal. Chem.*, 2010, **82**, 8766–8774.
- 17 J. B. Posthill, D. P. Malta, T. P. Humphreys, G. C. Hudson, R. E. Thomas, R. A. Rudder

- and R. J. Markunas, in *Film Synthesis and Growth Using Energetic Beams*, 1995, vol. 388, pp. 299–304.
- 18 Y. Mokuno, A. Chayahara and H. Yamada, *Diam. Relat. Mater.*, 2008, **17**, 415–418.
 - 19 C. F. Wang, E. L. Hu, J. Yang and J. E. Butler, *J. Vac. Sci. Technol. B Microelectron. Nanom. Struct.*, 2007, **25**, 730.
 - 20 J. Yang, C. F. Wang, E. L. Hu and J. E. Butler, in *Materials Research Society Symposim Proceedings*, 2007, vol. 956.
 - 21 C. Uzan-Saguy, C. Cytermann, R. Brenner, V. Richter, M. Shaanan and R. Kalish, *Appl. Phys. Lett.*, 1995, **67**, 1194.
 - 22 J. F. Ziegler, M. D. Ziegler and J. P. Biersack, *Nucl. Instruments Methods Phys. Res. Sect. B Beam Interact. with Mater. Atoms*, 2010, **268**, 1818–1823.
 - 23 J. O. Orwa, K. W. Nugent, D. N. Jamieson and S. Prawer, *Phys. Rev. B - Condens. Matter Mater. Phys.*, 2000, **62**, 5461–5472.
 - 24 D. P. Hickey, E. Kuryliw, K. Siebein, K. S. Jones, R. Chodelka and R. Elliman, *J. Vac. Sci. Technol. A Vacuum, Surfaces, Film.*, 2006, **24**, 1302–1307.
 - 25 P. Olivero, S. Rubanov, P. Reichart, B. C. Gibson, S. T. Huntington, J. R. Rabeau, A. D. Greentree, J. Salzman, D. Moore, D. N. Jamieson and S. Prawer, *Diam. Relat. Mater.*, 2006, **15**, 1614–1621.
 - 26 F. Bosia, N. Argiolas, M. Bazzan, P. Olivero, F. Picollo, A. Sordini, M. Vannoni and E. Vittone, *Diam. Relat. Mater.*, 2011, **20**, 774–778.
 - 27 J. F. Prins, *Mater. Sci. Reports*, 1992, **7**, 275–364.
 - 28 F. Bosia, S. Calusi, L. Giuntini, S. Lagomarsino, A. Lo Giudice, M. Massi, P. Olivero, F. Picollo, S. Sciortino, A. Sordini, M. Vannoni and E. Vittone, *Nucl. Instruments Methods Phys. Res. Sect. B Beam Interact. with Mater. Atoms*, 2010, **268**, 2991–2995.
 - 29 B. A. Fairchild, S. Rubanov, D. W. M. Lau, M. Robinson, I. Suarez-Martinez, N. Marks, A. D. Greentree, D. McCulloch and S. Prawer, *Adv. Mater.*, 2012, **24**, 2024–2029.
 - 30 S. Stoll and A. Schweiger, *J. Magn. Reson.*, 2006, **178**, 42–55.
 - 31 G. M. Eisenberg, O. Processes and W. St, *Ind. Eng. Chem.*, 1943, **15**, 327–328.
 - 32 N. Kabay and M. Bryjak, *Boron Removal From Seawater Using Reverse Osmosis*

Integrated Processes, Elsevier B.V., 2015.

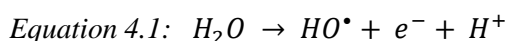
- 33 Y. Pauleau and P. B. Barna, *Protective coatings and thin films: synthesis, characterization, and applications*, Springer, 1997.
- 34 T. Shimada, S. Kubota, T. Yanase and T. Nagahama, *Carbon N. Y.*, 2014, **67**, 300–303.
- 35 H. Liu, Q. Xu and C. Yan, *Electrochem. commun.*, 2013, **28**, 58–62.
- 36 M. Pourbaix, H. Zhang and A. Pourbaix, *Mater. Sci. Forum*, 1997, **251–254**, 143–148.
- 37 D. A. Armstrong, R. E. Huie, W. H. Koppenol, S. V. Lymar, G. Merenyi, P. Neta and B. Ruscic, *IUPAC Tech. Rep.*, , DOI:10.1515/ci-2016-0217.
- 38 N. Vatisstas, *Int. J. Electrochem.*, 2012, **2012**, 1–7.
- 39 I. Morcos and E. Yeager, *Electrochim. Acta*, 1970, **15**, 953–975.
- 40 A. J. Bard and L. R. Faulkner, *Electrochemical Methods - Fundamentals and Applications*, Wiley, 2nd edn., 2001, vol. 2.
- 41 G. R. Buettner, *Free Radic. Bio. Med.*, 1987, **3**, 259–303.
- 42 J. A. Weil, *Phys. Chem. Miner.*, 1984, **10**, 149–165.
- 43 O. Simond, V. Schaller and C. Comninellis, *Electrochim. Acta*, 1997, **42**, 2009–2012.
- 44 J. Méndez-cute;az, M. Sánchez-Polo, J. Rivera-Utrilla, S. Canonica and U. von Gunten, *Chem. Eng. J.*, 2010, **163**, 300–306.
- 45 J. Weiss, *Adv. Catal.*, 1952, **4**, 343–365.
- 46 I. E. L. Stephens, A. S. Bondarenko, U. Grønbjerg, J. Rossmeisl and I. Chorkendorff, *Energy Environ. Sci.*, 2012, **5**, 6744–6762.
- 47 T. Mokudai, K. Nakamura, T. Kanno and Y. Niwano, *PLoS One*, 2012, **7**, e46392.
- 48 A. Gómez-Marín, J. Feliu and T. Edson, *ACS Catal.*, 2018, **8**, 7931–7943.
- 49 T. J. Schmidt, U. A. Paulus, H. A. Gasteiger and R. J. Behm, *J. Electroanal. Chem.*, 2001, **508**, 41–47.
- 50 B. G. Kwon, J.-O. Kim and J.-K. Kwon, *Environ. Eng. Res.*, 2012, **17**, 205–210.
- 51 E. Finkelstein, G. M. Rosen, E. J. Rauckman and J. Paxton, *Mol. Pharmacol.*, 1979, **16**, 676–85.

- 52 E. Finkelstein, G. M. Rosen and E. J. Rauckman, *Arch. Biochem. Biophys.*, 1980, **200**, 1–16.
- 53 G. R. Buettner and L. W. Oberley, *Biochem. Biophys. Res. Commun.*, 1978, **83**, 69–74.
- 54 T. Shoji, L. Li, Y. Abe, M. Ogata, Y. Ishimoto, R. Gonda, T. Mashino, M. Mochizuki, M. Uemoto and N. Miyata, *Anal. Sci.*, 2007, **23**, 219–221.
- 55 A. M. Held, D. J. Halko and J. K. Hurst, *J. Am. Chem. Soc.*, 1978, **100**, 5732–5740.
- 56 O. V. Reshetnyak and E. P. Koval'chuk, *Electrochim. Acta*, 1998, **43**, 465–469.
- 57 F. Bolleta, M. Ciano, V. Balzani and N. Serpone, *Inorganica Chim. Acta*, 1982, **62**, 207–213.
- 58 P. L. Zamora and F. A. Villamena, *J. Phys. Chem. A*, 2012, **116**, 7210–7218.
- 59 C. Liang and H.-W. Su, *Ind. Eng. Chem. Res.*, 2009, **48**, 5558–5562.
- 60 F. Zhang, Z. Sun and J. Cui, *RSC Adv.*, 2020, **10**, 33928–33936.
- 61 Irkham, T. Watanabe, A. Fiorani, G. Valenti, F. Paolucci and Y. Einaga, *J. Am. Chem. Soc.*, 2016, **138**, 15636–15641.
- 62 A. A. Zavitsas, *J. Phys. Chem. A*, 2003, **107**, 897–898.

Chapter 4: Understanding Anode Corrosion in BDD Advanced Oxidation Systems

4.1 Introduction

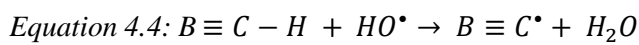
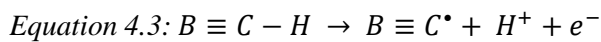
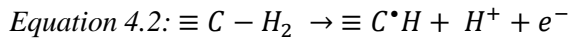
Electrochemical advanced oxidation (EAO) systems based on boron doped diamond (BDD) electrodes are already commercially available from a variety of manufacturers, with electrodes used in both freestanding and thin-film (attached to a support substrate) form. The main advantage of these EAO systems is their ability to remove a wide range of problematic chemical contaminants, such as phenolic acids, aliphatic acids and perfluorinated organics, amongst others.¹ These systems also have a relatively small installed size which allow them to be deployed in places where on-site wastewater treatment would usually be impossible.² The effectiveness of BDD-EAO systems results from the ability to generate highly oxidising free hydroxyl radicals ($\bullet\text{OH}$, Equation 4.1) electrochemically using BDD, which can react with species in solution. Direct electron transfer reactions provide an additional mechanism for the oxidation of species unreactive to $\bullet\text{OH}$.¹



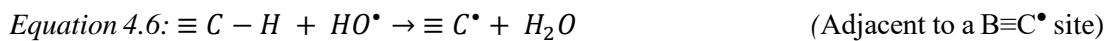
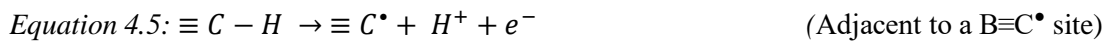
While BDD-EAO systems are seeing great success in some industrial wastewater applications, in other wastewater applications the corrosion of the BDD anode reduces the lifetime to a point where BDD based EAO systems are prohibitively expensive when compared to alternative treatment methods. Although limited studies into the solution and material effects on corrosion rate have been conducted the results give a far from complete picture.³⁻⁸ Additionally, almost all experimental work has been performed on thin-film BDD grown in-house, making comparison between literature difficult. Relatively few solution compositions have been tried in these tests. A full discussion of previous work on BDD anodic corrosion can be found in Chapter 1, Section 1.7.1. In industrial EAOPs applications it is not always possible to control, or even know the solution composition, which can make specific mitigation strategies difficult. As a result, it is critical to the continued use of BDD-EAO systems to identify contaminants for which BDD electrodes are unsuited, due to accelerated corrosion. Hopefully with this knowledge solution dependent and independent mitigation strategies can be developed.

Chaplin et. al. used a combination of experimental cyclic voltammetry (CV) and density functional theory (DFT) simulations to propose solution independent mechanisms for carbon corrosion in BDD.⁹ In their investigations they presented two routes for corrosion at BDD electrodes, the lowest energy of which proceeds via the formation of sp^2 carbon. For this to

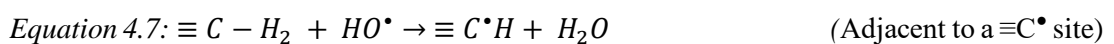
occur two adjacent C-H groups must both lose a hydrogen and reconstruct to minimise dangling bonds. The first step of sp^2 bond formation is the removal of a hydrogen atom from a C-H functionality. The first hydrogen can be removed electrochemically (Equations 4.2 – 4.3) or chemically (Equation 4.4). Chemical reactions are as a result of the reactions of $\bullet OH$ electrochemically generated on the electrodes surface (Equation 4.1).⁹ These $\bullet OH$ can react with CH functionality on the electrode surface in a barrierless reaction to leave carbon centred radicals on the BDD (Equation 4.4).



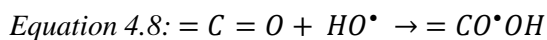
Once the first hydrogen has been removed adjacent C-H functionality can also loose a hydrogen. This can proceed as with the first hydrogen via Equations 4.2- 4.4 however, lower energy routes are available adjacent to the carbon radicals created by those processes. The $B \equiv CH$ sites were predicted by DFT to be the most reactive, followed by the $\equiv CH_2$ sites. For C-H functionality adjacent to a $B \equiv C^\bullet$ site Equations 4.5 and 4.7 are barrierless and result in surface reconstruction to form a stable double bond.



For C-H functionality adjacent to a $\equiv C^\bullet$ site equation 4.8 also results in double bond formation on the surface.



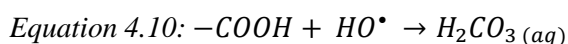
While this reaction is a low energy route to BDD surface changes, it is limited by the starting C-H coverage on the BDD surface. The creation of sp^2 bonded carbon on the surface is important as this will be much more susceptible to corrosion than the sp^3 surface from which it is created. BDD surfaces are grown in H rich environments and thus will be H-terminated. However, on term exposure to air, cleaning in acids, electrochemical oxidation results in oxygen terminations of the surface (e.g. C-OH, C-O-C, C=O).³ DFT simulations show that the corrosion of oxygenated carbon surfaces is a higher energy route than the creation of sp^2 bonded carbon via the C-H route.⁹ O-terminated surfaces corrode by oxidising the oxygen functional groups. Whereas C-H groups will be limited on an anodically polarised electrode C-O functionality will be prevalent due to the WOR. This process starts with the oxidation of a C=O site by an $\bullet OH$ generated on the BDD surface (equation 4.8).



Reconstruction of this $=CO^{\bullet}OH$ functionality on the surface requires removal of a hydrogen atom from an adjacent carbon electrochemically as per Equation 4.2 and 4.3, or chemically as per Equation 4.4.



Finally attack of a $^{\bullet}OH$ at the $-COOH$ site results in the formation of carbonic acid (H_2CO_3) which can then dissociate into the solution. This process has a relatively high activation energy of 59 kJ mol^{-1} and this may serve to explain why O-terminated BDD corrosion is more prevalent at higher current densities and temperatures.^{6,9} Equation 4.10 is expected to be the rate determining step for corrosion *via* C-O oxidation as it has the highest activation energy of the steps suggested by this mechanism.



During anodic polarisation outside of the aqueous solvent window (*i.e* the generation of $^{\bullet}OH$) C-O termination will be much more prevalent on the electrode surface than C-H termination. As such oxidation of the C-O functionality is likely to be the most significant contributor to anodic corrosion in BDD. However, formation of sp^2 carbon may be enhanced when the electrode undergoes cathodic polarisation alternately with anodic as cathodic polarisation could serve to increase the amount of C-H termination on the surface.¹⁰

Previous investigations of anodic corrosion in BDD use indirect measurements, such as CV, XPS or SEM to track corrosion on BDD electrodes.⁶ The aim of the work in this chapter is to directly measure the amount of material removed on a reasonable laboratory timescale of 72 hours. To this end a custom flow cell was designed and built and white-light interferometry (WLI) was used to directly measure the amount of material removed from the anode after a 72-hour electrolysis. WLI is a non-contact 3D imaging technique that allows for the resolution of nm height differences with a height range and area that is larger than the maximum achievable using atomic force microscopy. While “as-grown” electrodes with very rough surfaces ($RMS > 10 \mu m$) are often employed in BDD-EAOs, due to their higher surface area, highly polished disks of BDD were used for this work. This highly polished initial surface makes it easier to resolve small height differences in the WLI, as well as making roughness a meaningful metric for the severity of electrode corrosion. This work represents the first-time the amount of corrosion has been measured directly for these systems, rather than inferred from other measurements.

Using this novel method of tracking the rate of erosion the effect of several solution and operational conditions are investigated. The nature of organic species in the effluent is investigated by measuring the electrode corrosion in solutions of glucose and acetic acid at concentrations between 0.25 and 3 M. The relative corrosion rates of three different types of BDD are also investigated, two grades of commercially available free-standing BDD and one type of commercially available thin-film material. Current densities between 2,500 and 15,000 A m⁻² and the frequency of polarity switching between 6 and 600 seconds are investigated. Finally, recommendations made for the operation of BDD-EOPs made as a result of our findings.

4.2 Experimental Methods

4.2.1 BDD Materials

Three different BDD materials were investigated in this chapter. Freestanding electroprocessing grade (EP, Element Six Limited)¹¹ was used for most of this work. This material has been fully characterised and is electrode D in Hutton *et.al.*¹² This material was ~ 400 µm thick, resin bond polished on the growth face to ~3 nm RMS and the nucleation face lapped to ~100 nm RMS. Some experiments were conducted on freestanding electroanalytical grade (EA, Element Six Limited). This material has been fully characterised and is electrode E in Hutton *et.al.*¹² This material was 356 µm thick, resin bond polished on the growth face to ~1 nm RMS and the nucleation face lapped to ~100 nm RMS. Both freestanding materials were cut into 10 mm rounds using a 335 nm Nd:YAG 34 ns laser micromachining system (E-355H-3-ATHI-O) system, Oxford Lasers. After cutting the electrodes were acid cleaned and sputtered according to standard protocols (See Chapter 2).

Thin-film BDD was also utilised in this work. DIACHEM electrodes (CONDIAS, Germany) were used as supplied with no additional cleaning or contacting. DIACHEM electrodes consisted of a thin layer (~ 15 µm thick) of BDD deposited on an 8 mm diameter niobium substrate. These electrodes were used as grown with a roughness of ~4 µm RMS as they cannot be polished due to the weak bond between the niobium substrate and BDD and warping due to the coefficient of thermal expansion (CTE) mismatch.

All SEM of the surface of all BDD electrodes used in this work and EBSD of EP and EA-BDD can be found in Chapter 2 of this thesis.

4.2.2 Cell Design

The cell utilised in these experiments is a custom designed flow cell. The cell is 3D printed in High-Temperature Resin (FormLabs, Massachusetts, US) using a Form 3 (Formlabs,

Massachusetts, US) stereolithography 3D printer. The gaskets used to seal the cell are 1 mm thick Viton cut to size (Delta Rubber, UK).

4.3 Results and Discussions

4.3.1 *Experimental Methodology.*

As previously discussed, the existing methods of tracking the corrosion of BDD anodes are only making indirect measurements of the severity of corrosion.³⁻⁸ To study corrosion directly a custom flow cell was designed and fabricated (Figure 4.1). The cell comprises three stereolithography 3D printed parts, two brass electrode contacts, two Viton gaskets and hardware to secure the cell together. Two BDD electrodes, with the polished growth faces pointing forward, are placed opposite a channel through which the solution flows. In all cases the BDD material of interest is used as the anode and a disk of EP-BDD is used as the cathode. A Viton gasket is used to seal the electrode with a defined area exposed (8 mm for freestanding BDD and 6 mm for thin-film BDD). The masked surface also provides a reference for the height of the original surface. The electrodes are then connected to a variable DC power supply and sufficient potential applied to reach the desired current density for the duration of the experiment (72 hours). In the majority of the experiments a current density of $10,00 \text{ A m}^{-2}$ was employed. This current density is typically used for accelerated lifetime testing for EAO systems using thin-film BDD electrodes⁹ and is a typical for the operation of commercial EAO systems utilising freestanding BDD electrodes, such as Element Six's DIAMOX.¹³ Solution was flowed at a rate of 200 ml min^{-1} from a 1 litre reservoir in a temperature-controlled water bath at 60°C as the treated solutions are often hot from other processes at the point of treatment.

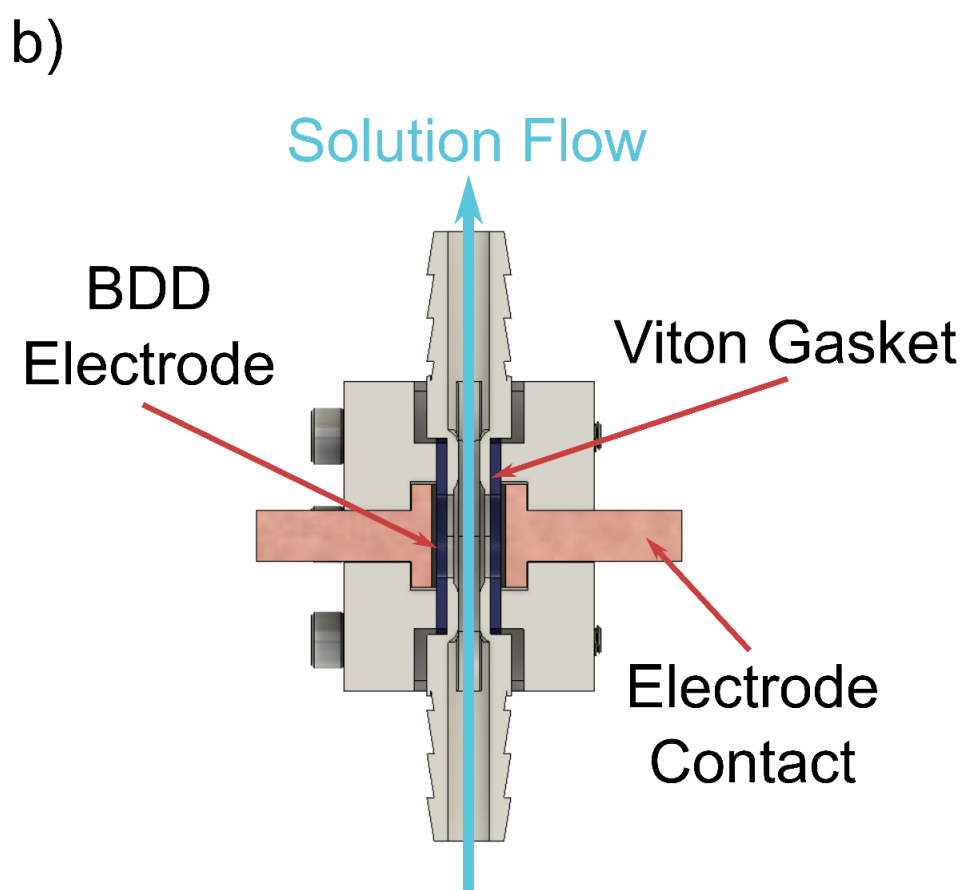
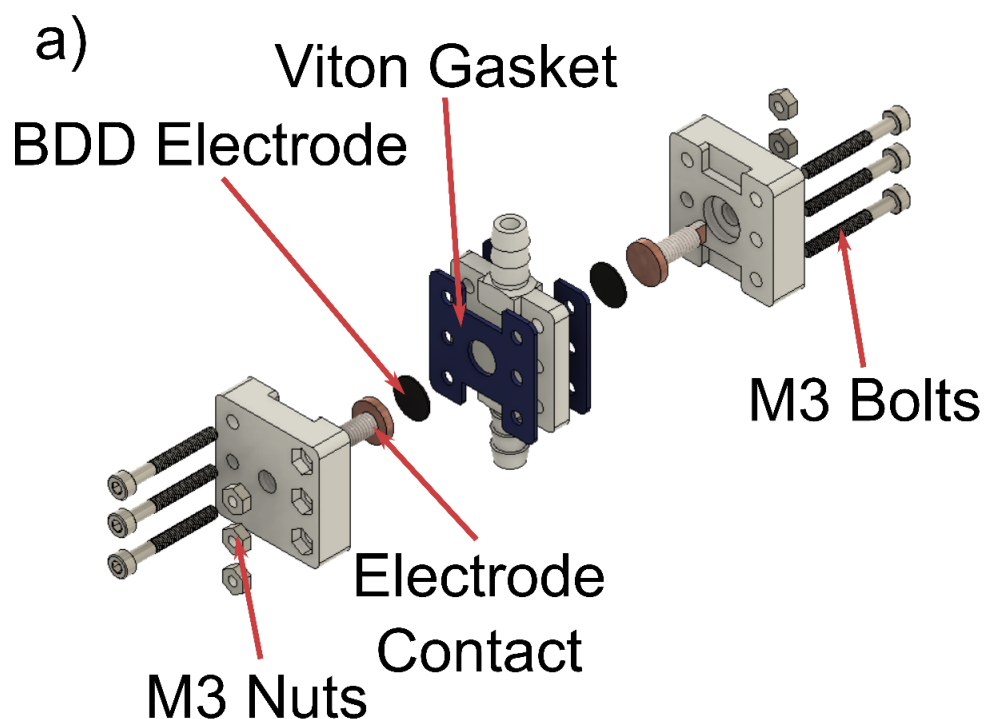


Figure 4.1: Rendering of the flow cell designed for BDD corrosion experiments. a) Exploded view showing all the cells components. b) Cross-section through the assembled cell showing the flow path for solution.

An initial experiment was run to validate the use of WLI as a measurement technique for tracking corrosion of the EP-BDD surface. An experiment was run for 72 hours in a solution of 0.5 M potassium sulphate (K_2SO_4) at a current density of $10,000 \text{ A m}^{-2}$. Typically, this current density required applied potentials of 10 – 15 V, although this varied with solution conductivity. This solution was chosen as it has been shown in the literature that aqueous sulphate solutions remove material slowly at $10,000 \text{ A m}^{-2}$.^{4,6} This electrolyte allows us to test if small differences in surface height, due to etching of the surface could be resolved by WLI.

After electrolysis electrodes were acid cleaned (Chapter 2, Section 2.3.2). The electrodes were then characterised by WLI. The cathode surface remained unchanged, with no appreciable increase in roughness. However, the anode showed noticeable changes to the surface (Figure 4.2). The region exposed to solution had increased in roughness from 4 nm RMS (the polished, un-corroded surface) to 30 nm RMS. The masked edge had no appreciable increase in roughness, confirming that it was successfully isolated from solution throughout the experiment. The average depth of the central eroded region is 113 nm compared to the masked edge. The corrosion rate in this solution is 1.57 nm hr^{-1} in this solution. Depth and roughness measurements of the eroded region are calculated over the entire eroded area seen in Figure 4.2, *i.e.* an area $\sim 2 \times 8 \text{ mm}$.

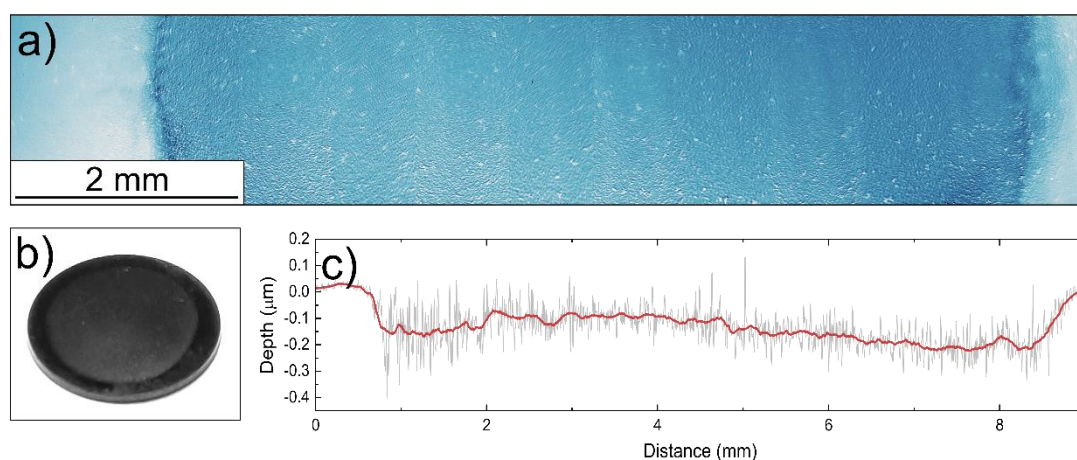


Figure 4.2: EP-BDD anode characterisation after a 72-hour electrolysis at $10,000 \text{ A m}^{-2}$ in 0.5 M K_2SO_4 . a) WLI image of the surface, showing the smooth masked edge and rough eroded region. b) photograph of the 10 mm diameter EP-BDD electrode showing the eroded region. c) Line profile in X across the centre of the WLI image showing the change in height.

Experiments in this solution were also repeated twice more to gauge the repeatability of the corrosion rate. The results of all experiments in 0.5 M K_2SO_4 can be seen in Table 4.1. These three experiments demonstrate excellent repeatability and provide confidence in measuring the corrosion rate by this method. It is worth noting that none of the cathodes showed signs of erosion in these repeat experiments. While BDD polarised in sulphate containing solutions is

often considered as lightly corroded in the literature,⁴ the rates measured here are still significant for electrodes deployed in the field for long timescales. This result is also odds with conclusions drawn by Kashiwada et. al. who suggested that BDD corrosion was not possible in solutions without organic species such as acetic acid present.⁶

Table 4.1: Tabulation of the corrosion depth and corrosion rate of three EP-BDD electrodes in 0.5 M K₂SO₄.

Electrode	Depth of Corrosion (nm)	Corrosion Rate (nm hr ⁻¹)
1	113	1.57
2	120	1.67
3	124	1.72
		1.65 ± 0.08

4.3.2 Solution Composition

As a result of the radical etch routes discussed in Chapter 3 of this thesis, WLI was initially used to study the difference in corrosion rates in solutions of three common salts. The salts chosen were KNO₃, KCl, and K₂SO₄ as these all give rise to different radical chemistry on electrolysis. As discussed in Chapter 3, the radical content of KNO₃ solutions will be low, with more radicals seen for KCl and K₂SO₄. A 72-hour electrolysis using EP-BDD electrodes was performed in 0.5 M solutions of potassium nitrate (KNO₃) and potassium chloride (KCl). The depth of the corroded region compared to the masked area for these electrodes was then compared to the electrolysis in a 0.5 M K₂SO₄ solution. Electrolysis in KNO₃ and KCl electrodes resulted in a step which was too small to be measured by WLI over the width of the round, indicating minimal corrosion. The BDD rounds have a slight curve, due to material strain, which prevented measurement of steps which are this small. However, it was possible to evaluate the severity of the corrosion by measuring the roughness in the centre of the corroded region (Figure 4.3).

Whilst by eye (Figure 4.3d) the KNO₃ electrode appeared the least eroded WLI (Figure 4.3a) indicated that the roughness in the corroded region has almost doubled to 7.5 nm RMS. In contrast visible corrosion was evident for the BDD treated in the KCl solution, Figure 4.3e. The erosion on this electrode is seen as a pronouncement of the grain structure and a lightening of the eroded surface, as opposed to the darkening seen on more heavily eroded samples. WLI of the central region of the electrode corroded in KCl gives an RMS roughness of 10 nm, only slightly higher than for the KNO₃ electrode. However, the grain structure of this electrode is far more obvious with the distinctive “Palm-Tree” structure of EP-BDD visible in the

topographical WLI image, Figure 4.3b. The structure of this material is discussed in more detail in Chapter 2, Section 2.1.2. This suggests that the grain boundaries, and possible also the grains themselves, have corroded more significantly in this solution than in KNO_3 . The K_2SO_4 electrode shows the greatest sign of erosion, as expected from the work in Chapter 3, with 37 nm RMS seen at the centre of the electrode. Interestingly, the grain structure is much less evident on this electrode than for the KCl electrode, this may simply be because more material has been removed (Figure 4.3c).

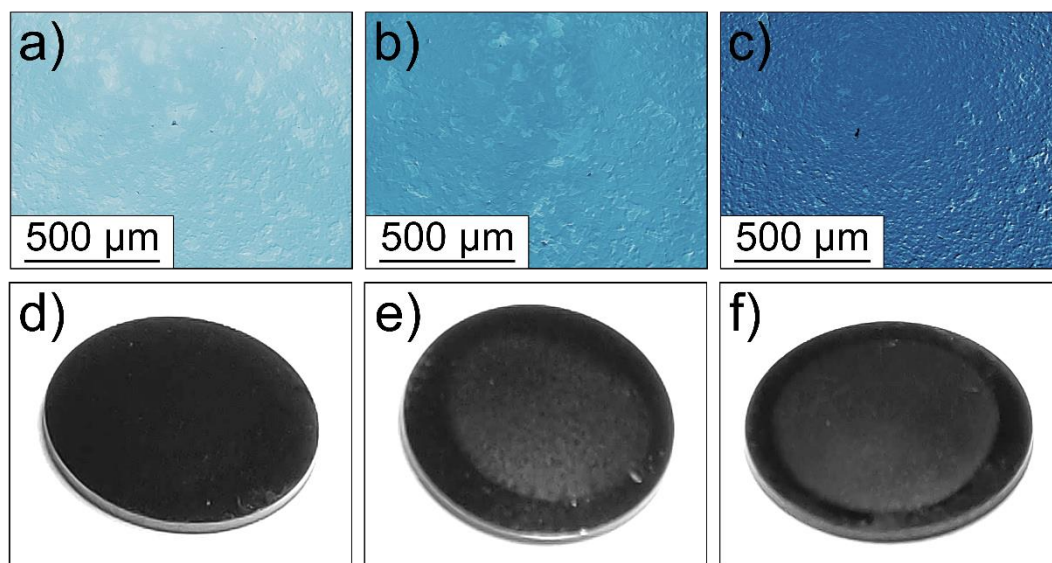


Figure 4.3: WLI of the EP-BDD anodes after electrolysis in a) 0.5 M KNO_3 , b) 0.5M KCl, c) 0.5 M K_2SO_4 . Photographs of the 10 mm diameter EP-BDD anodes after electrolysis in d) 0.5 M KNO_3 , e) 0.5M KCl, f) 0.5 M K_2SO_4 .

4.3.3 BDD Material

A variety of grades of BDD are available commercially, most commercial AO systems use thin-film ($\sim 15 \mu\text{m}$ thick) BDD (TF-BDD) grown on a conducting non-diamond substrate. This is because thin-film diamond is approximately 10% of the cost by area compared to freestanding EP-BDD, allowing the use of larger electrodes for the same cost, and thereby increasing the rate at which pollutants are removed from solution. However, the growth of thin layers of BDD onto non-diamond substrates is often likely to result in lower quality diamond with a higher density of NDC than freestanding material. NDC will corrode more rapidly than BDD which means that NDC containing BDD is likely to be more susceptible to anodic corrosion.⁹ Any potential difference in wear rate is important to understand, as although thin-film diamond is cheaper by area, it is more expensive by volume, because EP-BDD is typically thirty times thicker than TF-BDD.

While commercial EAO systems utilising freestanding BDD such as Element Six's Diamox typically utilise EP-BDD due to its reduced cost when compared to EA-BDD the corrosion rate of EA-BDD was also investigated. Whilst EA grade is more expensive if the corrosion rates are noticeable slower than this factor may outweigh the higher cost of the material. EA-BDD material has a very different grain structure from EP-BDD due to its much slower growth rates (as discussed in Chapter 2, Section 2.1) which may provide insight into how changes in the BDD morphology changes the rate of corrosion. To investigate the difference in erosion rates all three electrode materials (EP-BDD, EA-BDD, and TF-BDD) were held at a potential sufficient to pass a current density of $10,000 \text{ A m}^{-2}$ in a solution of $0.5 \text{ M K}_2\text{SO}_4$. It should be noted that the TF-BDD electrodes have an as-grown starting surface, this is due to the difficulties in polishing these electrodes without delaminating the film from the substrate as discussed previously.

Interferometry on the TF-BDD electrodes was challenging as the high roughness of the as-grown starting surface makes the edge of the exposed region harder to resolve. Because of this limitation three experiments were run to improve the accuracy of the measurement. The corroded area of these electrodes was on average $3.75 \pm 0.2 \text{ } \mu\text{m}$ recessed compared to the masked area. This gives a wear rate of $52 \pm 2.7 \text{ nm hr}^{-1}$, over thirty times faster than that seen for EP grade freestanding BDD. It has been previously suggested that NDC plays a critical role in anodic wear.⁹ Due to the short growth times employed in thin film growth, the diamond grains of this material will be smaller than those in the freestanding BDD, this in turn increases the number of NDC containing grain-boundaries. This is likely to be the reason for the increase in this materials' susceptibility to anodic wear. Under this solution condition and current density, a TF-BDD electrode with a $15 \text{ } \mu\text{m}$ thick coating would last an average of 300 hours. In contrast, a $350 \text{ } \mu\text{m}$ thick freestanding BDD would last for an average of over 200,000 hours. As these electrodes are cheaper by area one possible solution is to run a larger electrode at a lower current density, decreasing the wear rate for the same amount of advanced oxidation work performed. This concept is discussed further in section 4.3.5.

Interestingly the EA-BDD gave an etch rate of only 0.69 nm hr^{-1} , less than half of that seen for the EP-BDD. EA and EP-BDD is grown under different conditions, with EP-BDD being grown faster to reduce the cost of the material. This results in several differences in the material, such as boron doping density crystal morphology and phase purity. Full characterisation of this material can be found in Chapter 2, Section 2.1.2. The difference in corrosion rate is unlikely to be due to boron content as the typical average boron incorporation for EA-BDD and EP-Grade are the same at $3 \times 10^{20} \text{ cm}^{-3}$.¹²

To our knowledge the only discussion of the effect of crystal morphology on corrosion rates in the literature has been conducted by Kashiwada et. al.⁶. In this work they saw that the [111] facets were removed preferentially to other facets during electrolysis at 5,000 A m⁻² in 1 M acetic acid. The [111] facets have been shown to incorporate 5× more boron than the [100] facets,¹⁴ and as such the authors suggest these corrode faster due to higher electrochemical activity at these facets.

It is not uncommon in diamond to see that different crystal orientations in diamond have different removal rates, such as is seen in mechanical polishing, which is discussed in more detail in Chapter 1. One explanation for this difference in corrosion rate could be that predominantly [110] textures presented to solution by polished BDD are more resistant to anodic corrosion than other crystal directions. As such the density of non-[110] orientated crystallites control the rate of erosion. These other phases will etch the fastest initially, becoming recessed into the surface, this recession will reduce the rate of the mass transport of rate enhancing species (like the sulphate anion) to this surface, thereby reducing the rate as the crystallite gets more recessed. The recession of these crystallites will expose the edges of the 110 oriented crystals, which will be differently oriented, and therefore potentially more susceptible to corrosion. As the EP-BDD has many more non-110 orientated crystals than EA-BDD this may explain the relatively higher corrosion rates seen for this material. This may also explain some of the increased corrosion rates seen for thin-film BDD, which has an as-grown surface which will present all possible crystal directions to solution at once, and thus facets may just corrode from an easy direction.

Another possible explanation is that inclusion of other crystal phases creates highly defective regions of small crystallites, as can be seen between larger grains of EP-BDD in the EBSD data in Chapter 2, Section 2.1.2. These highly defective regions may etch faster than the large grains. While this might explain why EP-BDD had a higher corrosion rate than EA-BDD on short timescales the relatively smooth surfaces seen at long timescales suggests that the entire surface corrodes at a similar rate. A third explanation could be that the stacking faults seen in the SEM images as striations in the EP-BDD grains result in surfaces which are more susceptible to corrosion due to these defects.

4.3.4 Organic Content Nature

Although in deployment it may be impossible to control what type of contamination an AO system is required to remove, by understanding the effects of solution chemistry advice can be given on which types of contaminants are to be avoided. It may also be possible to develop mitigation strategies that decrease the wear rate in some effluents. Glucose and acetic acid

were chosen as model pollutants for this work. Glucose was chosen as it represents a molecule that will increase the organic content of the solution, while being a large, uncharged molecule. Acetic acid was chosen due to its identification in the literature as causing high corrosion rates for BDD anodes.^{4,6} Erosion rates for 72-hour electrolysis in various concentrations of both organic molecules with a background electrolyte of 0.5 M K₂SO₄ can be seen in Figure 4.4.

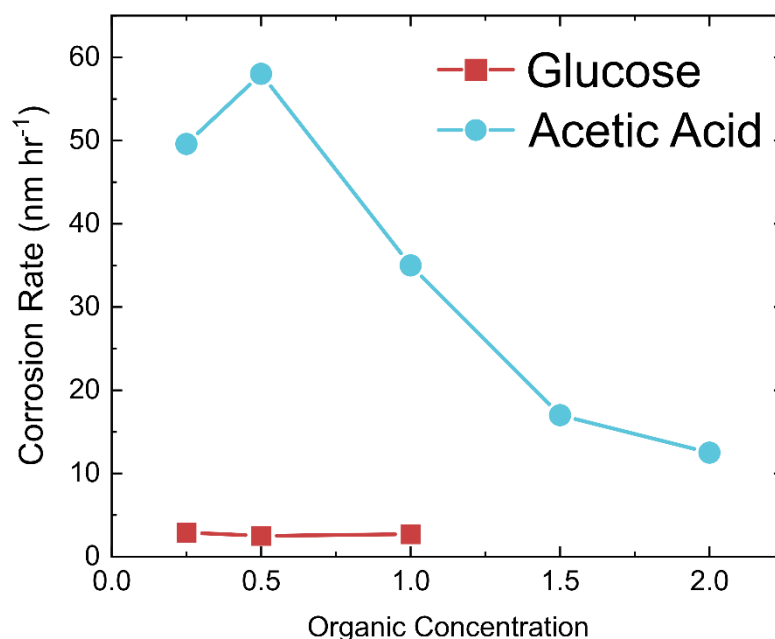
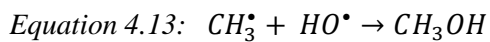
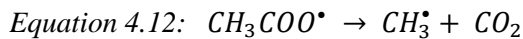
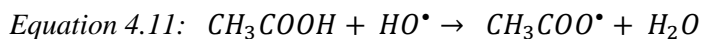


Figure 4.4: Corrosion rates seen during a 72-hour electrolysis at 10,000 A m⁻² in a 0.5 M solution of K₂SO₄ with varied concentrations of Acetic Acid or Glucose. The corrosion rate for an EP-BDD electrode in just 0.5 M K₂SO₄ is 1.65 ± 0.08 nm hr⁻¹.

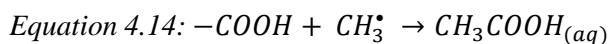
Adding 0.25 M glucose is seen to increase the erosion rate slightly over the background electrolyte to 2.9 ± 0.2 nm hr⁻¹. However, no significant change in corrosion rate is observed when the concentration is increased further to 0.5 and 1 M. It is interesting to note that on electrolysis all glucose solutions take on a deep caramel colour, suggesting that incomplete oxidation of glucose is occurring, resulting in glucose based polymeric species.¹⁵ It has been previously suggested that sugars can act as radical scavengers, reacting with the •OH giving rise to less reactive carbon centred radicals.^{16,17} With this in mind it is not entirely surprising that the addition of glucose to the effluent only gives a slight increase in corrosion rate, as the resultant radicals are weak, and likely incapable of reacting with the BDD surface.

Adding acetic acid results in a much larger change in the corrosion rate over the background electrolyte. Adding 0.25 M of acetic acid serves to increase the corrosion rate to 49.6 nm hr⁻¹, an increase of over 40 × from the background electrolyte alone. This measurement supports previous work suggesting that acetic acid causes significant corrosion to BDD anodes, even

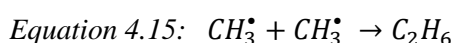
on relatively short timescales.^{4,6,18} The oxidation of acetic acid is thought to produce a number of organic radical intermediates, Equations 4.11 - 4.13.¹⁹



It has been previously hypothesised that the CH_3^\bullet is the species responsible for the high corrosion rates seen in acetic acid containing solutions.⁶ While no concrete mechanism has been proven in this work the original authors⁶ suggested that the CH_3^\bullet can abstract OH groups from the diamond surface, leaving carbon radicals behind.⁶ However, this hypothesis doesn't align with the work of Chaplin et. al.⁹. We would instead suggest that the CH_3^\bullet could replace the $\bullet\text{OH}$ in equation 4.10, giving rise to equation 4.14, with acetic acid as a product.



When the concentration of acetic acid is increased to 0.5 M the corrosion rate increases further to 58.0 nm hr⁻¹, however when the concentration is increased further (1 – 2 M) the corrosion rate decreases reaching 12.5 nm hr⁻¹ at 2 M. This decrease in corrosion rate provides further evidence for involvement of a radical species, as radical recombination (Equation 4.15), is a key termination mechanism for radical reactions.¹⁹ As the concentration of acetic acid in solution increases the concentration of CH_3^\bullet near the electrode surface will also increase, leading to an increased prevalence of Equation 4.15, which will ultimately reduce the number of CH_3^\bullet available to corrode the BDD surface.



The rate of erosion dropping dramatically with increasing concentration of acetic acid is a significant finding. Acetic acid is widely used in the manufacture of vinyl plastics, adhesives, paints, and textiles, and had a global demand of 6.5 million tons in 2014.²⁰ Due to this widespread use acetic acid (and other organic acids) are often a major component of industrial wastewater and must be removed before discharge back into a water system. Previous literature has suggested that BDD-EAOs are unsuitable for this task, due to the high rate of corrosion, however here we demonstrate that provided the concentrations are sufficiently high the corrosion rate may be low enough that these systems could be employed for these applications.

4.3.5 Current Density

It has been widely suggested that running EAO systems at lower current densities reduces the rate of corrosion seen at the anode however, to the authors knowledge this has never been shown experimentally.^{6,9} While reducing the current density might seem to be an obvious solution to reduce corrosion at the BDD electrodes the current passed through the electrode directly affects the amount of waterborne contaminant removed. As a result, reducing the current density reduces the effectiveness of contaminant removal, in turn reducing the usefulness of the system, unless larger electrodes are used. The effect of current density on erosion rate in a solution of 1 M acetic acid with 0.5 M K₂SO₄ present is summarised in Figure 4.5. An acetic acid containing solution was used to exacerbate the differences in corrosion rate to make it easier to measure differences the corrosion rate. Current densities were selected so as to centre around the 10,000 A m⁻² value chosen for the other experiments, whilst maintaining a wide range of current densities.

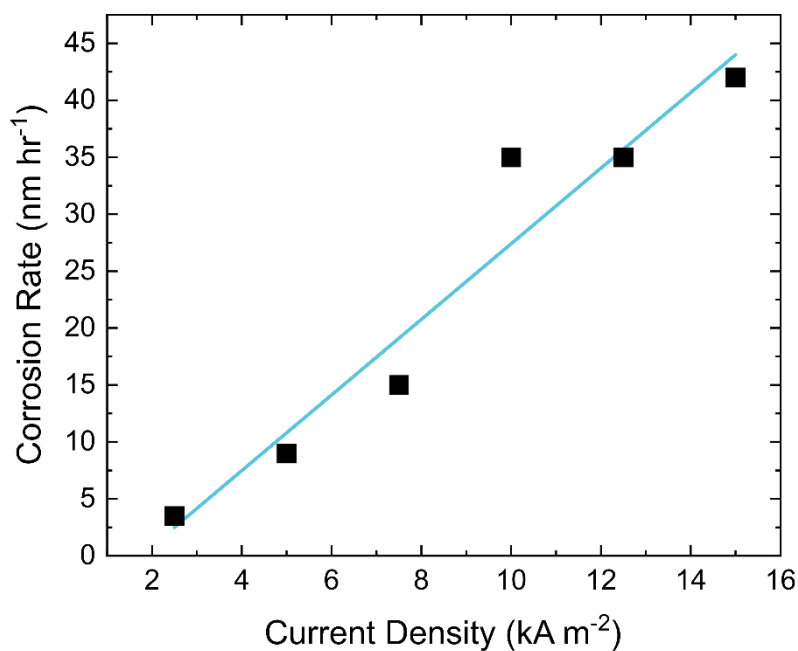


Figure 4.5: Corrosion rates seen during a 72-hour electrolysis at in a solution of 1 M acetic acid and 0.5 M K₂SO₄ at current densities from 2,500 to 15,000 A m⁻².

As expected from the literature,^{6,9} the BDD corrosion rate increases approximately linearly ($R^2 = 0.935$) with current density, indicating there is no significant change in the reactions happening at the electrodes surface as the current density is increased. At higher current densities the rate of water oxidation must increase to pass the additional current, producing more radicals. The rate of Equation 4.10 will increase as a result, ultimately increasing the rate of corrosion. A linear increase in corrosion rate is also unsurprising given that even the

lowest current density ($2,500 \text{ A m}^{-2}$) requires a potential of $\sim 8 \text{ V}$ to be applied between the electrodes, which is already well into water oxidation processes on BDD. Understanding the effect of current density is important for evaluating how appropriate a BDD-EAO system is for a particular application.

Returning to the erosion rate of thin-film BDD as discussed in section 4.3.3, it was demonstrated that thin-film material eroded about 30 times faster than EP-BDD, whilst being about 10% of the cost by area.^{21,22} If the trend in corrosion rate seen for freestanding material holds for thin-film, you would need a thin-film electrode with an area $7.5\times$ larger than its freestanding equivalent to have comparable corrosion rates whilst maintaining the same advanced oxidation ability. This thin-film electrode would have an initial start-up cost of 75% of the cost of freestanding BDD, and a much shorter lifetime of 300 hours (assuming a BDD thickness of $15 \mu\text{m}$), compared to $450 \mu\text{m}$ thick freestanding BDD which would last for over 250,000 hours in a solution of $0.5 \text{ M K}_2\text{SO}_4$.

4.3.6 Polarity Switching

In commercial EAO systems it is common to switch the potential so that the opposite electrode acts as the anode.¹³ Polarity switching is employed in order to minimise fouling and equalise electrode wear by having all the electrodes act as the anode half the time. Alternating cathodic polarisation could serve to increase the rate of anodic wear by changing the surface structure, such as switching the surface termination from H to O or *vice versa*.^{3,9} To investigate if the rate of polarity switching affected the rate of anodic corrosion experiments were conducted with switching intervals of 6 to 600 s, Figure 4.6. During this experiment each electrode spends 36-hours as the anode, so erosion rates are calculated based on a 36-hours of corrosion.

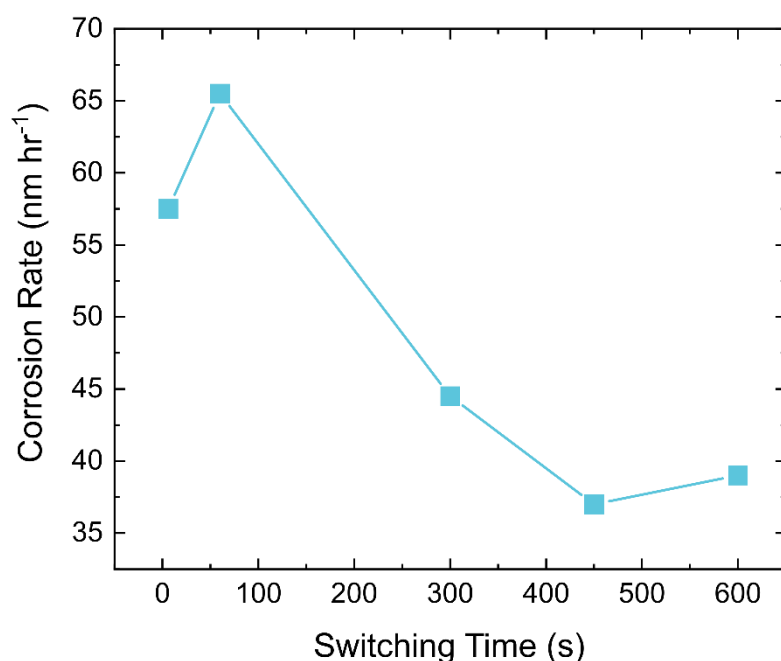


Figure 4.6: Average of the corrosion rates of both electrodes measured after a 72-hour electrolysis at $10,000 \text{ A m}^{-2}$ in a solution of 1 M acetic acid and 0.5 M K_2SO_4 . Switching intervals of 6, 60, 300, 450, and 600s were tested.

When the switching interval is decreased from 450 to 60s the average corrosion rate of both electrodes increases, almost doubling over this range. For switching frequencies of 450 and 600s the corrosion rate is similar to that of a 72-hour electrolysis with no switching (35 nm hr^{-1}). For the majority of switching intervals both electrodes have eroded evenly, with very similar erosion rates for both electrodes (Table 4.2).

Table 4.2: Corrosion rates for each electrode and the mean average of both for switching intervals of 6 to 600s in a solution of 1 M acetic acid and 0.5 M K_2SO_4 .

Switching Time (s)	Erosion Rate Electrode 1 (nm hr^{-1})	Erosion Rate Electrode 2 (nm hr^{-1})	Mean Erosion Rate (nm hr^{-1})
6	70	45	58
60	64	67	66
300	45	44	45
450	36	48	37
600	36	42	39

For a switching interval of 6s the wear on the electrodes is very uneven with one electrode showing an average depth of 2,500 nm for the corroded region and the other showing an average depth of 1,728 nm after the 36-hours that each spent as the anode. The origins of this

uneven erosion are unknown but may be due to limitations of the electronics used to switch polarity.

Regardless, this data demonstrates that alternating cathodic polarisation serves to increase the corrosion rate of the BDD electrode at switching intervals shorter than 450 s. It has been demonstrated that cathodic polarisation can convert surface termination from C-O to C-H_x functionality.¹⁰ This increase in C-H_x functionality could then serve to increase the prevalence of sp² carbon creation (equations 4.2 to 4.7) on the surface of the BDD, on its return to anodic polarisation. It has also been shown that severe cathodic polarisation can increase the conductivity of the BDD surface by sub-surface incorporation of hydrogen atoms.^{3,10} This increase in surface conductivity may also serve to increase the corrosion rate, as has been shown previously for heavily boron doped crystal facets versus less doped facets.⁶

Beyond the fundamental understanding this data also has significance for systems deployed in the field. It suggests that BDD-EAOs can continue to switch polarity to even out electrode wear and reduce fouling without concerns over increased electrode corrosion, provided the switching interval is more than 450s.

4.3.7 Perfluorooctane Sulfonic Acid

Perfluorooctane sulfonic acid (PFOS) and perfluorooctanoic acid (PFOA) are perfluorinated compounds (PFCs) which together account for the majority of environmental PFC contamination.²³ PFCs are utilised in a number of industries, including metal plating, semiconductors, household goods, and firefighting foams.^{23,24} The stability of the carbon-fluorine bonds results in these PFCs being extremely resistant to thermal or biological breakdown.²³ The absence of natural methods of environmental breakdown has resulted in the PFCs released into the environment accumulating to levels where they can pose a risk for human health.²³⁻²⁸ To date electrochemical advanced oxidation (on BDD electrodes) is the only advanced oxidation process that has shown promise in destroying these compounds.²⁴ While some other process begin to break down the PFCs, they simply produce other difficult to treat perfluorinated organic acids.²⁴ Given the importance of BDD-EAO for the removal of these compounds from industrial waste the effect of PFOS presence on BDD electrode corrosion rates was investigated.

A solution of the potassium salt of perfluorooctane sulfonate (PFOS-K) was made up to its saturation point (680 mg L⁻¹, ~ 1.25 mM) in 0.5 M K₂SO₄ and a 72-hour electrolysis at 10,000 A m⁻² performed. Surprisingly, during this electrolysis the BDD anode eroded less than it would have during an electrolysis of the background electrolyte (0.5 M K₂SO₄) alone. The amount of material removed was too small for the step to be measured by WLI, but the

roughness in the centre of the electrode (8.5 nm RMS) was found to be similar to that seen after electrolysis in a solution of KNO_3 . To our knowledge there is no evidence in the literature of species reducing the corrosion rate of BDD electrodes, so the origin of this decrease is currently unclear. However, the data bodes well for using BDD to remove PFOS from solutions. It may well be that the PFOS is acting as a highly effective radical sink, even at these low concentrations, preventing the generation or reaction of sulphate radicals from the electrolyte.

4.4 Conclusions

In this chapter the effect on corrosion rate of several solution and operational parameters for a BDD-EAO system have been tested. We have developed and demonstrated a methodology, utilising interferometry, to directly measure the amount of material removed, accurately, during BDD anode corrosion. This method could now be used to evaluate the suitability of a BDD-EAO system for any effluent system.

The effect of both common salts (KNO_3 , KCl , and K_2SO_4) and organic species (glucose and acetic acid) on corrosion rate were investigated. Changing common salt supporting electrolyte was found to have a slight effect on the rate of corrosion. However, organic content, in particular acetic acid, was shown to have a much more significant effect, with acetic acid showing the highest corrosion rate of any of the chemical species investigated.

Operational parameters such as current density and the frequency of polarity switching were also investigated. We provided further evidence that the long-held belief that the rate of corrosion is linear with current density was correct between 2,500 and 15,000 A m^{-2} , in solutions containing acetic acid and K_2SO_4 . We also investigated the effect of changing the frequency of polarity switching and showed that for switching frequencies slower than 8 minutes there was no meaningful increase in erosion rate. This is a significant finding as polarity switching is thought to be important for equalising electrode corrosion and reducing fouling.

Finally, corrosion rates for different BDD materials were investigated with a view to gaining understanding of the mechanism. In particular the corrosion rates of electroprocessing grade BDD, electroanalytical grade BDD and thin-film BDD were investigated. These experiments demonstrated that surface morphology is an important parameter to consider with different corrosion rates seen for all three materials. This data also raises questions about the suitability of thin-film BDD, which eroded thirty times faster than electrochemical processing grade BDD, for long-term electrochemical advanced oxidation applications.

4.5 References

- 1 B. P. Chaplin, *Environ. Sci. Process. Impacts*, 2014, **16**, 1182–1203.
- 2 A. De Battisti and C. A. Martínez-Huitle, in *Electrochemical Water and Wastewater Treatment*, 2018, pp. 119–131.
- 3 M. C. Granger and G. M. Swain, *J. Electrochem. Soc.*, 1999, **146**, 4551.
- 4 M. Panizza, G. Siné, I. Duo, L. Ouattara and C. Comninellis, *Electrochem. Solid-State Lett.*, 2003, **6**, 17–19.
- 5 N. Katsuki, E. Takahashi, M. Toyoda, T. Kurosu, M. Iida, S. Wakita, Y. Nishiki and T. Shimamune, *J. Electrochem. Soc.*, 1998, **145**, 2358–2362.
- 6 T. Kashiwada, T. Watanabe, Y. Ootani, Y. Tateyama and Y. Einaga, *ACS Appl. Mater. Interfaces*, 2016, **8**, 28299–28305.
- 7 X. R. Lu, M. H. Ding, C. Zhang and W. Z. Tang, *Thin Solid Films*, 2018, **660**, 306–313.
- 8 F. C. I. Catalan, N. Hayazawa, Y. Yokota, R. A. Wong, T. Watanabe, Y. Einaga and Y. Kim, *J. Phys. Chem. C*, 2017, **121**, 26742–26750.
- 9 B. P. Chaplin, D. K. Hubler and J. Farrell, *Electrochim. Acta*, 2013, **89**, 122–131.
- 10 H. Girard, N. Simon, D. Ballutaud, M. Herlem and A. Etcheberry, *Diam. Relat. Mater.*, 2007, **16**, 316–325.
- 11 Element Six Ltd., *DiafilmTM EP A solid solution for sanitising and electrochemical processing*, 2020.
- 12 L. A. Hutton, J. G. Iacobini, E. Bitziou, R. B. Channon, M. E. Newton and J. V. Macpherson, *Anal. Chem.*, 2013, **85**, 7230–7240.
- 13 *DiamoxTM An on-site electro-oxidation solution for the toughest of wastewaters transforms wastewater treatment*, 2020.
- 14 T. Kolber, K. Piplits, R. Haubner and H. Hutter, *Fresenius. J. Anal. Chem.*, 1999, **365**, 636–641.
- 15 A. Golon and N. Kuhnert, *J. Agric. Food Chem.*, 2012, **60**, 3266–3274.
- 16 A. Matros, D. Peshev, M. Peukert, H. P. Mock and W. Van Den Ende, *Plant J.*, 2015, **82**, 822–839.

- 17 B. C. Gilbert, D. M. King and C. B. Thomas, *J. Chem. Soc. Perkin Trans. 2*, 1981, 1186.
- 18 T. Sumi, T. Saitoh, K. Natsui, T. Yamamoto, M. Atobe, Y. Einaga and S. Nishiyama, *Angew. Chemie Int. Ed.*, 2012, **51**, 5443–5446.
- 19 A. Kapalka, B. Lanova, H. Baltruschat, G. Fóti and C. Comninellis, *J. Electrochem. Soc.*, 2008, **155**, E96.
- 20 K. D. Patil and B. D. Kulkarni, 2014, **1**, 13–18.
- 21 E6 Webshop, <https://e6cvd.com/us/application/electrochemistry.html>, (accessed 23 April 2022).
- 22 CONDIAS DIACHEM, <https://www.condias.de/en-gb/products/DIACHEM®-Electrodes>, (accessed 23 April 2022).
- 23 P. Zareitalabad, J. Siemens, M. Hamer and W. Amelung, *Chemosphere*, 2013, **91**, 725–732.
- 24 K. E. Carter and J. Farrell, *Environ. Sci. Technol.*, 2008, **42**, 6111–6115.
- 25 J. M. Conder, R. A. Hoke, W. De Wolf, M. H. Russell and R. C. Buck, *Environ. Sci. Technol.*, 2008, **42**, 995–1003.
- 26 F. Fàbrega, V. Kumar, M. Schuhmacher, J. L. Domingo and M. Nadal, *Toxicol. Lett.*, 2014, **230**, 244–251.
- 27 E. D. Van Asselt, R. P. J. J. Rietra, P. F. A. M. Römken and H. J. Van Der Fels-Klerx, *Food Chem.*, 2011, **128**, 1–6.
- 28 E. D. Van Asselt, J. Kowalczyk, J. C. H. Van Eijkeren, M. J. Zeilmaker, S. Ehlers, P. Fürst, M. Lahrssen-Wiederholt and H. J. Van Der Fels-Klerx, *Food Chem.*, 2013, **141**, 1489–1495.

Chapter 5: The Importance of Stable Non-Diamond Carbon in Electrochemical Generation of Ozone using Boron Doped Diamond Electrodes

5.1 Introduction

Ozone is a highly oxidising molecule capable of existing in the gas or dissolved phase, with applications including sterilisation and sanitisation,¹ deodorisation,² and decolourisation.³ One of the chief advantages of using ozone over other oxidisers is the absence of harmful residues. Most commonly ozone is employed in water treatment industries where it is used to remove contaminants in the treatment of both waste and drinking water, via oxidation to harmless products.^{4,5} However, due to the limited half-life in water of ca. 20 minutes,⁴ ozone must be generated in-situ.

Traditionally ozone is generated in the gas phase using corona discharge, wherein a high voltage is applied between two electrodes with an oxygen containing gas between them.⁶ This high energy pulse creates single oxygen atoms, which can recombine to form ozone. While this method has several drawbacks, not limited to its high energy use and prohibitively expensive initial set-up cost, the most significant drawback is that gas phase generation requires the ozone gas to be dissolved into the water to be treated post-production before it can be useful. This also prevents the safety concerns related to the inhalation of ozone when using gas-phase ozone generators, as the ozone is never present in the gas phase when generated with EOP.

Studies have tackled how to optimise electrochemical ozone production (EOP), focusing mainly on electrode geometry, water flow rate and temperature and non-diamond carbon (NDC) content of the BDD electrodes.⁷⁻¹¹ For those studies employing freestanding BDD it was found that the hole geometry, in particular the edge length of the hole (or in their particular case slot) was closely linked to EOP output. A significant increase in EOP output and current efficiency was seen with increased edge length.⁷ Finally, the surface of the BDD electrode has been debated in the EOP literature. Early literature commented on the preferred use of a pure sp^3 bonded diamond surface.^{7,8} However, more recent experimental work found that non-diamond carbon impurities (here referred to as sp^2 bonded) present in the BDD could increase ozone output.^{9,12} However, this work emphasised the importance of keeping the fraction of sp^2 bonded carbon impurities low in order to retain the durability of the electrode and maintain the structural stability of the BDD thin film employed, grown on a perforated silicon support substrate.¹² For these studies,¹² the sp^2 bonded carbon was introduced, both into the bulk and surface of the BDD, by varying the boron to carbon feedstock ratio from 0.1 % to 5%, during

chemical vapour deposition (CVD). As both boron concentration and sp^2 bonded carbon content were varied at the same time, it was also difficult to account for the impact of a changing material conductivity (from varying the boron concentration) in the results obtained.

In this chapter the role of NDC in EOP is explored in greater detail, given that proposed EOP mechanism¹³ suggests that very weakly bound radicals¹⁴ are not appropriate for optimising ozone output, as discussed previously in Chapter 1, Section 1.7.2. However, it is important that any NDC introduced to the BDD surface is also durable and robust under the EOP operating conditions. Recently it has been shown that ns laser micromachining of a BDD surface results in the formation of non-diamond carbon (NDC).¹⁵ This surface NDC seems to consist of approximately 50 nm of graphite, oriented perpendicular to the diamond surface, capped with ~ 5 nm of amorphous carbon. As discussed in Chapter 1, Section 1.4.2, the NDC is shown to be chemically resistant to the strong acid cleaning treatment (discussed in Chapter 2, Section 2.3.2) using high resolution transmission electron microscopy (TEM)¹⁵ and electrochemical measurements and exposure to strongly alkaline solutions (via electrochemical measurements).¹⁶ By using the laser micromachining system to define the holes (or slots) in the BDD electrode surface, the inner walls of the holes will be coated in a layer of NDC. In this way it is possible to both change the electrode geometry and create defined but variable NDC to sp^3 bonded carbon ratios for investigation of the effect this has on EOP.

5.2 Experimental Methods

5.2.1 Cell Design and Construction

Fusion 360 (Autodesk, USA) was used to design the EOP cell bodies. Each cell design comprises of two separate half cells whether operating with perforated or solid electrodes. The half-cells were 3D printed using a Form 3 (FormLabs) and UV polymerising clear polymethylmethacrylate (PMMA) resin (FormLabs Standard Clear, FormLabs), as discussed in Chapter 2, Section 2.6. The support material was then removed, and the mating faces polished using CarbiMet paper (Buhler, USA) until flat. Electrodes were adhered to the recess in each half-cell using UV resin (FormLabs Clear, FormLabs). Silver epoxy (Conductive Epoxy, CircuitWorks, Chemtronics) was used to make electrical contact to the electrode contact. The resulting half-cells are identical and are labelled A and B. For renders of the planar and perforated cell designs see Figures 5.2 and 5.3 respectively. Each half cell can serve as either the anode or cathode. Before cell testing, electrodes were polished with alumina microparticles (0.05 μm , Buehler, Germany) on a wetted microcloth pad (Buehler), and then on a wetted alumina-free microcloth pad. For a tight seal, elastomeric 3D printed gaskets

(FormLabs Elastic 50A, FormLabs, USA) were placed into the recess on each half-cell to seal around a Nafion membrane (Nafion 424 reinforced with poly(tetrafluoro-ethylene) fibre, 0.33 mm, Sigma-Aldrich), which was placed between the half cells before bolting them together. There are two embodiments of EOP cells used in this work, one set with perforated electrodes and the other with perforated Nafion both of which are discussed in more detail later in this chapter.

5.2.2 Planar Electrode Creation

Planar electrodes were machined as 10 mm diameter disks from a freestanding polycrystalline electroprocessing grade¹⁷ BDD wafer polished on the growth face to ~nm roughness and lapped on the nucleation face to ~500 nm with an overall thickness of 357 μm using a 355 nm Nd:YAG 34 ns laser micromachining system (E-355H-ATHI-0 system, Oxford Lasers). To incorporate controlled amounts of NDC the electrodes were laser machined in defined locations using a 532 Nd:YAG 15 ns laser micromachining system (A-Series, Oxford Lasers) with a fluence of $\sim 30 \text{ J cm}^{-1}$. The electrodes were machined with parallel single beam width (20 μm) stripes crossing the entire electrode, the spacing of which was used to define the amount of the surface ablated. The spacing of the lines was decreased in order to increase the amount of NDC integrated into the surface. After cutting the electrodes were acid cleaned and contacted as described in Chapter 2, Section 2.3.2. The machined surfaces were also characterised with white light interferometry (WLI) Figure 5.1, to understand the roughness, area and structure of the surface (Table 5.1). The 100% electrode was machined so as to leave none of the original BDD surface, while retaining a similar grooved structure to the other electrodes.

The NDC proportions for these planar electrodes are calculated using the WLI measurements presented in Figure 5.1. The width of the regions of unchanged surface were compared to the width of the machined regions to calculate the NDC proportion.

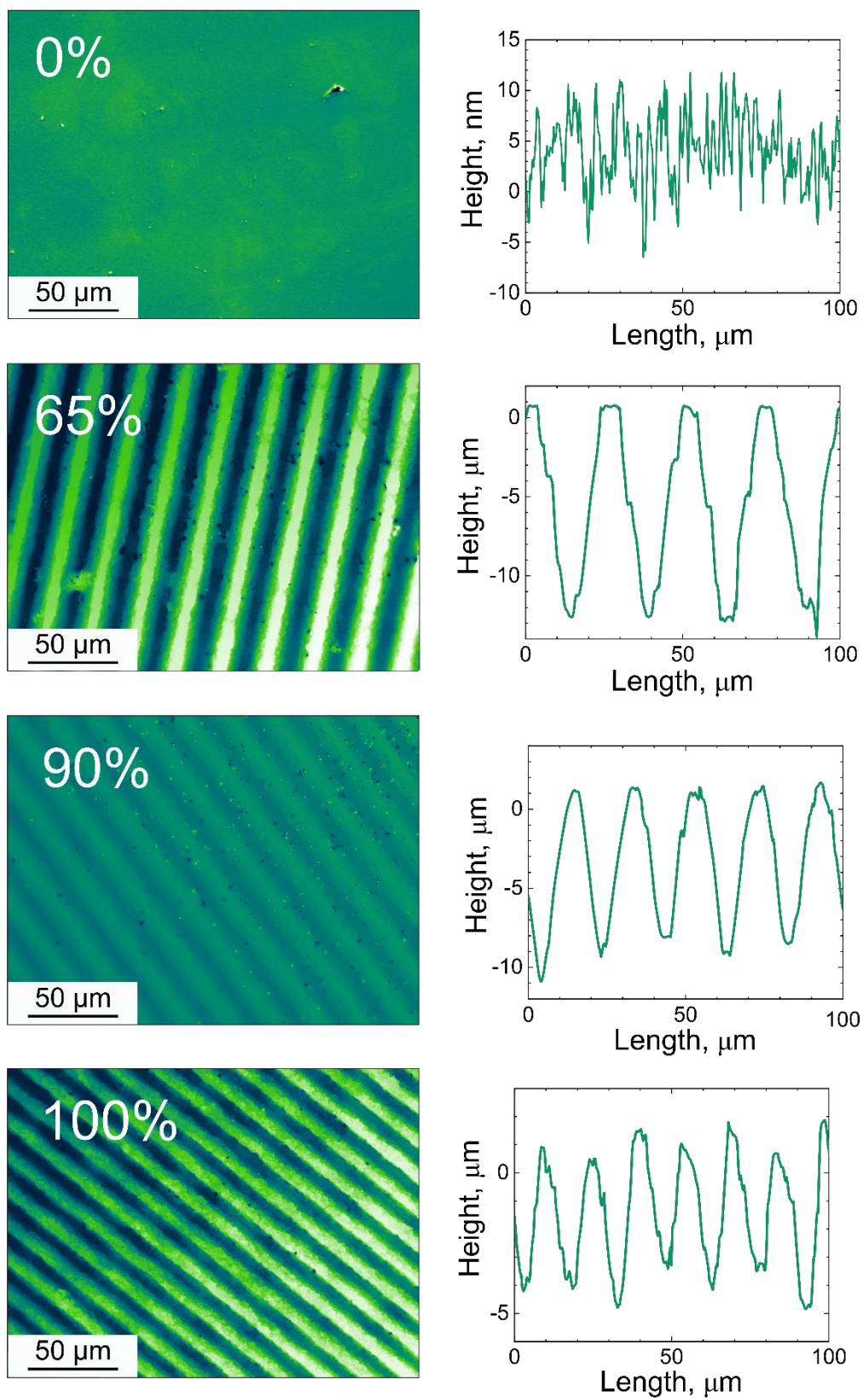


Figure 5.1: Left, white light interferometry images of the planar electrode surfaces. Right, surface profiles showing the surface structure.

Table 5.1: RMS roughness and area of each planar electrode design.

Cell Name	Roughness (RMS)	Electrode Area (cm ²)
0%	7.8 nm	0.79
65%	5.1 μ m	1.58
90%	4.5 μ m	2.20
100%	2.3 μ m	1.32

5.2.3 Planar Electrode Cell Assembly

The planar electrode half-cell comprises a recess for the planar electrode, 3D printed gaskets, a 6 mm diameter brass contact, and perforated Nafion to allow solution flow across the front face of the electrode as shown in Figure 5.2. The perforated Nafion membrane was designed to cover approximately half of the total electrode area in 1.3 mm wide bands to create a flow path between the electrodes. The design was cut into the Nafion with a CNC knife cutter (Maker, Cricut, USA) using a point knife tool.

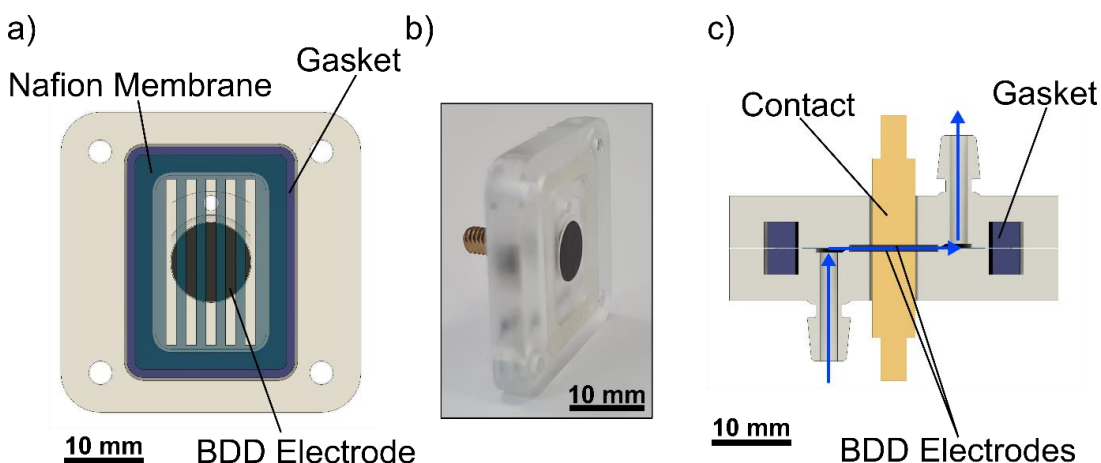


Figure 5.2: a) Render showing an internal view of one planar electrode half-cell with key components labelled. b) Photograph of the half-cell, showing the electrode, seal, and contact. c) Render of the full cell cross section, with blue arrows denoting the flow path through the cell.

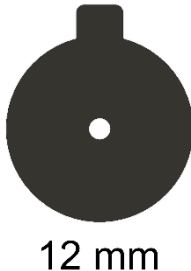
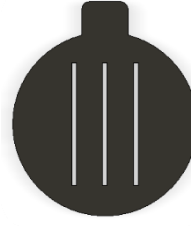
5.2.4 Perforated Electrode Creation

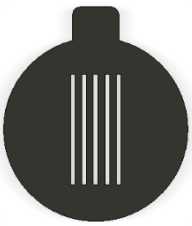
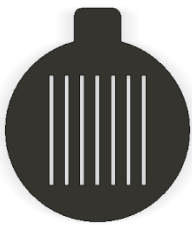


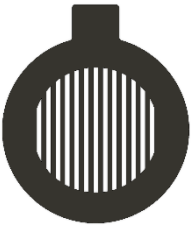
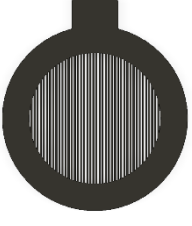
The perforated electrodes were machined from a freestanding as grown polycrystalline electroprocessing grade, BDD wafers (200, 320, 420 or 700 μ m thickness) using a 355 nm Nd:YAG 34 ns laser micromachining system (E-355H-ATHI-0 system, Oxford Lasers). The growth-face of the as-grown wafer had a roughness of ~ 15 μ m RMS, while the nucleation face roughness was ~ 100 nm RMS, both measured using WLI.

The trepan system was used to widen the laser spot diameter to 50 μm in order to make the cut trench wider. Electrodes were cut using two passes with a fluence of 760 J cm^{-1} per pass. BDD was cut into rounds of different 12 mm diameters with a 3×2 mm tab for electrical contacting. Through holes of different geometries were cut from the central region. The nucleation face of the contact tab was laser-roughened with a fluence of 20 J cm^{-2} as discussed in Chapter 2, section 2.3.1.

To calculate the NDC proportion and areas of the perforated electrode the face of the BDD that is pressed in contact with the Nafion membrane is considered solution excluded. The solution accessible areas, which are taken as the accessible electrode area, are the wetted (back) face area plus the areas of the flow-through slots machined (and thus containing NDC) in the BDD. The proportion of NDC is expressed as a ratio of the laser micromachined areas (i.e. the internal walls of the slot) to the solution accessible area (wetted back face plus internal slot area). It is acknowledged that this is likely an underestimate, as it fails to account for any NDC inherent in the BDD as a result of the CVD growth process, however this is likely to be minimal compared to the amount introduced by laser micromachining.

Table 5.2: Comparison of electrode areas, NDC proportion and geometries. Electrodes of the same geometry as the 70% are also used in Figures 5.9, 5.10, and 5.13.

Proportion of NDC (%)	Description of Geometry	Solution Accessible Area (cm^2)	Schematic of Electrode
5	1.4 mm Diameter Hole	0.57	
30	300 μm Slots	0.71	

40	300 μm Slots	0.78	
50	300 μm Slots	0.86	
60	600 μm Slots	0.67	
69	400 μm Slots	0.85	
70	300 μm Slots	1.01	
80	100 μm Slots	1.51	

5.2.5 Glassy Carbon Electrode Creation

Glassy carbon (GC) electrodes were cut from 400 μm thick SIGRADUR G (HTW, GmbH, Germany) GC was cut into the geometry of the 70% NDC BDD electrodes using the same laser parameters. GC electrodes were not acid cleaned or given a metal contact after cutting.

5.2.6 Perforated Electrode Cell Assembly

The perforated electrode half-cell comprising perforated electrodes contains a recess to accommodate a BDD electrodes, a 3D printed gasket, slot for a copper tab contact and a channel for solution flow across the backside of the electrode, as shown in Figure 5.3. A close-up schematic of the expected flow profile can be found in Figure 5.3d. For perforated electrode cells a 2 cm diameter round of reinforced Nafion membrane was used. In the case of the perforated electrode cell the Nafion separates the anode and cathode chambers, resulting in a two-compartment electrochemical cell. As a result of this the products of each electrode can be kept separate, if desired. However, for the purposes of this work it was chosen to combine the products for ease of experimental set-up.

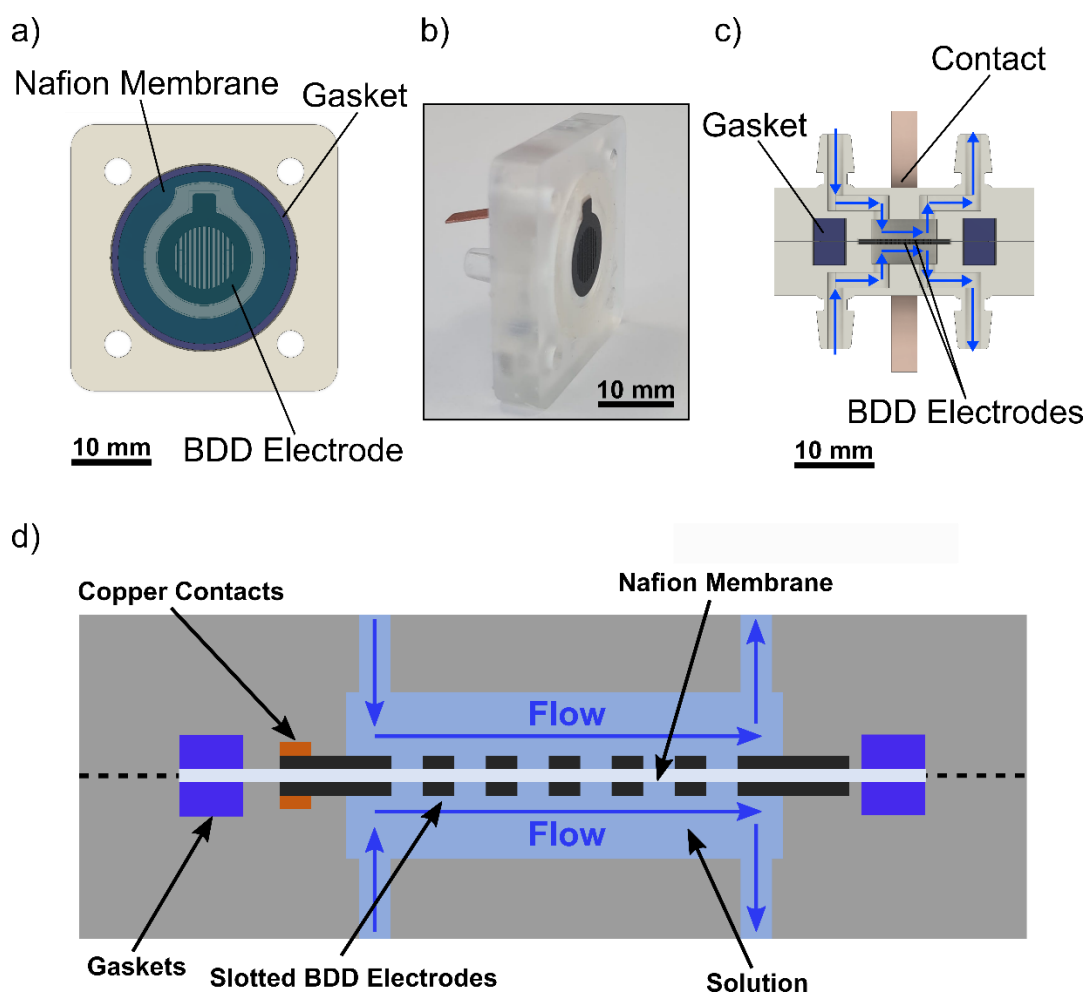


Figure 5.3: a) Render showing an internal view of one perforated electrode half-cell. b) Photograph of the half-cell. c) Render of the full cell cross section, with blue arrows denoting the flow path through the cell. d) Example flow profiles of the perforated electrode cell showing the BDD electrodes (Black), Nafion membrane (Light Grey), cell body (Dark Grey), copper contacts (Orange) and flow path (Blue).

5.2.7 Ozone Measurements

Ultrapure water (Milli-Q, resistivity $> 18.2 \text{ M}\Omega \text{ cm}^{-1}$) was flowed into the BDD ozone generation cell from a 1 L reservoir via a 6 V DC diaphragm pump (SC3701PW, Skoocom Electronic Co. Ltd.), at a rate of $\sim 200 \text{ ml min}^{-1}$ for the planar cell design ($\sim 330 \text{ ml min}^{-1}$ for the perforated cell design) as shown in Figure 5.4. A 2 ml aliquot was taken from the cell outflow when each required current was reached. The cell was galvanostatically operated with currents ranging from 0.1 to 0.6 A in 0.1 A increments were passed using a Voltcraft VLP-2602 OVP power supply (Voltcraft). Ozonated water aliquots (2ml) were collected after achieving stable potential readings (i.e. varying by no more than $\pm 0.1 \text{ V}$). Ozone

concentrations were determined by recording the absorbance in a Lambda 850 UV/Vis spectrometer (Perkin Elmer) and then using the Beer-Lambert law, Equation 5.1.¹⁸

Equation 5.1: $A = \epsilon c l$

Where A is the absorbance at 258 nm, ϵ is the extinction coefficient of ozone ($2900 \text{ M}^{-1} \text{ cm}^{-1}$),¹⁹ c the concentration of ozone in the aliquot, and l the optical path length (1 cm in a quartz cuvette, Hellma Analytics).

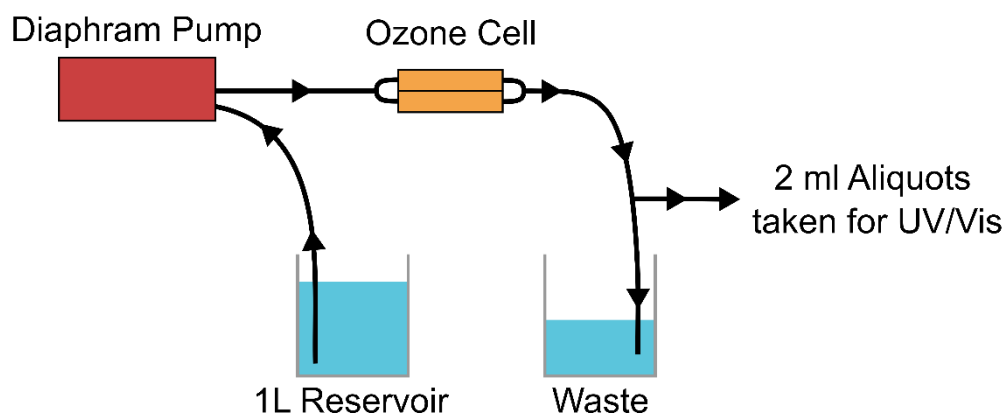


Figure 5.4: Schematic of the experimental set-up for ozone calibrations.

To hydrate and protonate the Nafion[™] membrane prior to use, one side of the cell was run at 0.6 (Perforated Electrodes) or 0.3 A (Planar Electrodes) for 5 minutes. The pre-treatment was first applied with the A side BDD electrode connected as the anode, before immediately recording the triplicate calibration of ozone output versus current with side A as the anode (and thus side B is the cathode). Then, the pre-treatment was applied again with the B side BDD electrode connected as the anode, before immediately recording the triplicate calibration with side B as the anode. The conditions selected gave a stable response between repeated calibrations, producing consistent current/voltage and current/ozone output data.

5.2.8 Long-Term Testing

For long term cell stability testing, the UV absorbance at 258 nm was recorded as a function of time over a 20 h continuous operation time period at a constant current of $\sim 0.3 \text{ A}$. Calibration triplicates were collected with electrode A and then B operated as the anode for ozone production before and after long term testing. A 10 L DI water reservoir was recirculated through the ozone cell using a diaphragm pump. Water from the reservoir flows through the ozone cell, exiting to a flow through cuvette (45FL; FireflySci) in the UV-vis system, through a home-built “ozone destroyer” system and then back into the 10 L reservoir,

Figure 5.5.²⁰ The “ozone destroyer system” consisted of a high surface area quartz tube system between two 254 nm UV lamps as at 254 nm dissolved ozone is converted to oxygen.²¹

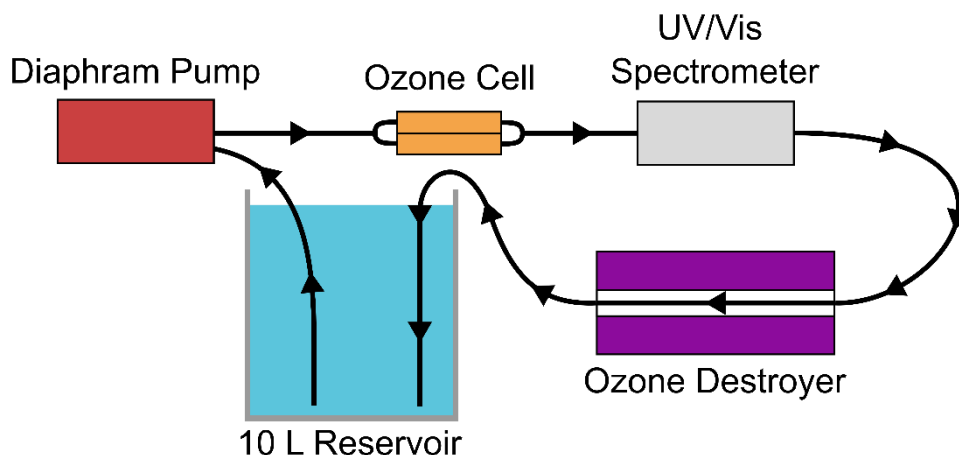


Figure 5.5: Schematic of the experimental set-up for long-term experiments.

5.2.9 Hydrogen Plasma Treatment

The BDD perforated electrodes were exposed to hydrogen plasma (as grown faces first followed by the nucleation faces) prior to incorporation into the cell. The treatment was performed in a Carat Systems SDS6U microwave plasma chemical vapour deposition (MPCVD) system on a molybdenum holder. The microwave power and pressure conditions were 5.5kW and 85 torr respectively. The gas flow was maintained at 300 sccm of H₂ supplied by a F-DGSi COSMOS.MF.H2.1000 hydrogen generator. The power and pressure in the system was ramped up in 2.5 minutes under a hydrogen atmosphere followed by a hold time of 90 minutes at the set conditions. At the end of the 90 minutes, the power and pressure in the chamber was slowly ramped down in 3 minutes under hydrogen atmosphere. Including the ramp up and ramp down time the total exposure time of the electrodes is 95.5 minutes for each side.

5.3 Results and Discussions

5.3.1 Measurement Metrics

Electrolytic Ozone Production Gradient: The EOP gradient (ppm A⁻¹) is calculated by applying a least-squares linear fit of the applied current (in A), x axis, vs. measured ozone concentration (in ppm), y axis, for three repeats. Ozone concentration was measured over a constant current range of 0.1 to 0.6 A in 0.1 A increments for all cells.

Area Normalised Electrolytic Ozone Production Gradient: The area-normalised EOP gradient (A cm⁻² ppb⁻¹) is calculated by applying a least-squares linear fit of the applied current density

(in A cm⁻²), y axis, vs. measured ozone concentration (in ppb), x axis, for three repeats. Ozone concentration was measured over a constant current range of 0.1 to 0.6 A in 0.1 A increments for all cells. Due to the different electrode geometries investigated, it is necessary to normalize the applied currents with respect to the solution accessible area of the electrode for ease of comparison. The steeper the gradient the more area and current efficient the electrode is at producing ozone.

Current Efficiency: Current efficiencies (ε) were calculated using Equation 5.2:

$$\text{Equation 5.2: } \varepsilon = 2 \times \frac{100 \times n F v C}{i}$$

Where n is the stoichiometric number of electrons transferred, F is the Faraday constant in C mol⁻¹, v is the solution flow rate in L s⁻¹, C is the concentration of dissolved ozone in mol L⁻¹, and i is the applied current in A.^{7,20} Current efficiencies were calculated for all points on the calibration curve. The highest value, for all current efficiencies calculated, was chosen as the peak current efficiency, consistent with the current literature approach.^{7,8,20,22}

In previous literature, some EOP cells have been operated with each side of the membrane as a separate compartment, where the anode products (i.e. ozone) are separated from the cathode products.^{7,22} Whilst our perforated electrode cell can deliver cathode/anode products in isolation, all data discussed herein was collected by combining the flow streams for anode and cathode, due to a more facile set-up. Combining flow streams dilutes the maximum ozone output of the perforated electrode cells two-fold. A factor of two was therefore introduced into the current efficiency equation to account for the fact that the ozone concentration from the anode is diluted. In the planar electrode cell, products cannot be separated, and thus to calculate current efficiency for these cells Equation 5.1 is used without the two times multiplier.

5.3.2 The Effect of NDC Incorporation into Planar Electrodes

Whilst most previous BDD-EOP cell designs use perforated electrodes sandwiched between a Nafion membrane this design presented some issues for our initial investigations. Chief among these issues is that electrode area, hole size (and by extension amount of NDC), and the amount of Nafion membrane exposed to solution are all intrinsically linked. Therefore, to investigate the effect of NDC incorporation while inducing minimal changes in the electrode design a novel ozone generation cell designed to utilise planar electrodes was developed. In this cell, the Nafion membrane rather than the electrodes is perforated to provide a path through the cell for solution while the BDD electrodes are solid disks, which are then patterned to incorporate NDC. Electrodes were patterned with NDC in a 10 μ m wide strips by laser

ablation, with the spacing between strips acting to control the proportion of the electrodes surface patterned with NDC. This results in electrodes with varying NDC proportions which are homogenous on the macroscale. The ozone output and current efficiency as a function of NDC proportion (calculated geometrically) for these electrodes was also determined (Figure 5.6).

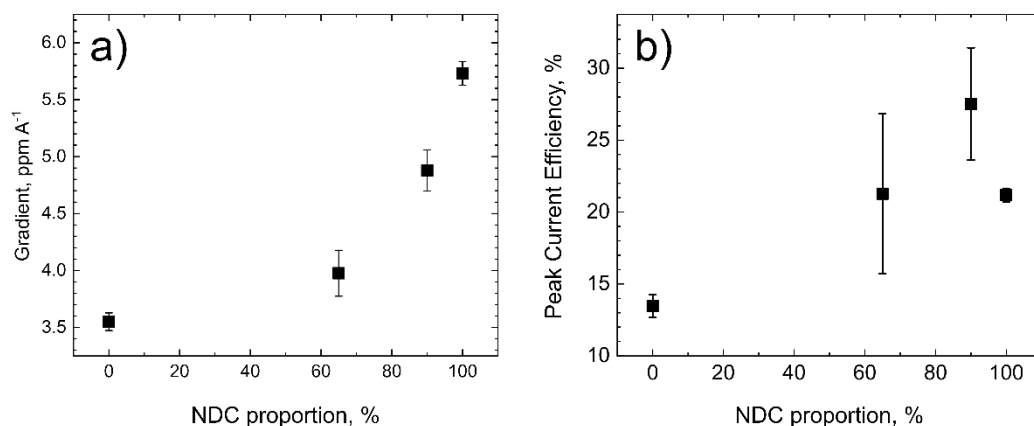


Figure 5.6: a) EOP gradient in ppm A⁻¹ versus the deliberately incorporated solution accessible NDC fraction of the planar BDD electrodes. b) Peak current efficiency versus the solution accessible NDC fraction of the planar BDD electrodes. The potentials, ozone output, current efficiency, EOP gradient, and adj-R² for these data points can be found in the appendix, section A5.1.

Data on the planar electrodes revealed a clear increase in the ozone EOP gradient from 3.6 ppm A⁻¹ to 5.7 ppm A⁻¹ as the deliberately incorporated NDC proportion increased from 0 to 100%, demonstrating that the higher the % of NDC the more ozone is generated under the same conditions. The surface roughness and area alone cannot be the only factor here as the 90% NDC electrode is rougher, and therefore has a larger surface area than the 100% NDC electrode. The peak current efficiency versus NDC proportion increases from 0 – 90% NDC proportion, with the 90% electrode showing a current efficiency of 27.5% however the 100% electrodes then show a decrease in current efficiency.

As both NDC and BDD have high overpotentials for OER the origin of the increased ozone output and efficiency when NDC is present is unlikely to be due to decreased competition from the OER. If anything, the addition of NDC is likely to increase the prevalence of the OER. Instead, the observed improvements are thought to be related to the strength with which radicals are adsorbed onto the electrode's surfaces, a critical factor in a surface driven process such as ozone generation.

In Chapter 1 we discussed how the mechanism of EOP is driven by oxygen centred radicals bound to the electrode surface (Section 1.7.2, Equations 1.1 to 1.7). BDD electrodes are unique

in that oxygen centred radicals are known to be very weakly adsorbed on the electrodes surface,¹⁴ resulting in them being able to detach from the electrode with relative ease and react with species in solution.^{14,23} It is as a result of this property that BDD electrodes are widely studied for electrochemical advanced oxidation, where hydroxyl radicals are of critical importance. This radical detachment will result in a lower overall current efficiency as oxygen centred radicals can no longer contribute to either ozone production or OER and instead will react with solution components.

Conversely, oxygen centred radicals will be much more strongly adsorbed to regions of the electrode with integrated NDC, resulting in a higher concentration of adsorbed radicals, and ultimately producing more ozone, however this may be a double-edged sword. The lower current efficiency of the 100% electrode may be due to the high coverage of NDC resulting in many strongly bound O[•], decreasing the chances of them encountering two more O[•] radicals before evolution, making O₂ evolution more likely than O₃. Therefore, it seems like a mixed surface of NDC and sp³ BDD gives an optimum oxygen centred radical mobility for EOP.

5.3.3 The Effect of NDC Incorporation on Perforated Electrodes

Once the improvement in ozone generation with NDC proportion had been shown for the planar electrode system several perforated electrode designs with different proportions of NDC were fabricated and tested to more closely mimic the cells used in commercial BDD-EOP applications, the results of which can be seen in Figure 5.7. As these electrodes are of very different designs and areas it is no longer useful to compare just the ozone output and instead an normalised EOP gradient, which considers the solution accessible (active) electrode area was used.

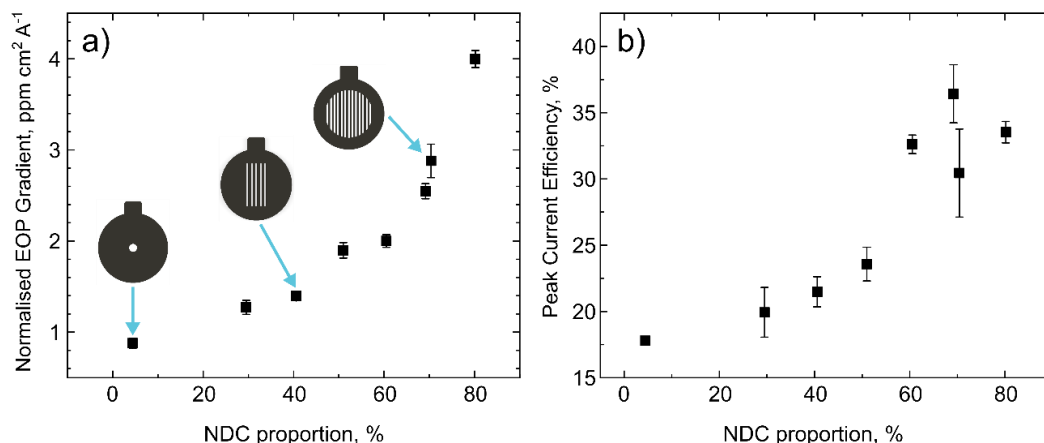


Figure 5.7: a) Normalised EOP gradient in ppm cm² A⁻¹ versus the solution accessible sp² fraction of the perforated BDD electrodes. b) Peak current efficiency versus the solution accessible sp² fraction of the perforated BDD electrodes. Insets, schematics of some electrode geometries, schematics of all geometries can be found in Table 5.2. The potentials, ozone output, current efficiency, EOP gradient, and adj-R² for these data points can be found in the appendix, section A5.2.

Increasing the NDC content from 5% to 60% serves to gradually increase the normalised EOP gradient, (0.88 to 1.99 ppm cm² A⁻¹) as seen in Fig. 5.7a. However, increasing the NDC ratio from 60% to 80% results in a much more rapid increase in normalised EOP gradient (1.99 to 4.00 ppm cm² A⁻¹). The trend in current efficiency, Figure 5.7b is similar, showing a slow increase from 5% to 50% NDC content (17.8% to 23.6%), with a steeper increase seen above 60% up to NDC to levels of 80%. This suggests that 60% NDC content is the critical ratio for building efficient perforated BDD-EOP flow cells. With perforated cells it is challenging to create electrodes with a higher than 80% NDC content by this route, as removal of the material to create the slots makes these electrodes fragile. Both normalised EOP gradient and current efficiency show that similar trends to those observed for the planar electrodes, demonstrating the importance of NDC also applies to this more commonly utilised perforated electrode design.

The best peak current efficiency demonstrated here (36% for the 69% sp² carbon electrode) is comparable with the work done by Arihara et.al on freestanding BDD electrodes where they reached a peak current efficiency of 47%.⁷ While our current efficiency is slightly lower, their work operated each half of the cell with a separate pump and used a much lower flow rate for the cathode as well as using a Pt cathode. If these electrodes were to be used in an application where the cells did not need to be moved the current efficiency could likely be improved by adopting a similar approach, or by recirculating a conductive electrolyte optimised for hydrogen evolution (such as strong acids) on the cathode side. Decreasing the temperature and

pH of the water in which the ozone is to be generated could also help to increase the concentration of ozone produced by extending the half-life of generated ozone.²⁴

Another route to forming high NDC content electrodes is to deliberately incorporate NDC into the material during CVD growth of the BDD electrodes.^{9,22} This approach is useful for thin-film BDD electrodes where a flow through structure is obtained by growing the BDD on a mesh support. However, as the NDC is incorporated throughout the material, it is limited to low NDC contents before the film becomes unstable, leading to concerns about an electrodes long term stability, a problem highlighted by Honda *et. al.*^{22,25}

5.3.4 Performance of a Glassy Carbon Electrode

It may seem like the obvious route to high NDC content electrodes is to use an entirely non-sp³ bonded carbon electrode material such as GC. Generally glassy carbon is formed by the pyrolysis of organic polymers, which retain much of their original structure through this process.²⁶ Some electron microscopy characterisation of the Sigradur G (HTW, Germany) glassy carbon has been conducted in the past,²⁷ this revealed a porous structure and the presence of layered fullerene like structures within the material. Although GC electrodes have previously been demonstrated for EOP, the electrodes had to be used in strong acids and internally cooled to reduce the rate of corrosion enough to have a useful lifetime.²⁸ Current efficiencies of up to 35% were seen at 0.6 A cm⁻², although the use of 7 M Fluoroboric Acid (HBF₄) as an electrolyte makes this system impractical for most applications of dissolved ozone. To get an idea of the lifetime of GC electrodes in our system a pair of GC electrodes geometrically identical to the 70% NDC BDD electrode were made. Glassy carbon electrodes were cut from a 300 µm thick sheet into an identical geometry to the 70% BDD electrodes using the same laser parameters. After cutting the electrodes weren't acid cleaned or sputtered, but cell assembly was performed in the same way. This GC electrode cell did not even preform a single calibration before the anode began to corrode, showing significant damage, likely due to the high potentials (typically 10 – 20 V across the calibration range) applied, Figure 5.8. This experiment demonstrates the robustness of the NDC introduced by lasering and acid cleaning into the BDD surface. It is also interesting to note that no ozone was generated during this experiment. These results using GC serve to reinforce our beliefs that the NDC formed on the surface of the BDD after laser cutting and acid cleaning is highly stable.

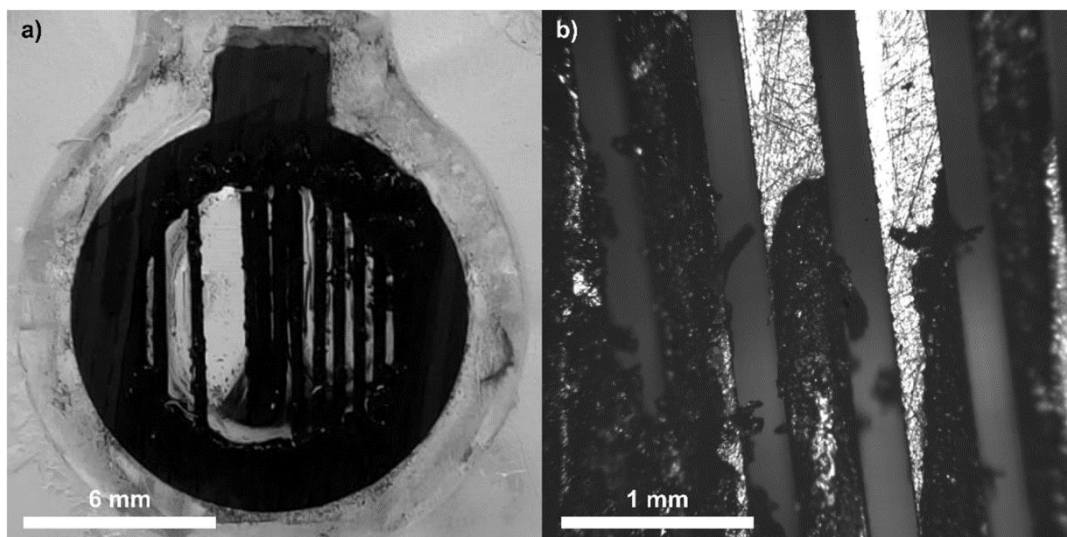


Figure 5.8: a) Photograph of the damage to a 300 μm thick glassy carbon electrode cut with identical geometry to the 70% NDC electrode after a single calibration from 0.1 to 0.3A operating as the anode (half a run, electrode operating for less than 10 minutes). b) Optical microscopy of the electrode from a showing the severe etching on the remaining bars.

5.3.5 Effect of Electrode Thickness on Perforated Electrode Performance

One route to increasing the NDC content of electrodes without changing the geometry is to increase the thickness of the BDD used. Electrodes of identical geometry to the 70% electrode were cut from 200, 300, 420, and 700 μm thick as grown BDD, with NDC proportions varying from 53 - 80%, Figure 5.9. Note, the standard thickness used in this work is 420 μm

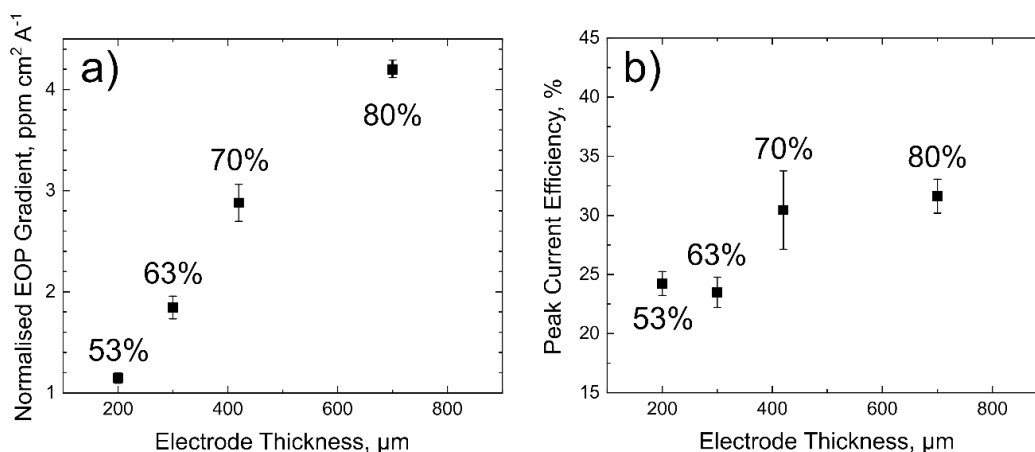


Figure 5.9: a) Ozone gradient versus electrode thickness for a single perforated electrode design. b) Peak current efficiency versus electrode thickness for a single perforated electrode design. Inset, NDC content percentages for each electrode. The potentials, ozone output, current efficiency, EOP gradient, and adj- R^2 for these data points can be found in the appendix, section A5.3.

Increasing the thickness of the slotted electrode from 200 to 700 μm results in a sharp increase in the normalised EOP gradient. The current efficiency increases steadily from the 200 μm thick to the 420 μm thick electrode, and then levels out as the thickness is increased to 700 μm . Interestingly, the highest current efficiency for the 700 μm thick electrode is seen at 0.6 A (i.e., the highest current) suggesting that higher efficiencies may be possible at higher currents.

Another factor that may change as the electrode thickness is increased is the flow profile over the electrode. This change in flow profile may be because of the change aspect ratio of the slots, which are 300 μm wide in this design. As the electrodes need the transport of solution in, and gases out increasing the thickness of the electrode may serve to make these processes more difficult, and thus increasing the thickness may not always result in an increased ozone output.

Not only does the data in Figure 5.9 prove the importance of surface NDC for EOP but it also shows that in this arrangement the ‘Triple Point’ theory as proposed by Kraft et.al,²⁹ does not completely apply to this EOP set-up. In this piece of work the authors state that only regions of the BDD electrode near both the Nafion membrane and solution are active for the generation of ozone. Since all the electrodes in Figure 5.9, have an identical slot length (and therefore triple-point length, which is 170 mm for this design) if the triple-point theory was correct they should both have the same ozone output and current efficiency, which is not the case. This highlights that it is more than just the triple point regions which are contributing to the observed increase in EOP. It also confirms that the NDC is resulting in this increase in EOP and not just geometric effects such as slot design and length.

5.3.6 Long-Term Testing

To test the lifetime and long-term stability of these BDD-EOP cells a 20-hour experiment monitoring the ozone output of the 70% NDC cell was performed in Figure 5.10, the 20-hour monitoring of the ozone output can be found in the appendix to this chapter, as Figure A5.1. The long-term ozone trace shows no significant change in absorbance at 258 nm over the 20-hours. The 70% cell was chosen due to concerns about mechanical robustness of the 80% cell. After the long-term experiment was complete the Nafion membrane was replaced, and the cell recalibrated to make sure changes in EOP performance were not due to Nafion degradation.

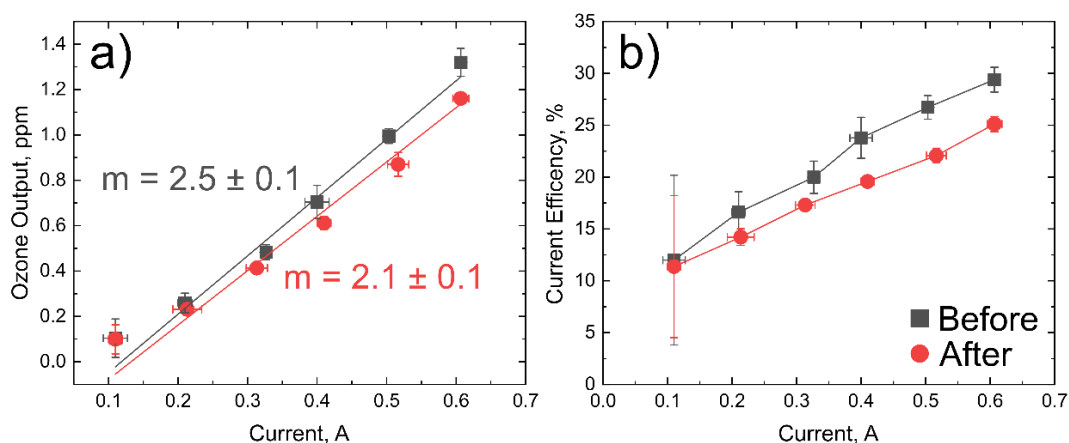


Figure 5.10: a) Ozone output in ppm vs current for the 70% NDC electrode before and after 20-hour testing. b) Peak current efficiency versus current before and after long-term testing. EOP gradient, and adj- R^2 for these calibrations can be found in the appendix, section A5.4.

After long-term testing the EOP gradient has dropped by 0.4 ppm A^{-1} , or 14%. While this is an appreciable change given the errors in the calibration plots it is a fairly small change given the harsh, oxidising nature of the EOP environment. There has also been a change in peak current efficiency, which shows a 3.7% decrease in peak efficiency after the 20-hour experiment. These small changes in ozone output after 20 hours of continuous generation highlight the stability of the NDC BDD surface. The stability of this material must then be as a result of the structure of the amorphous capping layer seen on top of the graphite attached to the BDD surface.¹⁵ While this reduction in performance would be acceptable for a domestic application, where 20 hours is likely to be a significant proportion of the device's total lifetime use, for industrial applications with higher duty cycles further work would have to be conducted to understand if further reductions were seen on these longer timescales.

5.3.7 Hydrogen Plasma Treatment on Perforated Electrodes

To ensure that the improvements seen in Figure 5.4 were a result of changing the amount of NDC and not the geometry, a 70% NDC cell was laser cut and hydrogen plasma treated as an attempt to try and remove the majority of the NDC from the BDD surface. To confirm that the amount of NDC on the surface of the electrode had been reduced by the hydrogen plasma treatment, quinone surface coverage (QSC) measurements were performed, as shown in Figure 5.11a for an acid cleaned cell and Figure 5.11b for the hydrogen plasma treated electrode. QSC measurements are more fully described in Chapter 2, Section 2.5.1.

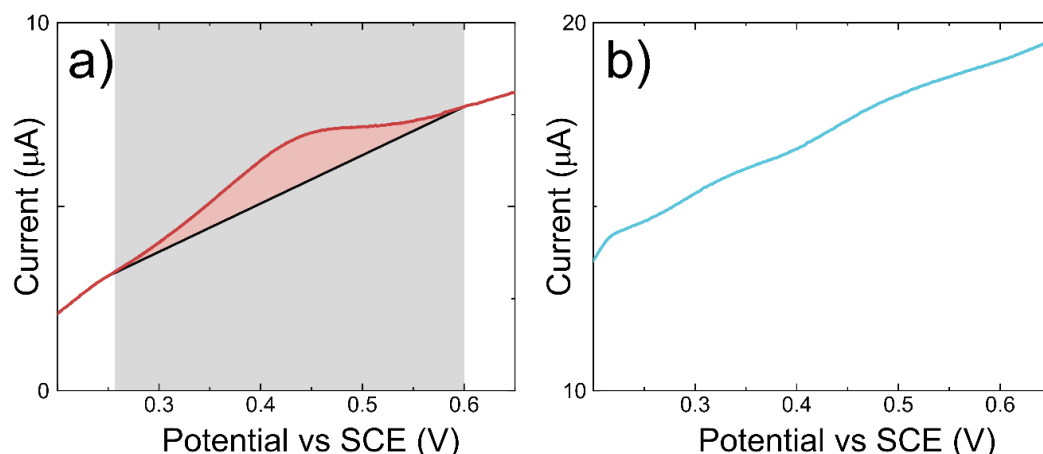


Figure 5.11: QSC Measurements of a) the 70% NDC electrode and b) the Hydrogen plasma treated 70 % electrode. Three CVs were collected in pH 2 Carmody buffer at 100 mV s^{-1} with the oxidative sweep of the third scan presented.

It is clear from these QSC measurements that the 70% NDC electrode has a peak related to quinone oxidation in the window suggested by Ayres et. al.³⁰ It is also clear that after hydrogen plasma treatment the electrode has no single peak in that window, suggesting the number of surface quinone groups and therefore NDC carbon content has been significantly reduced. Full quantification of the quinone surface coverage is not performed as the baseline is sloped, potentially due to the cell used in this measurement. This plasma treatment results in a geometrically identical electrode to the 70 % electrode but with significantly reduced NDC. Note more work is still required to fully understand the impact H plasma treatment has on the underlying BDD electrode and the mechanism of NDC removal. The EOP gradients and current efficiency of this electrode can then be compared to the 70% electrode with NDC present, Figure 5.12.

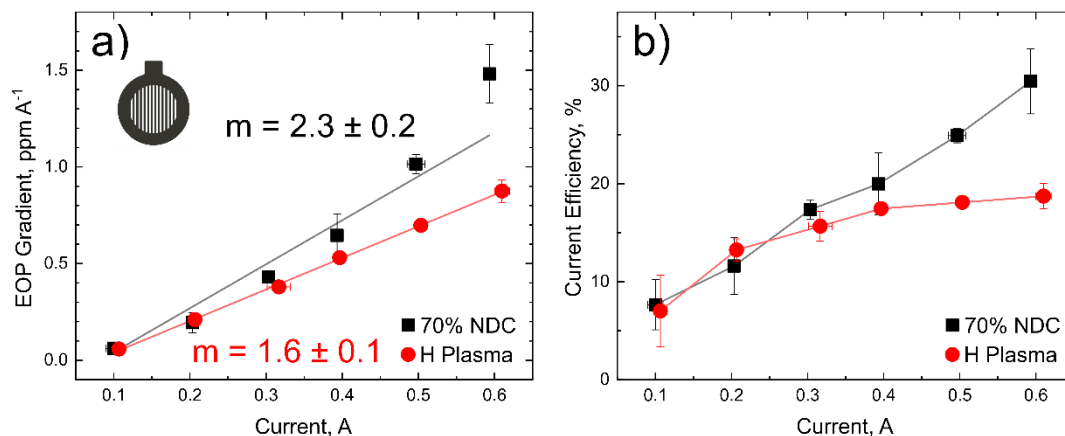


Figure 5.12: a) Ozone output in ppm vs current for the 70% NDC and hydrogen plasma treated electrodes. b) Peak current efficiency versus current for both electrodes. Inset, schematics of both electrode geometries. EOP gradient, and adj-R² for these calibrations can be found in the appendix, section A5.5

This data shows clearly that the 70% NDC electrode outperforms a geometrically identical hydrogen plasma treated electrode in both ozone output and current efficiency. This once again affirms the belief that NDC is important for efficient ozone generation on BDD.

5.4 Conclusion

This work serves to demonstrate the importance of NDC incorporation in both a planar and perforated embodiment of a BDD-EOP cell. Incorporating NDC into a BDD electrode surface as a meaningful fraction of the surface serves to increase its ozone output by four times, compared to BDD electrodes with only NDC created during growth present. The addition of this NDC also results in the current efficiency doubling from 18 to 36%, demonstrating significantly more efficient EOP is possible with NDC present. The 69% NDC cell in this study demonstrates a peak current efficiency of 36%, which is comparable with those seen in previous BDD-EOP literature.

We hypothesise that the reason for this increase in output and efficiency is due to the increased strength of bonding of OH and O radicals to NDC versus purely sp³ BDD. This increased binding strength increases binding time, and therefore radical density on the surface, ultimately resulting in a higher ozone production.

However, the biggest value of this work is in the additional understanding of the importance of NDC on EOP using BDD electrodes. While the cells built and tested are undoubtedly on a lab scale, the understanding of how to efficiently integrate NDC and treat it to form the highly robust NDC into BDD will no doubt assist in further BDD-EOP optimisation work. The novel design of zero-gap EOP cell built for planar electrodes illustrates the flexibility of EOP cell

design and provides an alternative cell design for situations where perforated electrodes are impractical. It was also demonstrated that by acid cleaning the electrodes after machining a highly robust NDC material is formed. Subjecting this material to EOP conditions for 20-hours only results in a small drop in EOP performance.

5.5 References

- 1 M. Takayama, K. Ebihara, H. Stryczewska, T. Ikegami, Y. Gyoutoku, K. Kubo and M. Tachibana, *Thin Solid Films*, 2006, **506–507**, 396–399.
- 2 T. M. Pan, K. Shimoda, Y. Cai, Y. Kiuchi, K. Nakama, T. Akimoto, Y. Nagashima, M. Kai, M. Ohira, J. Saegusa, T. Kuhara and K. Maejima, *Exp. Anim.*, 1995, **44**, 255–259.
- 3 M. Gao, Z. Zeng, B. Sun, H. Zou, J. Chen and L. Shao, *Chemosphere*, 2012, **89**, 190–197.
- 4 R. G. Rice, C. M. Robson, G. W. Miller and A. G. Hill, *J. / Am. Water Work. Assoc.*, 1981, **73**, 44–57.
- 5 R. G. Rice, *Ozone Sci. Eng.*, 1996, 18, 477–515.
- 6 J. C. Devins, *J. Electrochem. Soc.*, 1956, **103**, 460.
- 7 K. Arihara, C. Terashima and A. Fujishima, *J. Electrochem. Soc.*, 2007, **154**, E71.
- 8 K. Arihara, C. Terashima and A. Fujishima, *Electrochem. Solid-State Lett.*, 2006, **9**, D17.
- 9 T. Watanabe, Y. Honda, K. Kanda and Y. Einaga, *Phys. Status Solidi Appl. Mater. Sci.*, 2014, **211**, 2709–2717.
- 10 Y. Nishiki, N. Kitaori and K. Nakamuro, *Ozone Sci. Eng.*, 2011, **33**, 114–120.
- 11 P. A. Christensen, T. Yonar and K. Zakaria, *Ozone Sci. Eng.*, 2013, **35**, 149–167.
- 12 Y. Honda, T. A. Ivandini, T. Watanabe, K. Murata and Y. Einaga, *Diam. Relat. Mater.*, 2013, **40**, 7–11.
- 13 L. M. Da Silva, L. A. De Faria and J. F. C. Boodts, *Electrochim. Acta*, 2003, **48**, 699–709.
- 14 N. Vatisstas, *Int. J. Electrochem.*, 2012, **2012**, 1–7.
- 15 S. J. Cobb, F. H. J. Laidlaw, G. West, G. Wood, M. E. Newton, R. Beanland and J. V. Macpherson, *Carbon N. Y.*, 2020, **167**, 1–10.

- 16 A. J. Lucio, R. E. P. Meyler, M. A. Edwards and J. V. Macpherson, *ACS Sensors*, 2020, **5**, 789–797.
- 17 L. A. Hutton, J. G. Iacobini, E. Bitziou, R. B. Channon, M. E. Newton and J. V. Macpherson, *Anal. Chem.*, 2013, **85**, 7230–7240.
- 18 D. F. Swinehart, *J. Chem. Educ.*, 1962, **39**, 333.
- 19 J. Hoigné and H. Bader, *Water Res.*, 1976, **10**, 377–386.
- 20 G. F. Wood, I. M. Terrero Rodríguez, J. J. Tully, S. Chaudhuri and J. V. Macpherson, *J. Electrochem. Soc.*, 2021, **168** 126514
- 21 S. T. Summerfelt, M. J. Sharrer, J. Hollis, L. E. Gleason and S. R. Summerfelt, in *Aquacultural Engineering*, Elsevier, 2004, vol. 32, pp. 209–223.
- 22 Y. Honda, T. A. Ivandini, T. Watanabe, K. Murata and Y. Einaga, *Diam. Relat. Mater.*, 2013, **40**, 7–11.
- 23 B. Marselli, J. Garcia-Gomez, P.-A. Michaud, M. A. Rodrigo and C. Comninellis, *J. Electrochem. Soc.*, 2003, **150**, D79.
- 24 J. L. Sotelo, F. J. Beltran, F. J. Benitez and J. Beltran-heredia, *Ind. Eng. Chem. Res.*, 1987, **26**, 39–43.
- 25 T. Batakliiev, V. Georgiev, M. Anachkov, S. Rakovsky and G. E. Zaikov, *Interdiscip. Toxicol.*, 2014, **7**, 47–59.
- 26 E. I. Kurolenskin, Y. S. Lopatto, D. K. Khakimova and Y. S. Virgul'ev, *Solid Fuel Chem.*, 1982, **16**, 105–112.
- 27 P. J. F. Harris, *Philos. Mag.*, 2004, **84**, 3159–3167.
- 28 P. C. Foller and M. L. Goodwin, *Ozone Sci. Eng.*, 1984, **6**, 29–36.
- 29 A. Kraft, M. Stadelmann, M. Wünsche and M. Blaschke, *Electrochem. commun.*, 2006, **8**, 883–886.
- 30 Z. J. Ayres, S. J. Cobb, M. E. Newton and J. V. Macpherson, *Electrochem. commun.*, 2016, **72**, 59–63.

Appendix to Chapter 5:

This appendix to Chapter 5 contains raw calibration parameters from all cells discussed in that chapter. Including, the average potential of the triplet calibration, the average concentration of ozone produced, the current efficiency at each current, the EOP gradient and the solution accessible area.

A5.1 Planar Electrode Cells

Planar electrodes with 0%, 65%, 90%, and 100% NDC integrated into their surfaces were prepared and calibrated. Critical parameters from the calibrations are collected in Tables A5.1 to A5.4.

Table A5.1: Mean parameters for a triplicate run of the 0% NDC Planar Electrode Cell.

Current / A	Potential / V	[Ozone] / ppm	Current Efficiency / %	EOP Gradient / ppm A ⁻¹	adj-R ²
0.1	6.6	0.28	10.4	3.55	0.992
0.2	8.4	0.55	11.2		
0.3	10.4	0.98	12.8		
0.4	12.3	1.34	13.1		
0.5	14.4	1.70	13.5		
0.6	16.6	2.02	13.4		

Table A5.2: Mean parameters for a triplicate run of the 65% NDC Planar Electrode Cell.

Current / A	Potential / V	[Ozone] / ppm	Current Efficiency / %	EOP Gradient / ppm A ⁻¹	adj-R ²
0.1	12.3	0.59	21.3	3.98	0.958
0.2	15.7	1.02	19.7		
0.3	17.9	1.46	18.8		
0.4	19.6	1.94	18.6		
0.5	20.8	2.26	17.4		
0.6	21.7	2.50	16.3		

Table A5.3: Mean parameters for a triplicate run of the 90% NDC Planar Electrode Cell.

Current / A	Potential / V	[Ozone] / ppm	Current Efficiency / %	EOP Gradient / ppm A ⁻¹	adj-R ²
0.1	7.9	0.70	27.5	4.88	0.977
0.2	9.3	1.26	25.7		
0.3	10.5	1.86	24.7		
0.4	11.6	2.37	24.6		
0.5	12.9	2.78	22.8		
0.6	13.9	3.10	20.8		

Table A5.4: Mean parameters for a triplicate run of the 100% NDC Planar Electrode Cell.

Current / A	Potential / V	[Ozone] / ppm	Current Efficiency / %	EOP Gradient / ppm A ⁻¹	adj-R ²
0.1	6.5	0.35	13.9	5.73	0.994
0.2	8.4	0.92	17.9		
0.3	10.0	1.53	20.0		
0.4	12.2	2.02	20.3		
0.5	13.3	2.67	21.1		
0.6	14.2	3.20	21.2		

A5.2 Perforated Electrode Cells

Perforated electrodes with 5%, 30%, 40%, 50%, 60%, 69%, 70% and 80% NDC integrated into their surfaces were prepared and calibrated. Critical parameters from the calibrations are collected in Tables A5.5 to A5.12.

Table A5.5: Mean parameters for a triplicate run of the 5% NDC Perforated Electrode Cell.

Current / A	Potential / V	[Ozone] / ppm	Current Efficiency / %	EOP Gradient / ppm A ⁻¹	adj-R ²	Area (cm ²)
0.1	7	0.03	4.2	1.55	0.947	0.57
0.2	8.6	0.11	6.9			
0.3	9.8	0.24	10.6			
0.4	11.3	0.39	12.9			
0.5	12.8	0.57	15.4			
0.6	14.4	0.80	17.8			

Table A5.6: Mean parameters for a triplicate run of the 30% NDC Perforated Electrode Cell.

Current / A	Potential / V	[Ozone] / ppm	Current Efficiency / %	EOP Gradient / ppm A ⁻¹	adj-R ²	Area (cm ²)
0.1	5.2	0.03	4.6	1.79	0.941	0.71
0.2	6.1	0.08	5.2			
0.3	7.4	0.25	11.0			
0.4	8.4	0.43	14.1			
0.5	9.3	0.66	17.3			
0.6	10.2	0.91	19.9			

Table A5.7: Mean parameters for a triplicate run of the 40% NDC Perforated Electrode Cell.

Current / A	Potential / V	[Ozone] / ppm	Current Efficiency / %	EOP Gradient / ppm A ⁻¹	adj-R ²	Area (cm ²)
0.1	7.3	0.09	12.4	1.80	0.989	0.78
0.2	10.5	0.24	15.2			
0.3	12.6	0.41	17.8			
0.4	14.3	0.60	19.7			
0.5	15.9	0.77	20.0			
0.6	17.2	1.00	21.5			

Table A5.8: Mean parameters for a triplicate run of the 50% NDC Perforated Electrode Cell.

Current / A	Potential / V	[Ozone] / ppm	Current Efficiency / %	EOP Gradient / ppm A ⁻¹	adj-R ²	Area (cm ²)
0.1	5.2	0.06	7.2	2.22	0.967	0.86
0.2	6.0	0.13	8.1			
0.3	6.9	0.33	14.0			
0.4	8.0	0.59	19.0			
0.5	9.0	0.87	22.0			
0.6	9.7	1.10	23.6			

Table A5.9: Mean parameters for a triplicate run of the 60% NDC Perforated Electrode Cell.

Current / A	Potential / V	[Ozone] / ppm	Current Efficiency / %	EOP Gradient / ppm A ⁻¹	adj-R ²	Area (cm ²)
0.1	5.3	0.06	7.9	2.98	0.980	0.67
0.2	6.6	0.20	13.3			
0.3	8.2	0.58	24.9			
0.4	9.9	0.85	27.0			
0.5	11.6	1.16	29.4			
0.6	13.3	1.52	32.6			

Table A5.10: Mean parameters for a triplicate run of the 69% NDC Perforated Electrode Cell.

Current / A	Potential / V	[Ozone] / ppm	Current Efficiency / %	EOP Gradient / ppm A ⁻¹	adj-R ²	Area (cm ²)
0.1	6.1	0.20	25.8	3.00	0.982	0.85
0.2	8.5	0.39	24.8			
0.3	10.8	0.78	33.6			
0.4	12.2	1.07	35.0			
0.5	13.5	1.34	35.4			
0.6	14.1	1.64	36.4			

Table A5.11: Mean parameters for a triplicate run of the 70% NDC Perforated Electrode Cell.

Current / A	Potential / V	[Ozone] / ppm	Current Efficiency / %	EOP Gradient / ppm A ⁻¹	adj-R ²	Area (cm ²)
0.1	5.8	0.06	7.7	2.84	0.935	1.01
0.2	7.4	0.19	11.6			
0.3	9.3	0.43	17.4			
0.4	10.8	0.65	20.0			
0.5	12.8	1.01	24.9			
0.6	14.5	1.48	30.4			

Table A5.12: Mean parameters for a triplicate run of the 80% NDC Perforated Electrode Cell.

Current / A	Potential / V	[Ozone] / ppm	Current Efficiency / %	EOP Gradient / ppm A ⁻¹	adj-R ²	Area (cm ²)
0.1	6.7	0.19	23.2	2.64	0.990	1.51
0.2	9.1	0.46	29.5			
0.3	10.6	0.78	33.0			
0.4	11.4	0.99	32.7			
0.5	12.4	1.26	33.5			
0.6	13.9	1.48	32.7			

A5.3 Perforated Electrode Cells with Different BDD Thicknesses

Perforated electrodes in the same geometry as the 70% NDC electrode were cut from 200 μm , 300 μm and 700 μm thick and calibrated. Critical parameters from the calibrations are collected in Tables A5.13 to A5.15.

Table A5.13: Mean parameters for a triplicate run of the 200 μm thick cell.

Current / A	Potential / V	[Ozone] / ppm	Current Efficiency / %	EOP Gradient / ppm A ⁻¹	adj-R ²	Area (cm ²)
0.1	10.6	0.12	14.6	1.79	0.968	0.64
0.2	15.1	0.32	20.7			
0.3	18.2	0.54	23.4			
0.4	21.2	0.76	24.2			
0.5	23.4	0.91	23.2			
0.6	25.4	0.98	20.8			

Table A5.14: Mean parameters for a triplicate run of the 300 μm thick cell.

Current / A	Potential / V	[Ozone] / ppm	Current Efficiency / %	EOP Gradient / ppm A ⁻¹	adj-R ²	Area (cm ²)
0.1	7.4	0.078	9.5	1.59	0.957	0.81
0.2	9.4	0.163	9.9			
0.3	11.3	0.296	12.3			
0.4	13.1	0.445	13.7			
0.5	14.7	0.623	15.8			
0.6	16.6	0.880	18.3			

Table A5.15: Mean parameters for a triplicate run of the 700 μm thick cell.

Current / A	Potential / V	[Ozone] / ppm	Current Efficiency / %	EOP Gradient / ppm A ⁻¹	adj-R ²	Area (cm ²)
0.1	5.8	0.07	8.1	2.85	0.973	1.49
0.2	7.1	0.22	14.1			
0.3	8.8	0.54	23.4			
0.4	10.1	0.78	26.7			
0.5	11.5	1.16	31.1			
0.6	12.7	1.42	32.6			

A5.4 Long Term Testing

The 70% NDC electrode was subject to long-term testing and then recalibrated. Critical parameters from the calibrations are collected in Tables A5.16 and A5.17.

Table A5.16: Mean parameters for the triplicate run of the 70% NDC cell before long-term testing.

Current / A	Potential / V	[Ozone] / ppm	Current Efficiency / %	EOP Gradient / ppm A ⁻¹	adj-R ²	Area (cm ²)
0.1	6.7	0.10	12.0	2.47	0.974	1.01
0.2	8.6	0.26	16.6			
0.3	10.9	0.48	20.0			
0.4	12.1	0.70	23.8			
0.5	13.6	1.00	26.7			
0.6	14.9	1.32	29.4			

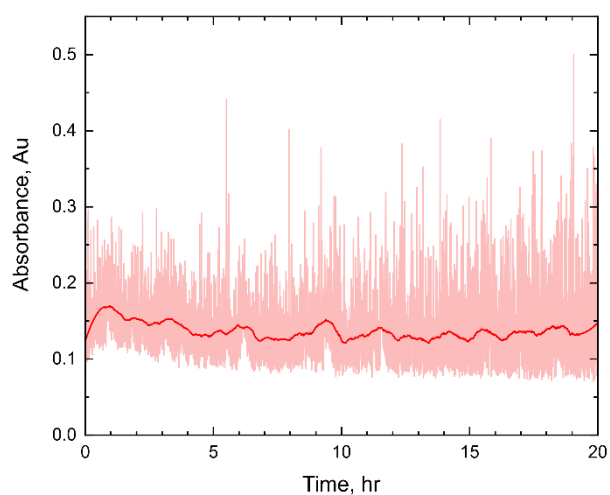


Figure A5.1: UV absorbance at 258 nm over 20 hr with the A side as anode for the 70% NDC electrode cell. Data was smoothed using a second order polynomial Savitzky-Golay filter with a smoothing window length of 500 points.

Table A5.17: Mean parameters for the triplicate run of the 70% NDC cell after long-term testing.

Current / A	Potential / V	[Ozone] / ppm	Current Efficiency / %	EOP Gradient / ppm A ⁻¹	adj-R ²	Area (cm ²)
0.1	6.7	0.10	11.4	2.12	0.974	1.01
0.2	8.3	0.23	14.2			
0.3	9.8	0.41	17.3			
0.4	11.0	0.61	19.6			
0.5	12.3	0.87	22.1			
0.6	13.4	1.16	25.1			

A5.5 Hydrogen Plasma Treatment

A 70% NDC electrode was subject to a hydrogen-plasma treatment and then calibrated.

Critical parameters from the calibration are collected in Table A5.18.

Table A5.18: Mean parameters for the triplicate run of the hydrogen plasma treated cell.

Current / A	Potential / V	[Ozone] / ppm	Current Efficiency / %	EOP Gradient / ppm A ⁻¹	adj-R ²	Area (cm ²)
0.1	6.7	0.06	7.0	1.63	0.988	1.01
0.2	8.6	0.21	13.2			
0.3	10.3	0.38	15.7			
0.4	11.3	0.53	17.5			
0.5	12.5	0.70	18.1			
0.6	13.7	0.88	18.7			

Chapter 6: A Do-It-Yourself Method for Making Custom Rotating Ring Disk Electrodes.

6.1 Introduction

The rotating ring disk electrode (RRDE) is a powerful electrochemical tool for the mechanistic analysis of electrochemical reactions at electrode surfaces.^{1,2} This is due to the ability of the RRDE to detect the products of an electron transfer reaction occurring at the inner disk electrode using the outer ring electrode.² In this way RRDEs can be employed to identify different mechanistic pathways in an electron transfer process.³ RRDEs in particular have found use as a method for assessing electrocatalyst activity for processes such as the oxygen reduction reaction (ORR),⁴⁻⁶ the nitrogen reduction reaction,⁷ and carbon dioxide reduction.^{8,9} The ring electrode could also be used as a pH sensor to detect pH changes resulting from reactions on the disk.¹⁰

In a RRDE, the ring and disk electrodes can be made from the same, or different, electrode materials, dependent on the electron transfer process to be studied. For some electrocatalytic studies, the electrocatalyst can be deposited onto the disk electrode, with the pre-requisite that the disk has significantly lower electrocatalytic activity than the deposited material, and thus will not interfere with the reaction of interest.¹¹⁻¹⁶ The entire electrode system is typically encased in an insulating housing containing the contacts and threads required to attach and independently electrically connect the two electrodes to the rotating apparatus. As the RRDE is rotated, solution is moved from the bulk toward the face of the disk electrode, which then exits parallel to the electrode surface, flowing over the ring electrode as it moves outward towards the edge of the RRDE. Due to the well-defined hydrodynamic flow, not only is transport of species from the disk to the ring greatly enhanced, compared to stationary conditions, but it is possible to quantify what proportion of electroactive species produced at the disk should be detected on the ring. This is defined as the collection efficiency and is an intrinsic property of each RRDE design which depends on the relative radii of the ring and disk electrodes.²

While commercial RRDEs are widely available the electrode selection is typically limited to combinations of the more common electrode materials such as gold, platinum, and glassy carbon. Even with these standard materials, the electrodes can be costly (> £1k) and moving to more specialized RRDEs produced from less commonly used materials drives the cost even higher, which can prohibit their use. To the best of our knowledge, there are only two published papers on in-house built RRDEs,^{17,18} however the focus of both of these papers is in building an RRDE with a removable central disk, a feature which has since been adopted

commercially, rather than providing a guide to follow. As a result, both papers provide only limited guidance on the design and construction processes. In contrast this work aims to serve as an easy-to-follow guide to make a simple, yet effective RRDE made from a variety of different electrode materials.

To prove the effectiveness of our approach to producing do-it-yourself (DIY) RRDEs, we focus on the production of boron doped diamond (BDD) based RRDEs, a material not commonly integrated into RRDEs due to perceived difficulty. The method presented is applicable to any electrode material which can be produced in rod, foil, or wafer form. To the best of our knowledge there are no examples of all-BDD RRDEs in the literature to-date, which also exemplifies the versatility of the approach outlined. BDD has many useful electrochemical attributes in aqueous solutions, which include, extremely low background currents, high resistance to corrosion under both acid and alkali conditions,^{19,20} and an even lower electrocatalytic activity than non-diamond carbon (NDC) electrodes. All these properties make BDD a very useful electrocatalyst support electrode.²¹

For this work, the DIY RRDE electrode was used to investigate the impact of NDC presence in BDD on the prevalence of ORR via the 2-electron pathway.²² To this end NDC was introduced to the BDD surface using a ns laser ablation process.^{23–25} This procedure has been used previously as a means of conferring increased electrocatalytic activity on a BDD electrode.^{24,26} Whilst in these previous studies^{24,26} a microdot pattern was adopted, in this work the entire surface was converted to NDC in order to probe the ORR response of this carbon material, created by laser ablation. To investigate the ORR mechanism (i.e. 2-electron versus 4-electron), the ring electrode was held at a sufficiently oxidising potential to detect hydrogen peroxide (H₂O₂), which is a product of the 2-electron transfer pathway, Equation 6.1.²⁷



To improve the electrocatalytic efficiency of the BDD ring electrode towards H₂O₂ oxidation, the surface of the ring was modified by electrochemical deposition of platinum NPs.¹¹ Pt NPs on carbon materials (such as glassy carbon) have been used previously for the electrochemical detection of H₂O₂.^{12,13}

6.2 Experimental Methods

6.2.1 Electrode Preparation

The BDD ring and disk electrodes were made from 360 µm thick freestanding electroanalysis grade BDD supplied by Element Six Limited.²⁹ The growth face (used as the electrode face) was polished to ~ 2 nm RMS and the nucleation face lapped to ~ 500 nm RMS. The electrodes were cut from the wafer using a 355 nm Nd:YAG laser micromachining system (E-355-

ATHI-O system, Oxford Lasers Ltd. UK) with a nominal pulse-length of 34 ns. Cutting was performed in three passes using a trepan system with a fluence of 760 J cm^{-1} . The disk electrode was either used as is, or the entire surface laser was ablated with a fluence of 14 J cm^{-1} , (i.e. just above the ablation threshold of BDD)²⁴ in a spiral pattern of increasing diameter to leave a layer of NDC integrated into the entire BDD surface. Once the electrodes were cut, they were acid cleaned as described in Chapter 2, Section 2.3.2, and then all but the NDC disk air annealed as described in Chapter 2, Section 2.3.3, and contacted as discussed in Chapter 2, Section 2.3.4.

6.2.2 3D Printing

Non-conductive parts of the electrode body were designed in Fusion 360 (Autodesk, USA) and printed on a Form 3 (FormLabs, USA) stereolithography (SLA) 3D printer using standard clear resin (Formlabs, USA) at a $50 \mu\text{m}$ layer height. Once printed, parts were post processed as discussed in Chapter 2, Section 2.6.

6.2.3 Bill of Materials

Table 6.1: Bill of materials for a single RRDE electrode.

Part	Estimated Cost RRDE	Notes
Brass Body	£5	Machined in House
Insulating Body (3D Printed)	£2	Printed on a Form 3 (SLA)
Insulating Body (PEEK)	£5	Machined in House (Optional)
Silver Epoxy	£2	Chemtronics CW2400 Conductive Adhesive
Epoxy Resin	£3	If the body is SLA printed that UV resin should be used for sealing as this will ensure adhesion. If PEEK is used a resin with good adherence to PEEK should be used.
Total:	£20 Per RRDE	Not including electrodes or assembly time.

6.2.4 Electrochemical Characterisation

A 760e CHI BiPot (CH Instruments, Texas, USA) was used for all electrochemical measurements (excluding uncompensated resistance measurements) alongside a saturated calomel reference electrode (SCE, CH Instruments Inc, USA) and Pt coil counter. All solutions were prepared in ultrapure water ($>18.2 \text{ M}\Omega \text{ cm}^{-2}$, Milli-Q, Millipore Corp, USA).

Solvent window measurements were performed by cyclic voltammetry (CV) in 0.1 M potassium nitrate KNO_3 (99%, Sigma-Aldrich, UK). Redox mediator measurements were performed by CV in a solution of 1 mM (ferrocenylmethyl)trimethylammonium, (FcTMA^+) in 0.1 M KNO_3 as described in Chapter 2, Section 2.5.2. Determination of the collection efficiency was performed using linear sweep voltammetry (LSV) on the disk electrode and current time (i-t) on the ring.

Uncompensated resistance measurements were conducted using chronoamperometry with 0.1 V steps, the non-faradic decay was then fitted to extract R_u .^{30,31} In order to collect enough data points over the short timescale of the decay a potentiostat fitted with a fast scan module was used (PGSTAT128N with ADC10M.S, Metrohm Autolab, Switzerland) was used. The data was analysed as discussed in Chapter 2, Section 2.5.3.

6.2.5 Pt Deposition

The protocol for Pt-NP deposition on the BDD ring electrode was adapted from Hutton *et al.*¹¹ The electrode was held at -1.00 V *vs* SCE in a solution of hexachloroplatinate (K_2PtCl_6 , 99%, Sigma-Aldrich, UK) in 0.1 M hydrochloric acid (HCl , 99%, Sigma-Aldrich, UK) for 300 s. During deposition, the electrode was rotated at 1,500 rpm to ensure any hydrogen gas produced on the electrode during electrodeposition did not block the surface, as well as to increase mass transport to the surface.

6.2.6 Hydrogen Peroxide Experiments

After Pt deposition the ring electrode response to H_2O_2 (30% w/w, Sigma-Aldrich, UK) in 0.1 M Perchloric Acid, (HClO_4 , 70%, Sigma-Aldrich, UK) was calibrated. The RRDE electrode was rotated at 2,000 rpm, the ring held at 1.00 V *vs* SCE and the current response recorded for 30 s at each concentration. This potential was chosen to give the maximum overpotential for H_2O_2 oxidation *i.e.* just before the oxidation of water starts to compete (*vide infra*).^{12,13} The Pt NP-BDD ring was calibrated for 11 concentrations in equal increments (0.14 mM) between 0 and 1.4 mM. The upper end was chosen by considering the saturation point of O_2 in water is 1.22 mM.³² As an approximation this value was assumed to be the dissolved O_2 concentration in the O_2 saturated, HClO_4 solution. Assuming a 1:1 ratio and 100% conversion (Equation 1) this means the maximum concentration of H_2O_2 which could possibly be produced is ~ 1.22 mM. The current average over the last 5 s of the chronoamperometric response for each concentration was used to construct the current versus H_2O_2 concentration calibration plot.

After calibration, the electrodes were used to perform generation-collection experiments in 0.1 M HClO_4 at 2,000 rpm. The disk electrode was swept from 0.00 to -0.80 V *vs* SCE, a region where ORR should be observed, at a scan rate of 5 mV s^{-1} , with the Pt NP-BDD ring

electrode held at 1.00 V *vs* SCE. After a generation collection experiment the H₂O₂ calibration was repeated and the data from that run only used if the gradient of the after calibration was within 10% of the before calibration. To create an O₂ saturated solution, O₂ (99.5% Purity, BOC, UK) was bubbled through a solution of 0.1 M HClO₄ for a period of 100 minutes (assuming two minutes for every ml of solution). During the experiment pure O₂ was flowed across the top of the solution to maintain saturation.

6.3 Results and Discussions

6.3.1 RRDE Fabrication

An RRDE with a 5 mm diameter disk and a ring with an inner and outer diameter of 7 and 9 mm respectively was chosen for this work. The electrode sizes chosen are common in commercial RRDEs. A slightly larger ring-disk gap (1 mm as compared to 0.5 mm), when compared to commercial RRDEs, has been adopted to make the DIY fabrication process easier, although smaller gaps would also be possible. In this work, the RRDE is designed to integrate with a commercial rotator, here a Pine Research Modulated Speed Rotator, however, the designs could be easily modified for any rotator system. The RRDE itself consists of five components, Figure 6.1a, which can be used with electrode materials in formats such as a rod, wafer, or foil. The five components include: (i) the insulating outer case, which lies co-planar with the ring and the disk; (ii) the brass outer core, which serves as both the ring contact and main body; (iii) the brass inner core, the disk contact; (iv) the insulating tube, which separates and spaces the brass inner and outer cores and (v) the insulating spacer, which prevents the two brass parts from touching. While the brass parts are made using traditional machining techniques on a lathe, the insulating parts are designed to be printable using stereolithography (SLA) 3D printing.³³

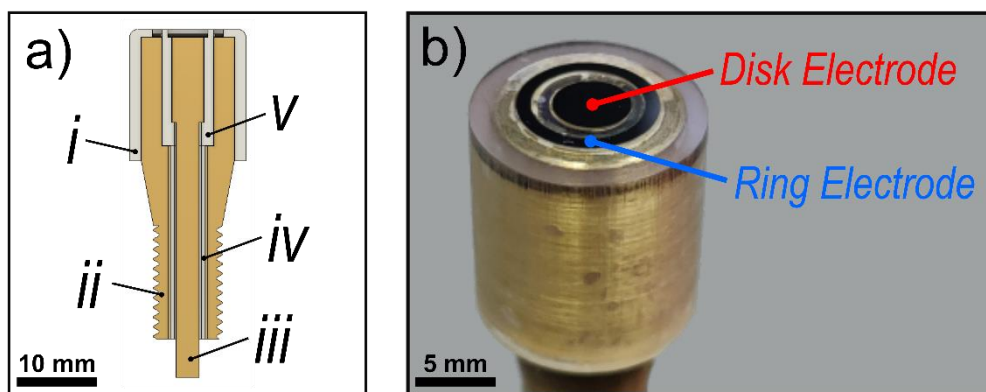


Figure 6.1: (a) Render of a cross-section through the centre of the RRDE electrode, showing the arrangement of the ring and disk contacts. The five components are labelled as: (i) insulating outer case; (ii) brass outer core; (iii) brass inner core; (iv) insulating tube, and; (v) insulating spacer. b) Photograph of an assembled RRDE containing BDD ring and disk electrodes.

The RRDEs consist of five parts, designed to be made in advance, so that the electrodes can be assembled as needed without the need for specialist tools or equipment. Three of these parts have been designed with SLA 3D-printing in mind however if access to an SLA printer is not possible, they could also be made traditionally. The two brass parts are designed to be fabricated on a lathe, as most research institutions have some form of mechanical workshop which could easily produce these parts from metal. If no access to a mechanical workshop was possible the manufacture of these parts could be outsourced, or a metal selective laser sintering 3D printer could be used with some modification to the design. A sixth component can also be produced which acts as a stand to ensure the ring and disk electrodes remain planar during construction. This is not used as part of the RRDE, so can be reused if multiple RRDEs are being produced.

6.3.2 Thread Sizing

One of the critical things to get right when trying to integrate a custom RRDE electrode into a commercial rotator system is to ensure that the threads match so that everything can screw together. We reached out to the manufacturer of our rotator system (Pine Instruments, USA), who said that they couldn't tell us the size of the thread, so we had to size it ourselves. When we sized it, we found it was a combination of metric and imperial standards, so that it was impossible to match it to a standard thread it's 9 mm outer diameter (metric) with 24 Threads per Inch (imperial). We considered cutting a new standard thread into the RRDE shaft, but this would have prevented it being compatible with commercial RRDE electrodes so instead threads matching the shaft were cut into the electrodes on the lathe.

6.3.3 Step-By-Step Assembly

1. Collect all the parts for the RRDE the electrodes, (i) the insulating outer case (which prevents the brass being exposed to the solution and lies co-planar with the ring and the disc), (ii) the brass outer core (which serves as both the ring contact and main body), (iii) the brass inner core, (the disk contact), (iv) and optionally, a stand to assist with assembly, (v) the insulating spacer (which prevents the two brass parts from touching), (vi) the insulating tube (which separates and spaces the brass inner and outer), and (vii) the ring and (ix) disk electrodes. As well as an insulating resin, rapid epoxy, and conductive epoxy.
2. If using 3D printed parts remove from the supports and remove any defects from printing with a knife or file.
3. Dry fit all the parts together to ensure they fit before gluing. Ensure that the brass inner fits flush with the brass outer. If it doesn't, sand the back of the insulating inner until they do.



Figure 6.2: Steps 1-3 of RRDE assembly. a) collecting all the parts: i) insulating outer case, ii) brass outer core, iii) brass inner core, iv) RRDE assembly stand, v) insulating spacer, vi) insulating tube, vii) BDD Ring Electrode, ix) BDD Disk Electrode. b) Removing 3D-printed sparts from support. c) Checking alignment between inner and outer brass parts with a ruler.

4. Glue all the body parts together with a rapid epoxy, starting with the inner brass core and working outwards. Leave the RRDE face up for 30 minutes to allow the rapid epoxy to set. A spare insulating outer can be used as a stand for the RRDE.
5. Once set dry fit the ring and disk electrodes into the recesses widening with a knife as required.
6. Mix the conductive epoxy (if using) according to the manufacturer's instructions and apply a small amount to the brass ring and disk contacts.



Figure 6.3: Steps 4-6 of RRDE fabrication including, a) attaching the parts together with a rapid epoxy. b) Test fitting the ring and disk electrodes. c) adding conductive epoxy to the brass contacts.

7. Place the electrodes on top of the conductive epoxy and invert onto the stand. The stand ensures that the electrodes are kept aligned and coplanar as the epoxy cures. Cure the conductive epoxy according to manufacturer's instructions leaving the RRDE on the stand throughout.
8. Once the conductive epoxy is set flood the front face with the insulating epoxy chosen for sealing. It is advantageous to heat the RRDE and resin to approximately 60°C to lower the viscosity of the resin and ensure a good seal around the electrodes. Try not to fill the surface with resin past flush as this will make it harder to polish the surface co-planar in later steps.
9. Cure the insulating resin according to manufacturer's instructions.



Figure 6.4: Steps 7-9 of RRDE fabrication including, a) curing the conductive epoxy on a stand to ensure the electrodes are co-planar. b) Flooding the electrodes surfaces with insulating resin. c) UV curing the insulating resin.

10. Once the insulating resin is cured it can be polished away to reveal the surface of the electrodes, increasingly fine grades of abrasive paper can be used until the electrode surfaces are completely exposed.

11. After the electrode surfaces are exposed, and before each use the surfaces should be alumina polished to ensure the electrodes are clean.

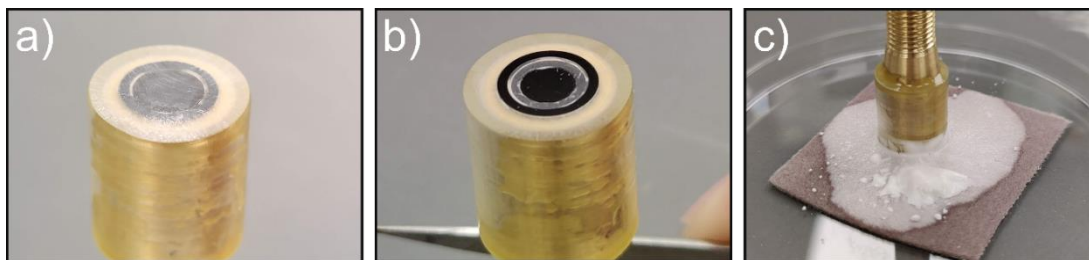


Figure 6.5: Steps 10 and 11 of RRDE fabrication including, a) sanding the insulating resin to expose the electrodes. b) The electrodes are exposed. c) Alumina polish to clean the electrodes.

6.3.4 Rough Electrodes

In the case of a ring or disk electrode with significant (> 100 nm) surface texture it may be desirable to protect the surface prior to Step 8 where the face is flooded with epoxy. This could be achieved in two ways; the first method would be to place a piece of Kapton tape over the electrode before Step 6. This Kapton mask is easy to remove by polishing and should leave no residue. The second method is to flood the surface with a partially hydrolysed polyvinyl alcohol (PVA Glue) before Step 8. The PVA glue is easy to remove by polishing but can also be electrochemically removed by cycling in a dilute acid such as $0.1 \text{ M H}_2\text{SO}_4$.

6.3.5 Foil and Rod Materials

While the method of fabrication used was designed for freestanding sheet material ($> 100 \mu\text{m}$ thick) it could be easily adapted for other electrode formats. If foil electrode material ($< 100 \mu\text{m}$ thick) was to be used the authors suggest attaching it to both the brass inner and outer between Steps 3 and 4 and then omitting steps 5-7. Using rod material would be wasteful due to the large amount of material that would need to be removed, however this could also be done, electrodes could be turned to size on a lathe and the RRDE assembled as normal. If the electrodes are thicker than the $500 \mu\text{m}$ for which the RRDE parts are designed, it would be essential to increase the height of both the insulating inner and outer to accommodate for this additional thickness.

6.3.6 RRDE Characterisation

To verify that the individual electrodes of the RRDEs were functioning appropriately, the CV responses of both the two BDD rings, one BDD disk and one BDD disk with NDC integrated into the surface, were recorded in 1 mM FcTMA⁺ in 0.1 M KNO₃ at 100 mV s⁻¹, under stationary conditions. Peak to peak separations, ΔE_p , in the range 69 – 88 mV were recorded, Figure 6.6.

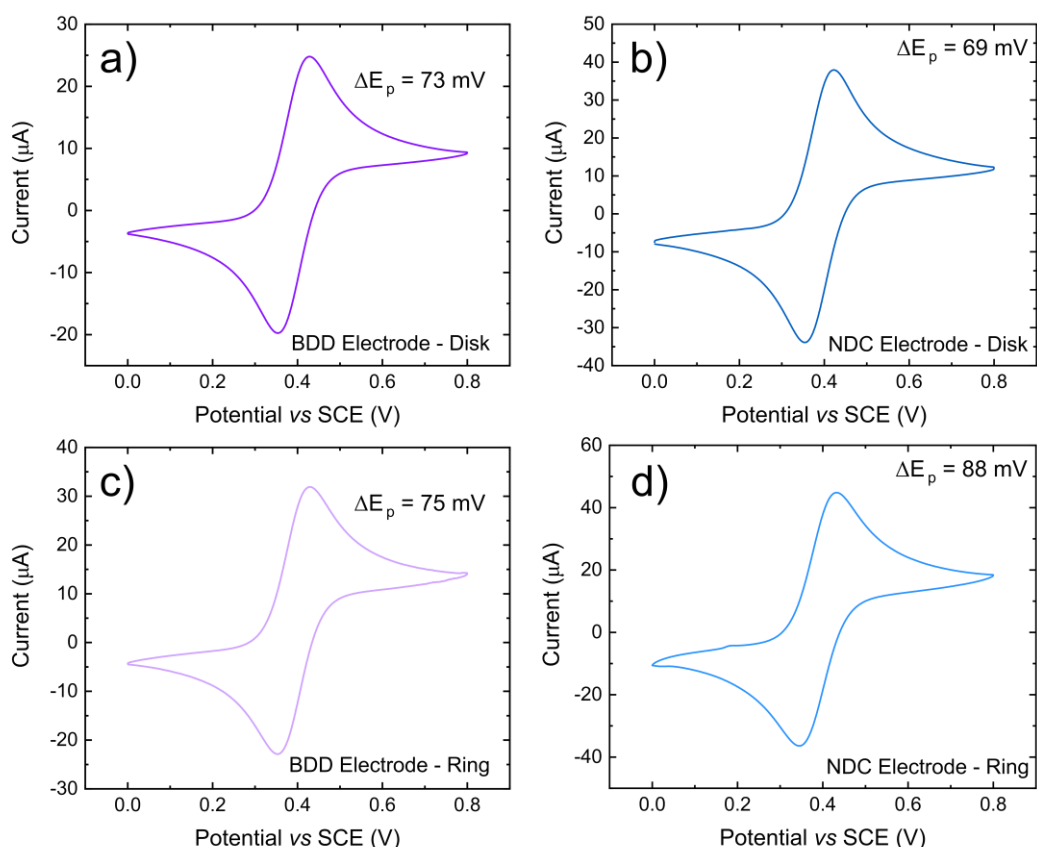


Figure 6.6: Cyclic Voltammetry for ring and disk electrodes in 1 mM FcTMA⁺ made up in 0.1 M KNO₃. a) Disk electrode of the blank RRDE. b) Disk electrode of the NDC RRDE electrode. c) Ring electrode of the blank RRDE. d) Ring electrode of the NDC RRDE. Presented data is the third scan of three.

Uncompensated resistance, R_u , measurements recorded in a solution of 0.1 M KNO₃, using chronoamperometry,³¹ recorded in a non-faradaic region of the CV (0.0 to 0.1 V vs SCE $n = 5$) were used to assess for any possible contact resistance issues.^{30,31} All the electrodes gave low R_u values < 115 Ω (Table 6.2) suggesting the electrodes were appropriately contacted, and that charge transfer resistance,³⁴ is likely to be playing a larger role in the observed ΔE_p values than contact resistance.

Table 6.2: Uncompensated Resistance Values for all electrodes.

Electrode	R_u (Ω)	R_u Error (Ω)
Blank – Disk	100	1
Blank – Ring	61	1
NDC – Disk	114	5
NDC – Ring	59	1

The surface roughness of the disk electrodes was characterised by white light interferometry (Figure 6.7) to understand the effect of the laser ablation on surface morphology and to provide a measurement of electrode surface area.

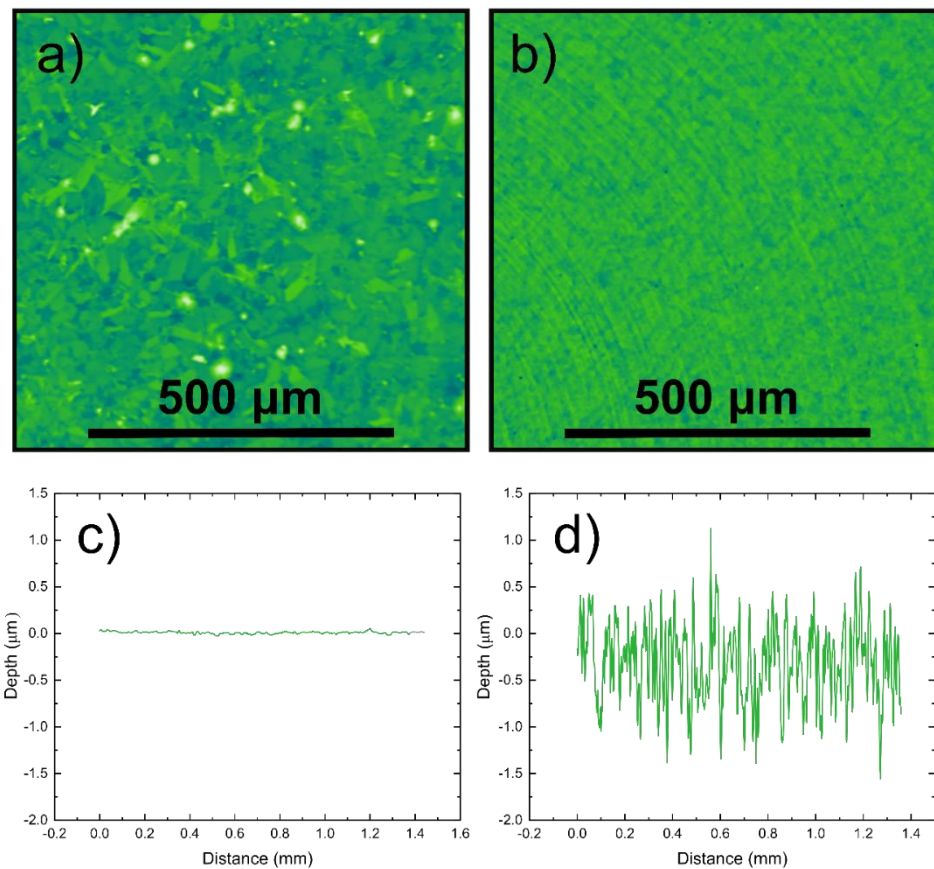


Figure 6.7: White Light Interferometry images using a 5 \times objective of a) The blank BDD disk electrode, giving an RMS of 10 nm. b) The sp^2 BDD disk electrode, giving an RMS of 460 nm. The circular tracks in this image are the raster of the laser micromachining system. c) Line profile diagonally across a showing the surface height variation. d) Line profile diagonally across b showing the surface height variation.

The BDD disk was shown to be smooth with an RMS of 10 nm RMS, slightly rougher than the bulk wafer measurement as a result of roughening during air annealing. Incorporation of NDC into the surface by laser ablation increased the roughness of the disk to 460 nm RMS. The surface integrated quinone electrochemical response was used to provide an indication of NDC content of the surface (Figure 6.8).³⁵

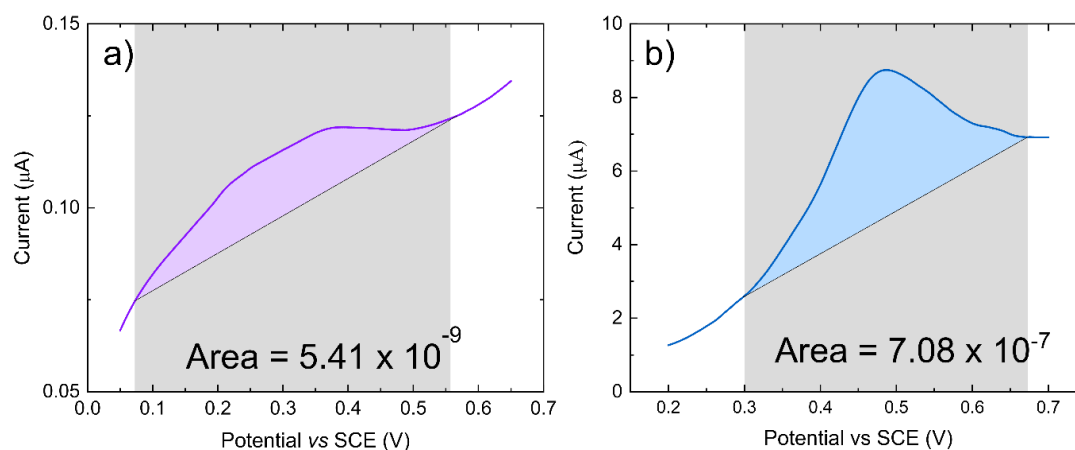


Figure 6.8: QSC Measurements of a) Blank b) sp^2 disk electrodes. Measurements conducted in pH 2 Carmody Buffer at 0.1 V s^{-1} scan rate. Note that a different integration window had to be chosen for each electrode due to the difference in peak shape and position.

It has been previously shown that there is a direct relationship between the quinone surface coverage and amount of NDC present in BDD electrode surfaces.³⁵ The quinone peak has an area of 5.41×10^{-9} and 7.08×10^{-7} for the Blank and NDC disks respectively. These areas can then be converted to surface coverage as discussed in Chapter 2, Section 2.5.1. This indicates that the NDC modified disk had two orders of magnitude more quinone groups ($2.56 \times 10^{-10} \text{ mol cm}^{-2}$) in the surface than the BDD disk ($1.98 \times 10^{-12} \text{ mol cm}^{-2}$). The presence of quinones in the BDD disk is likely to be due to a small contribution of NDC from the laser-cut disk edge, which may be slightly exposed.³⁴

6.3.7 Collection Efficiency Characterisation

The collection efficiency of the RRDEs for the redox couple $\text{FcTMA}^+ / \text{FcTMA}^{2+}$ were measured for comparison with the theoretical efficiency for both the BDD disk (Figure 6.9a) and the NDC coated disk (Figure 6.9b) RRDEs. In both experiments the potential of the disk electrode was swept from a value where no electron transfer occurred (0.00 V vs SCE) to one where the oxidation of FcTMA^+ to FcTMA^{2+} was mass transport limited. The potential of the BDD ring was held at a value where reduction of FcTMA^{2+} was also mass transport limited (0.05 V vs SCE). The experiments were performed as a function of rotation rate from 1000 rpm to 2500 rpm in 500 rpm steps.

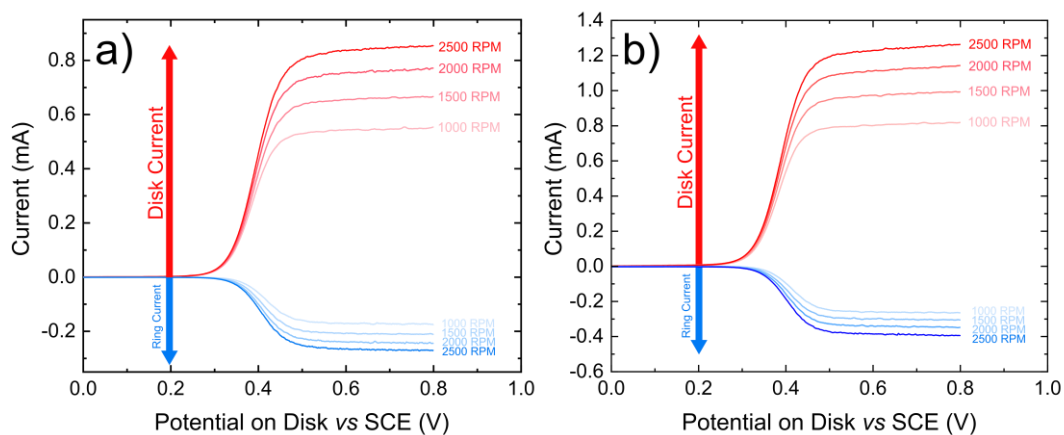


Figure 6.9: LSVs for a) blank disk RRDE, and b) NDC disk RRDE. Recorded at 100 mV s^{-1} in an aerated solution of 1 mM FcTMA^+ in 0.1 M KNO_3 . Ring held at 0.05 V vs SCE .

From these generation-collection experiments the empirical collection efficiency ($N_{\text{empirical}}$) of each RRDE was calculated by taking the ratio of the disk to ring currents in the limiting current region (0.60 V vs SCE) according to Equation 6.2.^{2,36}

$$\text{Equation 6.2: } N_{\text{empirical}} = \frac{|Disk \text{ Current}|}{|Ring \text{ Current}|} \times 100$$

Based on the disk (diameter = 5.00 mm) and ring dimensions (inner and outer diameter = 7.00 and 9.00 mm) the theoretical current efficiency,³⁶ of these electrodes is 35% . The BDD disk and ring RRDE has an empirical collection efficiency of 32% , very close to the theoretical value. The NDC coated disk and BDD ring electrode has a very slightly lower empirical collection efficiency of 31% .

The disk electrode currents on both RRDEs were plotted against rotation rate to extract diffusion coefficients for FcTMA^+ (Figure 6.10). A disk electrode with ideal hydrodynamics should have good agreement with the Levich equation, Equation 6.3.³⁷ Where I_L is the limiting current, n is the number of electrons transferred, F is Faraday's constant, A is the electrode area, D is the diffusion coefficient, ω is the rotation rate, ν is the kinematic viscosity of the solution, and C is the concentration of the analyte.

$$\text{Equation 6.3: } I_L = (0.620) n F A D^{\frac{2}{3}} \omega^{\frac{1}{2}} \nu^{-\frac{1}{6}} C$$

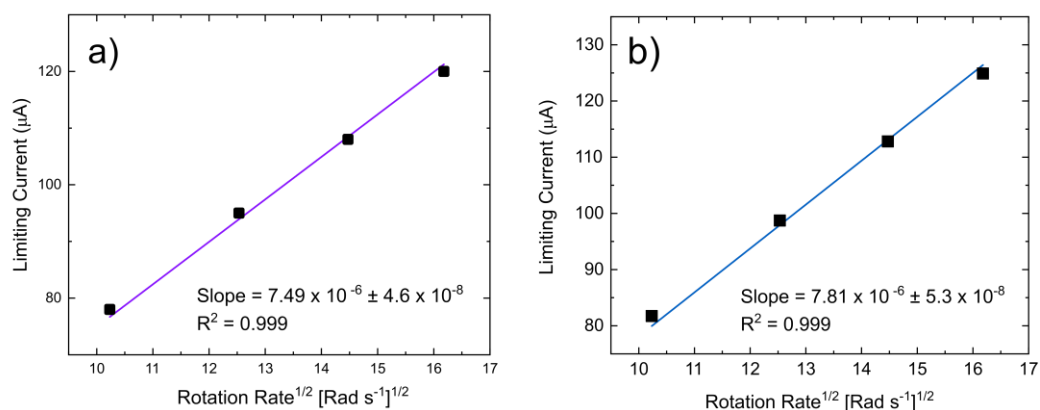


Figure 6.10: Levich analysis for the disk of a) blank disk RRDE, and b) NDC disk RRDE in 1 mM FcTMA⁺ in 0.1 KNO₃ at rotation rates from 1,000 to 2,500 rpm.

Levich analysis of the blank disk gives an R² of 0.999, demonstrating that this electrode performs in agreement with the theory. Extracting a diffusion coefficient from the gradient gives a D value for FcTMA⁺ of $5.1 \times 10^{-6} \text{ cm}^2 \text{ s}$, a slight overestimate from the value of 5.08×10^{-6} measured on a 25 μm diameter Pt UME. Levich analysis of the NDC disk also demonstrates a good adherence to theory with an R² of 0.999. Extracting a FcTMA⁺ diffusion coefficient from this data gives a value of $4.9 \times 10^{-6} \text{ cm}^2 \text{ s}$.³⁸

6.3.8 Pt Deposition and Hydrogen Peroxide Calibration

Initially the detection of H₂O₂ was trialled on the BDD ring, however no H₂O₂ peak was observed (data not shown). Thus, before carrying out ORR measurements, it was first necessary to verify that the BDD ring electrode could be sensitized towards H₂O₂ detection. Sensitization was achieved by electrodeposition of Pt NPs on the ring surface (see experimental section). After electrodeposition, SEM imaging revealed a high-density of Pt-NPs 10's of nm in size on the electrode surface (Figure 6.11).

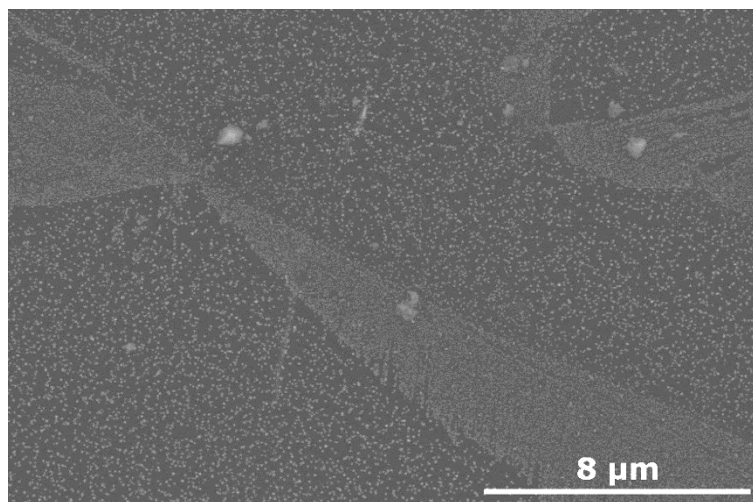


Figure 6.11: FE-SEM image of the Pt-Np modified ring electrode.

The response of the Pt-NP BDD ring electrode to H_2O_2 in 0.1 M HClO_4 was first studied under stationary conditions (0 rpm) to identify the H_2O_2 oxidation peak (Figure 3a) for a range of H_2O_2 concentrations ($[\text{H}_2\text{O}_2]$) from 0.00 – 3.37 mM. The CV commenced at 0.6 V *vs* SCE and was scanned positive to 1.5 V *vs* SCE and then negative to -0.2 V *vs* SCE. Three CVs were recorded per concentration. To focus on the H_2O_2 oxidative response the oxidative window only of the third CV (for each concentration) is presented in Figure 6.12.

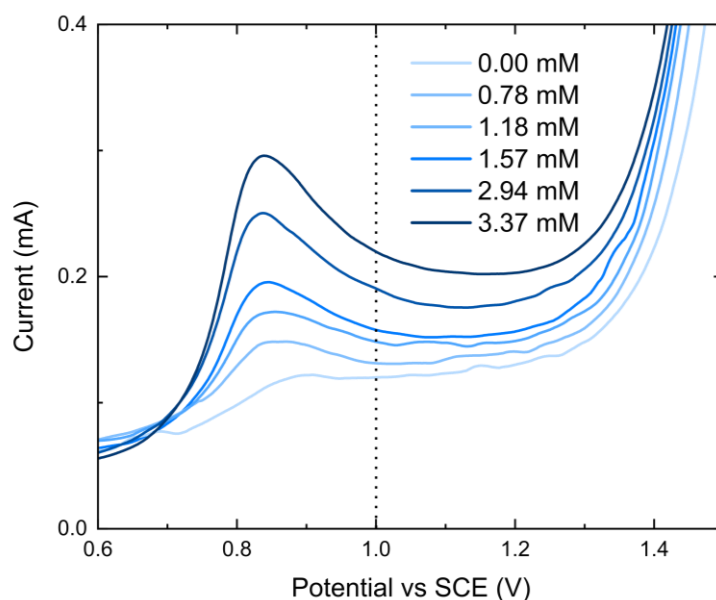


Figure 6.12: Forward sweep of CVs on the Pt-NP BDD ring in 0.1 M HClO_4 with increasing concentrations of H_2O_2 from 0 to 3.37 mM. Dotted line, the potential chosen (1.00 V *vs* SCE) for the ring in H_2O_2 generation collection experiments.

The CVs revealed an oxidative peak at ~ 0.85 V *vs* SCE which increased with H_2O_2 concentration, demonstrating good linearity ($R^2 = 0.993$, data not shown). A ring potential of

1.00 V vs SCE was chosen for H_2O_2 generation collection experiments, as a compromise between providing sufficient overpotential to drive the oxidative reaction but free from any currents associated with the electro-oxidation of water on the Pt NPs. The value of 1.00 V vs SCE is similar to those in the literature for H_2O_2 oxidation on Pt.^{4,39,40}

H_2O_2 concentration ($[\text{H}_2\text{O}_2]$) calibration experiments were recorded immediately after electrodeposition of the Pt NPs, as detailed in the experimental section. A typical calibration plot is shown in Figure 3b. Generation-collection experiments to study ORR were then performed, and the ring electrode calibrated again for $[\text{H}_2\text{O}_2]$ post experiment. Each ORR generation-collection experiment was only considered valid if the pre- and post-calibration gradients (in mA mM^{-1}) were within 10% of each other. The pre-calibration gradient was employed to calculate $[\text{H}_2\text{O}_2]$ from the ring currents. Each Pt NP deposited ring electrode was only used for one set of ORR generation collection experiments (a maximum of three LSVs) to alleviate any possible concerns about the long-term stability of the Pt-NPs under rotation. Before and after $[\text{H}_2\text{O}_2]$ calibrations of the Pt NP-BDD ring electrodes for both RRDEs can be found in Figure 6.13 for the BDD disk and Figure 6.14 for the NDC modified disk.

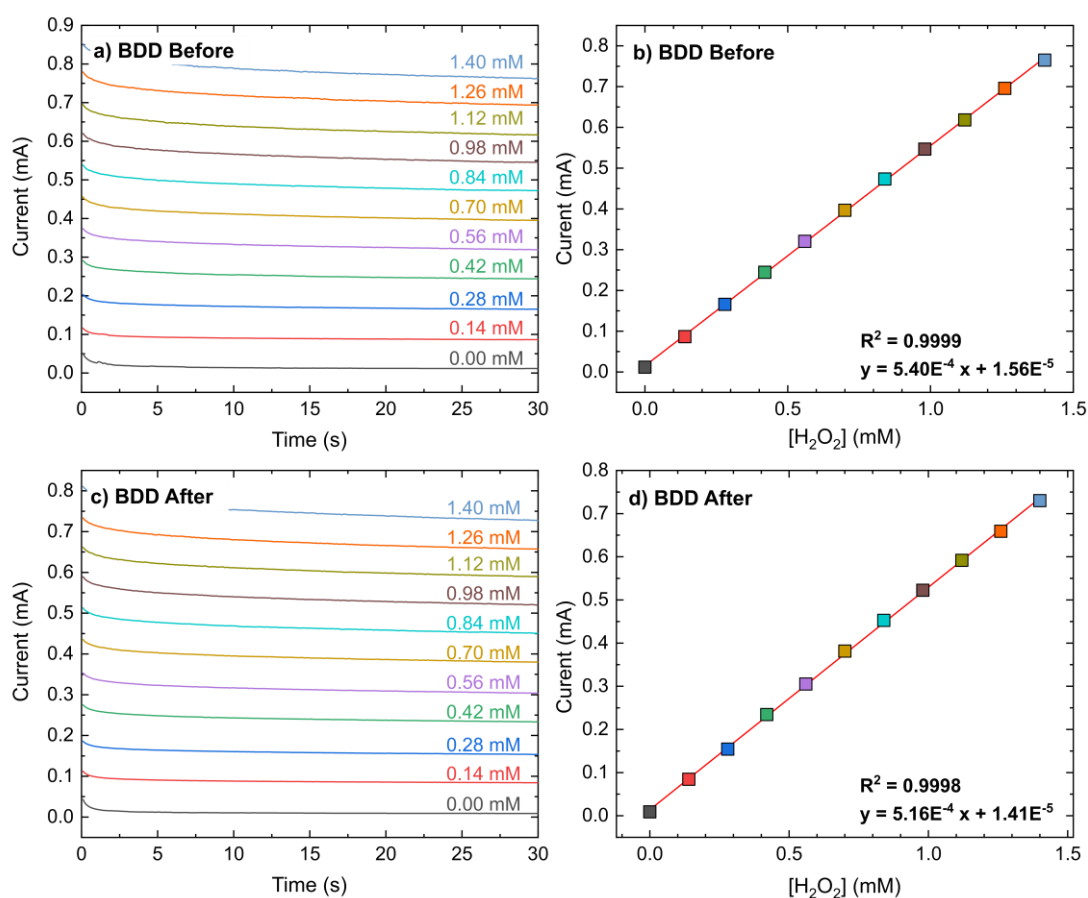


Figure 6.13: Before and after calibrations for the Pt nanoparticle deposited ring on the RRDE with blank BDD disk electrode. Ring held at 1.0 V vs SCE and H_2O_2 added via standard

addition. a) Current-time responses for the ring before generation-collection experiments. b) Calibration plot of the average current over the last 5s vs H_2O_2 concentration before generation-collection experiments. c) Current-time responses for the ring after generation-collection experiments. d) Calibration plot of the average current over the last 5s vs H_2O_2 concentration after generation-collection experiments. The ring was calibrated before and after generation-collection experiments to ensure that the before calibration was still valid.

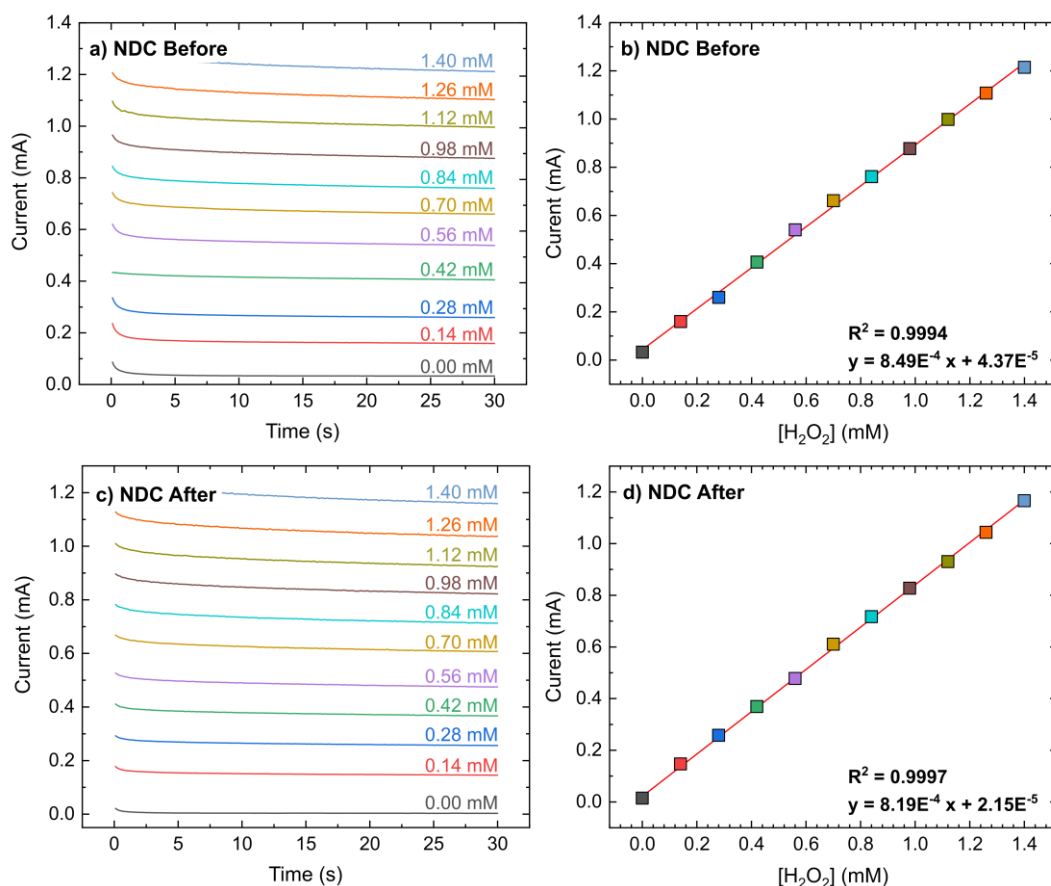


Figure 6.14: Before and after calibrations for the Pt nanoparticle deposited ring on the RRDE with NDC modified BDD disk electrode. Ring held at 1.0 V vs SCE and H_2O_2 added via standard addition. a) Current-time responses for the ring before generation-collection experiments. b) Calibration plot of the average current over the last 5s vs H_2O_2 concentration before generation-collection experiments. c) Current-time responses for the ring after generation-collection experiments. d) Calibration plot of the average current over the last 5s vs H_2O_2 concentration after generation-collection experiments. The ring was calibrated before and after generation-collection experiments to ensure that the before calibration was still valid.

6.3.9 Case Study: Hydrogen Peroxide Generation

For ORR, the two disk electrodes were scanned over a reductive potential range from a value where no current flows (at 0.00 V vs SCE) into the start of the reductive solvent window (-1.00 V vs SCE) in both aerated and O_2 saturated, 0.1 M HClO_4 (Figure 6.15a). The Pt NP-

BDD ring electrode was held at +1.00 V throughout to detect any H_2O_2 formed during ORR. Here the ring currents for H_2O_2 detection have been converted to a concentration using the acquired calibration gradients from before the ORR experiment as well as the empirical collection efficiency (Figure 6.15b).

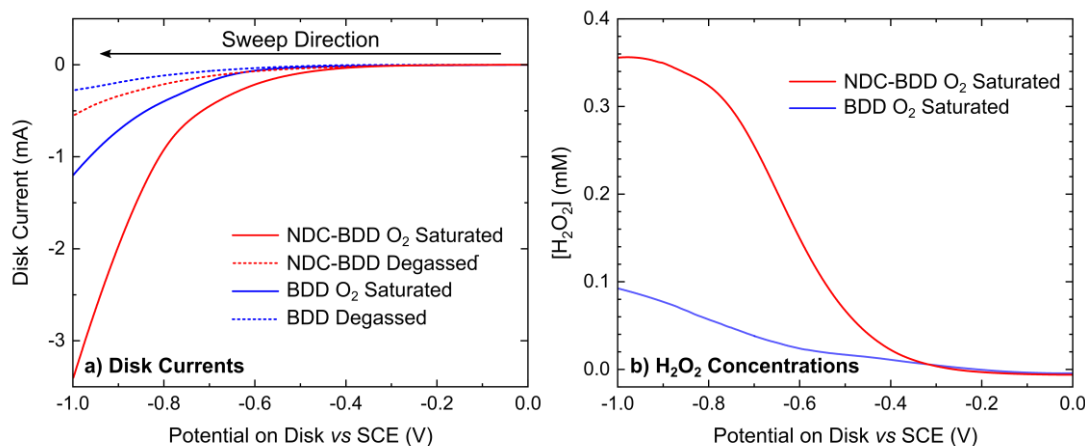


Figure 6.15: Generation collection experiments conducted at 2000 rpm in 0.1 M HClO_4 on both RRDE in oxygen saturated and degassed conditions: a) LSVs on the disk electrodes scanned at 5 mV s^{-1} . b) Generated H_2O_2 concentration vs disk potential for the oxygen saturated condition.

For the NDC modified BDD disk, in the presence of saturated dissolved O_2 , (solid red line), when comparing against the de-aerated solution response (dashed red line), ORR appears to commence just before reduction of protons (0.1 M HClO_4) starts to dominate the LSV response, the latter occurring ca. -0.75 V vs SCE . Thus, no steady-state response for ORR is observed. This is not surprising as ORR is known to be sluggish on carbon surfaces in acid electrolytes.²² However, ORR becomes much clearer when observing the generated $[\text{H}_2\text{O}_2]$ as a function of disk potential, solid red line in Figure 4b. Here the $[\text{H}_2\text{O}_2]$ can be seen to increase from 0 mM, at a disk potential of 0.00 V vs SCE to a maximum, constant value of $\sim 0.36 \text{ mM}$, for disk potentials of ca. -1.00 V vs SCE . The $[\text{H}_2\text{O}_2]$ data thus enables the potential at which ORR begins to be more clearly identified. On the BDD disk electrode in the O_2 saturated solution (blue solid line, Figure 4a), the LSV response towards ORR appears even more catalytically hindered. This is again in agreement with the $[\text{H}_2\text{O}_2]$ ring data (blue line, Figure 4b) which shows a notable rise in concentration only when the potential is made more negative than ca. -0.60 V vs SCE . At -1.00 V vs SCE , the $[\text{H}_2\text{O}_2]$ has reaches a maximum value of 0.9 mM. This data highlights the ability of the NDC to increase the electrocatalytic activity of the BDD surface towards ORR and highlights the prominence of the 2-electron transfer pathway. The faradaic efficiency (FE) for H_2O_2 generation each electrode was calculated at -0.60 , -0.70 , and -0.80 V vs SCE according to Equation 6.5,³⁷ and are summarised in Table 6.3.

$$\text{Equation 6.4: } \%FE = \frac{i_{Ring}}{i_{Disk} N_{Empirical}}$$

Table 6.3: Faradaic efficiencies for the generation of hydrogen peroxide on both disk electrodes.

Disk Electrode	% CE	Potential (V) vs SCE	Disk Current (mA)	Ring Current (mA)	% FE
Blank	32	- 0.6	0.0646	0.0054	26%
		-0.7	0.1814	0.0078	13%
		-0.8	0.3980	0.0011	1%
NDC	31	- 0.6	0.2154	0.0427	64%
		-0.7	0.4511	0.0697	50%
		-0.8	0.9241	0.0868	30%

For both disk electrodes the highest FE is seen at the least negative potential (-0.60 V vs SCE) with 26% for the BDD electrode and 64% for the NDC modified BDD electrode. As the potential becomes increasingly negative, the FE decreases, reaching 1% (for NDC) and 30% (for BDD) at -0.80 V. This is not surprising, as proton reduction (0.1 M HClO₄) is now competing with ORR. Determining mechanistic pathways for ORR is far simpler when the ORR process is isolated from the electrolyte reduction reaction. Higher faradaic efficiencies are seen for the NDC-BDD electrode at disk potentials closer to the switch on potential (-0.3 V vs SCE), however the ring currents are much closer to the background currents in these regions.

6.4 Conclusions

This chapter describes a DIY guide incorporating 3D printing to constructing a RRDE using any electrode material that can be produced in rod, wafer or foil form. It is also extendable to materials made in powder form that can be pressed into a pellet, or materials that can be deposited onto a conductive substrate by processes such as physical/chemical vapour deposition, sputtering/evaporation. Electrodes fabricated by these methods can also be modified in conventional ways, such as drop casting or electrodepositing electrocatalysts onto the surface. This approach thus widens the range of possible electrode materials usable in the

RRDE set-up, increases accessibility of the technique and enables a larger range of RRDE applications, especially in the electrocatalysis field.

The DIY approach is illustrated via the first-time construction of a RRDE containing both coplanar BDD disk and ring electrodes. The collection efficiency of the BDD RRDE was shown to be very close to that theoretically predicted (using a simple redox species $\text{FcTMA}^+/\text{FcTMA}^{2+}$). The impact of NDC presence in BDD on its electrocatalytic activity towards ORR in acid electrolyte was investigated by employing NDC-BDD disk electrodes in the RRDE set-up. Sensitization of the BDD ring electrode towards H_2O_2 detection was achieved by functionalizing with electrodeposited Pt NPs. Even though the ORR signal on the NDC-BDD disk was mostly obscured by proton reduction, a clear response for H_2O_2 detection was observed on the ring, rising in concentration with increasing disk potential, until a limiting value was reached. Over the same potential range, the bare BDD disk showed much more sluggish electroactivity towards ORR. The ORR signal is barely discernible, and reduced concentrations of H_2O_2 are detected. This data also highlights the use of BDD as an excellent electrocatalyst support material given its very low electrocatalytic activity. For work requiring acid or alkaline solutions and high oxidizing potentials BDD also serves as an ideal corrosion free support.

6.5 References

- 1 A. N. Frumkin, L. N. Nekrasov, B. Levich and J. Ivanov, *J. Electroanal. Chem.*, 1959, **1**, 84–90.
- 2 W. J. Albery and S. Bruckenstein, *Trans. Faraday Soc.*, 1966, **62**, 1920–1931.
- 3 J. Albery, W and I. Hitchman, M, *Ring-Disc Electrodes*, Oxford University Press, 1971.
- 4 U. A. Paulus, T. J. Schmidt, H. A. Gasteiger and R. J. Behm, *J. Electroanal. Chem.*, 2001, **495**, 134–145.
- 5 A. Bonakdarpour, M. Lefevre, R. Yang, F. Jaouen, T. Dahn, J. P. Dodelet and J. R. Dahn, *Electrochem. Solid-State Lett.*, , DOI:10.1149/1.2904768.
- 6 C. Du, Y. Sun, T. Shen, G. Yin and J. Zhang, *Applications of RDE and RRDE Methods in Oxygen Reduction Reaction*, Elsevier B.V., 2014.
- 7 M. Ferrara, M. Bevilacqua, C. Tavagnacco, F. Vizza and P. Fornasiero, *ChemCatChem*, 2020, **12**, 6205–6213.
- 8 Z. Duan and G. Henkelman, *Langmuir*, 2018, **34**, 15268–15275.
- 9 J. Zhang, W. J. Pietro and A. B. P. Lever, *J. Electroanal. Chem.*, 1996, **403**, 93–100.
- 10 S. Hessami and C. W. Tobias, *AIChE J.*, 1993, **39**, 149–162.
- 11 L. Hutton, M. E. Newton, P. R. Unwin and J. V. Macpherson, *Anal. Chem.*, 2009, **81**, 1023–1032.
- 12 Y. Tang, G. P. Kotchey, H. Vedala and A. Star, *Electroanalysis*, 2011, **23**, 870–877.
- 13 S. Guo, D. Wen, Y. Zhai, S. Dong and E. Wang, *ACS Nano*, 2010, **4**, 3959–3968.
- 14 R. hai Tian and J. fang Zhi, *Electrochem. commun.*, 2007, **9**, 1120–1126.
- 15 Y. Zhang, S. Asahina, S. Yoshihara and T. Shirakashi, *Electrochim. Acta*, 2003, **48**, 741–747.
- 16 J. Kruusma, C. E. Banks and R. G. Compton, *Anal. Bioanal. Chem.*, 2004, **379**, 700–706.
- 17 W. Kennedy and H. Linge, *Rev. Sci. Instrum.*, 1983, **54**, 361–365.
- 18 S. Menezes, L. F. Schneemeyer and B. Miller, *J. Electrochem. Soc.*, 1981, **128**, 2167–2169.

- 19 J. V. Macpherson, *Phys. Chem. Chem. Phys.*, 2015, **17**, 2935–2949.
- 20 S. J. Cobb, Z. J. Ayres and J. V. Macpherson, *Annu. Rev. Anal. Chem.*, 2018, **11**, 463–484.
- 21 D. Wakerley, A. G. Güell, L. A. Hutton, T. S. Miller, A. J. Bard and J. V. Macpherson, *Chem. Commun.*, 2013, **49**, 5657–5659.
- 22 E. Yeager, *Electrochim. Acta*, 1984, **29**, 1527–1537.
- 23 Z. J. Ayres, A. J. Borrill, J. C. Newland, M. E. Newton and J. V. Macpherson, *Anal. Chem.*, 2016, **88**, 974–980.
- 24 T. L. Read, S. J. Cobb and J. V. Macpherson, *ACS Sensors*, 2019, **4**, 756–763.
- 25 S. J. Cobb, F. H. J. Laidlaw, G. West, G. Wood, M. E. Newton, R. Beanland and J. V. Macpherson, *Carbon N. Y.*, 2020, **167**, 1–10.
- 26 Z. J. Ayres, A. J. Borrill, J. C. Newland, M. E. Newton and J. V. Macpherson, *Anal. Chem.*, 2016, **88**, 974–980.
- 27 E. Yeager, *J. Mol. Catal.*, 1986, **38**, 5–25.
- 28 S. Yang, A. Verdaguer-Casadevall, L. Arnarson, L. Silvioli, V. Čolić, R. Frydendal, J. Rossmeisl, I. Chorkendorff and I. E. L. Stephens, *ACS Catal.*, 2018, **8**, 4064–4081.
- 29 L. A. Hutton, J. G. Iacobini, E. Bitziou, R. B. Channon, M. E. Newton and J. V. Macpherson, *Anal. Chem.*, 2013, **85**, 7230–7240.
- 30 S. J. Cobb and J. V. Macpherson, *Anal. Chem.*, 2019, **91**, 7935–7942.
- 31 A. W. Colburn, K. J. Levey, D. O'Hare and J. V. Macpherson, *Phys. Chem. Chem. Phys.*, 2021, **23**, 8100–8117.
- 32 W. Xing, M. Yin, Q. Lv, Y. Hu, C. Liu and J. Zhang, *Oxygen Solubility, Diffusion Coefficient, and Solution Viscosity*, Elsevier B.V., 2014.
- 33 J. J. Tully and G. N. Meloni, *Anal. Chem.*, 2020, **92**, 14853–14860.
- 34 J. Li, C. L. Bentley, S. Y. Tan, V. S. S. Mosali, M. A. Rahman, S. J. Cobb, S. X. Guo, J. V. Macpherson, P. R. Unwin, A. M. Bond and J. Zhang, *J. Phys. Chem. C*, 2019, **123**, 17397–17406.
- 35 Z. J. Ayres, S. J. Cobb, M. E. Newton and J. V. Macpherson, *Electrochem. commun.*, 2016, **72**, 59–63.

- 36 Z. Jia, G. Yin and J. Zhang, *Rotating Ring-Disk Electrode Method*, Elsevier B.V., 2014.
- 37 A. J. Bard and L. R. Faulkner, *Electrochemical Methods - Fundamentals and Applications*, Wiley, 2nd edn., 2001, vol. 2.
- 38 H. Zhang, K. Aoki, J. Chen, T. Nishiumi, H. Toda and E. Torita, *Electroanalysis*, 2011, **23**, 947–952.
- 39 N. M. Markovic, H. A. Gasteiger and P. N. Ross, *J. Phys. Chem.*, 1995, **99**, 3411–3415.
- 40 T. J. Schmidt, U. A. Paulus, H. A. Gasteiger and R. J. Behm, *J. Electroanal. Chem.*, 2001, **508**, 41–47.

Chapter 7: Conclusions and Future Work

In recent years lab-grown diamond has found several applications for which it is uniquely suited, or better than all other alternatives. Boron Doped Diamond (BDD) especially has found widespread use as an electrode material due to its best-in-class electrochemical properties and resistance to chemical degradation. Over the course of this thesis several applications of diamond materials have been investigated.

In Chapter 3 an implantation and lift-off method for producing thin diamond membranes was investigated. Numerous solution chemistries were employed with a view to speeding up the electrochemical removal of an implanted layer of sp^2 carbon within a single crystal diamond plate, freeing a sub-micron diamond membrane. By carefully tailoring the solution chemistry etch rates 40× faster than those previously reported can be accessed. EPR spectroscopy was also employed to get a better idea of the nature of the radical mechanisms at play, revealing an unusual chaining mechanism which allowed radical species to exist in solution much longer than was expected.

Further work in this area could include investigating how the material properties single crystal diamond into which the sp^2 carbon is implanted, influence the etch rate. This would include investigating the differences between HPHT and CVD diamond and looking at diamond substrates implanted both along and through the growth direction. This insight could lead to different sample preparation procedures which result in even shorter etch times. Employing this lift-off method on polycrystalline material is also worth exploring. If this was successful thin (electron transparent) membranes of BDD would be interesting platforms for tandem electrochemical transmission electron microscopy. Finally, we believe there are wider benefits to be gained in diamond nanofabrication by using this combined implantation, non-contact electrochemical etching approach, for example in the nanofabrication of diamond pillars, channels, or pores.

In Chapter 4 several factors affecting the corrosion of BDD when used as an anode in electrochemical advanced oxidation systems are investigated. To do this a novel and direct method of measuring the etch rate on laboratory timescales was developed, utilising white light interferometry to characterise the amount of material removed after a 72-hour electrolysis. It was demonstrated that solution composition had a major effect on anodic corrosion, particularly the nature of any organic species. Operational parameters like current density and polarity switching frequency were also investigated, demonstrating that corrosion rate is approximately linear with current density and that polarity switching has no affect on

corrosion rate as long as the polarity is switched less frequently than once every 450s. The most significant findings however concerned the choice of BDD material employed. Three BDD materials were trialled, an electroanalytical (EA) grade freestanding BDD, an electroprocessing grade (EP) freestanding BDD, and some thin-film BDD. The EA grade corroded at half the rate of the EP grade, however the thin-film material eroded thirty times faster than EP grade. These initial results raise questions about the use of thin-film BDD in electrochemical advanced oxidation systems.

Further work in this area could include, using AFM to study the initial stages of electrode corrosion over the first few hours. This would be especially interesting if it could be performed in an “identical-location” fashion where data from AFM, EBSD, SEM and Raman mapping could be correlated before and after erosion. XPS measurements on the corroded surfaces after electrolysis in different solutions could also be enlightening as the surface chemistry may be different for different solution compositions. Following on from this the corrosion of BDD single crystals of different orientations would also help to elucidate if there is in fact quick and slow corrosion orientations in BDD, as suggested in Chapter 4. Finally, EA-BDD and thin-film corrosion experiments could be run in acetic acid solutions, to see if the ratios of corrosion rates stay the same in this solution.

In Chapter 5 the effect of electrode design on the ozone output and current efficiency of a small-scale electrochemical ozone generator is investigated. Here the idea that efficiency and output of cells with perforated electrodes are governed by a catalytic “triple-point” is challenged and we instead believe that the non-diamond carbon content; rather than geometry, of the electrodes is the critical factor. We also demonstrate a novel non-perforated cell design which has not been previously reported, demonstrating the flexibility of electrochemical ozone production cells. While these cells currently have a lower current efficiency than the perforated cells in this work this could likely be improved with further development. We also demonstrate that the non-diamond carbon formed by laser micromachining and acid cleaning is highly stable, with the EOP gradient and current efficiency showing only a slight decrease after 20-hours of continuous operation.

Further work in this area could look at the optimisation of the non-perforated cell design to improve its performance. The effect of material choice for the cathode could also be investigated to improve the power efficiency of the cell, choosing a cathode which is more catalytically active towards hydrogen evolution may reduce the potentials needed to run the cell at a given current density. Similarly, the effect of the catholyte on ozone output could be investigated in cells with anode and cathode compartments that can be separated. Decreasing the temperature of the anolyte may also serve to increase the concentration of ozone produced,

by preventing degradation of generated ozone and increasing its solubility in water. Transmission electron microscopy studies of thin cross-sections of the ozone generation electrodes may help to elucidate the nature of any changes in the electrodes surface as a result of 20-hour long term experiments as well as helping to understand its remarkable stability.

In Chapter 6 a highly versatile and low-cost rotating ring disk has been designed and built. The electrodes are designed with simple construction in mind, allowing them to be assembled as needed without access to specialist facilities or tools. The effectiveness of this method is demonstrated by fabricating two all-BDD rotating ring disk electrodes and demonstrating their adherence to theory. The electrodes were then used to demonstrate that the addition of non-diamond carbon to the disk surface increases BDDs catalytic activity towards producing H_2O_2 via the two-electron oxygen reduction reaction.

Further work in this area could include adapting the design to incorporate different ring and disk electrodes to study other reactions. To push the concept of low-cost RRDEs even further an entirely 3D printed RRDE could be designed. Using this method an RRDE could be fabricated for less than £5, allowing it to be used in both teaching and research environments without concerns over cost or breakage. The RRDE could be made from a relatively inexpensive material, carbon filled polymer, and could be printed in either one piece or several parts, allowing it to be made on a variety of 3D printers.